2015

Magnetically levitating low-friction test stand for the evaluation of micro-thrusters

Amit Patel

MAGNETICALLY LEVITATING LOW-FRICTION TEST STAND FOR THE EVALUATION OF MICRO-THRUSTERS

by

AMIT PATEL

A THESIS

Submitted in partial fulfillment of the requirements
for the degree of Master of Science in Engineering
in
The Department of Mechanical and Aerospace Engineering
to
The School of Graduate Studies
of
The University of Alabama in Huntsville

HUNTSVILLE, ALABAMA

2015

In presenting this thesis in partial fulfillment of the requirements for a master's degree from The University of Alabama in Huntsville, I agree that the Library of this University shall make it freely available for inspection. I further agree that permission for extensive copying for scholarly purposes may be granted by my advisor or, in his/her absence, by the Chair of the Department or the Dean of the School of Graduate Studies. It is also understood that due recognition shall be given to me and to The University of Alabama in Huntsville in any scholarly use which may be made of any material in this thesis.

Amit Patel

11/13/15

(date)

THESIS APPROVAL FORM

Submitted by Amit Patel in partial fulfillment of the requirements for the degree of Master of Science in Engineering in Mechanical Engineering and accepted on behalf of the Faculty of the School of Graduate Studies by the thesis committee.

We, the undersigned members of the Graduate Faculty of The University of Alabama in Huntsville, certify that we have advised and/or supervised the candidate of the work described in this thesis. We further certify that we have reviewed the thesis manuscript and approve it in partial fulfillment of the requirements for the degree of Master of Science in Engineering in Mechanical Engineering.

Dr. Jason Cassibry	11/13/2015 (Date)	Committee Chair
Dr. David Lineberry	11/13/2015 (Date)	
Dr. Robert Frederick	11/13/2015 (Date)	
Dr. Keith Hollingsworth	11/13/15 (Date)	Department Chair
Dr. Shankar Mahalingam	11/13/15 (Date)	College Dean
Dr. David Berkowitz	12/2/15 (Date)	Graduate Dean

ABSTRACT

School of Graduate Studies
The University of Alabama in Huntsville

Degree Masters of Science in Engineering College/Dept. Engineering/Mechanical and Aerospace Engineering

Name of Candidate Amit Patel

Title Magnetically Levitating Low-Friction Test Stand for the Evaluation of Micro-thrusters

A new magnetically levitating low-friction test stand was developed for the purpose of ground testing micro-propulsion devices. The goal was to evaluate the performance characteristics of micro-thrusters by taking measurements during individual firings and calculating specific impulse and impulse-bit in the milli-Newton second range under atmospheric pressure. The test stand utilized a magnetic levitation controller to suspend a payload containing the necessary firing and data collection electronics. Upon firing, the levitating payload rotated (similar to a thrust balance configuration) and the lateral acceleration and angular velocity data were collected. Sensor calibration experiments, performed with a high speed camera, verified proper function of the gyroscopic sensor. Uncertainty analysis was performed on a series of data from atmospheric experiments. Uncertainty for impulse-bit measurements generally ranged from 6.8% - 8.1% and specific impulse uncertainty ranged from 10%-23%. The micro-thrusters analyzed had an impulse-bit range from 0.1 - 2.75 mN-s and a specific impulse range from 30 - 400 seconds.

Abstract Approval: Committee Chair

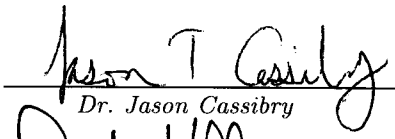

Dr. Jason Cassibry

Department Chair

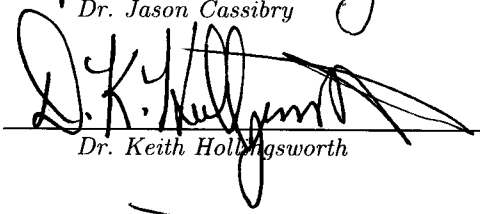

Dr. Keith Hollingsworth

Graduate Dean

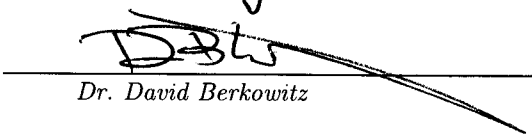

Dr. David Berkowitz

ACKNOWLEDGMENTS

My journey all started as a young boy looking up at the stars. Many years later I'm a young man looking up at the stars. Nothing has changed except my toys are bigger and my goals are higher. I have truly enjoyed the opportunity to do research at the UAH Propulsion Research Center. Over the past few years I have had the great pleasure in getting to know everyone and sharing adventures. The people helped make the PRC a fun place to work.

My advisor, Dr. Jason Cassibry, deserves much of the credit for providing excellent leadership and much needed stability to my research. Drs. Robert Frederick, David Lineberry, and Richard Tyson also provided fantastic mentoring. I would like to acknowledge Dr. Nathan Slegers for initially bringing me onto the project and laying the foundation for my research. I am absolutely honored and privileged to have learned from the best.

Of course none of this would have been possible if not for the sacrifices and tireless efforts made by my parents, Sharad and Parulata. They have been my inspiration and have challenged me to exceed my own expectations. Their encouragement and unconditional support have been essential to following my interests. Because of their advice and guidance I am able to chase my dreams. I am proud to be their son.

Lastly, I want to thank Anthony, Tony, John, Matthew, Jake, Ben and all the other PRC members for the help and support I received. All we do is win!

TABLE OF CONTENTS

LIST OF FIGURES

FIGURE PAGE

LIST OF TABLES

TABLE PAGE

LIST OF SYMBOLS

SYMBOL	DEFINITION
a	Linear Acceleration in units of m/s^2
a_t	Tangential Acceleration in units of m/s^2
A	Dynamic Matrix
A_s	Exhaust Area in units of m^2
α	Angular Acceleration in units of rad/s^2
α_{stiff}	Controls the Size of the Stiffness
$ATOM$	Autonomous Tracking and Optical Measurement Laboratory
$AIAA$	American Institute of Aeronautics and Astronautics
ABS	Acylonitrile Butadiene Styrene
$ABIP$	Air Bag Inflator Propellant
AN	Ammonium Nitrate
B	Magnetic Induction Field in units of A/m
β	Controls the amount of non-linearity in the restoring force
β_{System}	Systematic Error
bps	Bytes Per Second
c	Damping Constant in units of N·s/m

C	Constant Variable
$C\theta$	$Cosine(\theta)$
$C\tau$	$Cosine(\tau)$
$C1$	Connection Point at Top of Experimental Setup
CAD	Computer Aided Design
D	Overall Deflection Sensitivity in units of m
d	Thruster Distance from the Rotational Axis in units of m
dt	Derivative of Time in units of s
δ	Size of the Dampening
δ_{twist}	Rise Due to Twist
δ_{total}	Total Error
ΔM	Change in Mass in units of g
$\Delta\omega$	Change in Angular Velocity in units of rad/s
$\Delta\Theta$	Change in Angular Position in units of rad
Δv	Change in Velocity in units of m/s
Δx	Radius of Accelerometers in units of m
Δx_{SS}	Change in steady state position in units of m
$DSSP$	Digital Solid State Propulsion
DC	Direct Current

$DFPCB$	Dual-Fire Printed Circuit Board
DAQ	Data Acquisition
dps	Degrees Per Second
DRE	Data Reduction Equation
E	Young's Modulus in units of N/m^2
E_o	Energy in units of J
E_e	Electric Field in units of A/m
E_K	Kinetic Energy in units of J
E_p	Potential Energy in units of J
ϵ	Random Error
ε	Amount of Non-Linearity
ε_0	Permittivity of the Vacuum
ε_r	Relative Permittivity
$ECESP$	Electrically Controlled Extinguishable Solid Propellants
ESP	Electrically-Controlled Solid Propellant
F	Thrust in units of N
F_{net}	Net Force in units of N
F_q	Electrostatic Force in units of N
$F(t)$	Applied Force in units of N

F_{cal}	Calibration Force in units of N
F_t	Tangential Force in units of N
F_S	Force from the Sensor Support in units of N
ft	Feet
FDM	Formative Deposition Modeling
$FEEP$	Field Emission Electric Propulsion
γ	Controls the Amplitude of the Periodic Driving Force
g	gram
g_0	Gravity Constant
h_p	Height of the Proof Mass from the Equilibrium Point in units of m
$HIPEP$	High Performance Electric Propellant
HAN	Hydroxyl Ammonium Nitrate
I	Mass Moment of Inertia in units of $kg{\cdot}m^2$
I_{zz}	Mass Moment of Inertia about the z-axis in units of kg$\cdot m^2$
$I_{bit,cal}$	Calibration Impulse in units of N·s
I_{bit}	Impulse Bit in units of N·s
I_L	Impulse Delivered in units of N·s
$I_{Pendulum}$	Pendulum Moment of Inertia in units of $kg{\cdot}m^2$
I_t	Total Impulse in units of N-s

IR	Infrared
Isp	Specific Impulse in units of s
j	Current Density in units of C/m
J	Joule
J_{ep}	Impulse Bit of Electric Propulsion in units of N-s
JRC	Johnson Research Center
k	Effective Spring Constant in units of N/m
K	Kelvin
K_d	Derivative Gain
K_p	Proportional Gain
kg	kilo-gram
λ	Damping Factor
L	Angular Momentum in units of N·m·s
L_{sus}	Suspension Length
L_{cal}	Calibration Force Location in units of m
L_c	Counterweights Center of Mass in units of m
l_{cm}	Distance from Center of Mass in units of m
l	Length of Moment Arm in units of m
l_T	Length of the thruster arm in units of m

$l_{Pendulum}$	Wire Length of the Pendulum in units of m
$\vec{l}$	Angular Momentum in units of kg$\cdot m^2$/s
$LVCTF$	Large Vacuum Chamber Test Facility
L_S	Length of the Sensor Arm in units of m
L_{mT}	Location of Thruster Center of Mass in units of m
L_B	Length of the Beams Center of Mass in units of m
L_t	Length of Moment Arm in units of m
L_{pm}	Point Distance in units of m
$\vec{L}$	Total Angular Momentum in units of kg$\cdot m^2$/s
LED	Light Emitting Diode
M	Mass in units of g
$M_{applied}$	Applied Moment Ignoring Drag in units of N-m
$M_{Gondola}$	Gongola Mass in units of g
M_{Proof}	Proof Mass in units of g
$M_{Thruster}$	Thruster Mass in units of g
m	meter
mm	milli-meter
m_0	Initial Mass in units of g
m_{bit}	Mass Bit in units of g

mN	milli-Newton
$mdps$	Milli-Degrees Per Second
μ	Distribution Mean
μ_e	Exhaust Velocity in units of m/s
μN	micro-Newton
μs	Micro-seconds
μF	Micro-Farad
$\dot{m}$	Mass Flow Rate in units of kg/s
MIT	Massachusetts Institute of Technology
MLC	Magnetic Levitation Controller
MAE	Mechanical and Aerospace Engineering Department
M_P	Moment of Propellant Pipe and Wires in units of kgm^2
$MOSFET$	Metal-Oxide-Semiconductor Field-Effect Transistor
$MEMS$	Microelectromechanical Systems
N	Newton
nN	nano-Newton
ω	Angular Velocity in units of rad/s
ω_n	Natural Frequency in units of rad/s
ω_f	Natural Frequency

ω_F	Controls the Frequency of the Periodic Driving Force
$OPSD$	Onboard Payload Stabilization Device
P_{ext}	Exhaust Pressure in units of N/m^2
P_s	Chamber Pressure in units of N/m^2
PPT	Pulsed Plasma Thruster
pfn	Pulsed Forming Network
PCS	Payload Constraint System
PD	Proportional-Derivative
PCB	Printed Circuit Board
R	Distance from the Centerline Axis to Thrust Vector in units of m
r	Radius in units of m
RP	Rapid Prototyping
s	Second
σ	Distribution Standard Deviation
S_x	Sample Standard Deviation
S_i	Standard Deviation Estimate for the Random Uncertainty
S_{b_i}	Standard Deviation Estimate for the Systematic Uncertainty
S_{cal}	Test Stand Sensitivity
$S\theta$	$Sine(\theta)$

$SPITfire$	Specialized Payload Intended for Thruster Firing
SCR	Silicon Controlled Rectifier
SOP	Standard Operating Procedure
t	Time in units of s
t_p	Pulse Length in units of s
t_b	Duration of Thrust in units of s
T	Tension in Strings
T_p	Period of Oscillations
$\vec{\tau}_{net}$	Net Torque in units of N-m
Θ_{max}	Initial Release Angle in units of rad
T_1, T_2	Force from Thrusters in units of N
Θ	Angular Position in units of rad
$\dot{\Theta}$	Angular Velocity in units of rad/s
$\ddot{\Theta}$	Angular Acceleration in units of rad/s^2
$\ddot{\theta}$	Angular Acceleration or Second Derivative of θ with Respect to Time
TTL	Transistor-Transistor Logic
τ	Torque in units of N-m
TSM	Taylor Series Method
U_r	Overall Uncertainty

$USSR$	Union of Soviet Socialist Republics
UAH	University of Alabama in Huntsville
UMF	Uncertainty Magnification Factors
UPC	Uncertainty Percentage Contribution
UAV	Unmanned Aerial Vehicle
u_c	Combined Standard Uncertainty
u_e	Exhaust Velocity in units of m/s
V	Volts
V_{pmax}	Maximum Velocity of Proof Mass in units of m/s
VAT	Vacuum-Arc Thruster
$VAHPER$	Variable Amplitude Hanging Pendulum with Extended Range
x	Displacement with Respect to Time
$\bar{X}$	Sample Mean
$\dot{x}$	Velocity or First Derivative of x with Respect to Time
$\ddot{x}$	Acceleration or Second Derivative of x with Respect to Time
x_{FS}	Maximum Linear Deflection in units of m
x'_{max}	Maximum Horizontal Displacement from the Gondola Equilibrium Point in units of m
w	watt
W	Weight in units of N

ζ	Damping Coefficient
$\underline{z}$	State Vector

To my loving parents, for helping me reach for the stars.

Live as if you were to die tomorrow; learn as if you were to live forever.

—Mahatma Gandhi

CHAPTER 1

INTRODUCTION

1.1 Overview

With the ever increasing use of small satellites (i.e. cubesats, cansats, spinsats) there has been a corresponding need for micro-thrusters for drag make-up, orbit changes, and attitude control. Development and testing of such propulsion systems require measuring milli-Newton-second (mN) range impulse-bits. One of the most common types of propulsion used for these applications are pulsed plasma thrusters (PPTs), in which a high voltage capacitor discharges an arc across a surface of solid propellant. The discharge times are of the order of microseconds (μs), the impulse bit (I_{bit}), the time integration of thrust, is on the order of a few mN-s. Performance measurements (thrust, impulse bit, and specific impulse) are challenging for such small thrusts and time scales due to low levels of impulse bits produced. This requires sensitive equipment to take measurements.

A new thrust stand has been developed at the University of Alabama in Huntsville (UAH) for measuring mN-s impulse bits at both atmosphere and vacuum pressures. The thrust stand consists of a magnetic levitation control system that is used to hover a payload to create a low-friction environment. Thrusters are mounted

to the hovering payload with the necessary electronics in order to wirelessly ignite the thrusters. Accelerometers and gyroscopic sensors measure linear acceleration and angular velocity of the payload. Theses measurements are then used to calculate the thrust and impulse bit.

1.2 Thrust Stands for Pulsed Plasma Thrusters

Different electric propulsion devices and test stands have been developed for the purpose of assessing micro-thruster to meet requirements of small satellites and spacecrafts. One of the engineering challenges with creating this type of test stand is the need for complex setups in order to capture the low thrust pulses from miniaturized thrusters. Small calibration errors can result in high uncertainty in final solutions. Recently, there have been efforts in potentially simplifying thrust measurements by reducing the number of moving parts in the system. These micro-thruster test stands use very precise equipment and calibration practices in order to reduce the displacement error following individual firings. Currently three different types of test stands exist for this particular testing. These types of test stands that have been used and can be found in the literature are the Hanging Pendulum, Inverted Pendulum, and the Thrust Balance [15]. These thrust stands will be discussed more in depth in the literature review in Chapter 2.

1.3 Objective

The objective of the project is to develop a thrust stand for the purpose of evaluating performance characteristics of micro-thrusters. There was a need to take

Isp, $\dot{m}$, and I_{bit} measurements for a PPT in the mN-s range. The existing thrust stand technology enabling such measurements frequently involves a pendulum type or spring based stand which involves long settling times. High data rates with a large number of small thrusters were required. To meet some of these requirements alternatives to existing thrust stand technology were explored.

1.4 Recent Developments

A recent stand developed at MIT utilized a system in which the propulsion system is suspended by magnetic field for low, constant force measurements of an ion thruster [41]. A similar measurement system was developed for the evaluation of a pulsed system. The new thrust stand was designed and fabricated which uses a magnetically levitating platform to which micro-thrusters are mounted and the effect of firing on the motion of the platform is measured. The low thrust measurements were to be made at atmospheric pressure and under vacuum conditions. The objective of this thesis was to develop and utilize the system for taking measurements on a commercial pulsed thruster.

1.5 UAH Test Stand

The thrust stand, seen in Figure 1.1 was developed with the intended purpose of providing performance characteristics, such as thrust, impulse-bit, and specific impulse of thruster technology while providing an assessment of repeatability, thrust variation, and reliability for atmospheric and reduced pressure testing. The use of aluminum slotted bars created a rigid structure for mounting the components for

a magnetically levitating system in order to create a low-friction environment for a levitating platform. Data acquisition and thruster firing components were secured to the levitating payload and computer would download the necessary information wirelessly. Details of the design, construction, calibration, uncertainty analysis, and measurement techniques will be discussed in Chapter 3. Section 1.5.1 is a summary of the basic component and integration of the design, discussion of the diagnostics utilized, and a description of how these diagnostics are used to make the desired measurements.

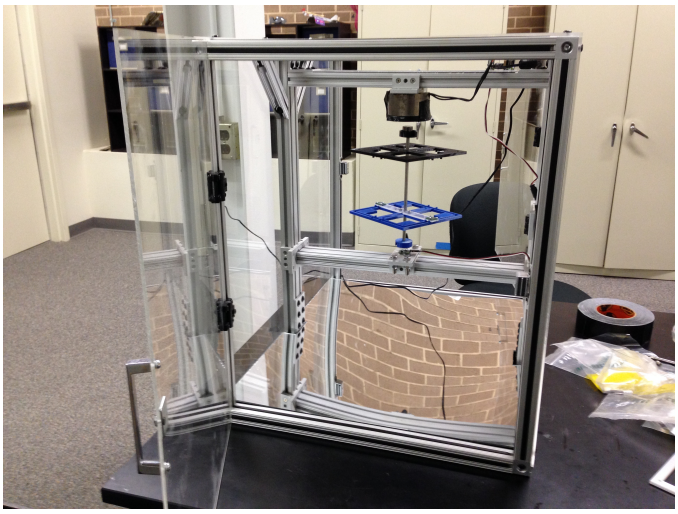

Figure 1.1: UAH Test Stand

1.5.1 Test Stand Components

The basic components of the thrust stand consist of a magnetic levitation controller (MLC), a levitating platform or payload containing the necessary data acquisition and firing components, and a computer to send and receive information

wirelessly to the payload. The MLC used an electromagnet, Hall Effect sensor and a feedback control unit to maintain the vertical position of the payload to simulate a low friction environment. The data acquisition system had a sensor package which used two accelerometers and a gyroscope that would collect and wirelessly transmit data to a computer. The firing circuit consisted of a printed circuit board, power supply and micro-thruster that would fire based on commands wirelessly received from a computer.

1.5.2 Thruster Performance

All thruster performance measurements presented in this thesis are derived from precise measurement of angular velocity, knowing the mass moment of inertia of the payload, seen in Figure 1.2, and mass per shot. Mass per shot was determined by weighing the thruster typically every 10 shots and taking an average per shot. Mass moment of inertia was challenging to determine because of the complex circuit arrangement and wiring. In order to simplify the process of computing this parameter, a non-linear dynamics method called Poincaré-Lindstedt Method was used to determine the mass moment of inertia of the payload [35]. The Poincaré-Lindstedt method uses geometry and the Duffing Oscillator to approximate solutions to weakly non-linear systems. To perform the necessary experiments the UAH MAE ATOM Laboratory was utilized.

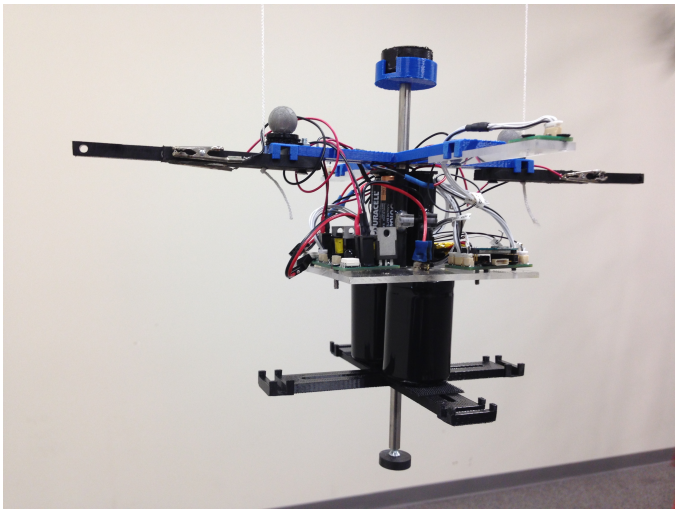

Figure 1.2: Test Stand Payload

The magnetically levitating thrust stand was designed for atmospheric and vacuum chamber operation. Facility preparations for reduced pressure testing included maintenance of the LVCTF at the JRC on UAH campus. The mechanical and diffusion pumps were inspected for proper operation and fluids were replaced. An active cooling system was designed and integrated to keep test stand electromagnet at nominal operating temperatures. Atmospheric electronic components were replaced with vacuum rated components. Modifications were made to the magnetically levitating platform and the control algorithm was reconfigured on the maglev controller.

The remainder of the thesis is organized as follows. Chapter 2 contains the summary of literature review on space propulsion, electric propulsion, pulsed plasma thrusters, micro-thruster test stands, and test stand calibration methods. Chapter 3 provides details to the experimental apparatus, technical approach, and uncertainty analysis methodology. The data and discussion of results is provided in Chapter 4.

Finally, Chapter 5 contains final remarks and thoughts as well as recommendations for future refinements and scaling capabilities for this research.

CHAPTER 2

LITERATURE REVIEW

2.1 Space Propulsion

The increase in deployment of nano and micro-satellites have led to the development of propulsion systems operating in the μN to nN thrust levels [4, 7]. Currently, there are various efforts in miniaturizing propulsion technologies appropriate for the size of cubesats [2]. To meet the strict size, weight, and power requirements new micro-thrusters are constantly being developed to provide crucial attitude and orbital maneuvering capabilities to satellites for position control, drag compensation, and de-orbiting maneuvers [5, 6]. At present, the micro-thrusters widely used are of cooling gas, chemical, and electrical types [2, 7].

2.2 Micro-Satellite Trends

Cubesats and Nano-satellites are one of the fastest growing sectors in the space industry. These communication devices allow for cheap access to space in addition to completing complex mission requirements. They are normally launched in sun-synchronous orbits usually ranging in an altitude of about $600-650$ km. A market analysis study conducted by SpaceWorks Enterprise (Figure 2.1) showed that based

on current projections between 121 and 188 spacecrafts weighing 1-50 kg will need to be launched by year 2020. This is representative of a 16.8% growth over a seven year period from 2013−2020 [3].

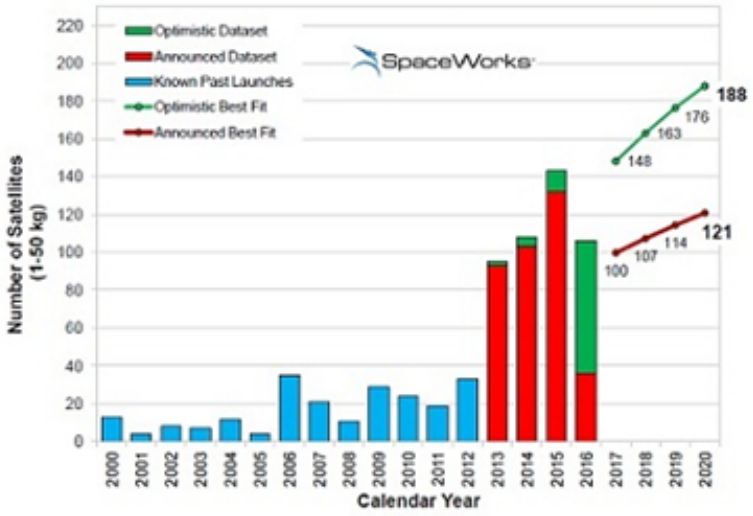

Figure 2.1: Nano/Micro-Satellite Launch Projections [3]

While this sector is growing at a rapid pace and missions thus far have been successful in advancing technology, limitations still apply. These small satellites are currently limited in active orbit control or Δv capability and therefore their lifetime in orbit is reduced due to natural, drag-induced, de-orbiting. The enabling technology for such complex missions such as autonomous propulsion and active attitude control with high accuracy remains elusive [1, 2]. The real challenge in creating an appropriate propulsion system stems from the difficult task of reducing the size of existing propulsion concepts. Structural, mechanical and power limitations dominate the design and manufacturing of these systems [1].

The tight size and mass constraints of cubesats makes development of micro-thrusters even more challenging. The mass budget for a 1U satellite is 1 kg and the mass budget for a 3U satellite is 3 kg. With this in mind most cubesat propulsion systems are limited to 120 g (excluding margins) which includes: the mass of the whole thruster assembly, electronics, capacitors and propellant. Due to these limitations, the mass of the propellant is generally around 10 g and power limitations for the system is 0.3 w of average power consumption [1]. The full document of CubeSat design specifications and standards developed by the California State Polytechnic University can be seen in [45].

2.3 Propulsion Options for Micro-Satellites

This section of the literature review discusses current micro-propulsion designs for use with nano and micro-satellites. Chemical propulsion technology is the preferred method due to fast development. However, electric propulsion technology show promising results for future use on these devices. The following sections will provide more details for the propulsion options.

2.3.1 Chemical Propulsion

To keep up with the requirements of producing very small thrusters with accurate forces miniaturizing existing conventional thrusters is still the preferred method. Solid propellant thrusters are good candidates for low thrust impulse. These propulsion devices use the chemical energy stored in a substance to produce thrust by accelerating the ejected gas through a nozzle. This system consists of a propellant

tank that contains solid fuel, an igniter, and a nozzle to accelerate the gas. Typical solid propellant thrusters are expected to deliver 30 mN−300 N of thrust over a few hundred milli-seconds [8].

2.3.2 Electric Propulsion

Electric propulsion systems are used because they provide higher exhaust speeds than chemical thrusters. This allows for significant propellant savings for space applications. Past near-Earth flight missions show encouraging signs of electric propulsion application for the use of planetary and deep space exploration. Electric propulsion has demonstrated several system advantages over chemical propulsion. First is the high specific impulse that leads to propellant savings. Even at comparable specific impulse levels to chemical systems the electric propulsion has longer life and less toxic propellant and propellant leakage [9].

Over the past several decades, the investment in the research and development of electric propulsion systems has yielded a variety of flight qualified micro-thrusters. These devices cover a wide range of specific impulse and efficiency. A summary table of various PPTs can be seen in Table 2.1.

Table 2.1: Thrust and Mass Ablation Characteristics of Various PPTs [9]

Thruster	E_o,J	Type	I_{sp},s	I_{bit}, $\mu N - s$	$\frac{I_{bit}}{J}$, $\frac{\mu N - s}{J}$	$\frac{\Delta M}{E_o}$, $\frac{\mu g}{J}$	$\frac{\Delta M}{area}$, $\frac{\mu g}{cm^2}$
LES-6	1.85	Breech-fed	300	26	14	4.8	3.3
SMS	8.4	Breech-fed	450	133	15	3.4	3.9
LES-8/9	20	Breech-fed	1000	297	15	1.5	4.8
TIP-11(NOVA)	20	Breech-fed	850	375	19	2.3	5.7
MIT Lab	20	Side-fed	600	454	23	2.8	4.3
MIPD-3	100	Side-fed	1130	2250	23	2.0	4.3
Millipound	750	Side-fed	1210	22,300	30	2.5	27.7
Primex-NASA	43	Breech-fed	1136	737	17	1.5	2.6
IL PPT-3 Lab	7.5	Coax-side-fed	600	450	60	10.0	36.0
Japan Lab	30.4	Breech-fed	423	469	15	3.7	6.4
China Lab	23.9	Breech-fed	990	448	19	1.9	5.3

These systems are organized into three main categories of electric propulsion: electrothermal, electromagnetic, and electrostatic propulsion. These are then organized into five different flight qualified systems: two are electrothermal (resistojet and arcjet), one is electrostatic (ion thruster), and two are electromagnetic (Hall thruster and the PPT). Today, the application of electric micro-thrusters as onboard propulsion for space systems extends the orbit, lowers drag makeup, increases formation and

attitude control [9]. Pulsed plasma thrusters, feature structural simplicity and adapt very well to low power consumption applications due to pulsed mode operation. This fact and the ability of the PPT to deliver small impulse bits with high reliability make them well suited for precise formation attitude control [2].

The basic subsystems of the electric propulsion thruster are: an energy source for electrical energy, a method of converting and transporting the electrical energy from the source to the thruster, the propellant, and the thruster structure itself [25].

2.3.2.1 Electrothermal

Electric propulsion can be classified in thermal and non-thermal systems based on the design of the propulsion device. Electrothermal propulsion calls for electrically heating a propellant and allowing it to thermodynamically expand. Then the heated propellant is accelerated to extremely high velocities out of the nozzle. There are two types of electrothermal thrusters in use today: The resistojet and the arcjet [25].

The resistojet uses conventional conduction, convection, and radiation heat transfer to heat the propellant. This is done by flowing the propellant over a hot metal surface such as: a heater coil, through heated hollow metal tubes, over a heated flat plate, or over heated cylinders. The material constraints limit the operating temperatures under 2700 K which can yield a typical specific impulse around 300 s. The thruster efficiencies of resistojets range from $65-85\%$. Figure 2.2, from Sutton and Biblarz [25], shows an example of a resistojet. In practice there are many reasons why resistojets are used. They are relatively simple devices that are easy to control and have relatively high thrust and efficiency. They can use gaseous propellants.

However, they provide lower specific impulses, than most other electric options, due to temperature limitations and experience heat loss and gas dissociation [25].

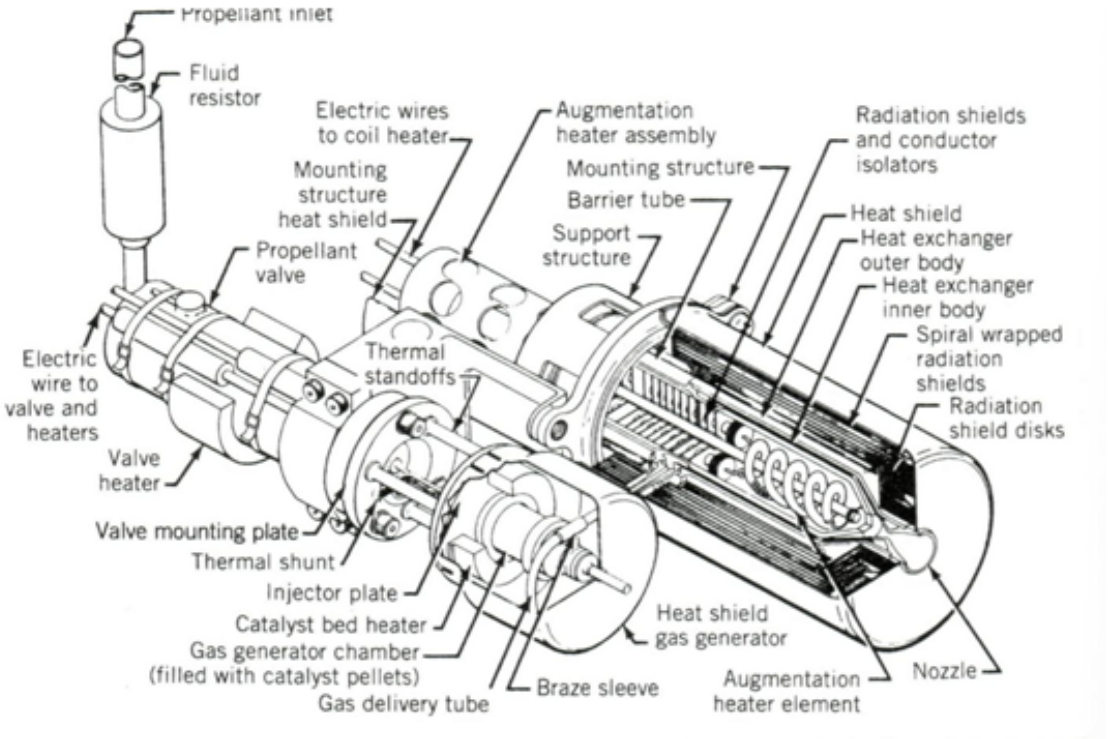

Figure 2.2: Resistojet Example [25]

The arcjet is another type of electrothermal thruster that functions in a similar fashion as an electromagnetic thruster. In the arcjet setup, current, supplied by electrical input, flows through the bulk of propellant gas that becomes ionized and accelerated out of the nozzle. This is different from resistojets since the arcjet uses an electrical arc to directly heat the propellant in order to overcome temperature limitations. In reality, the generated arcs heat only a small portion of the flowing gas if the throat dimension is not small. The arcs are mostly unstable and they can only be controlled by utilizing an external electric field control. Compared to the

resistojet they can operate at higher temperatures, but that also have relatively low specific impulses ($400 - 600$ s). Arcjets produce a high level of thrust for a electric propulsion system. However, they require heavy wiring and a more complex power conditioning for the amount of specific impulse and thrust generated [25].

2.3.2.2 Electrostatic

Electrostatic propulsion is a form of non-thermal propulsion. With this method acceleration occurs when electrical energy is applied to the propellant particles which cause interactions with the atomic ions or colloids. This method uses the Coulomb force to accelerate charged particles in the propellant exhaust. The electrostatic thrusters use positive ions to create momentum forces. This can be accomplished by either using an electron bombardment thruster or field emission thruster. The electron bombardment thruster produces positive ions by bombarding propellant particles with free electrons until the positive ions are separated. Then a separate electrical conducting grid accelerates the particles. With field emission thrusters the positive ions are separated from a liquid metal source that is subjected to a high electric field. This concept can operate with specific impulse values in the range of $8000-9000$ s. While high specific impulse and high efficiency can be achieved with this methodology the complex power conditioning, high voltage input, heavy power supplies, and low thrust per unit area make the technology less desirable. Figure 2.3, from Sutton and Biblarz [25], shows an example of an electron bombardment device for ion thruster development.

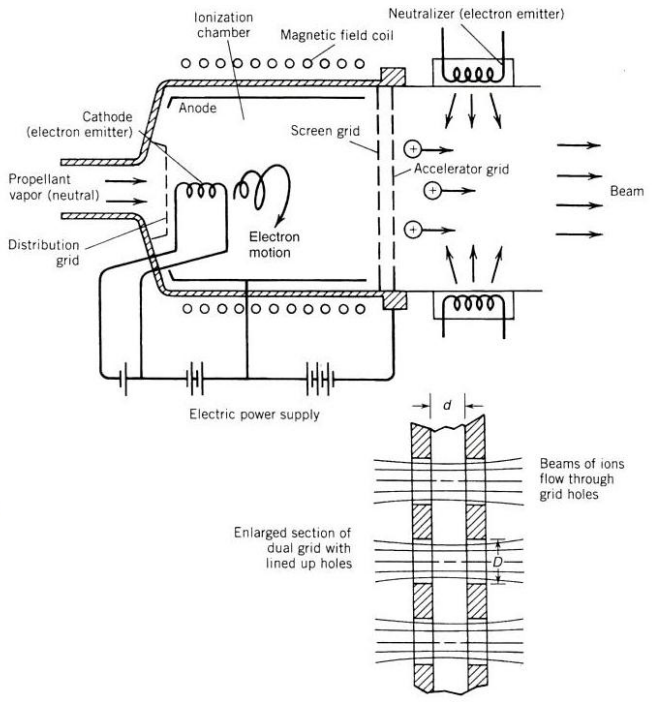

Figure 2.3: Electron Bombardment Ion Thruster Example [25]

2.3.2.3 Electromagnetic

In electromagnetic systems, electrical energy is applied to the propulsion device that causes interactions within the electric and magnetic fields of plasma that is accelerated through the thruster. Plasmas are mixtures of electrons, positive ions, and neutral particles that conduct electricity at high temperatures. This is usually above 5000 K. Theoretically, when a current is applied perpendicular to a magnetic field; a force is exerted perpendicular to both the current and magnetic fields. This is termed the Lorentz force. The simplest version of an electromagnetic thruster is the pulsed plasma thruster. In this setup a capacitor is charged using a power source and then all of the energy is dumped from the circuit to two electrodes that create a spark

and current flow. This burst is discharged quickly through the flow of the plasma and accelerated through the exhaust. Different configurations have been developed for this concept. The pulsed thrusting is very popular for precise control and positioning systems. The performance is characterized by measuring the total impulse per pulse or impulse-bit [25].

Hall Effect thrusters are another type of electromagnetic thruster. This thruster performance becomes significant when plasma densities are lower or electric fields are high. In these thrusters propellant is fed through by the anode. The cathode is placed at the end of the discharge chamber and the ionized particles are accelerated through the chamber in the direction perpendicular to the electric and magnetic fields. Figure 2.4, from Sutton and Biblarz [25], shows an example of a Hall Effect thruster. Unlike the electrostatic thruster, the electromagnetic thrusters have a neutral exhaust and relatively high thrust per unit area. They are simple devices that are compact, require low power have desirable specific impulse ranges and do not require much propellant configuring. They do however, have low thrust and may be inefficient [25].

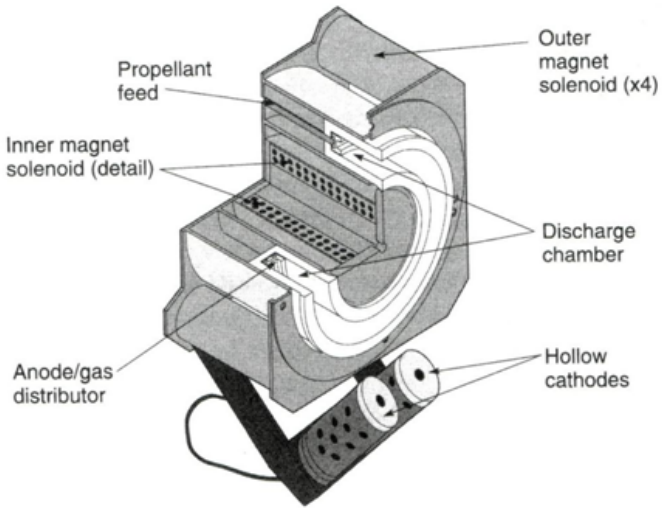

Figure 2.4: Hall Effect Thruster Example [25]

2.3.3 Comparison

The different types of electric micro-propulsion devices must be evaluated based on the mission requirements. The recent interest in small space vehicles has opened the door for more research low thrust propulsion systems. Most of these micro and nano satellites have limitations on weight and power. Power levels below 500 w and thrusts below 1 mN are needed since total vehicle mass is less than 100 kg. This makes pulsed-plasma thrusters the most ideal fit for these missions [25]. Table 2.2 and Figure 2.5 both show the relationship between performance and required power input for various electric propulsion systems.

Table 2.2: Performance of Electric Propulsion Devices [25]

Type	$Thrust\ Range(mN)$	$Specific\ Impulse\ (sec)$	$Thruster\ Efficiency\ \%$	$Thrust\ Duration$	$Typical\ Propellants$	$KineticPower\ perUnit\ Thrust(w/mN)$
Resistojet(thermal)	200-300	200-350	65-90	Months	NH_3,N_2H_4,H_2	0.5-6
Arcjet(thermal)	200-1000	400-1000	30-50	Months	H_2,N_2,N_2H_4,NH_3	2-3
Ion thruster	0.01-500	1500-8000	60-80	Years	Xe,Kr,Ar,Bi	10-70
Solid pulsed plasma (PPT)	0.05-10	600-2000	10	Years	Teflon	10-50
Magnetoplasma dynamic (MPD)	0.001-2000	2000-5000	30-50	Weeks	Ar,Xe,H_2,Li	100
Hall thruster	0.01-2000	1500-2000	30-50	Months	Xe,Ar	100
Monopropellant rocket	30-100,000	200-250	87-97	Hours or minutes	N_2H_4	

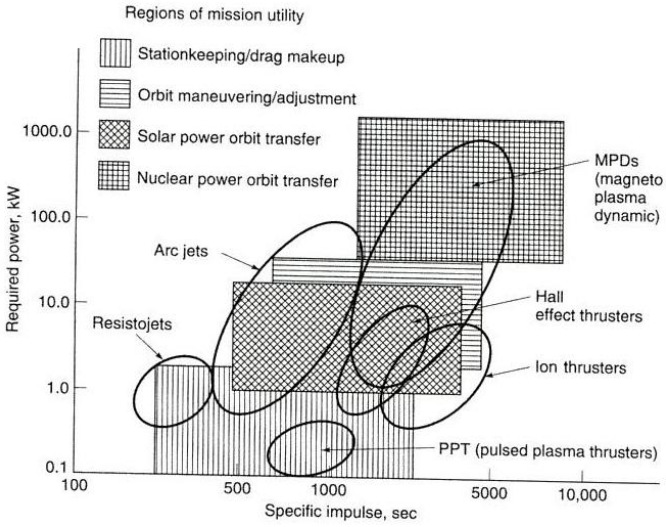

Figure 2.5: Power vs. ISP of Electric Propulsion Devices [25]

2.3.4 Electro-Chemical Propulsion and ECESP Performance

Over the past few years increased attention has been brought to using alternative propellants to PPTs other than Teflon. Solid propellants are preferred when creating rocket motors because there are fewer moving parts compared to liquid systems. However, many problems with controllability and restarting exist with solid propellant rocket motors.

Funding has increased in the research and development of electrically controlled extinguishable solid propellants (ECESP). ECESP are capable of multiple start/stop ignitions and throttling with the use of electrical power. Recently, a solid solution propellant with molecularly uniform non granular structure, known as ASPEN, has been created and tested. The propellant was shown to be insensitive to flame ignition and are non-initiating without the use of an appropriate amount of electrical power. Ignition can be controlled to the point where only one propellant grain is ignited when electrical power is supplied without the unwanted ignition of other grains [20].

Varying performance had been observed during the initial test phase of ECESP with different solid propellant formulations. Each one had shown lower performance than Teflon and the electrical dynamics of PPTs were not as suitable for ECESP. The ECESP are generally too conductive for the electrical plasma arc to short through the propellant. Ongoing research has led to the discovery of higher performance ECESP solutions. Figure 2.6 shows a series of frames demonstrating the start/stop capability of ECESP [20].

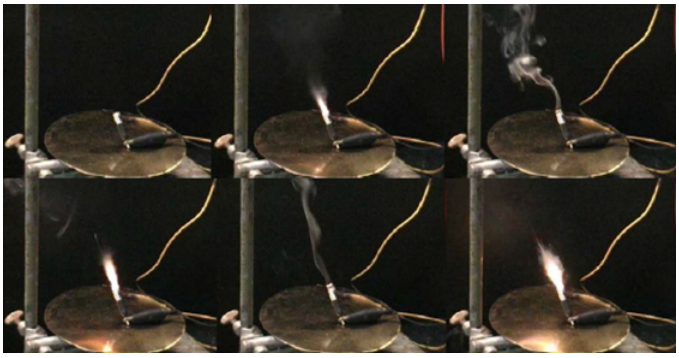

Figure 2.6: Coaxial Micro-Thrusters Start/Stop Demonstration [20]

This technology is very attractive for satellite applications, such as micro and nano satellites. Like PPTs they reduce the propellant leakage hazards associated with pure solid and liquid systems. They are also easy to replace and service. Like PPTs the level of thrust can be varied based on electrical input. ECESP have other safety advantages that include: low chance of accidental ignition, nontoxic propellant, low failure modes, storable, and no propellant leakage [20].

2.3.5 Performance Measurement

As part of the research and development of micro-thrusters, performance measurement is required at all stages in order to determine the operating characteristics of the devices. Two of the most important performance parameters that must be quantified are thrust and impulse bit [5]. Making accurate and direct measurement of thrust or impulse bit is very challenging. The American Institute of Aeronautics and Astronautics has started an initiative to create standards in measurement processes for electric propulsion [15]. In the work presented in Chapter 3 of this thesis

the goal was to use simple measurement devices to make these types of impulse bit and thrust measurements.

2.3.6 Funded Research

As a result of the high level of interest in producing very small thrusters, micro-propulsion has been a very active field of research and miniaturization of conventional thrusters have been actively investigated [8]. Clyde Space Ltd., Mars Space Ltd. And the University of Southampton has started a study funded by the ESA ITI program in order to adapt a Teflon-fed Pulsed Plasma Thruster (PPT) to a 3U Cubesat. The aim with this study is to double the lifetime of the satellite thus increasing its marketability [1]. A laser interferometer space antenna, a space mission jointly planned by the European Space Agency and NASA to detect gravitational waves, will use the drag-free control with micro-thrusters to control the system [6]. Another plasma thruster currently under study at the University of Witwatersrand is the Vacuum-Arc Thruster (VAT). The VAT is a small thruster that uses a high current vacuum arc pulse to generate a plasma jet from solid fuel. Typical impulses are measured as small as 0.5μN-s [5].

2.3.6.1 SpinSat

The SpinSat mission was a joint small satellite research project by the Naval Research Laboratory and Digital Solid State Propulsion (DSSP) LLC. The two primary goals of the research mission was to characterize the on-orbit performance of electrically controlled solid propellant (ESP) technology in space and provide a cal-

ibrated drag experiment at high solar activity. The project called for the design of a 22″ diameter spherical spacecraft (Figure 2.7) that was fitted with ESP thruster modules and satellite laser ranging sensors [21].

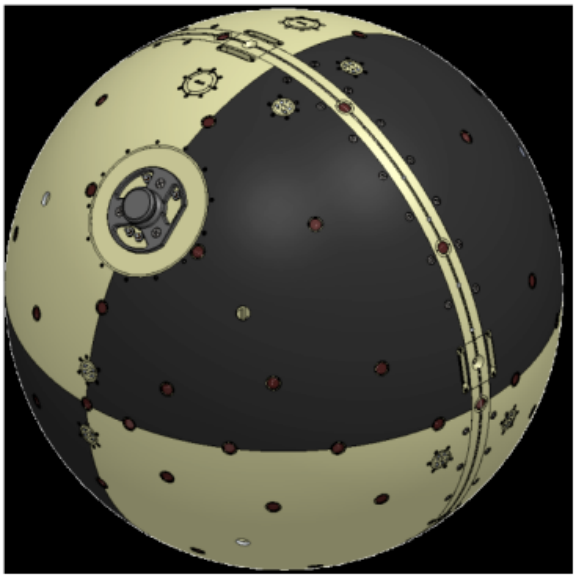

Figure 2.7: SpinSat Spacecraft [21]

The thruster modules were physically arranged to provide basic spin-up and de-spin maneuvers and normal thrust maneuvers. For the spin-up procedure thruster co-aligned 180° apart would fire and for the de-spin of an opposite pair of thrusters provide the opposing force. A total of seventy-two micro-thrusters were fitted to the 57 kg satellite [21].

2.3.6.2 Micro-Thruster and Firing System

The micro-thrusters used in this experiment were part of DSSP's first generation micro-thruster design. The micro-thrusters consisted of two coaxial electrodes

separated by 1 mm of ESP propellant. The material of the inner electrode was stainless steel while the outer electrode was made from aluminum. The length of the thruster was approximately 13 mm and each one had around 0.1 g of propellant [21].

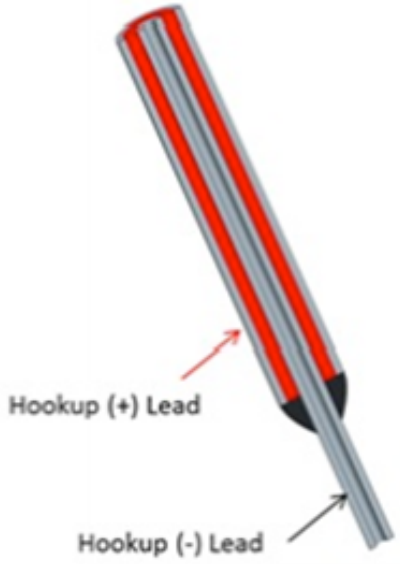

Figure 2.8: DSSP Micro-Thruster [21]

Figure 2.8 shows the basic schematic of the DSSP micro-thruster. One of the key features of the design is that an insulating plastic is placed on the outside of the inner electrode with a small section exposed near the nozzle. This leaves a small conductive path for the current to ignite the surface of the propellant. As the propellant burns away so will the insulation. This will create an even burn down to the base. Cluster modules were created for the SpinSat spacecraft. Within these modules several micro-thrusters were clustered to increase the total thrust of the firings. Figure 2.9 shows the micro-thruster cluster module from the SpinSat system. A common

electrical connection was used for the outer electrodes from aluminum. The modules were supplied with an appropriate amount of energy to ignite the propellant.

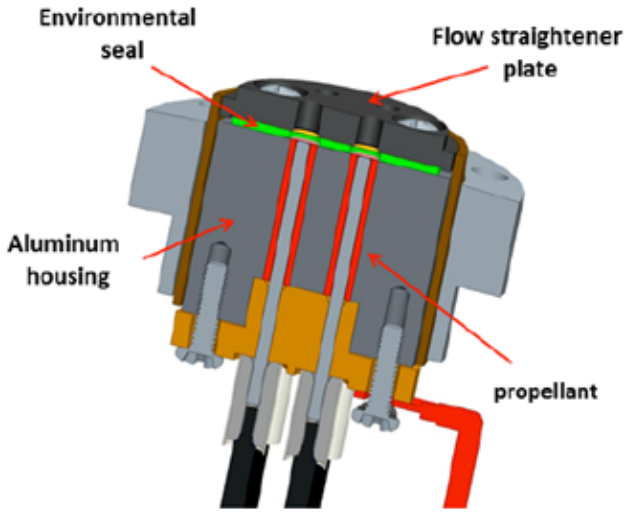

Figure 2.9: SpinSat Micro-Thruster Module [21]

2.4 Review of Thrust Measurements for Pulsed Plasma Thrusters

Pulsed plasma thrusters (PPTs) are categorized as a form of unsteady electromagnetic propulsion device. Typically, the propellant is ionized and accelerated by electromagnetic and electrothermal forces driven by an external pulsed power circuit. The former acceleration mechanism is the so-called j×B Lorentz force, where j is the current density and B is the magnetic induction field. The force is perpendicular to both the current density and the magnetic field. Because the current discharges through the plasma, resistive heating results in a pressure gradient which produces the electrothermal component of the acceleration.

The most common type of circuit is the resistive (R), inductive (L), capacitive (C) type frequently abbreviated RLC, and there are numerous variations in which capacitors, switches, and inductors are connected to tailor the pulse shape in a so-called pulsed forming network (pfn). The basic time dependent current is often a decaying sign wave, although a pfn can approximate a square wave or other desired shapes.

The common attribute which links this class of thrusters is that the propulsion is derived from discrete pulses rather than a continuous discharge. There are three potential advantages in the operation of these devices in an unsteady state. First, in unsteady state these thrusters improve thrust efficiency as the discharge current increases. Electrode erosion at high steady currents may be severe and otherwise limited by available power. Pulsed systems can reach much higher instantaneous power and current, potentially enabling higher thruster efficiency during the pulses. Second, brief pulses can also help avoid free electrons from thermalizing with high energy stream ions, thus using majority of the energy for accelerating plasma. Finally, unsteady pulsed operation produce beneficial electromagnetic field effects [39].

The rest of this chapter is organized as follows. For completeness, a review of ablative-fed pulsed plasma thrusters since it is the type of miniaturized propulsion devices used for testing of the thrust stand. Next, a review of the different types of thrust stands used for making performance measurements. Finally, some ideas, from literature, for test stand calibration are presented.

2.5 Ablative Fed Pulsed Plasma Thruster Overview

Ablative pulsed plasma thrusters have been chosen as propulsion subsystems due to their high scalability, power input, and performance. They are also easy to control and have high reliability [1]. Pulsed plasma thrusters were first flown in space on the Soviet Zond-2 mission. Ever since then PPTs have been used in a variety of space missions. Typical energy levels up to one hundred joules may be experienced upon discharge during flights [2].

2.6 PPT History

The first known pulsed thruster came from Russia in 1934. This thruster created gas pressure by discharging capacitively stored energy into a plenum lined with plastic, using a converging-diverging metallic nozzle to expand and accelerate the gases. This was created for experimentation purposes, but was never flight tested. Based on this design description it was determined that this acceleration mechanism was purely electrothermal. These designs can be seen in Figure 2.10. The schematic on the left in Figure 2.10 represents the electrothermal system [9, 54].

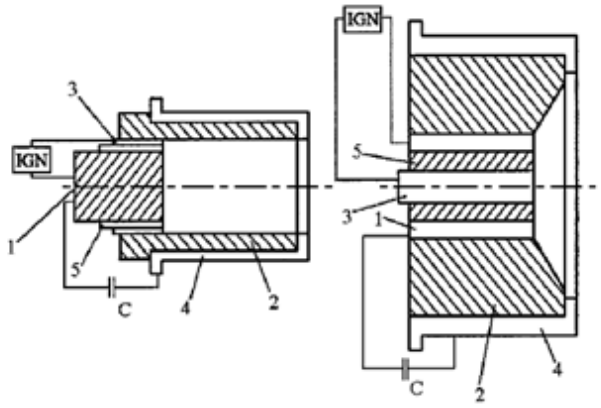

Figure 2.10: First PPT designs. Electro-thermal (left) and Electro-magnetic (right) [9]

Antropov and Khrabrov (scientists in the USSR) developed two PPT designs like the ones seen in Figure 2.10, one with an electromagnetic and one with a thermal acceleration mechanism. On November 30, 1964 the Soviet Union launch the Zond-2 spacecraft towards Mars and with it the first use of PPTs as a form of electric propulsion for spaceflight application. The second version of Antropov and Khrabrovs design was used on the Zond-2 spacecraft. It was a breech-fed, coaxial erosion type design and six thruster were used on the spacecraft. Teflon tubes were used as the propellant. However, several months later the spacecraft radio communication was lost and with it the power of the electric attitude control propulsion system. Soon after this the United States began applying PPTs to satellites. The efforts started with experimental research to understand the basic PPT physics and development of flight qualified thrusters. The successful applications began with the launch of the LES-6 satellite in 1968, the start of ten years of service in attitude control. The

thruster used solid Teflon propellant since early efforts to integrate a gas-fed system failed to perform on the satellite. Most PPTs today use the same concept [9].

During the 1970s and 1980s, much of the attention in space technologies remained on the Apollo missions, but studies continued on the micro-thrusters. In 1974, a PPT was used on the Synchronous Meteorological Satellite and in 1981 the U.S. Navy TRANSIT a navigation system on three spacecrafts called the TIP/NOVA program which used micro-thrusters to maintain a drag-free orbital position. An attempt was made to extend the performance of low energy PPTs, but efforts were discontinued when several problems with igniters and electrode degradation occurred. Also, capacitor lifetime issues with overheating and voltage reversal remained a main technological hurdle in meeting mission requirements. Research in this field also extended to China, Japan and Italy. The Chinese performed suborbital tests on PPTs and the other countries continued work on ablation-fed coaxial micro-thrusters [9].

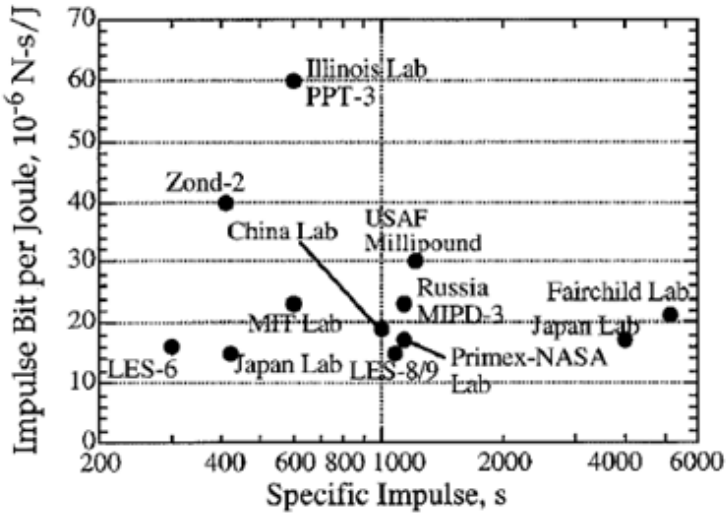

Figure 2.11: Impulse Bit per Joule vs. ISP for various PPTs [9]

Figure 2.11 displays the results for Impulse Bit per Joule of various PPTs. One of the thrusters displayed is the Russian MIPD-3 micro-thruster. The summary for the performance characteristics for this thruster comes from the work of Antropov et al. [9, 11, 12]. In his papers he included detailed diagnostics of the arc and plume. The thruster studied was a side-fed device with an Isp of 1130 s and an impulse bit of 2250 mN-s. Their sensors showed that during the first part of the firing, the j×B current front was moving in the flow direction up to 25 km/s and that the B-field lines were frozen into the plasma. The second part of the firing yielded different results with current distribution remaining stationary [9].

The work of Kimura et al. [9, 13] showed that by applying a magnetic field parallel to the self-induced field, control over the electromagnetic and electrothermal contribution could be demonstrated. By applying a magnetic field opposite the polarity of the j×B force could increase mass bit and impulse bit by as much as 66%. At this time researchers in China had designed, manufactured, flight qualified, and launched a pulsed plasma thruster on a sounding rocket. The design was a parallel plate, breech-fed design intended to study the effects of electrode geometry and energy on performance [9].

Throughout this era of research and development, electric propulsion failed to become a primary source of space propulsion. Through the four decades of continued research, PPTs remained the only form of electric propulsion that is applied to modern spacecraft. With the demands of an increasing market in this type of device research continues in this field. There is a need to create simple electric thrusters for use in complex space missions [9].

2.7 Basic PPT Physics

While the operation of a PPT may seem simple it actually integrates a series of complex interactions from electromagnetic and electrothermal processes. The PPT goes through ignition, discharge, plasma dynamics and mass loss to complete the firing cycle [9]. These processes are described below:

Ignition The complex process of PPT behavior starts with the ignition. An igniter plug is usually used to provide a spark for discharge. The plug is typically made of a semiconducting material. Since the energy and mass associated with the spark is much smaller than the value of the main charge the plasma effects of the igniter does not affect the performance of the PPT. Some variation may be noticed in the efficiency of the PPT thrust. This may result from variations in the applied voltage or surface-induced variations of the igniter plasma. The location of the igniter relative to the surface of the propellant plays a larger role in the design of the thruster [9]. This process along with the main discharge and mass loss through plasma acceleration can be seen in Figure 2.12.

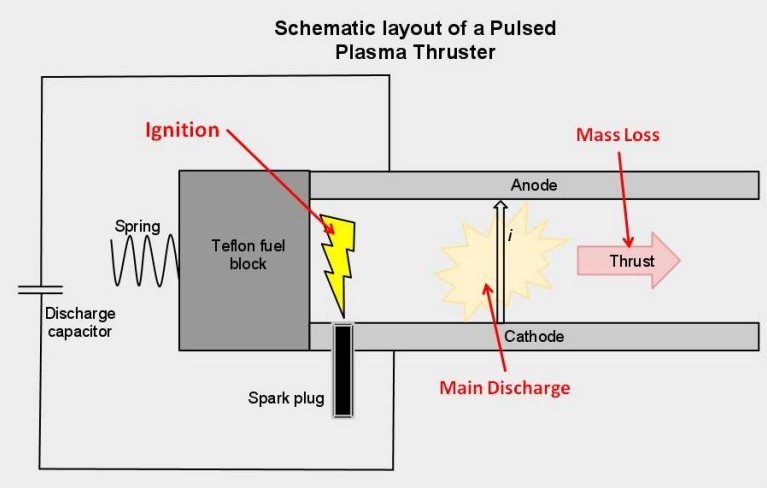

Figure 2.12: Pulsed Plasma Thruster Operation

Main Discharge Once the PPT is ignited, the main discharge rapidly becomes an arc between the positive and negative electrodes. The voltage drop is usually a few hundred volts. In the early stage of the current pulse, the discharge looks like a filament and the arc attaches at the electrodes which is typical of a low-current, low-pressure arc. As the current rises to kiloamps there is enough heat transfer at the lower particle densities that the current can overcome high plasma temperatures and conditions develop for arc diffusing. In an ideal scenario, the diffused arc covers the entire exposed surface of the propellant providing a uniform surface ablation [9].

Plasma Dynamics As the PPT discharges, the plasma has sufficiently high temperatures to provide interesting values of specific impulse when compared with chemical thrusters. Electromagnetic forces provide the high specific impulse component of the micro-thruster. Currents in the plasma discharge and the return, cause

electromagnetic acceleration of the plasma and a reaction force on the return. The magnetic field lines encircling the plasma tend to squeeze the plasma into a narrow column. Resistive heating in the discharge sustains the plasma at a high temperature, supplying energy to the solid propellant by heat conduction and radiation. For sufficient heat transfer, the propellant surface provides electrically conducting material. In other cases, the discharge follows the accelerated material at high velocity so that the PPT operates in the ″propagating″ or ″deflagration″ mode. For discharges going in the direction of the gases, the term ″detonation″ is sometimes used, except for when the PPT plasma propagates into a vacuum [9].

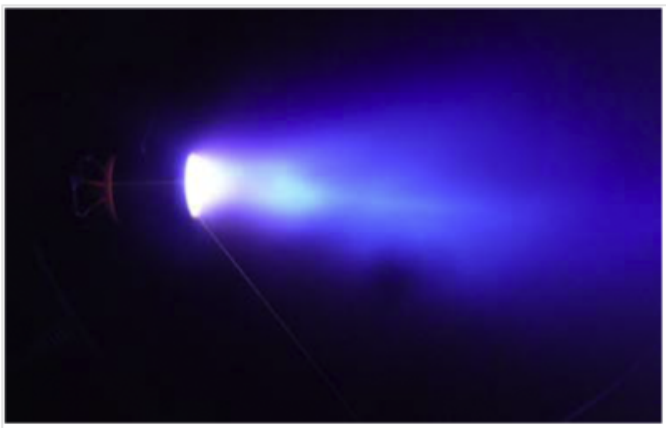

Figure 2.13: Plasma Plume of Coaxial Micro-thrusters [2]

Mass Loss The final component to the PPT firing process is mass loss. The mass loss can occur in several ways. One way the propulsion system loses mass is by simple evaporation during and following the discharge pulse. Another way can be the expulsion of macro-particles during the firing and/or erosion of electrodes and the igniter. The mass can be expelled at different velocities thus affecting the thrust

component. Exposure of the propellant surface to the arc discharge can lead to higher rates of evaporation toward the downstream as propellant temperatures increase. Not all the material leaving the surface, however, moves at a uniform velocity. Exhaust speeds can reach up to 50 km/s, depending on the details of the PPT design [9].

2.7.1 PPT Types

The Pulsed Plasma Thruster can be classified in four different configurations as seen in Table 2.3.

Table 2.3: Pulsed Plasma Thruster Types

Rectangular	Coaxial
Breech-fed	Side-fed

Figure 2.14 displays a schematic of a traditional, breech-fed, rectangular form PPT. In this arrangement, a solid propellant bar, usually Teflon, fills the gap between the cathode and anode. The electrodes are connected to charged capacitor [9].

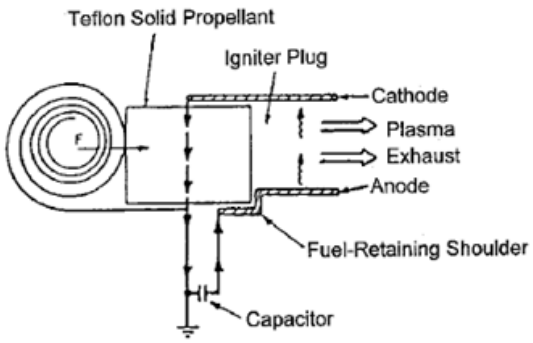

Figure 2.14: Traditional, Breech-fed, Rectangular PPT [9]

An igniter provides a small amount of initial plasma, triggering the main discharge across the propellant surface. Heat transfer from this discharge causes evaporation of propellant material, which is accelerated by the electromagnetic and pressure forces out of the nozzle [9]. Figure 2.15 shows the side-fed igniter-propellant-electrode configuration. In this configuration the propellant bars are advanced from opposite sides of the igniter plug. Both rectangular and coaxial variants of this set up exist [9].

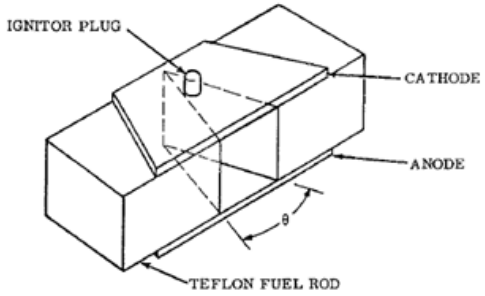

Figure 2.15: Side-fed Electrode-Propellant Configuration [9]

2.7.1.1 Rectangular

A common configuration is the breech-fed PPT with parallel rectangular electrodes. This configuration is driven by a long current pulse, as observed by the LES-8/9 and EO-1 thrusters. For this electrode configuration, the current and self-induced magnetic fields are transverse to the flow. The anode and cathode arc attachment regions are then free to move downstream along the electrodes [9]. Figure 2.16 shows a diagram of a regular configuration PPT.

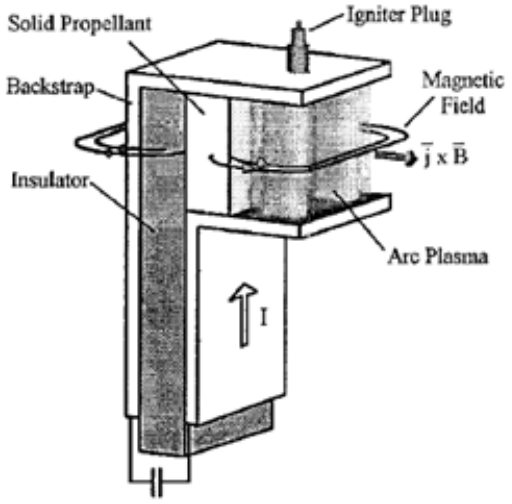

Figure 2.16: Rectangular Configuration PPT [9]

2.7.1.2 Coaxial

The coaxial configuration is usually of a conical shape with central and downstream electrodes. In most PPTs, the igniter plug is usually mounted in the cathode. This can be either the center or outer electrode in the coaxial configuration. The outer electrode is usually narrow, so the current flow attaches itself to a definite lo-

cation [9]. Figure 2.17 shows a simplified schematic of a coaxially configured PPT. The coaxial type ablative micro-thruster design offers favorable mechanical properties. Since the outer electrode fully encases the propellant and plasma it acts as a shield that protects the surrounding structure [2].

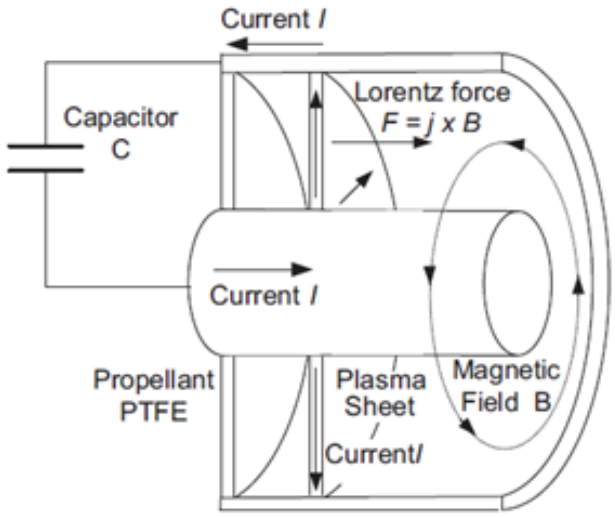

Figure 2.17: Coaxial Configuration PPT [9]

2.7.1.3 Breech-Fed

The ablation arc and propagating modes of the PPT are influenced differently depending on whether a breech-fed or side-fed configuration is used. The breech-fed PPT, such as the LES-6, has a current distribution that moves downstream of the ignition at a higher speed than the mass average velocity. This, in turn, suggests that the mass rate of ablation at the back of the arc is not good enough to provide spatial stabilization. Also, in this configuration the primary j×B force vector points away

from the ablating surface. So when the arc strikes, it moves off the surface. This reduces the ablation rate [9].

2.7.1.4 Side-Fed

In a side-fed system, the j×B force vector is parallel to the ablating surface, and the B field lines are normal to it. This provides a path for the electrons to reach the propellant and maintain the ablation rate [9]. Figure 2.18 shows an example of a side-fed PPT.

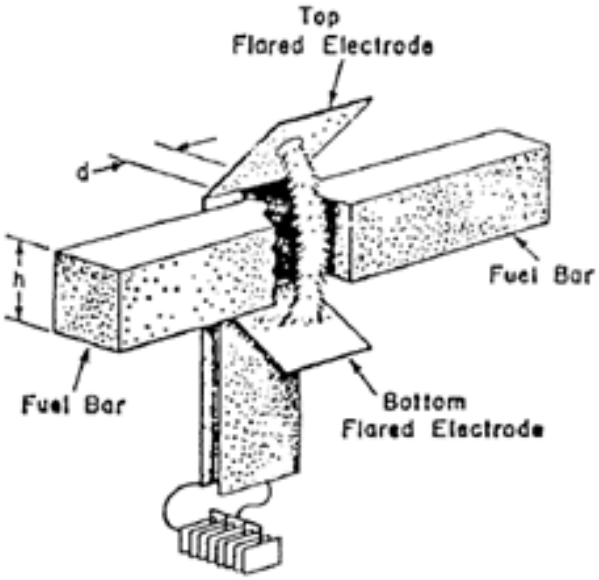

Figure 2.18: Side-fed PPT Configuration [9]

2.7.2 PPT Variations

In addition to the basic geometric configurations there are also propellant feed variations that must be considered when developing micro-thrusters. These variations

include: short pulse vs. quasi-steady; ablation area; the igniter; propellant choice; parallel vs. flared electrodes; ablating, non-ablating, nozzles; current; and applied magnetic field [9].

It is observed that in most PPTs the pulse length is long and that the pulse length, t_p, is greater than the acoustic time in the thruster. This allows the pressure to follow the power input and the flow field properties vary in a quasi-steady fashion along with the thruster current. In the rectangular geometry the plane electrodes are usually parallel; however, some thrusters increase performance by angling the electrodes away from the thrust axis providing a diverging nozzle effect. This angling can be seen in Figure 2.18 [9].

2.7.3 PPT Advantages

A systems case for PPT use was made by Palumbo and Guman [14]. They stated that the advantages of PPTs include: Zero warm up time, Inert and fail-safe, scalable to performance requirements, usable on spinning three axis satellites, solid propellant advantages, discrete impulse bits, variable thrust, compatible with attitude control, operates in large temperature range, and thrust vector control capability [9].

2.8 Micro-Thruster Test Stand Literature Review

Different types of micro pulsed plasma thrusters and solid propellant micro thrusters are being developed to meet the demands and requirements of space missions. Before these propulsion systems can be flight qualified extensive endurance testing must be done on the ground in order to evaluate the performance of the

thrusters. The thrust stand becomes an important tool in the development of the micro-thrusters and it plays a significant role in measuring a direct solution of thrust and uncertainty [6].

Electric propulsion systems provide high specific impulse, but low thrust, compared to chemical systems. This means that the sensitivity must be higher for ground testing electric propulsion devices. While the chemical thrusters performance is generally measured using load cells, the sensors for determining impulse bit of electric micro-thrusters more closely resemble sensitive laboratory mass scales. Sensitive measurement tools must be used since electric thrusters have very low thrust-to-mass ratios [10, 15].

2.9 Thruster Test Stands

Currently, three different distinct types of test stands exist for the particular application of backing out performance characteristics of micro-thrusters. The three configurations include: the hanging pendulum, inverted pendulum, and torsional pendulum balance which can be supported by two pivots or suspended by a fiber [6, 24]. These configurations have both advantages and disadvantages depending on the requirements and acceptable thrust range, accuracy, repeatability, and resources.

The conventional hanging pendulum is highly stable, but less sensitive than the other configurations. The inverted pendulum configuration is highly sensitive, but has the worst stability. The torsional pendulum balance configuration does not have the highest sensitivity or the greatest stability, but has been shown to be the most effective in measuring the performance of micro-thrusters. The major advantage

of the torsion-type tools is that the direction of the restoring force is vertical to the Earths gravitational acceleration; therefore, it can be independent of the thruster mass [6, 24]. The majority of these configurations are variations of a spring-mass-damper system [15].

As summarized by Polk et al. [15] the second order system relates the time rate of change of angular momentum to the sum torques. The general dynamics equation for all three types of test stands can be seen in the equation below [15, 24],

$$I\ddot{\Theta} + c\dot{\Theta} + k\Theta = F(t)l, \tag{2.1}$$

where Θ is the angular position relative to a reference point, I is the mass moment of inertia, c is the damping constant, k is the effective spring constant associated with restoring forces, and $F(t)$ is an applied force acting at a distance l from the pivot. I, c, and k are assumed constant based on theoretical calculations and experimental data from existing spring mass dampener systems [15]. Figure 2.19 shows an example of a handing pendulum thrust stand design.

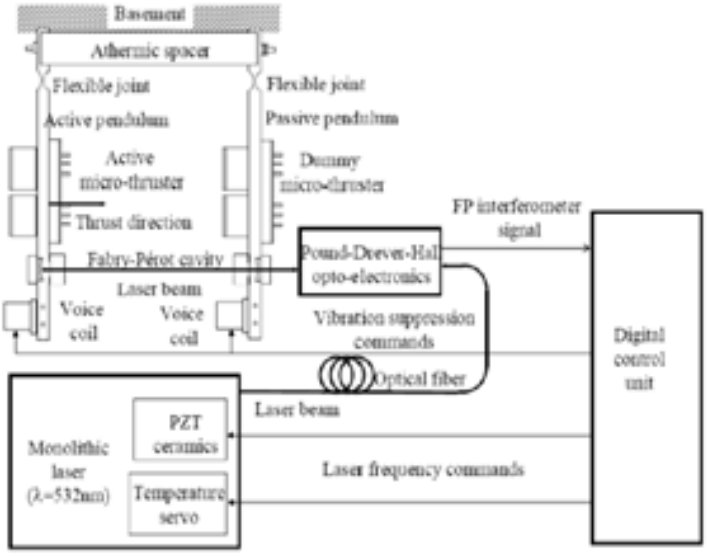

Figure 2.19: Example of Hanging Pendulum Thrust Stand [15]

Most thrust stands may include active components such as electronic dampers that introduce a frequency term into the analysis. This equation may be seen in the following form,

$$\ddot{\Theta} + 2\zeta\omega_n\dot{\Theta} + \omega_n^2\Theta = \frac{F(t)l}{I}, \tag{2.2}$$

where ζ is the damping coefficient,

$$\zeta = \frac{c}{2}\sqrt{\frac{1}{Ik}} \tag{2.3}$$

and ω_n is the natural frequency of the undamped system,

$$\omega_n = \sqrt{\frac{k}{I}}. \tag{2.4}$$

The biggest difference in the three types of pendulum test stands is how the gravity term affects the solution. Gravity acts as a restoring force in hanging pendulums, a deflecting force in inverted pendulums, and it has no influence on ideal torsional pendulums where the plane of motion is perpendicular. The gravity term affects the applied force term, $F(t)$, in the above equations. With this being the case the follow equation is the general torque equation with the gravitational force for hanging and inverted pendulums:

$$\tau_g = Mg_0 l_{cm} sin\Theta \cong Mg_0 l_{cm}\Theta \tag{2.5}$$

where M is the mass, g_0 is the acceleration due to gravity, and l_{cm} is the distance from the center of mass to the pivot location [15]. In the scenario where gravitational torque is proportional to the deflection, the spring torque term can be:

$$k = \begin{cases} k_s + Mg_0 l_{cm} & \text{for hanging pendulums} \\ k_s - Mg_0 l_{cm} & \text{for inverted pendulums} \end{cases} \tag{2.6}$$

This shows that for inverted pendulums the gravity torque must not exceed the spring torque or the restoring force is negative and the test stand becomes unstable [15].

Table 2.4: Typical Micro-Thruster Measurement Methods [4]

Author	Principle	Range	Precision
Stark et al. (1970)	Torsional Balance	4.4μN-222 mN	5%
Bailey et al (1972)	Microbalance	50-500μN	$\pm$2%
Haag (1997)	Torsional Pendulum	1-260μN	1%
Boccaletto et al. (2000)	Torsional Balance	1-100μN	<3%
Tew et al. (2000)	Torsional Balance	10μN-2mN	$\sim\pm$2%
Jamison et al. (2001)	Torsional Balance	88.8 nN, 734 nN	$\pm$11%
Gamero-Castaño et al. (2001)	Torsional Balance	0.1-1.1μN,5-30μN	0.01μN, 0.03μN
Ziemer (2001)	Torsional Balance or Pendulum	1-100μN	1μN, 1μNs
Nicolini et al. (2001)	Nulled-Pendulum	10-100μN	0.01μN
Rocca and Nicolini (2005)		0-220μN	
Merkowitz et al. (2002)	Torsional Balance	1-100μN	0.1μN
Bertinetto et al. (2002)	Double-Pendulum	-	-
Xiong et al. (2004)	Thin Cantilever Beam	1.75μN	$\sim$10%
Marhold et al. (2005)	Torsional Balance	2-45μN	5-14%
Phipps et al. (2005)	Torsional Balance	0.1-500μN	0.025μN
Polzin et al. (2006)	Hanging Pendulum	100μN-1N	$\sim$20%

Table 2.4 shows the different methods, found in the literature, on direct micro-thruster performance measurement. It can be seen that different performance characteristics such as accuracy, resolution, repeatability, and thrust range resulted in the use of different test stand configurations [4].

In order to make these measurements different types of sensors are used. In devices that measure displacement to calculate thrust elements such as an inductive proximity probe, an accelerometer, a linear voltage differential transformer, a capacitor system, or an optical angular system. In some cases an electromagnetic damper may be used [15].

2.10 Hanging Pendulum Type

Hanging pendulum test stands are, in concept, one of the easiest thrust stands to build and operate. A conventional hanging pendulum consists of a vertical arm attached at some pivot or flexure and the thruster is attached to a platform at the bottom of the moment arm. Over the years, this configuration has evolved into a design that yields high accuracy in measurements of micro-thrusters through the use of new, high accuracy instruments. These designs generally require some type of displacement sensor, damping mechanism, and calibration system like other thrust stands [15].

Figure 2.20 shows the basic setup of the impulse measurement system suggested by Kang et al. [23]. The system measured the angular velocity and the change of angle of pendulum swing times to calculate the applied thrust and impulse of the thruster. The initial condition given to the pendulum was an offset angle of 5° degrees from the vertical axis. The thruster fires at the same time the pendulum is released and a pair of sensors record the time at which the pendulum swings through a photo gate [23].

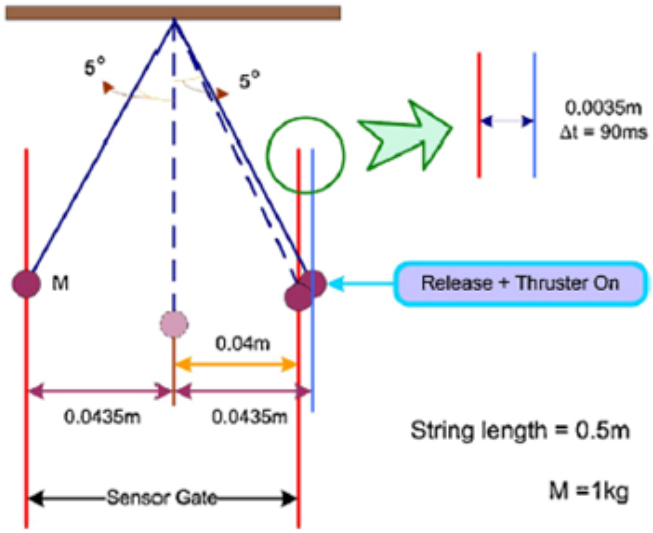

Figure 2.20: Hanging Pendulum with Sensor Gates [23]

The impulse calculation is performed by first finding the swing time of the release without thrust and then finding the swing time of the release with an applied thrust. The difference in the measured times is the relevant piece of information that is needed to complete the analysis.

Figure 2.21 shows a pendulum design developed and fabricated by Orieux et al. [8] to characterize solid propellant micro-thrusters. The thrust measurement system on this device consisted of a thin hanging pivot arm that rotated freely after thruster firing and a feedback controller. The thruster platform was attached at the base of the moment arm along with a coil. The coil is used to restore the arm to the reference position. A permanent magnet is positioned with a sensor transmitter. The deflection of the arm caused by the thrust was detected by a high frequency transmitter and antenna located on the copper plate. This distance is post processed

as a high frequency signal and the amplitude is used to determine the displacement and thus the force applied to the moment arm [8].

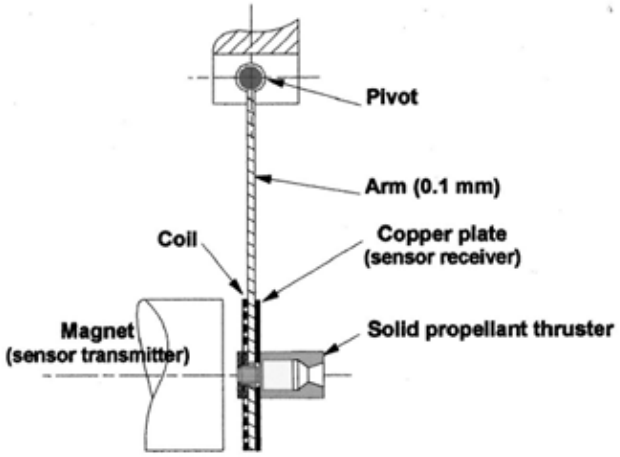

Figure 2.21: Solid Propellant Thruster Thrust Stand [8]

2.10.1 VAHPER Thrust Stand

Another conventional hanging pendulum design was that tested by Polzin et al. [10] This design converted horizontal deflections of the pendulum arm produced by the operating thruster into amplified vertical motions of another arm. The displacement is measured using a non-contact, gap displacement sensor. The oscillatory motion is dampened using an eddy-current damper. The design was called the Variable Amplitude Hanging Pendulum with Extended Range (VAHPER). The system provided adjustable sensitivity through the adjustment of a single arm. The displacement was measured on the vertical arm which eliminated the need for a separate reference structure [10]. Figure 2.22 shows the VAHPER Thrust Stand schematic.

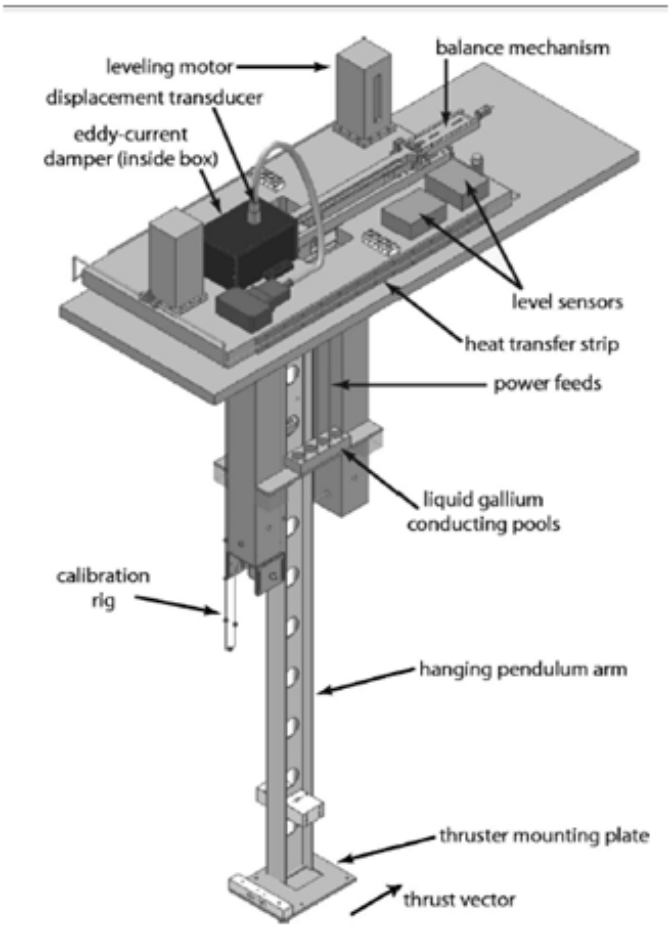

Figure 2.22: VAHPER Thrust Stand [10]

2.10.2 Leaf Spring Hanging Pendulum

Figure 2.23 shows a hanging pendulum design by Wang et al. [4] that incorporates a leaf spring as the beam. The thruster is mounted to one of the leaf spring while the other end is attached to the top of the test stand. During thruster operation the leaf spring will deform elastically based on the level of thrust. A sensor is placed on the test stand to measure the amount of linear displacement of the leaf spring [4].

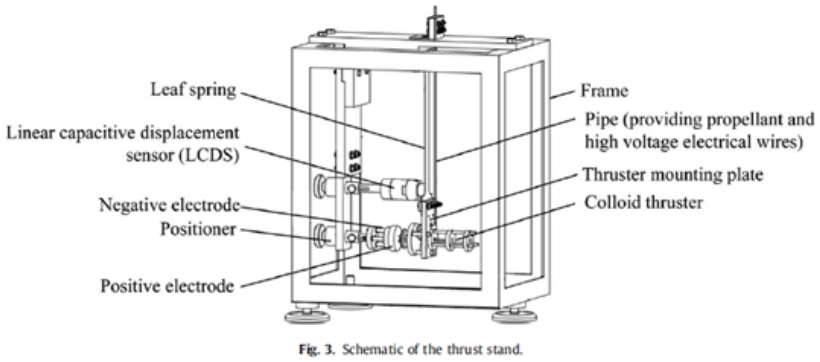

Figure 2.23: Leaf Spring Pendulum Test Stand [4]

The displacement for this test stand is characterized by using Hookes Law,

$$T = (Eah^3/4l^3)\delta, \tag{2.7}$$

where E is youngs modulus of the material, a, h and l are width, thickness and length of the leaf spring. With this technique the estimated accuracy of the measurement is ± 76 mN for the thrust level at 760 mN [4].

2.10.3 Advantages

The major advantage of the hanging pendulum design is the relatively high stability and ease of use. They are least affected by test conditions that cause changes in flexure stiffness (usually heating) which result in calibration issues [15].

2.10.4 Disadvantage

While the design of the hanging pendulum design tends to be very stable it, however, is least sensitive. In the design the effective spring constant of the solution comes from the weight of the device. The main parameter that controls the sensitivity of the test stand is the length of the pendulum arm. If one of the test requirements was to increase sensitivity to test in a reduced pressure environment a large facility would be needed. This type of application is not well-suited for small test chambers [15]. Therefore, conventional hanging pendulum thrust stands have been primarily used to test high thrust-to-weight devices [10]. Another disadvantage to the design is the result of the pendulums motion in the gravitational plane. This factor must be accounted for by taking into consideration the test stands orientation and understanding how thruster mass influences the stands response [15].

2.11 Ballistic Pendulum

Figure 2.24 displays a test stand developed by Lugini et al. [16] at the Spacecraft Robotics Laboratory of the Naval Postgraduate School. The test stand was built as part of research for characterizing small cold-gas nozzle on thrusters. The test stand is based on ballistic-pendulum principle, particularly the suspension of a gondola hosting the propulsion system. The gondola is suspended by nylon wires from the support chassis. The propulsion system is entirely self-contained and autonomous and is mounted to the gondolas base [16].

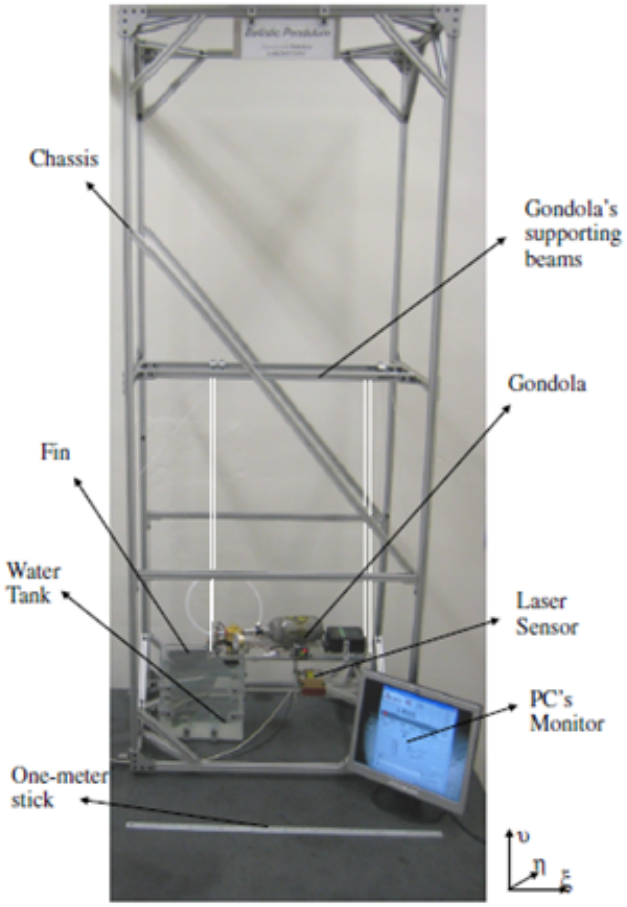

Figure 2.24: Ballistic Pendulum Test Stand [16]

Figure 2.25 shows the schematic for the ballistic pendulum setup. A key feature to the gondola is an equipped fin that is immersed in water. This acts as a torsional and lateral oscillation damper. A laser sensor measures the displacement of the gondola during thruster operation. [16]

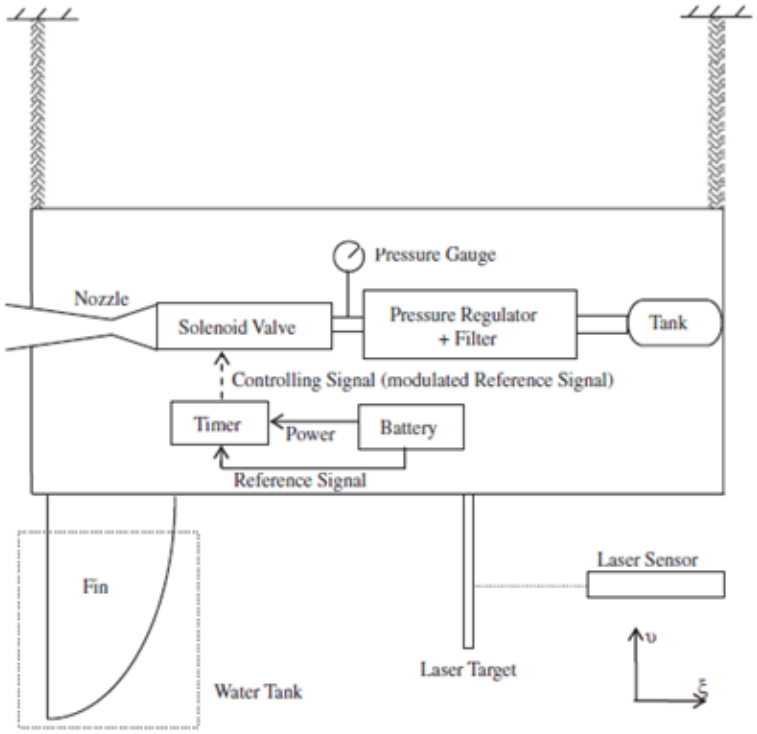

Figure 2.25: Schematic of Ballistic Test Stand [16]

After post processing the laser displacement data the final calculation of thrust can be given by the following equation,

$$\underline{z}(t) = \bar{T} e^{At} \int_0^{\Delta T} e^{-At} B d\tau, \tag{2.8}$$

where $\underline{z}$ is a state vector, T is the nozzle thrust, t is time, A is the dynamic matrix, B is the control distribution matrix [16].

2.12 Torsional

The torsional micro-thruster test stand is different from the hanging and inverted pendulum thrust stand configurations in that its rotational axis is parallel to the gravity vector. This makes the response independent of thruster mass. This makes it ideal for measuring thrusters that are either changing in mass or facility that requires testing over a large range of thrusters. Torsional balance configurations have been shown to have high sensitivity, making them well-suited for micro-propulsion. These types of test stands are inherently more stable than inverted pendulum thrust stands and offer a balance of high thrust sensitivity and low environmental noise sensitivity [15].

Torsional type thrust stands can resolve thrust measurements from hundreds of nano-Newtons to a few Newtons. This means it can be used for a broad range of electric propulsion devices like PPTs, FEEP, ion thrusters and hall thrusters. Figure 2.26 shows a schematic of a typical torsional thrust stand arrangement [15].

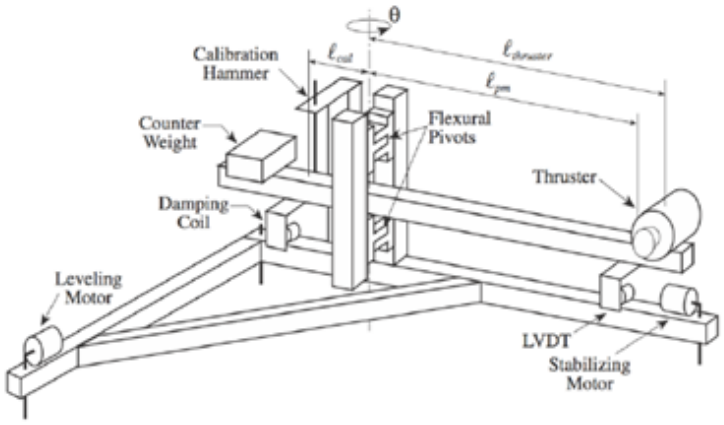

Figure 2.26: Torsional Pendulum Test Stand [15]

In regards to the torsional pendulum test stands, the effects of gravity have been documented by Ziemer [17] In this paper the affects of gravity on the measurement occur in two ways. The first is when the vertical rotation axis is offset by some angle. The second is when the center of mass is not properly aligned by the vertical axis. If the first case were to happen, when the offset angle is positive, the system is stable because the torque would work with the spring to resist deflections. If the angle becomes negative it will resist the spring constant and become an unstable system [17].

Ziemers analysis showed that three variables can be changed with this type of test stand. The first is the distance of the center of mass from the centerline axis. The second is the mass of the thruster counterweight and the third is the offset angle [17]. The simplest variable to change is the distance of the center of mass from the centerline axis. If this is done, counterweights on the opposite side of the beam have to be adjusted. This is necessary to level the beam and remove the effect of thruster mass from thrust measurements. Torsional thrust stand sensitivity can be changed via a number of factors: torsion spring constant, length of thrust stand beam, and measurement distance from centerline axis [15].

2.12.1 Torsional Balance

The primary advantages of the balance configuration is that they have the ability to support the complete thruster, they are easy to calibrate, have relatively good accuracy when measuring thrust and control capability, and results are repeatable. The downside of this type of setup is the complicated structures, such as, the

rotating arm that requires accurate installation and calibration in order to reduce uncertainties. Also, in the case of electric propulsion systems, high voltage lines could negatively affect the sensitivity of torsional balance systems. Some systems have used the approach of using torsion fibers or thin cantilever beams to compute thrust from displacement [4].

Torsional balances are generally designed so that the angular deflections remain within about 5° [15]. Figure 2.27 shows a torsional balance test stand developed by Yang et al. [6] for the Chinese Test of the Equivalence Principle with Optical readout space mission. The test stand used a suspending design to test pulsed plasma thrusters with impulse bits up to 1350 μN-s. Since the measurement accuracy of the torsion spring constant is the most important parameter special consideration was given to the suspension components. The suspending Tungsten fiber is from any operating current so that thermal effects are mitigated keeping the torsion spring constant consistent. A PPT is mounted to one end of the pendulum, and the nozzle axis is aligned to be tangent to the motion of the twist. The twist motion of the suspended torsional balance device is monitored by an additional imaging device [6].

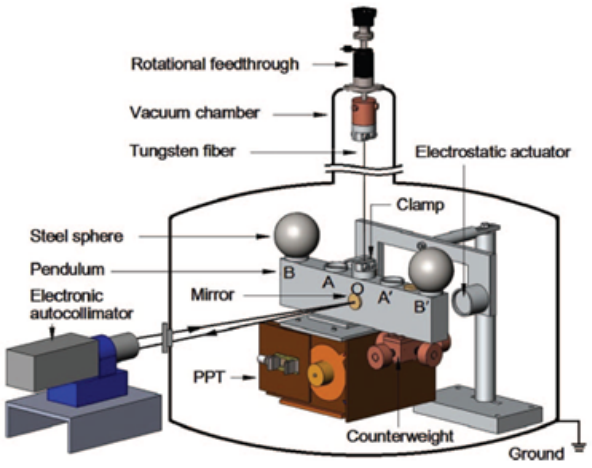

Figure 2.27: Torsional Balance Thrust Stand [6]

The motion of the torsional balance device using a torsion fiber can be characterized by a second order differential equation,

$$I_{Pendulum}\ddot{\Theta} + \lambda\dot{\Theta} + k\Theta = FR, \tag{2.9}$$

where $I_{Pendulum}$ is the moment of inertia of the pendulum, k is the torsion spring constant of the fiber, λ is the damping factor, Θ is the angular displacement of the pendulum, and $F(t)$ is the external force acting on the pendulum, R is the distance from the centerline axis to the thrust vector [6].

The final magnitude for the constant thrust force can be determined by,

$$F = \frac{I_{Pendulum}\omega_0^2}{R}\Delta\Theta = \frac{k}{R}\Delta\Theta, \tag{2.10}$$

where $\Delta\Theta$ is the difference in the equilibrium position of the pendulum. The moment of inertia of the device is determined by measuring the difference in pendulum periods of two steel spheres that are mounted to either end of the horizontal beam. After completing a series of repetitive PPT operation tests the repeatability was shown to be around 20% with the total relative error for the parameters of the thrust stand to be as low as 0.16% [6].

Figure 2.28, displays a test stand developed by Haag [19] at the NASA Lewis Research Center. The torsional-type thrust stand was designed and built specifically to test pulsed plasma thrusters for single shot and multiple shot operating modes. This stand determines the impulse bit as a function of deflection, spring stiffness, and natural frequency. The simple torsional test stand had only one rotational axis. The structure was free to rotate about a vertical axis with the thruster mounted on the end of the moment arm and a counterweight attached at the other end. The thrust axis is aligned to be tangent to the sweeping motion of the arm and when the thruster fires the moment arm will rotate around the pivot [19].

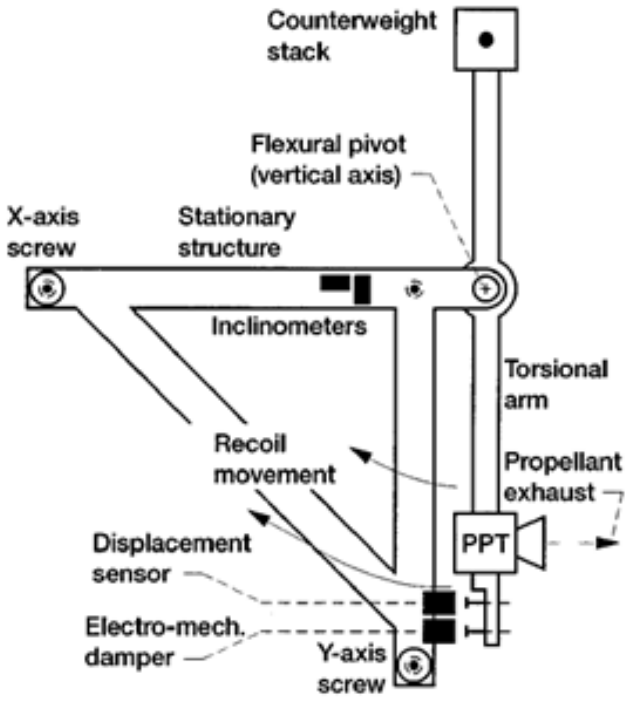

Figure 2.28: Torsional Thrust Balance [19]

The free suspended thruster will respond to a thruster firing such that,

$$I_L = M\dot{x}, \tag{2.11}$$

where the $\dot{x}$ is the recoil velocity, and I_L is the impulse delivered. The angular momentum of the device can be expressed as,

$$L = I_L r, \tag{2.12}$$

where L is the angular momentum, r is the radius of the applied force [19].

2.12.2 Torsional Pendulum

Torsional pendulum thrust stands have shown to provide the highest sensitivity but the worst stability. They are also known for providing effective performance measurements of pulsed thrusters [4].

Figure 2.29 shows a torsional pendulum setup by Lun and Law [5]. The thrust stand was designed to accommodate thrusters up to a maximum weight of 10 kg. The beam hinges on a flexural pivot which has low stiffness and is frictionless. Instead of using power cables the device used liquid gallium pots to transfer power to the thruster eliminating stiffness and friction from wiring. A series of demostrations were performed with VATs using a variety of propellants. It was observed that the displacement sensor output contributed a large portion of the thrust stand uncertainty. The setup showed that the measurement error was as low as 2.1% for thrusters that had impulse from 0.27μN-s to 600 μN-s [5].

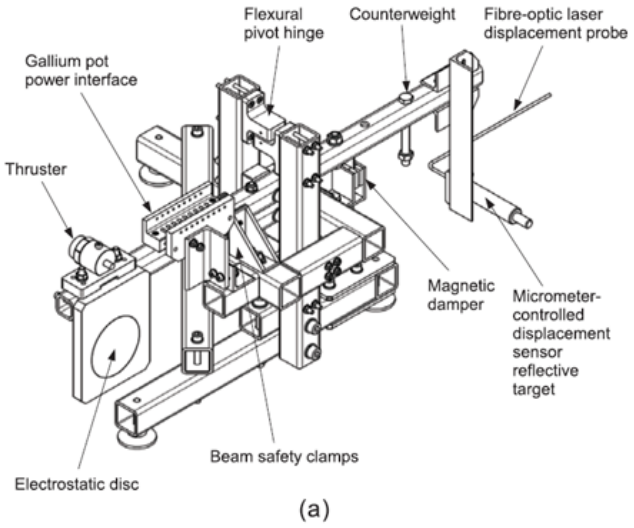

Figure 2.29: Torsional Pendulum Thrust Stand Schematic [5]

2.12.3 Advantages

One of the advantages to the torsional test stand design is the restoring force in the configuration rotates about an axis that is parallel to the gravity vector. Therefore, the analysis can be done independent of the gravity term. They have been shown to be effective in measuring the performance of pulsed plasma thrusters [10]. The torsional micro-thruster stand is different from the hanging and inverted pendulum thrust stand configurations in that its rotational axis is parallel to the gravity vector. This makes the response independent of thruster mass. This makes it ideal for measuring thrusters that are either changing in mass or facility that requires testing over a large range of thrusters [15].

2.12.4 Disadvantages

The primary disadvantage of this configuration is that the horizontal, asymmetric arrangement of its beams can be difficult to configure within a vacuum chamber that has limited space. The size of the beams needs to be large in order to increase its sensitivity. Its sensitivity does not readily allow for testing of higher power, steady-state thrusters [10].

2.13 Levitating Test Bed

At the Massachusetts Institute of Technology (MIT) a team of engineers characterized a magnetically levitating testbed for the purpose of testing an electrospray propulsion system. Hicks [41] looked at creating a zero friction environment for

measuring performance of ion thrusters. A design for a magnetically levitating payload was established using the thrust balance test stand concept. The payload was constrained to one degree of freedom, the rotational direction around the centerline vertical axis. An electromagnet was used controlled using a proportional-integral-derivative controller. The electromagnet would pull on a permanent magnet placed on the payload. The MIT concept can be seen in Figure 2.30.

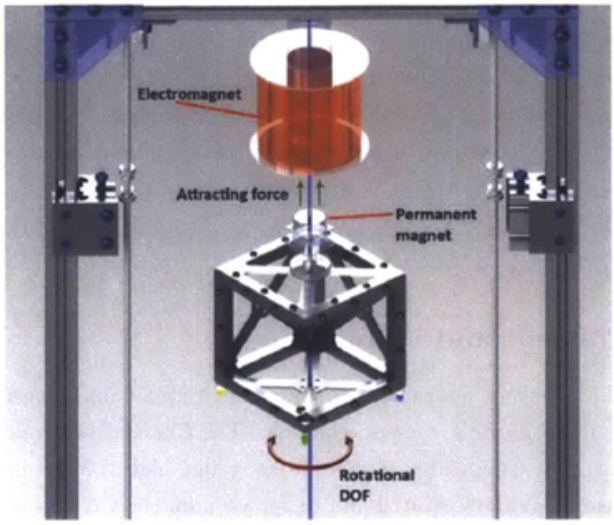

Figure 2.30: MIT Testbed Concept [41]

The constructed payload was designed to replicate a CubeSat with the appropriate electronics on board. In the test stand design, the electromagnet and vertical position sensor are placed at the top of the test stand and a magnetic dampener, charge sensor, and angular encoder are placed at the bottom of the test stand. The electromagnet received feedback control from the vertical position sensor, which tracked the position of the permanent magnet on the levitating testbed. The team

concluded on this method following trials using various magnets and Hall Effect sensors. A CAD rendering of the final MIT concept can be seen in Figure 2.31.

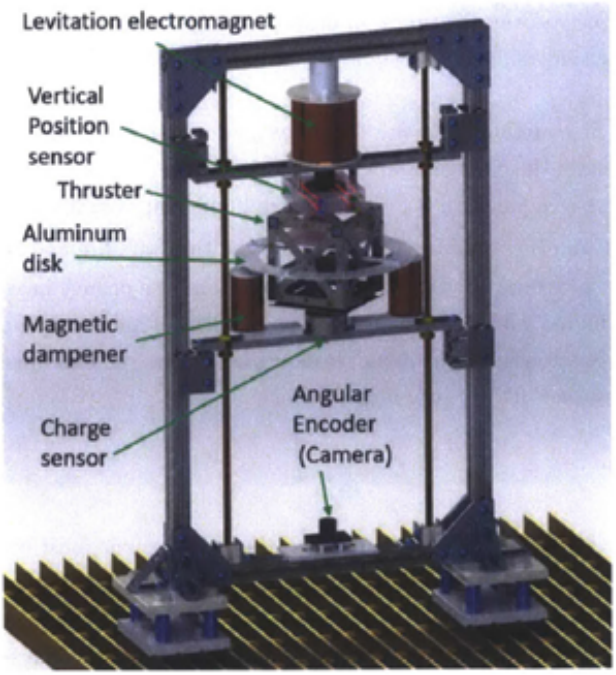

Figure 2.31: MIT Test Bed CAD Rendering [41]

In the experiment setup by Hicks [41], several methods were identified to measure performance characteristics. The first method was to measure the change in angular velocity of the levitated CubeSat using the angular encoder sensor on the bottom of the test stand. This sensor is a type of camera that extracts angular position information following each firing. Markers and the rotational axis are identified by the camera and the rotational rate is converted to angular velocity. This was the method used by the MIT group. The equation to determine the angular velocity can be seen below [41],

$$\Delta\omega = \int_{t_i}^{t_f} \frac{FR}{I} dt, \tag{2.13}$$

where $\Delta\omega$ is the proportionality between the time the thruster fires to the amount of thrust, F. R is the lever arm distance from the centerline axis to the thruster, I is the moment of inertia of the test bed [41].

Preliminary error and sensitivity analysis has been conducted based on estimated values; however, Hicks et al [41] did not mention actual thrust measurements in the documented work.

2.13.1 Advantages

The setup creates a low-friction environment for miniaturized propulsion devices. It reduced complexities by enabling a test environment using very few moving parts. Using the angular encoder to measure spin rate consists of a simple setup, although the frame rate must be high enough to capture the firings.

2.13.2 Disadvantages

One of the disadvantages to this system was the introduction of pendulum-like oscillations. The payload was put into a stable hover and then once the levitating testbed was rotating the payload would oscillate from side to side. Since the payload is not constrained any additional off-axial force can contribute to rotations in other degrees of freedom. While Hicks [41] says that the frequency of the oscillations was very stable he concluded that the frequency was affected by the moment of inertia. In

one experiment he showed that the period of oscillations were stable, but erratic. The strange behavior was also believed to been contributed by building and operational vibrations outside the test area. An electromagnetic dampener was used to induce eddy currents to counter the strange oscillatory behavior. The eddy currents produced would flow through the levitating test bed and generate opposing currents to the original currents created.

2.14 Inverted

An inverted pendulum micro-thruster stand is typically used when high sensitivity is needed and space is limited. In its simplest form, the test stand consists of a vertical arm that is attached to a pivot or flexure and a thruster mounted at the top of the arm. With this configuration the high stiffness of the elastic spring is countered by the destabilizing influence of the thruster weight. Most inverted pendulums thrust stands are very sensitive to shifts in the gravity vector. Few designs make use of counterweights in order to reduce this effect. They also use parallel links to the keep the thruster oriented horizontally throughout their motion [15].

An example of an inverted pendulum thrust stand can be seen in Figure 2.32. Side plates mounted vertically share the load of the propulsion system and maintain the top plate in a horizontal orientation. The arm of the inverted pendulum stand is primarily under compression stress by supporting the thruster weight. For angles of deflection less than five degrees, it is assumed that the applied thrust is proportional to the deflection. Measurement errors are seen in these stands mainly due to zero

drift and vibrations. The most common form of calibration to the pendulum is the application of known loads on the rigid thruster mount platform [15].

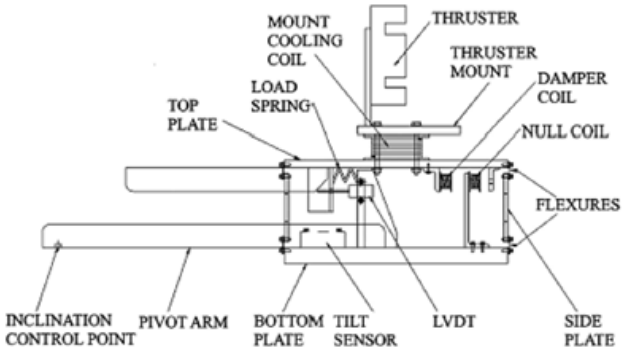

Figure 2.32: Inverted Pendulum Thrust Stand [15]

Assuming that the moment of inertia is $I \approx L_t^2 M_{Thruster}$, where $M_{Thruster}$ is the thruster mass, the natural frequency of the deflection can be expressed as,

$$\omega_n = \sqrt{\frac{k}{l^2 M_{Thruster}}} = \sqrt{\frac{(F/W)g_0}{x_{FS}}}, \tag{2.14}$$

where W is the thruster weight, g_0 is the gravity vector, x_{FS} is the maximum linear deflection, k is the spring torsion constant, and l is the length of the arm. Using this general expression an equation for finding thruster performance can be derived. Properly designed inverted pendulum thrust stands can evaluate micro-propulsion devices over a broad thrust range with low uncertainty and high repeatability [15].

Figure 2.33 displays an inverted pendulum system designed by Gong et al. [7] The system consists of the following parts: pedestal, vertical beam, rolling bearings, crossbeam, counterweight, thruster, thruster trestle, measurement sensor, propellant

pipe, and control wires. The whole system was monitored by a control box that was connected to a computer for data acquisition. The thruster was attached to the crossbeam via the thruster trestle. The counterweight, crossbeam, and sensors were attached to the rolling bearing from either side. Overall the design limited the maximum load for measurement up to 40 N [7]. In Figure 2.33 the numbering process for the schematic is as follows. 1: Pedestal; 2: Protection system; 3: Vertical beam; 4: Rolling bearings; 5: Propellant tank; 6: Counterweight; 7: Crossbeam; 8: Trestle; 9: Thruster; 10: Propellant pipe; 11: Control wire; 12: Standard ball; 13: Sensor; 14: Makeweight; 15: Automatic calibration component; 16: Control box; 17: Computer; 18: Iron core; 19: Electromagnetic coil; 20: Switch; 21: DC power [7].

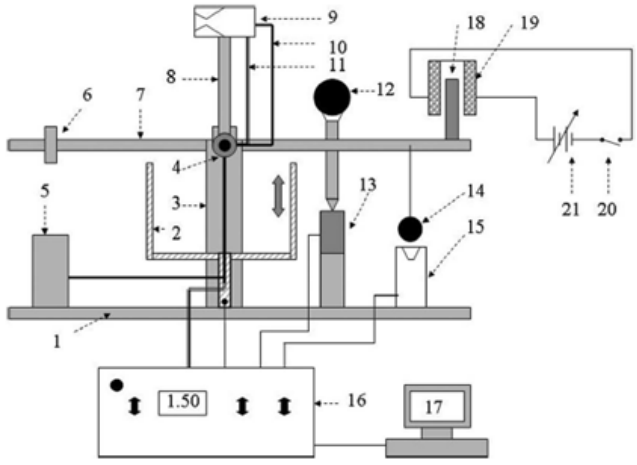

Figure 2.33: Pendulum Thrust Stand [7]

Figure 2.34 shows the freebody diagram of the inverted test stand operation. Due to the symmetrical structure of the crossbeam with respect to the bearings, the mass can be placed some location of vertical axis. Likewise, the thruster is placed at

the thruster center of mass. During the operation of the thruster, the force produced will cause the crossbeam to rotate. This displacement is captured by measurement devices and a signal is outputted to the computer [7].

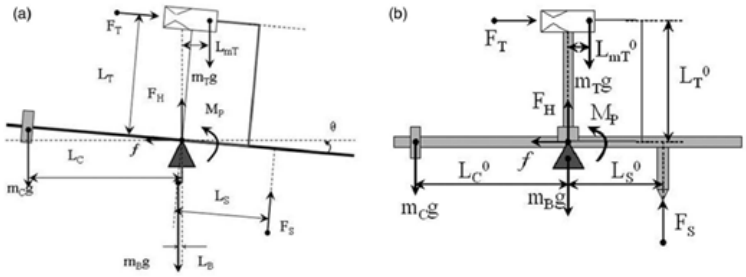

Figure 2.34: Freebody motion diagram of inverted pendulum device [7]

For steady state operation of the test stand the moment equation becomes,

$$F{\cdot}l_T + m_T g_0{\cdot}L_{mT} - M_p - F_s{\cdot}L_s - m_c g_0{\cdot}L_c - m_B g_0{\cdot}L_B = 0, \tag{2.15}$$

where F is the thrust, l_T is the length of the thruster arm, F_S is the force from the sensor support, L_s is the length of the sensor arm, M_P is the moment experience by the deformation of the propellant pipe and wires, L_{mT} is the location of the thrusters center of mass, L_c is the location the counterweights center of mass, L_B is the length of the beams center of mass, and g_0 is the acceleration due to gravity [7].

The final expression for the measured thrust is as follows,

$$F = \frac{F_S^T}{cos\Theta}{\cdot}\frac{L_S^0}{l_T^0} - m_T g{\cdot}sin\Theta - \frac{M_P}{l_T^0} + m_B g{\cdot}\frac{L_B}{l_T^0}, \tag{2.16}$$

The system was built for measuring low thrust values up to 1000 mN. The error in the full scale system was limited to 1% [7].

A test stand developed by Xu and Walker [18] used the theory and operation of a null-type, inverted pendulum concept. It was designed to support thrusters having a total mass up to 250 kg and used a null-type feature that was intended to eliminate thrust alignment error due to deflection of thrust. The nullification coil holds the thrust stand nearly stationary throughout the testing which also aids in reducing mechanical oscillations on the device. The test stand is similar to the one shown in Figure 2.35. The flexures of the stand were fitted with a load spring which would determine the level of deflection of the top plate. During thruster operation the top plate would deflect in the opposite direction of the thrust vector. The load spring can be varied to accommodate systems of varying masses. A thin M shaped metal band was used to form the shape of the load spring. This was done in order to reduce the bending moments that occur during thruster firing [18].

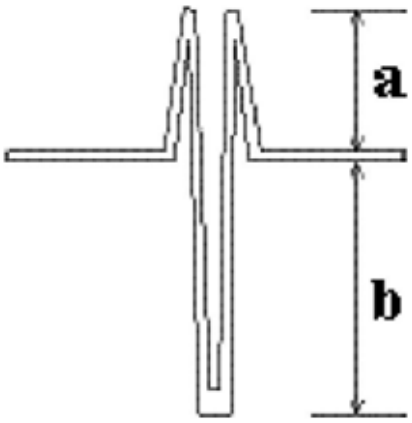

Figure 2.35: "M" Shaped Load Spring [18]

The overall deflection sensitivity for the device (D) can be given by the following expression [18] for an inverted pendulum,

$$D = \frac{F}{(k - W/R)}, \tag{2.17}$$

where k is the spring constant, R is the length of the thruster from rotational axis, F is the thrust force, W is the thruster weight. A leveling system was also used to ensure that the thrust remained perpendicular to the flexures. If the vector was offset it would have a vertical component thus inaccuracies would occur in the thrust measurement [18].

2.14.1 Advantages

Inverted pendulum thrust stands are least stable, but they have great sensitivity compared to other designs. They have been widely used for measuring performance of micro-thrusters of a broad range including: resistojets, electrothermal arcjets, hall thrusters, and ion thrusters [10]. In most inverted pendulum setups all movement during the thruster operation is limited to straight-line deflections. This is done by using parallel linkages. This non-rotational deflection is advantageous in that the center of mass of the thruster can be placed anywhere on the arm without significant impact on measurement accuracy. However, these advantages do come with complications. A parallel linkage thrust stand has more moving parts than a simple inverted pendulum. By adding more joints an increase in spring stiffness is

observed thus additional pendulum height or mass is required to maintain the original sensitivity [15].

2.14.2 Disadvantages

In practice, if the thrust is less than the weight of the thruster it is extremely difficult to read out thrust value from the measurement together [7]. A problem for the inverted pendulum configuration is that its stability is a strong function of the stiffness of the supporting beams. Additional thermal considerations for this must be accounted for. Due to their compact size, inverted pendulum thrust stands are susceptible to heat absorbed from the electric thruster operation. This may cause serious zero drift issues that must be mitigated with the use of thermal shrouds or active cooling. Most inverted pendulums thrust stands are very sensitive to shifts in the gravity vector. Few designs make use of counterweights in order to reduce this effect and those that do are not very compact. The use of short pendulum arms and large thrust-induced deflection can result in large angular deflections during tests. Significant rotations of the electric thruster are undesirable when taking plume diagnostics along with thrust measurements [15]. Thermal effects on the thruster arm may also be significant. In most cases an active cooling system must be employed in order to maintain equilibrium temperatures. Sometimes the test stand must be allowed to reach thermal equilibrium in order to reduce this uncertainty. Settling times may take up to ten minutes and may need recalibration [18].

2.15 Steady State Null Balance

The goal of a steady state thrust measurement is to be able to determine an unknown force in a laboratory environment and be able to distinguish transient variations in the thrust. The concept of a steady state null balance meets this constraint by applying controlled forces to the thrust stand deflection to quantify the unknown forces. When the deflection of the test stand is zero any applied control forces are assumed to be equal to the unknown force in the laboratory. The null control is used to absorb all of the unknown force during thruster operation thus reducing the uncertainties. With spring mass systems this is different as the load springs must be adjusted to absorb this unknown force. However, choosing a stiff load spring could result in the reduction of force measurement sensitivity. With a null balance, the thruster position is determined by a reference point and tuned using a feedback loop for stable operation [15].

2.16 Comparison

Compared to the other test stand designs, the hanging pendulum configuration has several design challenges in addition to the low sensitivity and gravitational influences. Proper design choices can help mitigate this effect. Both hanging and inverted pendulum types are typically less accurate than torsional based stands. This is due to the fact that they do not use counterweights to balance the test stand that reduce vibrations. While simple hanging pendulum test stands are not known for their sen-

sitivity or accuracy compared to inverted and torsional configurations several designs have achieved outstanding performance [15].

Another issue that complicates inverted and hanging pendulum designs is the deformation and generated stress from rotations on the propellant lines and wires connected to the thruster. While the thruster is on this can create some uncertainties in the calculations if not properly accounted for. Typically this value is assumed to be small thus neglected if the rotation angle is extremely small. In other cases redesigning the propellant lines and wires to be longer and of rectangular shape is needed to reduce the effects of deformation [7].

2.17 Test Stand Measurement Techniques

The impulse measurements differ greatly from conventional steady state measurements. One of the greatest challenges is measuring a transient force which may occur on low milli-second time scales and therefore difficult to measure. When designing a test stand for evaluating micro-thrusters the dilemma between sensitivity and bandwidth must be solved. In order to obtain high natural frequency of the system mechanical parts must be stiffened. This causes a decrease in measurement sensitivity and thus must be compensated by selecting highly sensitive equipment [8]. While many dynamic measurement tools are not well suited for measuring transient forces, the following sections try to summarize techniques for making good force measurements.

There are two kinds of approaches for measuring the thrust of pulsed plasma thrusters: (1) indirect, or (2) direct measurement. The indirect approach involves

keeping the thruster fixed to a test article and having the thrust go against a free-moving apparatus. The indirect techniques are very sensitive to small thrust forces, but they must be carefully designed to capture much of the ejected particles so as to give appropriate results [5].

The direct approach calls for more complex designs and are harder to build. The deflections seen by these systems are usually smaller than indirect systems. The most common type of direct impulse-bit measurement from pulsed micro-thrusters is pendulum mechanisms that detect sub-micron level. The most challenging aspects of a direct thrust stand design are: the use of low stiffness pendulum joints, the use of high-resolution displacement sensors, the elimination or minimization of friction and external disturbances, size limitations when operating in a high vacuum environment, and operating in the presence of electromagnetic noise [5].

2.18 Quality of Thrust Measurements

The quality of the thrust measurements are noted by Polk et al. [15] are expanded into seven thrust stand performance metrics. Those metrics include: Sensitivity, Repeatability and Long-term Stability, Accuracy, Resolution, Noise Spectrum, Response Time, and finally Predictability of the Response.

The sensitivity of the micro-thruster test stand is one of the most important design parameters. It is mostly responsible for the precision and resolution of the thrust measurements. In practice, the sensitivity of the device depends on the ability to measure the deflection of the moment arms. Stability of the thrust stand response is also important in long-duration, time-resolved thrust measurements. Repeatability

can be affected by drifts in the post test pendulum response or changing spring constants over the duration of an experiment. This can cause significant impacts on the accuracy of the test stand [15].

It is very important to ensure that the thrust stand is accurate within an acceptable range of measurement uncertainty. High accuracy in a precise thrust measurement is achieved by reducing the systematic errors. Calibration of sensors by applying known forces or impulses can also aid in reducing these uncertainties. The resolution which is defined as the smallest difference between two measurements can be observed in the responses. The resolution is limited to the level of noise in the test stand response. The sources of the noise can be from electrical influences with sensors, mechanical noise from vibrations in the laboratory, long time scales and thrust stand responses due to thermal effects. The level of noise can also be generated by the thruster. The response time of the thrust stand can be crucial for time-resolved thrust measurements. Finally the test stand response should be predictable [15].

2.19 Calibration Methods

Many calibration techniques have been used to establish the reliability and accuracy of micro-thruster test stands. Techniques such as gas calibration, electrostatic combs, impact hammers, and magnetic solenoids have been used. They are all complex to design, manufacture and handle, and they all require extensive and high accurate support equipment [5].

2.19.1 Zero Drift

Pendulum thrust stands are susceptible to a condition called ″zero drift.″ This means that when the thruster is turned off, the pendulum arm does not return to its initial position causing some offset. These are caused mainly from unsteady thermal loads and vacuum tank distortions during the period of an experiment. Any deviations can result in large uncertainties in the final calculation. It is a serious issue that may influence the measurement time. To mitigate thermal effects on structures and wires the test environment must be kept at constant balance temperature and or active temperature control is needed [5].

2.19.2 Application of Known Force

In order to perform the micro-thruster tests in the laboratory, complex interfaces between the propulsion device and the test facility are required. Calibration of these devices is needed in order to promote the accuracy of the results. The contributions of the error can be characterized individually to determine the test stand sensitivity. Calibration of applying know forces F_{cal} at a point L_{cal} from the pivot can be seen in the following expression [15],

$$S_{cal} = \frac{\Delta x_{SS}}{F_{cal}} = \frac{L_{pm} L_{cal}}{I \omega_n^2}, \tag{2.18}$$

To calculate the steady state thrust of a thruster from a measured displacement and the applied thrust forces [15],

$$F_t = \frac{(L_{cal}/l)}{S_{cal}} \Delta x_{ss}, \tag{2.19}$$

The calibration forces can be applied a number of ways. One approach is to do this by loading and unloading weights with known masses on a fiber and pulley system attached to the pendulum. The fiber and pulleys must be aligned properly so as not to introduce error. Figure 2.36 shows a schematic of two different make weight methods. The figure on the left shows an automatic calibration component while the figure on the right shows a fiber and pulley system [15].

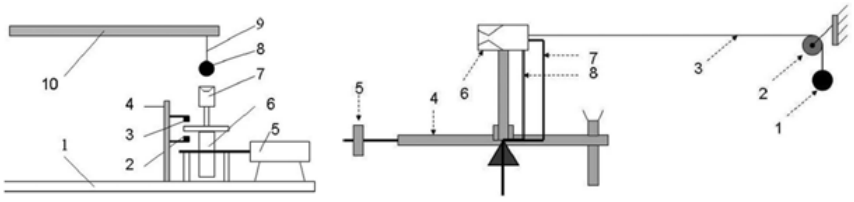

Figure 2.36: Schematic of Known Force Calibration [15]

In the study completed by Orieux et al. [8] the thrust stand was validated by using 4 mm diameter cylindrical thrusters. The theoretical thrust force was calculated using,

$$F = \dot{m} V_s + (P_{ext} - P_s) \times A_s, \tag{2.20}$$

where $\dot{m}$ is the mass flow rate, V_s is the exhaust velocity, A_s is the exhaust area, P_{ext} is the exhaust pressure and P_s is the chamber pressure. Uniform axial velocity and perfect gas assumptions were made in order to yield a theoretical force of 0.494

mN. After running a series of experiments the average measured thrust was 0.497 mN disregarding transients that occur with ignition and end burning [8].

2.19.3 Electostatic Calibration

In the study conducted by Lun and Law [5] calibration of the test stand was performed by using a device called the Electrostatic Calibration System. In this method two stainless steel discs were positioned in close proximity to one another and an electrostatic force was generated by creating a potential difference. The advantages to this method are the force is applied in a non-contact fashion, a wide range of forces can be applied and the calibration can be done without disrupting the testing [5].

Electrostatic force is a good option for calibration due to the sensitivity of most moment arms. The electrostatic force can be accurately calculated since there is no direct physical contact between the two disks during the test. The electrostatic force, F_q, exerted by an electric field on the surface of a conductor,

$$F_q = \frac{1}{2}\varepsilon_0 \varepsilon_r E_e^2, \tag{2.21}$$

where E_e is the electric field on the surface of the electrode, ε_0 is the permittivity of the vacuum and ε_r is the relative permittivity which is approximately 1 for air or vacuum [6].

Another method in calibration that has been discussed in the literature is the microbalance method. For this method to work a permanent magnet is attached to an electronic balance while a multi-turn coil is attached to a reference frame as

seen in Figure 2.37. A power source supplies the coil with a current which will repel the permanent magnet thus applying a force on a scale. The initial spacing between the coil and electrical input must be noted and recreated on the thrust stand. The calibration method has the following advantages: it is completely frictionless, the effect of axis misalignment between the coil and the magnet of a small displacement range can be ignored, the effect of the axial motion between the coil the magnet over a small displacement range can be ignored, the force created between the coil and the magnet can be controlled [24].

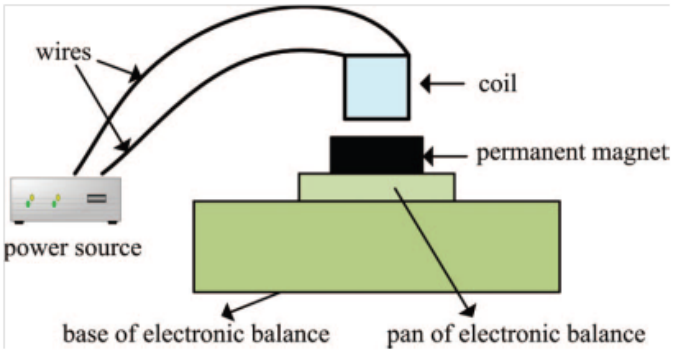

Figure 2.37: MicroBalance Method [24]

2.19.4 Application of a Known Impulse

Pulsed calibration is also used in practice to make impulsive measurements on thrust stand designs. The most common stands are designed to make impulse measurements and are free moving types as they are allowed to oscillate after perturbations. Calibration can be accomplished by applying known impulses $I_{bit,cal}$ at

a point L_{cal} from the pivot. The change in dynamic response can be outlined in the following way [15],

$$S_{cal} = \frac{\Delta\dot{x}(0)}{I_{bit,cal}} = \frac{L_{pm}L_{cal}}{I}, \tag{2.22}$$

Typical calibration methods for applying a known impulse include both contact and non-contact methods. The contact calibration methods include: swinging known masses, impact pendulums, and impact hammers. The non-contact calibration includes methods such as: gas dynamic calibration and electrostatic combs. Generally the impact hammer and electrostatic combs are used in practice [15].

In the study completed by Lugini and Romano [16] two methods were implemented in calibrating the test stand measurements. For the first calibration model, the inelastic collision theory was considered and a known impulse was given to the test stand. The collision resulted in an instantaneous gain of velocity which caused oscillation. Figure 2.38 shows the model for this calibration experiment. In order to cause the impulse a known mass was hung by a wire the same length as the gondola. It was then dropped from a known height in order to cause the collision. Since the mass was covered in a sticky material it remained attached to the test article [16].

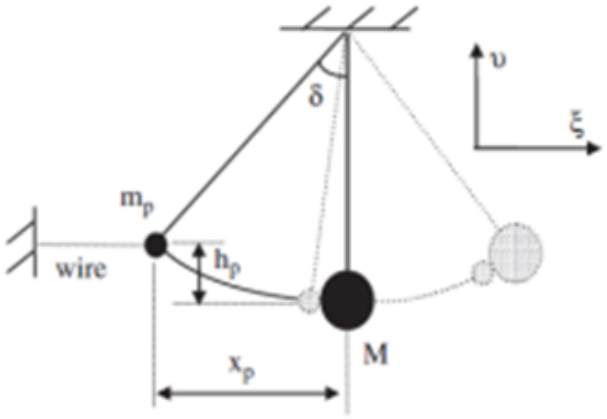

Figure 2.38: Calibration Model of Inelastic Collision Theory [16]

The mathematical model started with the conservation of mechanical energy for a proof mass,

$$E_K + E_p = C, \tag{2.23}$$

This is expanded into the following expression,

$$\frac{1}{2} M_{Proof} V_{pmax}^2 = M_{Proof} g_0 h_p \rightarrow V_{pmax} = \sqrt{2 g_0 h_p}, \tag{2.24}$$

Finally, the expression for finding the maximum horizontal displacement for the inelastic collision is derived,

$$x'_{max} = l_{Pendulum} \sqrt{1 - \left[1 - \frac{1}{2 g_0 l_{Pendulum}} \left(\frac{I_L}{M_{Proof} + M_{Gondola}}\right)\right]^2}, \tag{2.25}$$

After calculating the theoretical maximum horizontal deflection a laser was used to measure the experimental value of horizontal deflection during the first oscillation after the collision [16].

Figure 2.39 shows the impact pendulum calibration technique used by Haag [19] to calibrate the thrust stand. The momentum was directly delivered by a pendulum that was suspended the same height as the target. Optical devices monitored the motion of the pendulum [19].

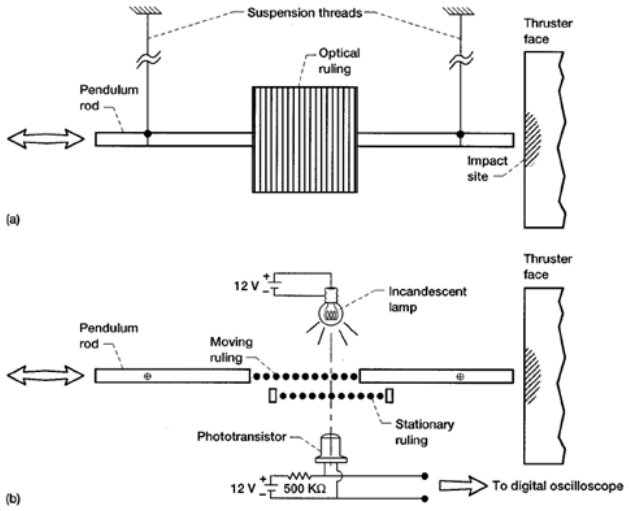

Figure 2.39: Impact Pendulum Calibration Technique [19]

CHAPTER 3

EXPERIMENTAL APPROACH

3.1 Product Conceptualization and Realization

To take measurements for the pulsed plasma thruster, a magnetically levitating test stand was developed in which the propulsion system would be suspended by a magnetic field for low, constant force measurements. The propulsion system consists of the micro-thruster, firing circuit, and power source. Also, mounted to the payload with the propulsion systems is the sensor package capable of detecting changes in acceleration and velocity. A wireless firing system enables the firing of the micro-thrusters. The motion induced by the firings is measured and used to determine the thrust and impulse bit. The following sections describe the details of the test stand and propulsion system. The design evolution of the final design is described in Appendix A of this document.

3.2 Atmospheric Test Stand

For the purpose of this research the test stand was developed to first perform a series of experiments in atmospheric pressure conditions. The test stand structure would have the capability to perform reduced pressure testing in the future. An elec-

tromagnet mounted on the test stand suspends the propulsion system. The strength of the electromagnet is controlled via a control circuit that uses a hall sensor to provide feedback information. The control circuit is programmed to suspend the payload at a specific location between the electromagnet and sensor. After the payload reaches a stable hover, a wireless firing system on board the payload transmits a command to fire two opposing thrusters to create a torque which rotates the thrust platform. The rotational system provides an advantage over a linear system because the combined effects of multiple firings can be evaluated to assess the total acceleration or deceleration of the thrust platform over a long period of time and consecutive firings.

During this process, analysis was done to show the engineering tradeoff between the allowable distance between the permanent magnet and electromagnet and the distance between the permanent magnet and hall sensor. This study resulted in changes to electromagnet size and hall sensor placement. The final maglev design and the control circuit, in Figure 3.7, are based on a magnetic levitation kit from ″Maglev Plus System Magnetic Levitation Experiment″[55].

The final atmospheric test stand, seen in Figure 3.1, was approximately 24″ x 24″ x 18″ in total volume. This relatively small size aided the mobility of the test stand. The structure's skeleton was fabricated from aluminum t-slotted rails, also known in industry as 8020 railing. The test stand had an enclosure that was fabricated from super abrasive scratch resistant clear acrylic. This enclosure was designed to reduce environmental effects on the testing.

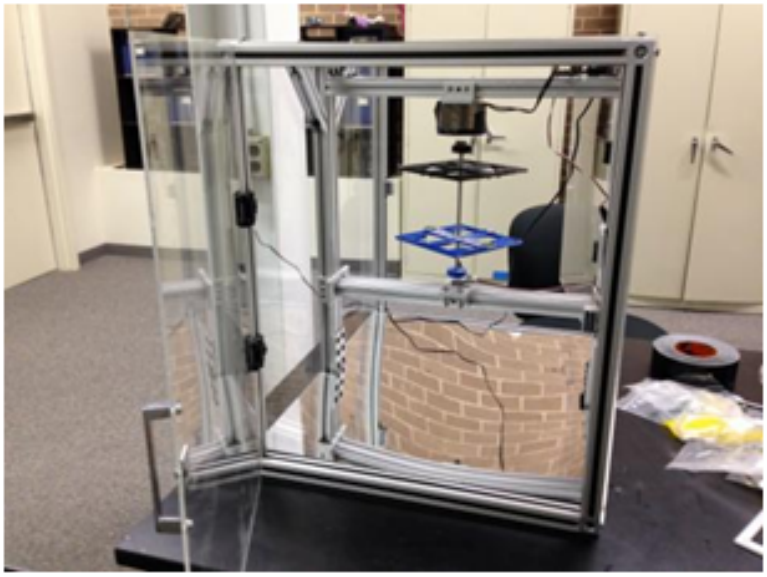

Figure 3.1: Payload Inside Enclosed Test Stand

During the final diagnostics of the MLC, instabilities were observed with the rotation of the levitated payload. It was observed that differences in internal calibration of the gains of the controller and vibrations external to the system caused additional vertical oscillations. The internal calibration error was due to differences in electromagnet and hall sensor placement. If the centerline axes of the electromagnet and hall sensor were not perfectly aligned the levitating payload would spin at an angle inducing off balance rotation. Other internal vibrations include those caused by the error in the MLC and small inefficiencies in manufacturing that caused center of mass balancing issues of the levitating payload. External vibrations were caused by vibrations of the building and affects of airflow in laboratory testing. The instabilities became worse after a series of rotations from the payload. To mitigate this condition a constraint was fabricated and mounted to the test stand.

Figure 3.2 shows the payload constraint system without the payload. The PCS was fabricated using 6010 Aluminum at a thickness of 1/8″. This Aluminum bar was attached to an 8020 rail guide using a 90° bracket and 1/4″-20 bolts. The reason for using the rail guide is for easy adjustment of the PCS during pretest procedure. 5/16″ holes were drilled into the aluminum bar in order to enclose the bottom standoff from the payload.

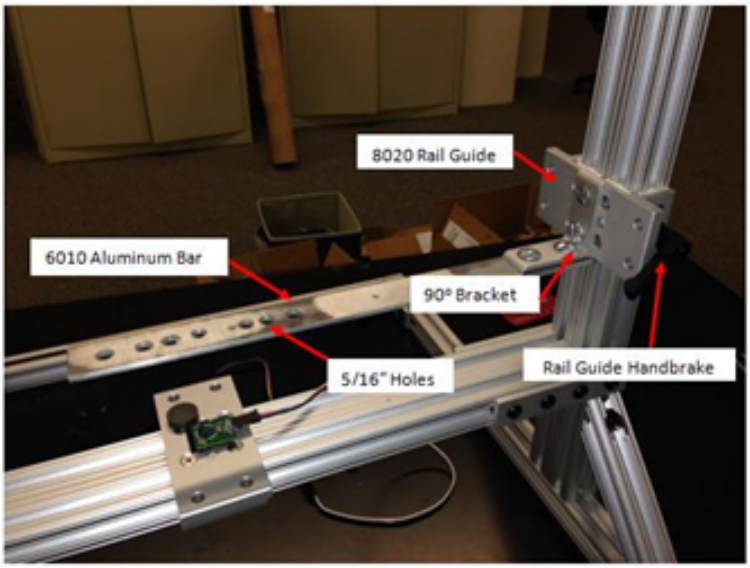

Figure 3.2: Payload Constraint System (PCS)

Additional test stand refinements were made in order to promote stability throughout experimentation. The test stand system was upgraded with new components for the MLC. These new components included a larger electromagnet and a fine-adjustment hall sensor lift. This would reduce time to stabilize the payload in a constant hover/levitation. These upgrades can be seen in Figure 3.3.

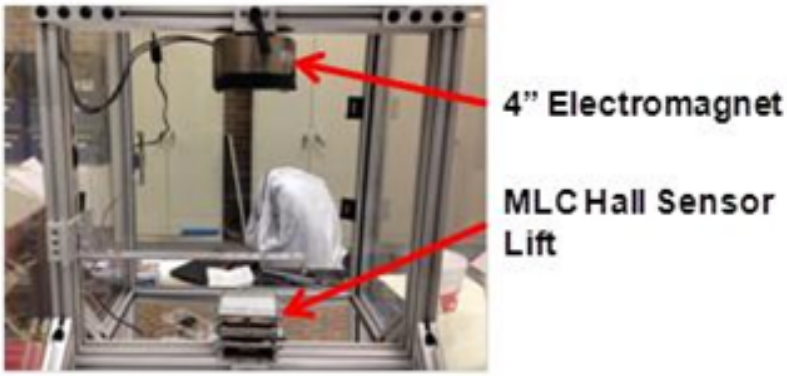

Figure 3.3: Magnetic Levitation Controller Upgrades

3.3 Magnetic Levitation Controller (MLC)

The MLC consists of an electromagnet, a hall sensor to measure the strength of the electric field and a control circuit that would regulate the amount of power distributed. The final assembled MLC circuit can be seen in Figure 3.4. The hall sensor, as seen in the Figure 3.4, consisted of a triad of hall sensors for the purpose of reducing the sensitivity of the feedback. These sensors detect the position of the levitating test platform.

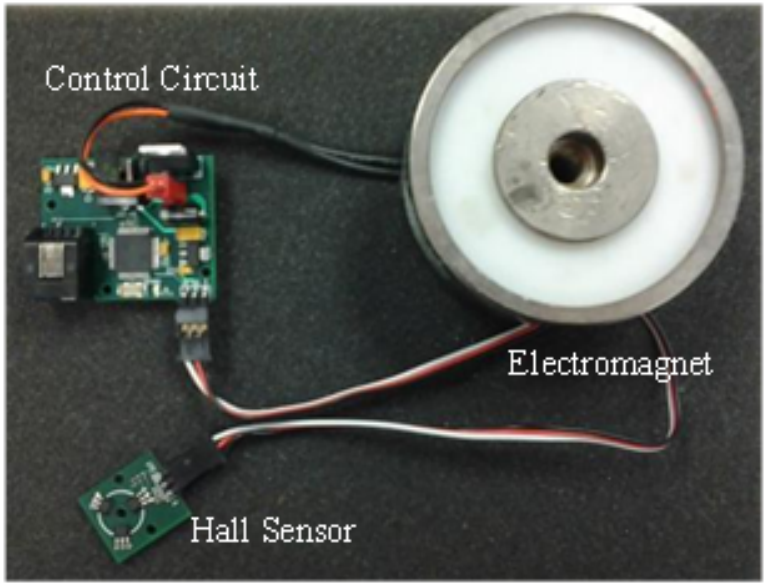

Figure 3.4: Assembled Maglev Control Circuit

The electromagnet is an APW Company EM400-6-212 4″ diameter round electromagnet. The input voltage for this electromagnet is 6 VDC and requires 3.33 A at the rated voltage. The electromagnet has a rated holding force of 640 lbf and works with a 4 A power supply for the control circuit [40]. The electromagnet can be seen in Figure 3.5. It is 1.65″ in height and 4″ in diameter. With this electromagnet the controllable region for the payload is 0.5″ to 1.5″ from the surface of the electromagnet.

Figure 3.5: Electromagnet

3.3.1 Electromagnet Control

A basic Proportional Derivative (PD) feedback control circuit, discussed in Tan et al.[28], was developed in order to provide the magnetically levitating test stand the appropriate control logic. The PD controller is a control loop feedback mechanism that calculates an error value as a measured process value and a desired set-point. Using this feedback mechanism, the PD control circuit distributes power to the electromagnet based on the level of magnetic flux detected by the hall sensor. If the value for this magnetic flux is higher or lower than the desired set point the power directed towards the electromagnet is adjusted. Four parameters were varied to provide stable controller feedback to levitate the payload. The four parameters were the hall sensor set-point, proportional gain, derivative gain and duty cycle for the electromagnet. The MLC feedback logic can be seen in Figure 3.6.

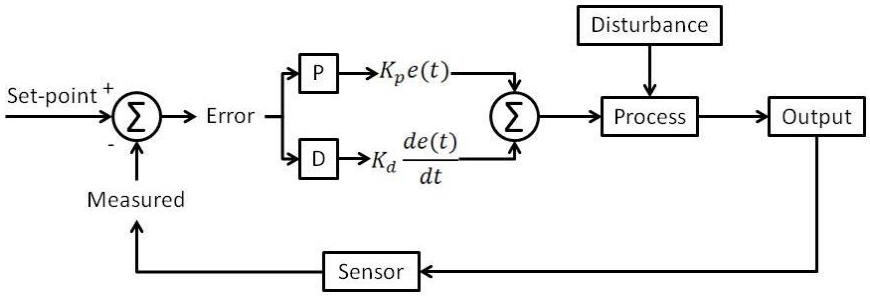

Figure 3.6: MLC Feedback Schematic

The set-point, which is the position of the bottom magnet relative to the hall sensor, is controlled by the user input into the control circuit and is measured by the hall sensor on the bottom of the MLC setup. The user inputs are coded into the program for the MLC micro-processor. The error between the user defined set-point and the hall sensor reading for the actual payload location is then fed into the Proportional-Derivative (PD) controller. The K_p and K_d, the proportional gain and derivative gain, respectively are additional user inputs. These are configured to give the best response of the control system. These values are then processed with additional payload disturbances and outputted as a pulse width modulation (PWM) response for the electromagnet.

The proportional gain term produces an output value that is proportional to the current error. The proportional response is adjusted by multiplying the error by a proportional gain constant. If the proportional gain is set too high this will result in a large change in the output for a given error value, thus creating a system that may become unstable. However, a proportional gain that is set too low will result

in a less responsive and less sensitive controller, thus the control action may be too small to respond to system disturbances. It is ideal in tuning theory and practice that the proportional term should contribute to the majority of the output.

The derivative gain term produces an output value by determining the slope of the error over time and multiplying this rate of change by the derivative gain term. The derivative term is used to predict a systems behavior and improve the stability of the system by improving the settling times. An integral gain term was not used for this particular application since the integral term responds to sum of instantaneous error over time. This can cause the present response to sometimes overshoot the set-point value. The derivative gain term helps speed up the dynamical response by predicting future errors and avoiding excessive over and under shoots [28].

The output of the control circuit is a pulse width modulation (PWM) signal to the electromagnet. PWM is widely used with control systems as a means of controlling the average value of a DC voltage. The amplified DC signal is divided into pulses, by varying the width of the pulses [50]. This pulsing signal allows for greater control of power supplied to the electromagnet. The advantages of using a PWM signal is it has low sensitivity to noise unlike an analog signal and additionally, no analog to digital conversion is necessary. However, the disadvantages are that a more complicated code is needed and the transmission rate is limited by period and resolution of the transmitting device. Three quantities describe a PWM signal. These quantities are the period, pulse width, and voltage. One way to further control the pulsing signal is by adjusting the duty cycle of the electromagnet. The duty cycle

describes the proportion of on time to the period of time and can be seen in the following expression:

$$DutyCycle = \frac{PulseWidth}{Period} \times 100\% \tag{3.1}$$

The higher the duty cycle the longer the signal is active before switching off. This technique allowed for a method to digitally encode analog signal levels and modulate the electromagnet [27].

3.3.2 Control Circuit

Figure 3.7 shows the circuit diagram for the MLC microcontroller. This control schematic was refined from a basic magnetic levitation circuit design in ″Maglev Plus System Magnetic Levitation Experiment″[55]. The maglev circuit was also designed to use larger electromagnets without significant modifications to the components. The three components of the MLC that were modified were the power supply, electromagnet, and MOSFET. The switching electronics uses an N-Channel MOSFET with a fly back diode to accommodate potential reverse voltage caused by inductive loads. The MOSFET is a three-terminal device that has a control electrode, or gate, that draws no DC current since it is insulated from the substrate to which it is attached. The gate lies between the other two pins, the drain and source. When the gate of the MOSFET is grounded, no drain-to-source current flows for a positive drain voltage. MOSFETs are very useful for this type of circuit since they are excellent high-current voltage-controlled switches [49].

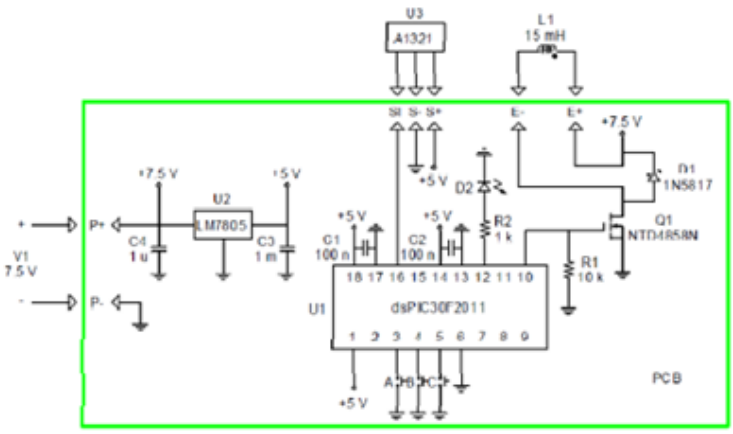

Figure 3.7: Magnetic Levitation Controller Circuit Design

3.4 Payload Design

A payload was designed in order to provide a platform for micro-thruster firing electronics. The platform was fabricated using available on-site rapid prototyping technology (RP). This technology greatly reduced manufacturing time and effort while increasing quality. The RP platform can be seen in Figure 3.8. A component mounting system was included in the design. The dimensions of these RP plates were 6″ x 6″ x .25″.

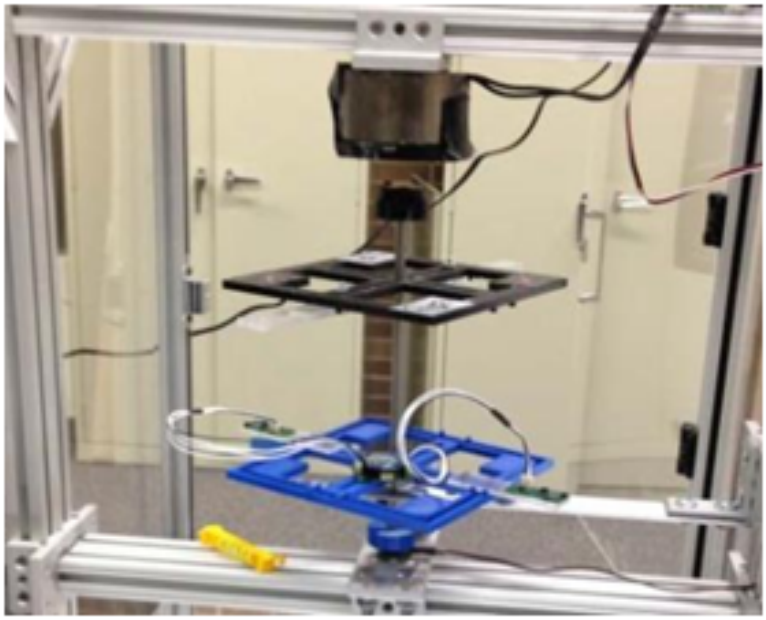

Figure 3.8: 2nd Generation Payload

3.5 Test Samples

The test samples used for the development of test stand technology was the electrical solid propellant micro-thrusters developed by DSSP. The micro-thrusters come from a line of high performance plastisol solid propellants that features electrical igniterless ignition. They use inert metal electrodes and are highly manufacturable using benign processes [22].

The micro-thrusters used in this experimentation were approximately $1''$ in length and around $1/4''$ in diameter. The supplier information provided stated that on average each thruster will fire for 1.5 s and will generate between 5-10 mN of thrust during that time. The pulse durations should be between $50-200$ ms. A control circuit to supply 300 VDC to the micro-thruster with a total of 45 J of energy

was developed. Figure 3.9 shows some sample data for thrust variation with increasing number of electrical pulses [22].

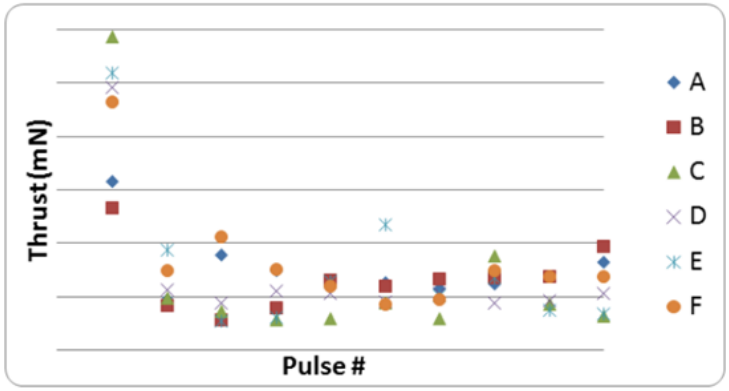

Figure 3.9: Sample Chart for Micro-Thruster Data [22]

3.6 DAQ and Firing Circuit

The test stand data acquisition (DAQ) system is composed of sensors, a firing circuit, a wireless firing system, and PCB. The micro-thruster required 45 J of energy for ignition. This was accomplished with a 300 V transformer and a 1000 μF capacitor. An MaxStream Xbee was used to transmit the firing command wirelessly from a laptop computer with the appropriate software to the microcontroller. The MaxStream XBee is a low-cost, low-power wireless sensor that would transmit data from the levitating payload to computer software. It has an indoor range of up to 100 ft and transmits at a baud rate of 57600 bps [53].

3.6.1 Firing Circuit

The design of the 300 V firing circuit using an inverted transformer included a charge completion indicator using a varistor with LED and an electrically controlled firing switch using a silicon controlled rectifier (SCR also called a thyristor). The circuit design for the firing system is shown in Figure 3.10. The primary components used in generating 45 J of energy were the transformer and capacitor. The capacitor used was a PHOTO flash PF360-1000μ. The maximum voltage and capacitance was rated at 360 V and 1000 μF, respectively [42]. The inverter transformer used in the circuit was the Xenon Flash Tubes XFT-5683-3v. This transformer would step up 3 V input to a 300 V output [43]. A microprocessor was used to generate a PWM signal to control the transformer. The PWM signal controls flow through the primary coil of the transformer using a MOSFET. The advantage of using a microprocessor to generate the transformer input is that the frequency can be controlled and the firing decision and charge monitoring can both be monitored actively. The firing signal was transmitted using transistor-transistor logic (TTL) devices. For this type of trigger signal the digital output of a TTL device is typically between 0 and 0.5 V for low voltages and between 2.7 V and 5 V for high input signals [49]. The capacitor voltage was actively monitored using an adjustable comparator circuit connected to the microprocessor. This feature allowed the charging to be stopped once a defined voltage had been reached. An MOC3020 optically isolated SCR driver was used to interface electronic controls and power the SCR at high voltages. The opto-isolator creates a state of electrical isolation between the input and output circuits by transmitting

the signal optically instead of transmitting via a hard wired electrical connection. The advantage of this component is to protect output circuits from excessive voltages that could damage critical components [49]. The microprocessor used in this development firing circuit was the PIC32 MX150F128B Microchip Technology microcontroller. The microprocessor consists of twenty-eight pins, has 128 KB of program memory, 32 KB of data memory and can operate at up to 50 MHz [46].

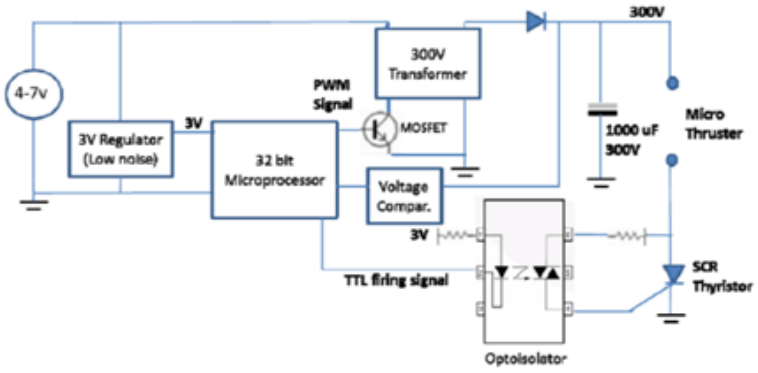

Figure 3.10: Revised 300 V Firing Circuit with Comparator and Optoisolator

The dual-thruster firing printed circuit board (DF PCB) is shown in Figure 3.11. It includes duplicate SCR firing circuits and transformers to simultaneously charge two capacitors from a single battery source. In addition, the firings of two thrusters are controlled using the same microprocessor allowing time syncing of both firing events.

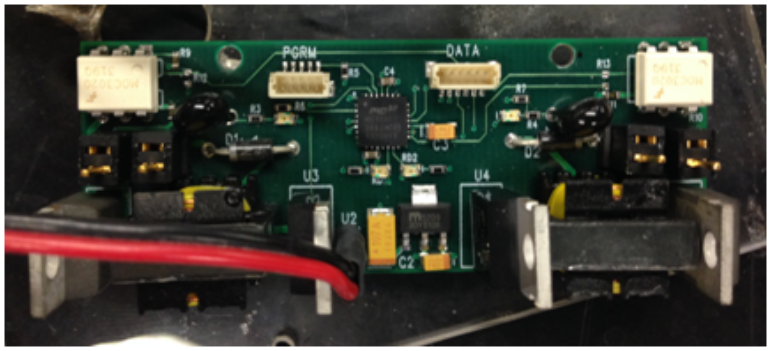

Figure 3.11: Dual Thruster Firing Printed Circuit Board

3.6.2 Firing Circuit Program

Figure 3.12 shows a flow chart for the microprocessor program for the DF PCB. The code monitors the charging of the 1000μF capacitor. When a power supply is applied to the DF PCB the microprocessor initiates the loop and the 300 V transformer continues to charge the 1000μF capacitor until it is charged to 300 V. When the capacitor reaches 300 V the microprocessor turns off the transformer and holds the charge until a fire command is recognized. Once the fire command is applied the for loop starts again since the voltage is discharged from the capacitor.

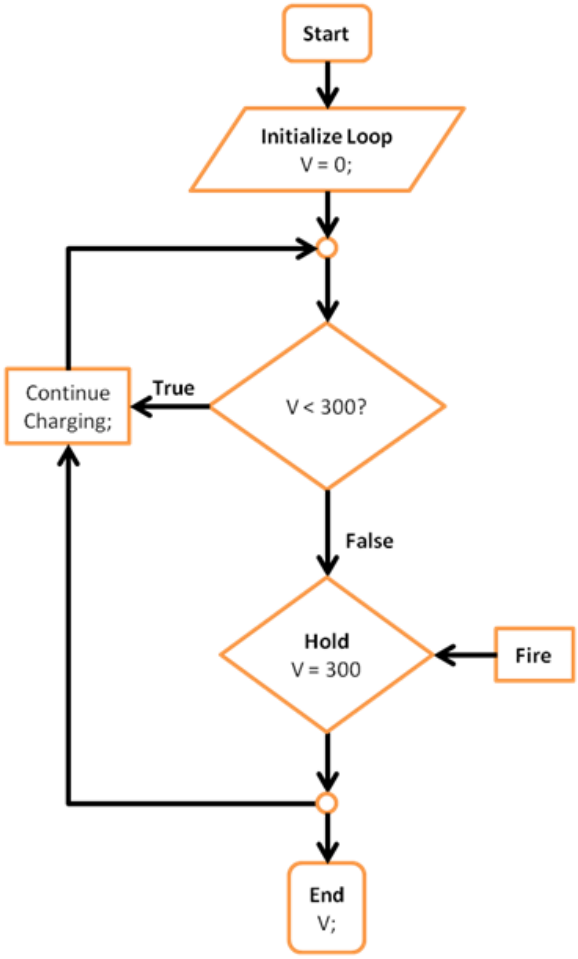

Figure 3.12: DF PCB Microprocessor Code

3.7 Components and Sensor for Thrust and Impulse Bit Measurement

The basic setup of this experiment consisted of two thrusters mounted at either end of a moment arm. However, in application, only one thruster was used for testing. A MEMS gyroscope and two MEMS accelerometers were mounted to the payload to take linear acceleration and angular velocity data after each individual firing. The experiment setup schematic can be seen in Figure 3.13. Both accelerometers would be

placed with the same radius in the negative and positive directions of the centerline. Upon ignition of the thrusters the force produced would cause the payload to rotate about a centerline axis. The gyroscope directly measures the payload angular velocity, ω. The angular velocity provides a measurement proportional to the time integral of applied force, which suitable for quantifying the thruster impulse response. However, to predict a thrust versus time profile requires numerical differentiation to calculate α, which because of sensor noise is impractical.

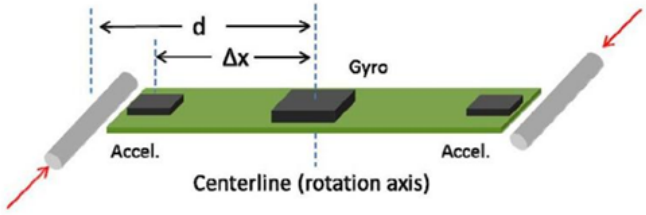

Figure 3.13: Experimental Sensor Setup

The accelerometers offset from the rotation axis by a distance Δx provides the following relationship between linear acceleration a and rotational acceleration α,

$$a = \Delta x \alpha. \tag{3.2}$$

The tendency of a force to rotate an object about an axis is physically defined as torque [31]. While force measurements were deemed impractical in this research the following methods would be used to determine force. To begin developing the equations of motion for finding force and impulse bit, Newton's second law of motion must be considered. Newton's Second Law of Motion states that [32],

$$F_{net} = ma. \tag{3.3}$$

The payload in the experiment represents a rigid body rotating about a centerline axis. This means that Newton's second law for rotation must be used. This can be done by changing the net force and acceleration to tangential components [32],

$$F_t = ma_t. \tag{3.4}$$

The torque acting on the system can be represented in the following equation [32],

$$\tau = F_t r = ma_t r. \tag{3.5}$$

The tangential acceleration term is a lateral acceleration which must be converted to an angular acceleration term. This can be done by substituting $a_t = \alpha r$, giving

$$\tau = m(\alpha r)r = (mr^2)\alpha. \tag{3.6}$$

By substituting the equation of rotational inertia for a mass rotating about a fixed axis, $I = mr^2$,[33] the radian measure torque equation becomes[32]

$$\tau = I\alpha. \tag{3.7}$$

To calculate torque the cross product of the radius and force vectors must be computed. The relative torque is now defined as[32],

$$\vec{\tau} = \vec{r} \times \vec{F}. \tag{3.8}$$

The torque, also known as moment of force, can also be represented in the following form [34],

$$\vec{M} = \vec{r} \times \vec{F}. \tag{3.9}$$

The payload on the rotational test stand responds with a rotational acceleration α in relation to the applied opposing thrusters according to,

$$\sum M_{applied} = d(T_1 + T_2) = I_{zz}\alpha. \tag{3.10}$$

where $M_{applied}$ is the applied moment ignoring drag, I_{zz} is the payload rotational inertia, d is the thruster distance from the rotational axis, and T_1 and T_2 are thrusts. The measurement equation of the combined thrusts becomes,

$$(T_1 + T_2) = \frac{I_{zz}\alpha}{d}. \tag{3.11}$$

From Eq. (3.11), the thrust can be determined if the angular acceleration α is known. No sensor directly measures α so the Δx is needed to find this value.

The completed electronic hardware printed circuit design is shown in Figure 3.14. The board has three primary sections: a main center module which contains the microprocessor, gyroscope and wireless communication, and two accelerometer modules. The gyroscope module can be placed anywhere on the payload. The two

accelerometers are placed on the payload offset from the rotation axis by a distance Δx. The linear acceleration measured by these accelerometers and the offset distance from the rotation axis are used to calculate the rotational acceleration α.

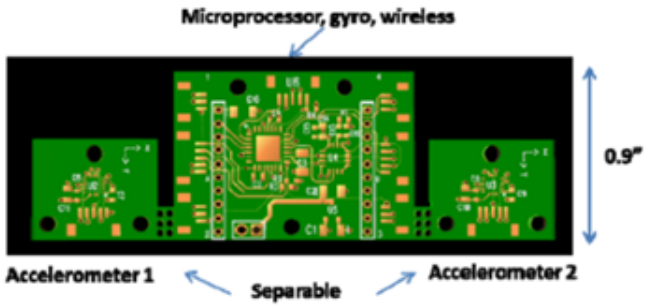

Figure 3.14: Sensor Printed Circuit Board Design

After the manufacturing of the angular rate and acceleration sensor PCB were completed the surface mount components was completed with the final assembled module shown in Figure 3.15. The MEMs gyroscope is an ST Electronics L3G4200D that has three full scales up to 2000 dps, 16 bit-rate value data output, and sensitivity up to 70 mdps/digits [47]. The MEMs accelerometer used is an ST Electronics LIS3DH that has four full scales up to 16gs, 16 bit-rate data output, and sensitivity up to 12 mg/digit [48].

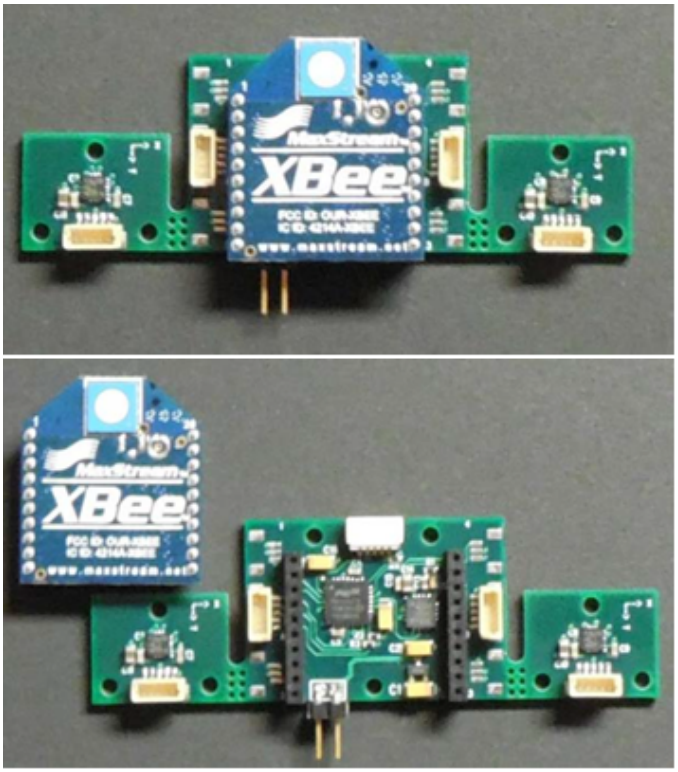

Figure 3.15: Assembled Angular Rate and Acceleration Sensor PCB

Figure 3.16 shows the program flowchart for the sensor package. When a power supply is applied the microprocessor begins the data capture process by initializing the loop. The buffer of the microprocessor continues to take values and transmits this data to a computer software when given a command. The lateral acceleration a and angular velocity ω are the two measurements taken by the sensor package. When the Calibrate command is given to the microprocessor the sensors take 200 values when the payload is not moving to use as a calibration point to reduce bias errors. The next command that is given to the microprocessor is the arm command. This command allows the microprocessor to continue adding measurements to the buffer

until a micro-thruster is fired. At this point 1000 data points are saved to the memory and saved using computer software. The final outputs are time, lateral acceleration, and angular velocity.

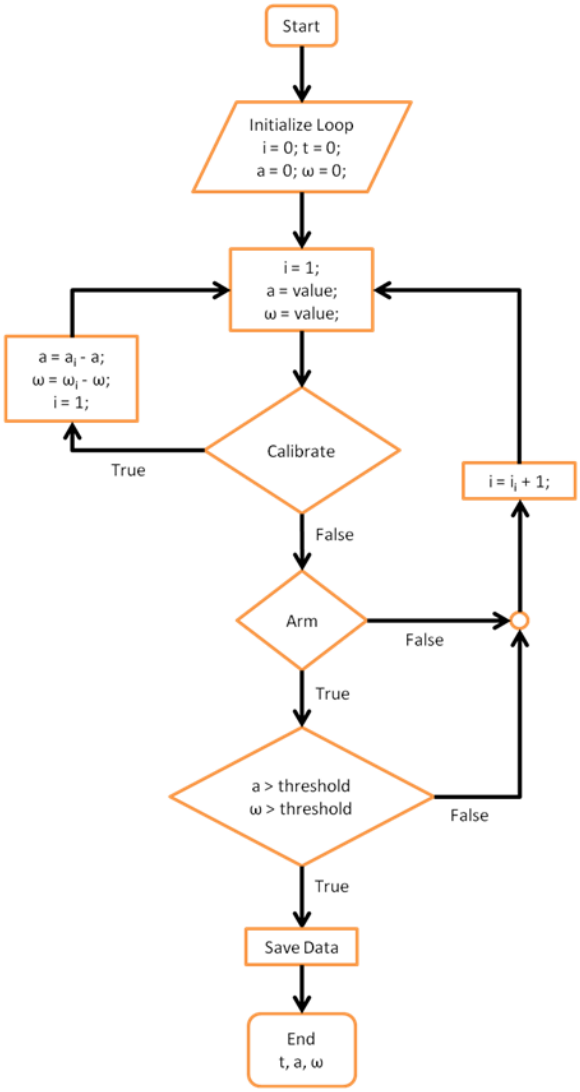

Figure 3.16: Sensor Microprocessor Code

Figure 3.17 shows the final controllability payload. The accelerometers and thrusters were mounted to the top RP plate via fabricated mounts from 1/4″ thick

clear scratch resistant acrylic material. The thrusters are inserted into through holes in the acrylic. These mounts were designed such that the radius can be varied to yield the most appropriate function of the system. The gyroscope was mounted to an acrylic plate located above the $1000\mu F$ capacitors. This acrylic support plate also allowed for mounting of the final firing components, the DF PCB, an AAA battery pack used to power the transformer, a lithium ion battery used to power the sensor package (measurement devices and wireless transmitter). The completed controllability payload was then placed in the test stand for experimentation. Figure 3.18 shows the propulsion payload in levitation.

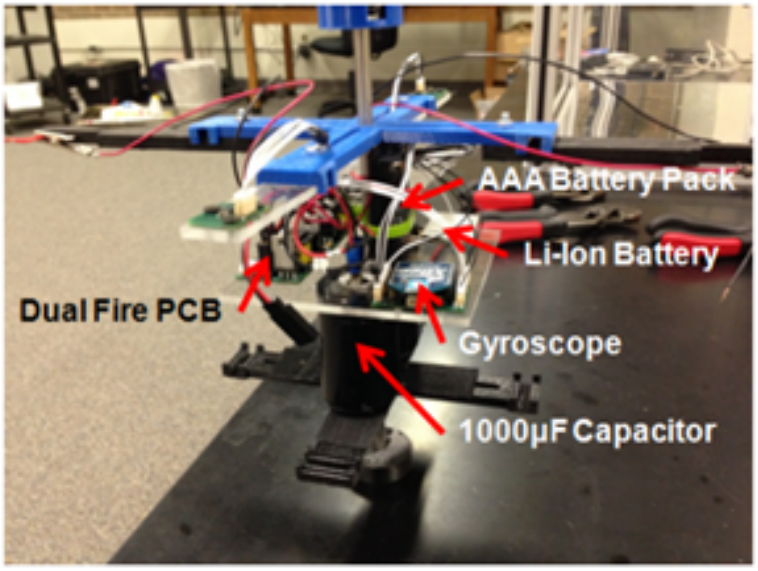

Figure 3.17: Modified Controllability Payload

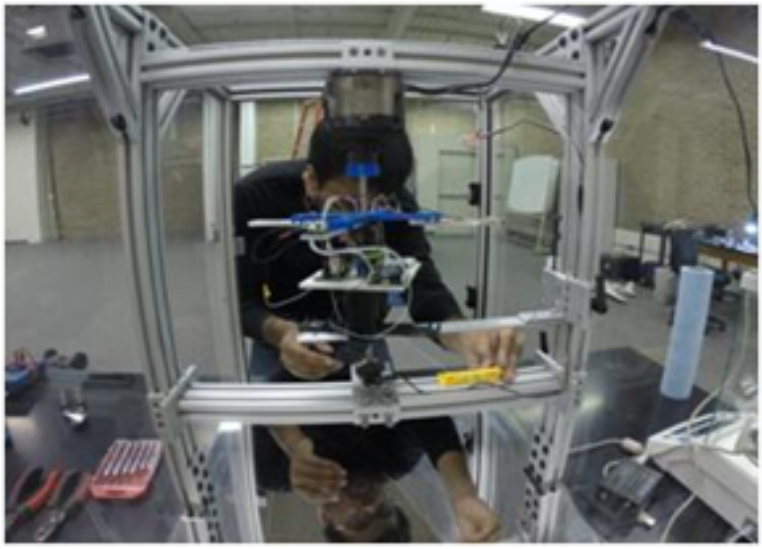

Figure 3.18: Setting Up Payload

3.8 Impulse

Propulsion is achieved by applying a force to a body or vehicle and accelerating the vehicle. This is done in propulsion by ejecting propellant at high velocities. The total impulse is amount of thrust integrated over the burn time seen in the following expression [25],

$$I_t = \int_0^t \mathrm{F}\,\mathrm{d}t \tag{3.12}$$

The total impulse is proportional to the total energy released by the propulsion system. The specific impulse is the total impulse per unit of weight of propellant consumed. This performance measurement in rocket propulsion is analogous to the concept of miles per gallon rating given to automobile combustion. Better propel-

lant performance is correlated to higher specific impulse. The expression for specific impulse can be seen below [25],

$$Isp = \frac{\int_0^t \mathrm{F}\,\mathrm{d}t}{g_0 \int \dot{m} dt}. \tag{3.13}$$

This equation gives an averaged specific impulse value.

The above fundamentals are used for propulsion systems in general. For the particular thrust and impulse bit measurement using the apparatus in this thesis, equations of angular momentum were used instead. The reason for this change was due to the low data rate of the accelerometers. It was observed that using gyroscopic data was more appropriate. The angular momentum vector can be related to torque. As seen in section 3.2, $\vec{\tau} = \vec{r} \times \vec{F}$ or $I\omega$. The following expression shows the relationship between torque and angular momentum [32],

$$\vec{\tau}_{net} = \frac{d\vec{l}}{dt}. \tag{3.14}$$

This equation shows that the net torque ($\vec{\tau}$) is equal to the change in angular momentum. The change in angular momentum can be expanded in the following form [32],

$$\frac{d\vec{l}}{dt} = \vec{r} \times \vec{F}_{net}. \tag{3.15}$$

Newton's second law of motion ($\vec{F}_{net} = m\vec{a}$) can be used to replace $\vec{F}_{net}$ [32],

$$\frac{d\vec{l}}{dt} = m(\vec{r}\times\vec{a}) = \vec{r}\times m\vec{a}. \tag{3.16}$$

Knowing that $\vec{a} = d\vec{v}/dt$ and integrating with respect to time the following definition for the angular momentum of a particle can be formed [32],

$$\vec{l} = m(\vec{r}\times\vec{v}). \tag{3.17}$$

After this the total angular momentum $\vec{L}$ for a system of particles can be formed by finding the vector sum of the angular momenta of the particles [32],

$$\vec{L} = \vec{l_1} + \vec{l_2} + \vec{l_3} + \cdots + \vec{l_n} = \sum_{i=1}^{n} \vec{l_i}. \tag{3.18}$$

The final two representative total angular momentum equations used in this data processing,

$$L = I\omega \tag{3.19}$$

$$L = r m_{bit} v. \tag{3.20}$$

where m_{bit} is the mass loss per firing. Combining these two equations and knowing the electric propulsion impulse $(J_{ep}) = m_{bit}v$ the equation for impulse bit for the experiment becomes,

$$J_{ep} = \frac{I\omega}{r} \tag{3.21}$$

or

$$J_{ep} = \frac{I\omega}{2r}, \tag{3.22}$$

for two thrusters. I is the mass moment of inertia of the test payload. *omega* is the change in angular velocity and r is the radius between the centerline axis and the thruster. The specific impulse equation then becomes,

$$Isp = \frac{I\omega}{2rm_{bit}g_0}. \tag{3.23}$$

These final two equations were used to post process the data in Chapter 4 of this thesis.

3.9 Data Post-Processing

Once acquired from individual firings, the data from the payload sensor package was saved into text files. The data was recorded at 1000 Hz. A MATLAB script file was created in order to read and calculate the thrust from the accelerometer data and angular velocity from gyroscope data. Figure 3.19 shows the lateral acceleration reading from both of the MEMS accelerometers used. The units of measurement are milli-gs or meters per second squared divided by gravitational constant. The accelerometer data is combined from sensor one and sensor two to find an average ac-

celeration from the rotating payload. This was done in order to collect more samples and reduce noise from payload sway. An example of this can be seen in Figure 3.19. The lateral acceleration, acquired by the accelerometers, is divided by the radius of the sensor location relative to the central axis to find the angular acceleration (Figure 3.21).

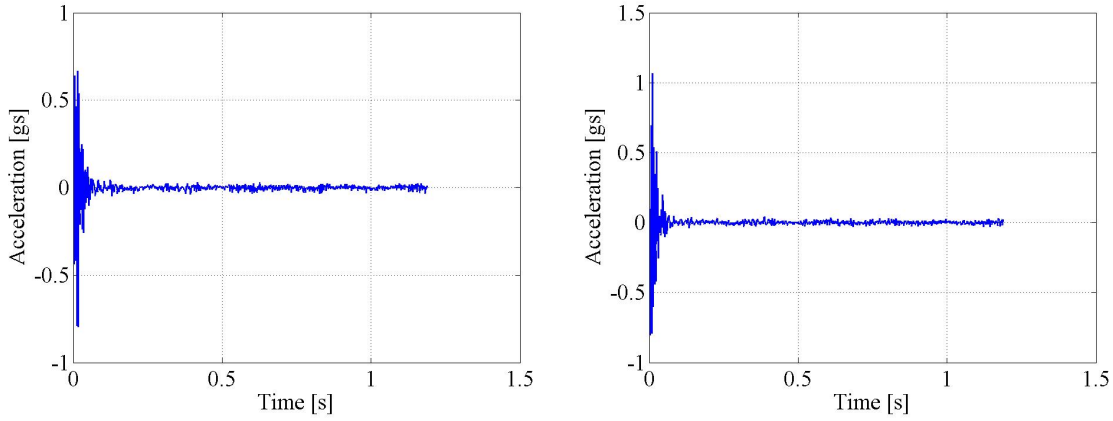

Figure 3.19: (a)Data from Accelerometer 1, (b)Data from Accelerometer 2

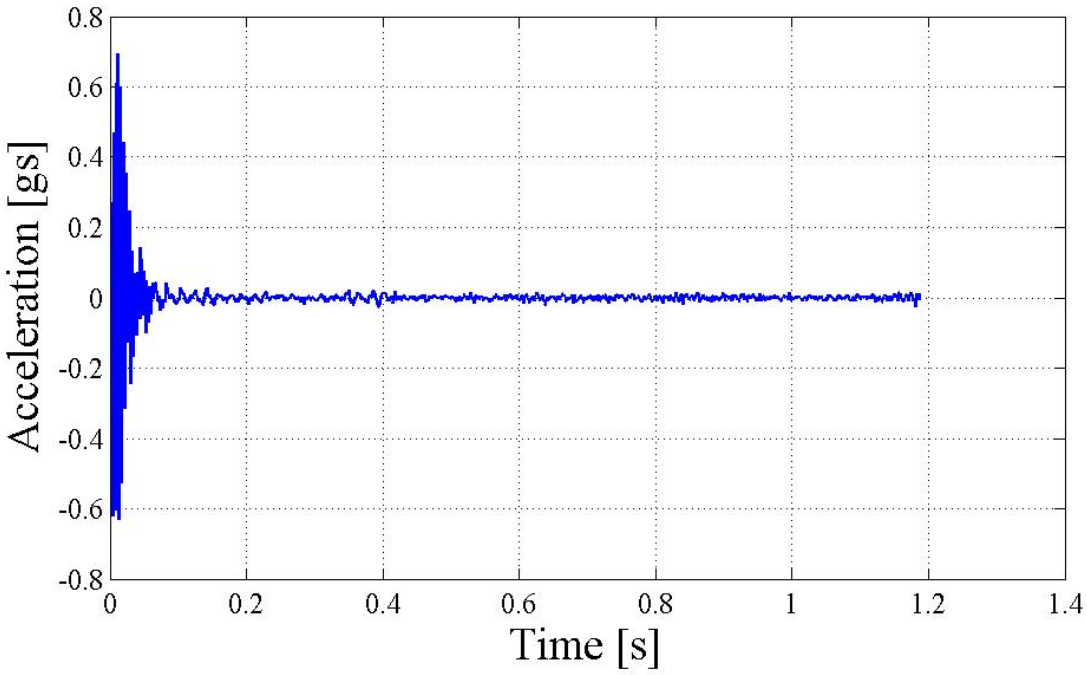

Figure 3.20: Accelerometer Data Combined

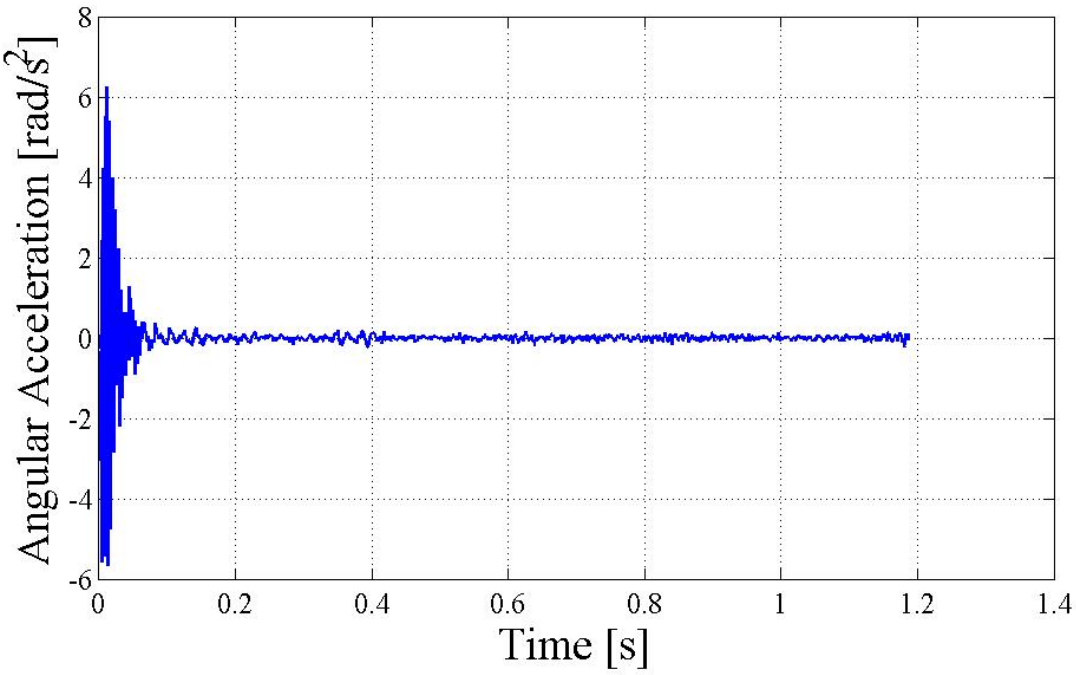

Figure 3.21: Angular Acceleration

The gyroscope data was used to calculate the impulse bit and specific impulse per pulse. The MEMs gyroscope recorded the angular velocity in degrees per second. This was first converted to radians per second to make units agree. The gyroscope data can be seen in Figure 3.22. The gyroscope data was post processed to eliminate the first few extreme spikes and the average angular velocity between 0.2 and 0.4 s was used for calculation.

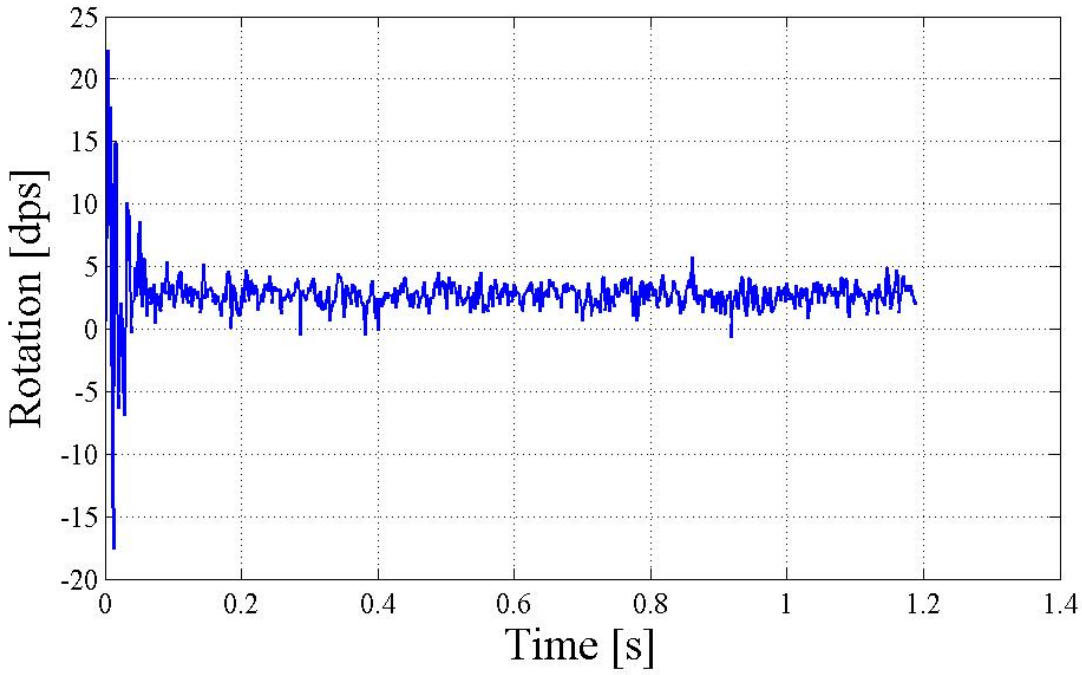

Figure 3.22: Gyroscope Data

3.10 Inertia Calibration Experiment

In order to back out the impulse produced by a thruster firing, the inertia of the thruster platform must be known. Because the geometry is complex and the thruster platform has several sensors, controllers, wires, and other electronic components the moment of inertia of the system is not easily determined through analytic calculations. The methodology uses the Poincaré - Lindstedt methodology. The thruster platform was suspended from the ceiling of the test bay using two equal lengths of string. Motion tracking sensors were placed on key points of the platform such that cameras in the test bay could record the motion of the platform. The platform was given an

initial rotational angle and released. As the payload oscillated, the motion of the payload was recorded. Assuming that the system is weakly damped and unforced, with a small initial angle offset, the mass moment of inertia could be calculated.

Figure 3.23 shows a picture of the payload being set up in the lab, and a plot of the results of the test. The plot shows both the measured oscillatory motion of the platform, and a theoretical model using the moment of inertia determined from the experiment. The data show that for a short window of time, the assumptions of no damping and unforced oscillation is valid and give confidence in the methodology used to determine the moment of inertia.

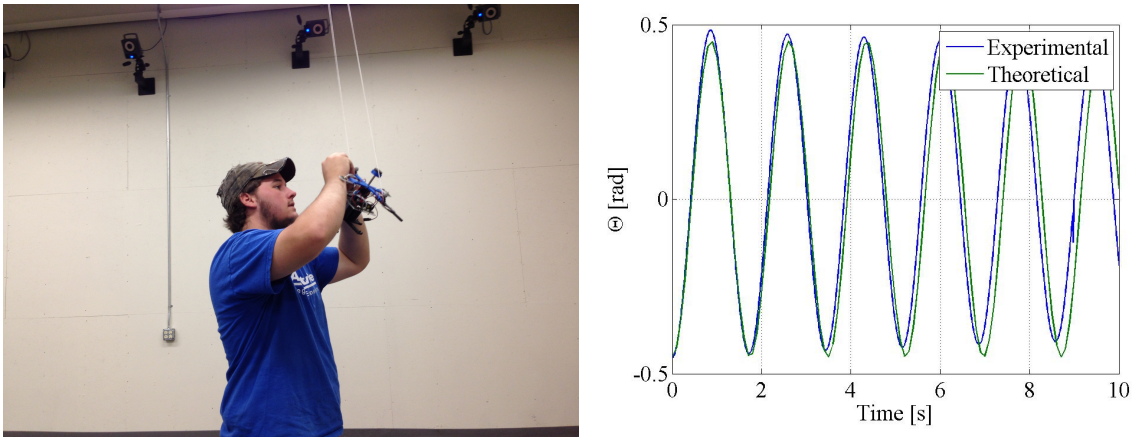

Figure 3.23: (a) Thruster Platform Inertia Experiment, (b) Plot of Predicted vs. Experimental Data for the Platform Motion after an Initial Input

The mass moment of inertia of the payload is needed in order to calculate thrust, impulse, and specific impulse of the micro-thrusters according to the equations in the earlier sections of this thesis. The equation to calculate the rotational Inertia for a mass rotating about a fixed axis, $I = mr^2$[33]. For the experimental payload

this would entail finding the center of mass and radius of each individual component. To model this or hand calculate is very time consuming and the objective of this research was to use a mathematical method to solving for the mass moment of inertia of complex payloads in order to simplify the process. Therefore, using the Poincaré-Lindstedt method to solve for the mass moment of inertia is advantageous in reducing effort. The approach and methodology is explained in more detail in Appendix B.

3.11 Uncertainty Analysis Methodology

Uncertainty analysis was conducted on the post processed experimental data to determine the level of error in the results. The total error (δ_{total}) in the experiment is the sum of the systematic or bias error and the random (or precision) error. The systematic error (β_{System}) is a constant error component while the random error (ϵ) is caused by repeatability error and precision error. The expression for total measurement error is [51],

$$\delta_{total} = \beta_{System} + \epsilon, \tag{3.24}$$

The finite number of measurements taken during an experiment represents a sample frame distribution. μ is the mean of the sample frame distribution and σ is the standard deviation of the sample frame data. Both μ and σ can be defined using the following expressions [51],

$$\mu = \lim_{N \to \infty} \frac{1}{N} \sum_{i=1}^{N} X_i, \tag{3.25}$$

$$\sigma = \lim_{N\to\infty}\left[\frac{1}{N}\sum_{i=1}^{N}(X_i-\mu)^2\right]^{1/2}. \tag{3.26}$$

The mean of the sample frame population is defined by [51],

$$\bar{X} = \frac{1}{N}\sum_{i=1}^{N} X_i, \tag{3.27}$$

where N is the number of individual readings X_i. By replacing the 1/N with 1/(N-1) in the above expression for σ the standard deviation can be solved for a sample frame population,

$$S_x = \left[\frac{1}{N-1}\sum_{i=1}^{N}(X_i-\bar{X})^2\right]^{1/2}. \tag{3.28}$$

The mean and standard deviation of the parent population must be normalized in order to properly relate it with the sample frame mean $\bar{X}$. The expressions for sample frame mean , $\sigma_{\bar{X}}$, and sample frame standard deviation, S_x, can be seen below,

$$\sigma_{\bar{X}} = \frac{\sigma}{\sqrt{N}}, \tag{3.29}$$

$$S_{\bar{X}} = \frac{S_{\bar{X}}}{\sqrt{N}}. \tag{3.30}$$

These equations are more appropriate for the level of statistical data analyzed in this thesis. One method in decreasing the random component of uncertainty is to

take as many reading as possible. Using this information the confidence intervals for sample frame populations can be established.

As stated by Coleman and Steele [51], the overall uncertainty of a measured value is the interval around the mean value in which the true value is believed to lie. To obtain the overall uncertainty, the random and systematic uncertainties must be appropriately combined. In 1993, the ISO guide [52] was developed in order to standardize methods for combining uncertainty estimates. It states that the variances or the squares of the standard deviations should be added for the estimates. Following the method described in the ISO guide, the combined standard uncertainty u_c for a variable i is,

$$u_c^2 = S_{b_i}^2 + S_i^2, \tag{3.31}$$

where S_i is the standard deviation estimate for the random uncertainty is S_i and S_{b_i} is the standard deviation estimate for the systematic uncertainty. The propagation of the systematic and the random uncertainties should be considered separately. This is also called a detailed uncertainty analysis. In general, the uncertainty of the DRE used for determining the confidence intervals can be written as,

$$U_r^2 = \sum_{i=1}^{J} \Theta_i^2 U_{X_i}^2, \tag{3.32}$$

where U_r is the overall uncertainty of the result, Θ_i is the sensitivity coefficient and can be expressed as: $\Theta_i = \partial r / \partial X_i$, and U_{X_i} are the uncertainties associated with X_i [51].

The factors that multiply the relative uncertainties of the variables are called uncertainty magnification factors or UMFs. They are defined as,

$$UMF_i = \frac{X_i}{r}\frac{\partial r}{\partial X_i}. \tag{3.33}$$

The UMF for a given X_i indicates the relative influence of the uncertainty in the variable on the uncertainty in the result. A UMF value greater than 1 indicates that the uncertainty in that variable is magnified as it goes through the DRE. A value less than 1 represents the opposite trend. The other uncertainty factor that is prominent is the uncertainty percentage contribution (UPC). It can be expressed as,

$$UPC_i = \frac{(\partial r/\partial X_i)^2 (U_{X_i})^2}{U_r^2} \times 100. \tag{3.34}$$

The UPC represents the percentage contribution of a specific variable in the final DRE. Since the UPC contains the effects of the UMF and the magnitude of uncertainty of the variable it is useful in predicting outcomes in the planning process [51].

3.12 Sensor Calibration Method

To find the uncertainty in the gyroscopic sensor a series of verification tests were performed. To calibrate the gyroscopic sensor a calibration method that involves striking the thruster holder with a known impulse needed to be selected to carry out the verification tests. During this evaluation, the impact hammer method was selected for calibration purposes. More test stand calibration methods were evaluated

and documented in Appendix C of this thesis. Figure 3.24 shows the elastic collision method for contact test stand calibration. The impact hammer scheme consists of hanging a rectangular mass, using four strings, from an integrated support on the test stand. In order to initiate the contact the mass would be pulled back and released to strike the thruster holder on the levitating payload. The impact hammer has several advantages. Most important is the stability and consistency of the impact. The four strings would mitigate the off axial movements during operation. A high speed camera will be used to image the motion of both the swinging mass and the payload. From the images the angular velocity of the payload can be determined and compared against the gyroscope data.

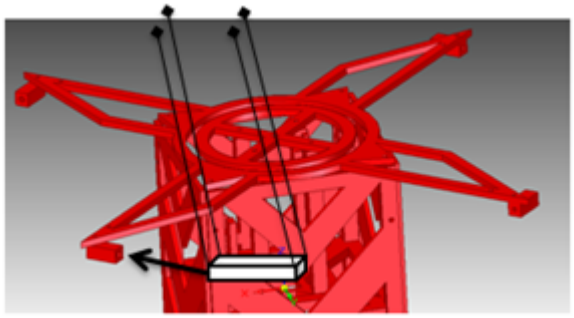

Figure 3.24: Impact Hammer

Figure 3.25 shows the laboratory setup for the impact hammer experiment. 8020 T-slotted aluminum material was used to integrate the pendulum structure to the existing test stand structure. A hard rubber mass was suspended by four strings and then adjusted to the appropriate height needed to strike the thruster holder. Reflectors were placed on the payload and a high speed camera was used to track the

reflectors at 200 frames per second. The frame by frame calculation and gyroscopic data would be compared to find the percent difference in measurement. Figure 3.26 shows the final setup with the high speed camera.

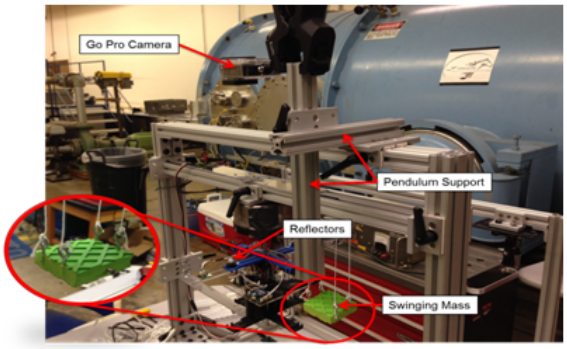

Figure 3.25: Laboratory Setup

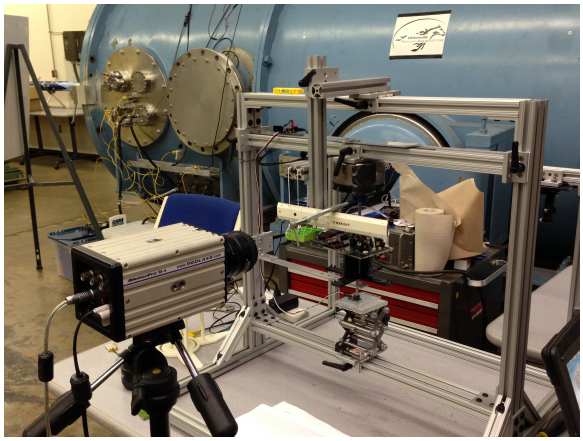

Figure 3.26: High Speed Camera

An existing MATLAB script, developed by Dr. David Lineberry (Principal Engineer at the UAH Propulsion Research Center), was used to post process the angular velocity of the payload from the high speed images. In the MATLAB program,

the image is adjusted from an 8 bit grayscale image to a 2 bit black and white image, based on an intensity threshold determined using an edge detection routine. From the adjusted images, a built-in MATLAB routine was used to locate the reflector and the center of the reflector. The center position of the reflector is tracked through the images. A linear regression is used to determine the derivative of the position, in pixels, versus time. This value is then converted to lateral velocity by multiplying it by the image scale. Diving the lateral velocity by the radius from rotation axis to the reflector will give angular velocity. This angular velocity is then directly compared to the data from the gyroscope.

CHAPTER 4

RESULTS AND DISCUSSION

The following chapter summarizes the data collected from the inertia calibration and thruster experimentation. Data from atmospheric tests and were organized for two different thruster batches. The first section will discuss results obtained from inertia calibration experiments. This provided the mass moment of inertia parameter used in calculating performance characteristics. The second section shows the results from baseline testing of the inertia calibration experiments to compare theoretical and experimental values of mass moment of inertia to compute the systematic uncertainty in the process. The third section discusses the data collected from a series of atmospheric micro-thruster experiments. The fourth section provides information for verification methods used to calibrate the gyroscopic sensor and uncertainty analysis.

4.1 Inertia Calibration Results

An inertia calibration experiment was conducted in order to calculate the mass moment of inertia for the payload seen in Figure 4.1. This was used as the levitating test platform for the atmospheric test data in the section below.

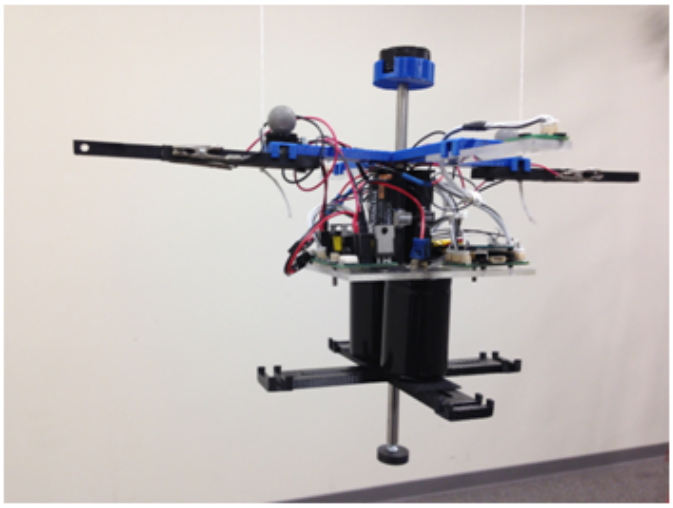

Figure 4.1: Payload Inertia Calibration Experiment

The data that is collected by the Vicon camera system is the x, y and z components of the individual reflectors. The individual reflectors are modeled on the Vicon camera software and post processed into a spreadsheet for analysis. On the example payload, three reflectors were placed 3" from the centerline axis and then the position with respect to time was captured throughout the duration of the experiment. To recall, manual input was given to offset the payload angle from the equilibrium position. The Figure 4.2 shows the x and y position of the reflectors relative to the global origin of the system.

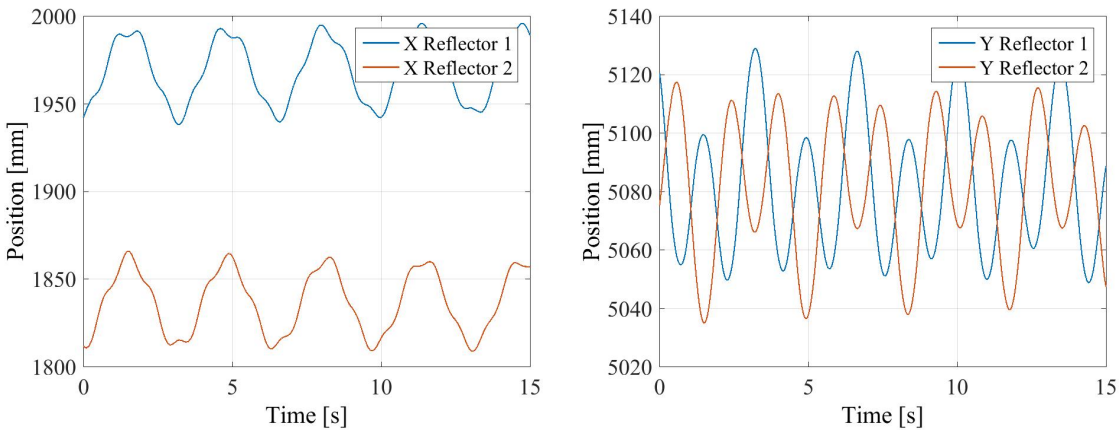

Figure 4.2: (a) X Position, (b) Y Position

The positions of the reflectors are relative to the global fixed frame that is configured for the enclosed volume during the camera calibration process. The position is captured in millimeters over a time span of 10 to 15 seconds. Some noise can be seen in the data as a result of tracking resolution error caused by the infrared reflection and some swinging motion in the x and y direction that is encountered during the experiment.

The position data were inserted into a MATLAB script and the atan2 function was used to calculate the angle with respect to time from the x and y position data. This function is used to compute the angle between the positive real axis and line from the origin [26]. Figure 4.3 shows the Θ vs. time plot.

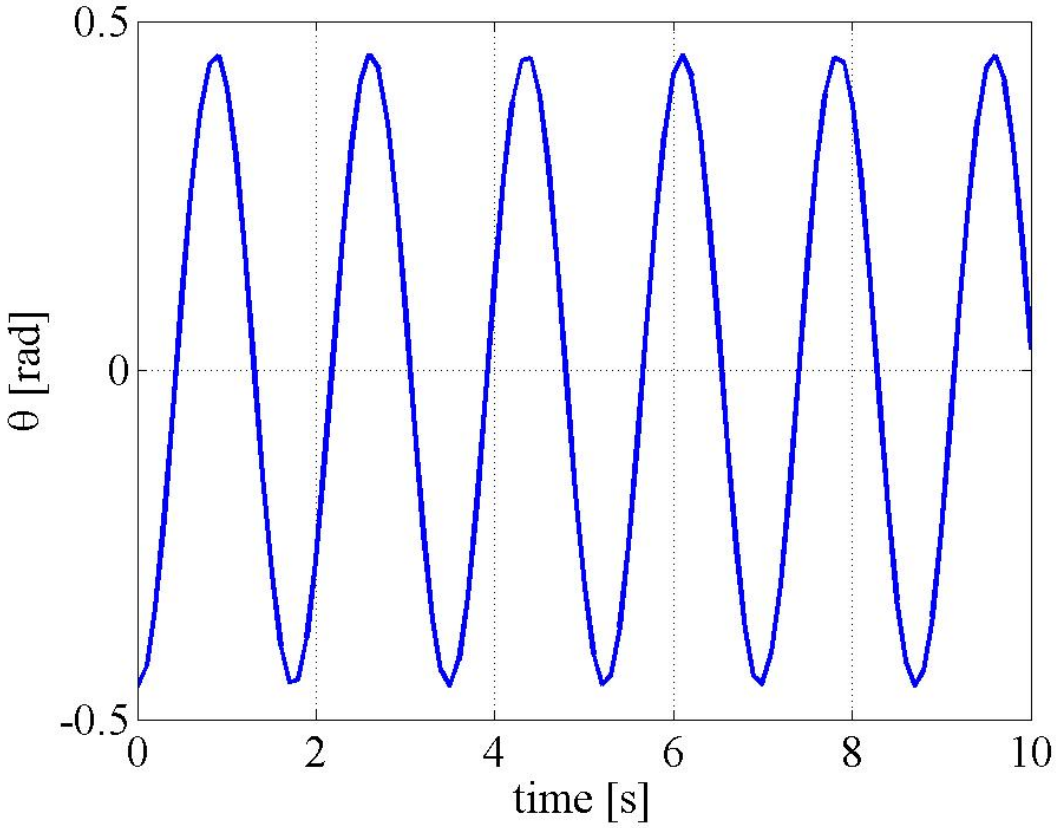

Figure 4.3: Θ Vs. Time

The main piece of information that was needed from the experimental data is the frequency of oscillations. This can be calculated using the period T_p by solving the following for frequency,

$$\omega_f = \frac{2\pi}{T_p}. \tag{4.1}$$

As a verification check against this, we can estimate the theoretical frequency using the Poincaré-Lindstedt method given this data. A comparison of the experi-

mental and theoretical angular positions are given in Figure 4.4. Good agreement is achieved during execution of 3 periods. The discrepancy increases with time due to the effects of dampening that begins to significantly reduce the amplitude of the angular position.

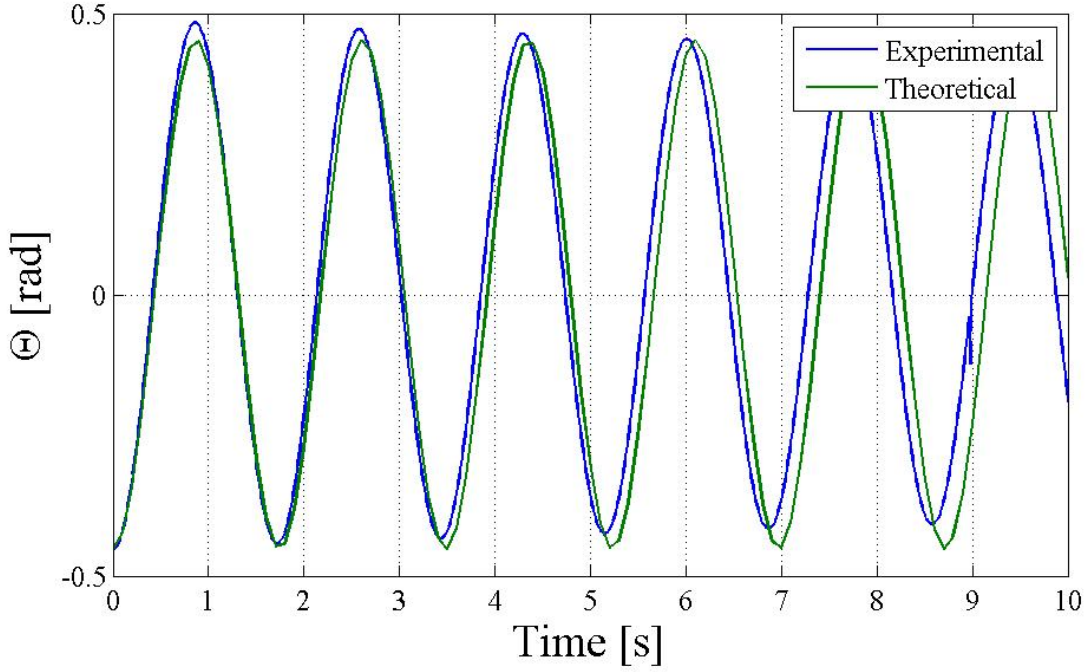

Figure 4.4: Comparison Θ Vs. Time

The final equation for determining the mass moment of inertia for a complex payload is as follows,

$$I = \left[\frac{\left(1 - \frac{b^2}{16}\right) \cdot \sqrt{\frac{m \cdot R^2}{L_{sus}}}}{\omega_f} \right]^2, \tag{4.2}$$

where b is the initial offset angle of rotation, m is the payload mass, R is the radius of the connection points, L_{sus} is the length of the suspension strings, and ω_f is the

oscillating frequency of the payload from the inertia calibration experiment. This equation was formed by solving for the second order linear differential equations for the duffing equation.

Table 4.1: Payload Inertia Values

Parameter	Measurement	Uncertainty
Initial Offset Angle	.524 rad	0.00005 rad
Payload Weight	5.296 N	0.00981 N
Connection Radius	3.25 in	1/16 in
Length of String	107 in	1/16 in
Oscillation Frequency	3.6062 Hz	0.01 Hz
Final Inertia Value	3.37 $lb{\cdot}in^2$	-

Using given information in Table 4.1, the mass moment of inertia for the experimental payload was approximately 3.37 $lb{\cdot}in^2$.

The region of interest is the first 5 seconds of data. At the beginning of the process it was assumed that the experiment was representative of a weakly nonlinear system that was undamped and unforced. However, the long, thin strings absorb energy over time. This in turn will apply some dampening to the system. That is seen in the comparison as the amplitude decreases and the frequency of oscillation slowly increases in the experimental plot.

4.2 Inertia Calibration Uncertainty

As part of the planning phase of the uncertainty analysis for the inertia calibration experimentation the data reduction equation and the UMF and UPC were computed. Table 4.1 shows the inertia calibration parameter measurements used to find the UMF and UPC of the payload.

Using the above parameters and the uncertainty analysis methodology from Chapter 3 it was calculated that the uncertainty of the inertia calibration experiment is 3.89%. The UMF and UPC for the experiment can be seen in Figure 4.5 and Figure 4.6, respectively. The UMF shows that the connection radius and oscillating frequency magnify the data reduction equation uncertainty the most. While the UPC shows that the connection radius yields the highest percentage contribution the final uncertainty.

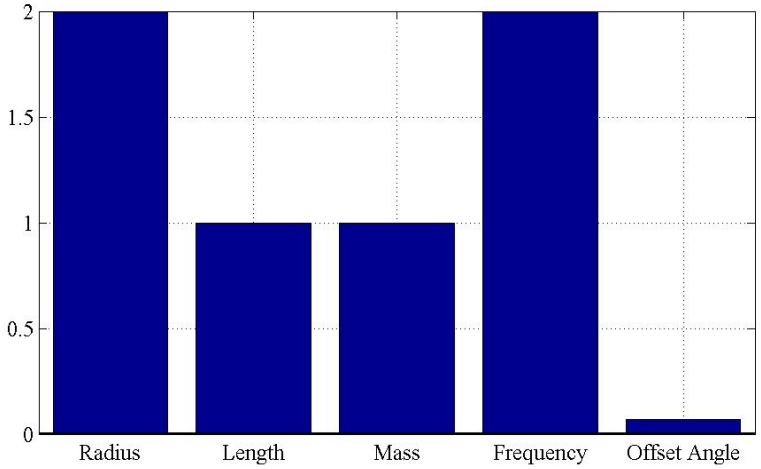

Figure 4.5: Payload Inertia Calibration UMF

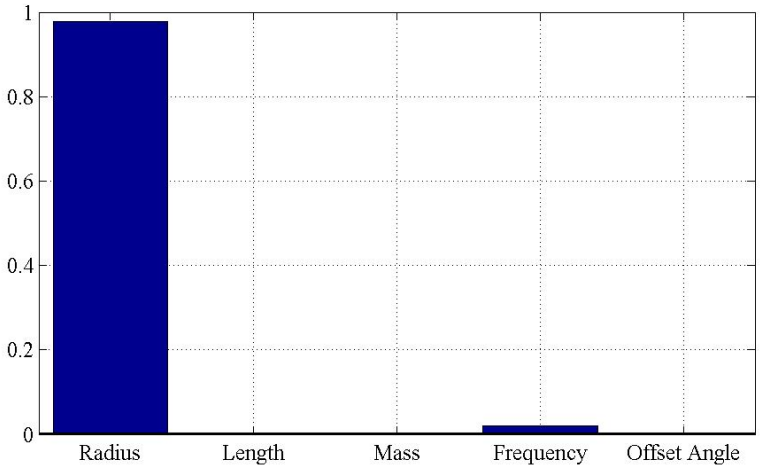

Figure 4.6: Payload Inertia Calibration UPC

4.3 Baseline Inertia Calibration Experiments

In order to validate this method for the purpose of determining the mass moment of inertia of objects a series of baseline experiments were conducted with simple payloads. The motivation for performing these experiments was to quantify possible systematic and bias errors with the Vicon camera system. The theoretical mass moment of inertia was calculated with a level of uncertainty and then compared to the experimental value. Appendix B contains some of the validation test information for the Poincaré-Lindstedt Method.

4.4 Atmospheric Test Data

A summary of the atmospheric micro-thruster tests are given in Table 4.2. These experiments were conducted from May 2014 through July 2014. Three DSSP

batch thrusters were fired each with different propellant formulation and electrode materials and configuration, batches H638, H806 and H898. However, firing data was only collected for two H638 thrusters for analysis. Anomalies were noted in the notes/results section of the table. Data is presented in section 4.4.2 of this document.

Table 4.2: Micro-thruster Test Summary

Batch	Date	Thruster Serial Number	# Firings	Notes/Results
H638	5/30/14 - 7/22/14	D77AY	87	Outer and Inner Electrode Degradation. Micro-thruster inactive after 87 firings
H638	7/22/14 - 7/25/14	D77AK	79	Inner Electrode Degradation. Functioned as intended

Dual thruster firing using new electronics on the atmospheric test stand were completed. Data was not recorded from these experiments. Anomalies consistent with those demonstrated were case and/or electrode degradation and propellant absence. Propellant was completely used within approximately 10 firings in most cases while UAH 22, from batch H806 lasted only 2 firings. Figure 4.7 is a sequence of frames at 60 frames per second intervals. The first frame shows an image before ignition. A smoke trail was observed coming from the thruster nozzle shortly before thruster firing. The second frame shows the initial ignition and the third frame is after firing.

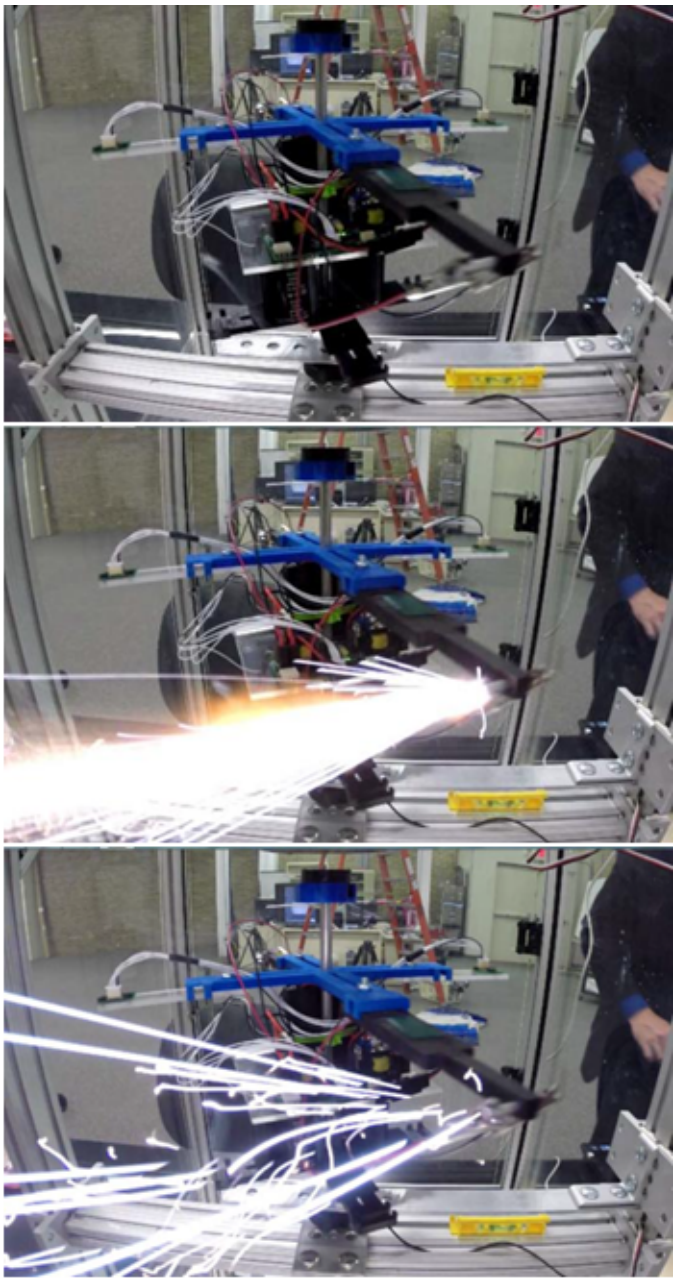

Figure 4.7: Three Sequential Frames from Micro-Thruster Firing

In many images a smoke trail was observed before actual firing. In addition, an unidentified odor was released after firing. On the last firing of UAH 22 it was observed that the entire propellant slug was ejected from case as shown in Figure 4.8.

Figure 4.8: Entire UAH 22 Propellant Slug Seen on the Bottom of the Test Platform

4.4.1 Process Flow

To recall, the first step in calculating the impulse bit and specific impulse of the micro-thruster firing is to collect, organize and store the data from the DAQ. This information is collected in text files for the individual firings and imported into a MATLAB script to post process. Accelerometer data was used in determining thrust per firing. Section 3.8 discusses the basic setup and equations for finding thrust. Equation 3.11 is used in finding the thrust for dual thruster firings. However, for single thruster firing the T_2 would become zero. In Equation 3.11 the I_{zz} comes from the inertia calibration experiments of the controllability payload. Distance d is measured and the lateral acceleration measurement from the accelerometers is manipulated using the substitution in equation 3.5 to find angular acceleration. All of

these parameters are imputed into equation 3.11. The maximum thrust measurement per firings is reported in the thrust vs. pulse charts in the following section.

After further consideration of the thrust data it was determined that the impulse bit and specific impulse data would provide more stable results for performance. The data post processing methodology was refined to use gyroscopic data to calculate the impulse bit and specific impulse per pulse. A MEMs gyroscope recorded the angular velocity in degrees per second. This was first converted to radians per second to make units agree. No further corrections are needed for this measurement. The methodology was further refined to eliminate the first few extreme spikes and the average angular velocity between 0.2 and 0.4 seconds was used for calculation. This value was inserted into an excel file used for data compiling. A similar process was used in calculating the specific impulse. The equations used for this post processing were 3.25 and 3.27 for impulse bit and specific impulse, respectively. The processes can also be seen in Figures 4.9 and 4.10. The average mass loss was used during firing intervals for finding the specific impulse.

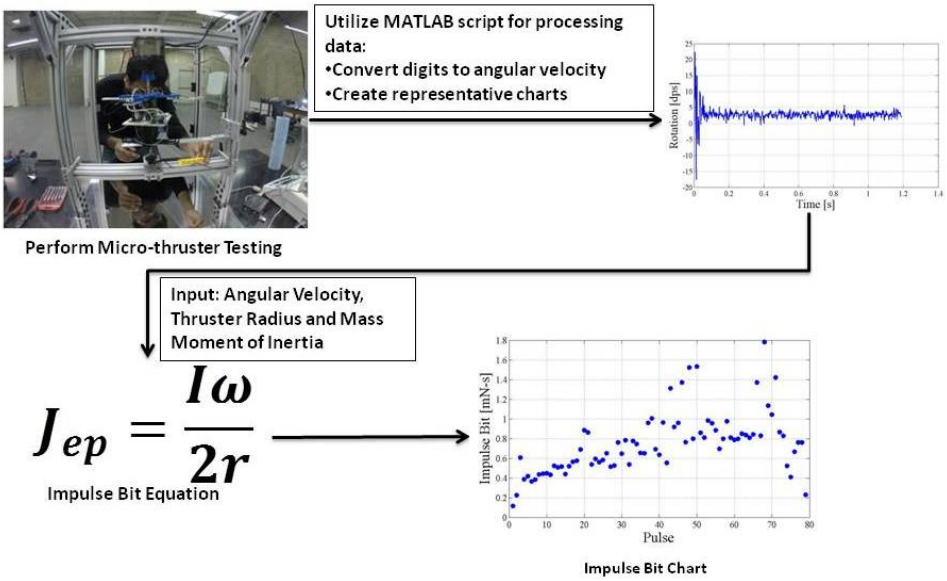

Figure 4.9: Impulse Bit Post Processing Method

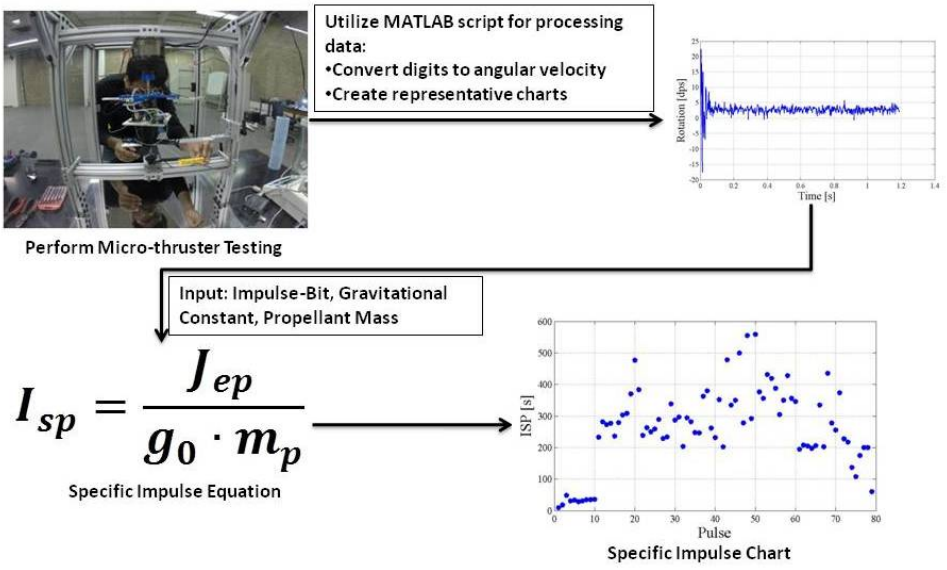

Figure 4.10: Specific Impulse Post Processing Method

4.4.2 Batch H638

The figures below show the data collected and post processed for the batch H638 micro-thrusters. Figure 4.11 shows an example of a H638 micro-thruster before and after firing.

Figure 4.11: Batch H638 Micro-Thruster

Figure 4.12 shows the impulse bit for Micro-Thruster D77AY. This data was post processed using the gyroscopic data. One interesting trend was noticed in this data and the thrust data above. According to vendor specifications the thrust and impulse bit should decrease as the number of pulses are increased. However, the opposite trend is observed in the following data. The initial ten firings showed a fairly constant impulse bit level of approximately 0.5 mN-s. However, thruster firings 11 through 60 showed a wide range of scatter in the calculated impulse bit. Impulse bit values for these firings ranged from 0.5 to 2.75 mN-s. The peak impulse bit was around 2.75 mN-s which occurred at approximately firing 37. The average impulse-bit for the data was around 0.698 mN-s.

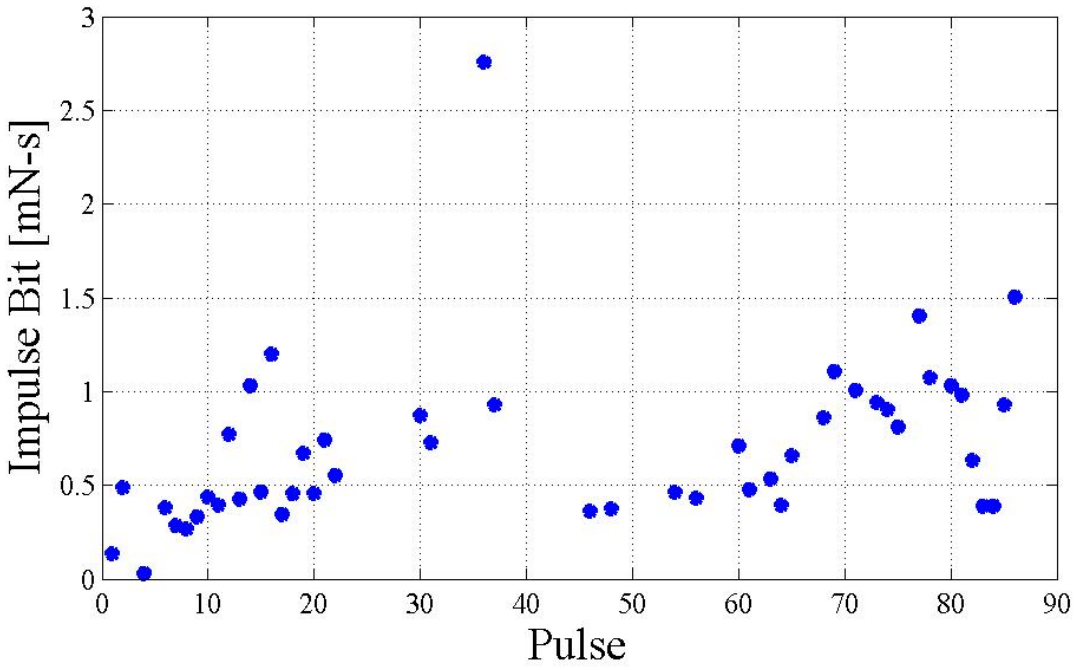

Figure 4.12: Impulse Bit for Micro-Thruster D77AY

The mass loss for micro-thruster D77AY as a function of firings is shown in Figure 4.13. During the experimentation, thruster mass was documented after each start/stop interval. This documentation was attempted every ten firing intervals. However, some mass readings were taken sooner. A large decrease in mass was noted between firings 39 and 45. Neglecting this significant drop, the slope of the mass loss appears fairly constant (i.e. the mass lost per firing appears fairly constant over the rest of the range). One hypothesis for the low initial thrust is the accumulation of fluid from the propellant at the nozzle. A few pulses must be used to clear the surface and increase impulse. Another hypothesis for this occurrence may be uncertainties in the insulation on the inner electrode near the nozzle. A possible reason for the

erratic behavior following the initial ten pulses may be voids in the propellant. When the ablative surface reaches voids in the propellant, the resulting thrust may become erratic and possible misfires may be observed. The gaps in firings in figure above are representative of no data collection. Ignition did occur at every pulse until firing 87. In Figure 4.13 the increasing negative slopes between pulses 34−44 and pulses 60−70 are due to erosion of electrode material.

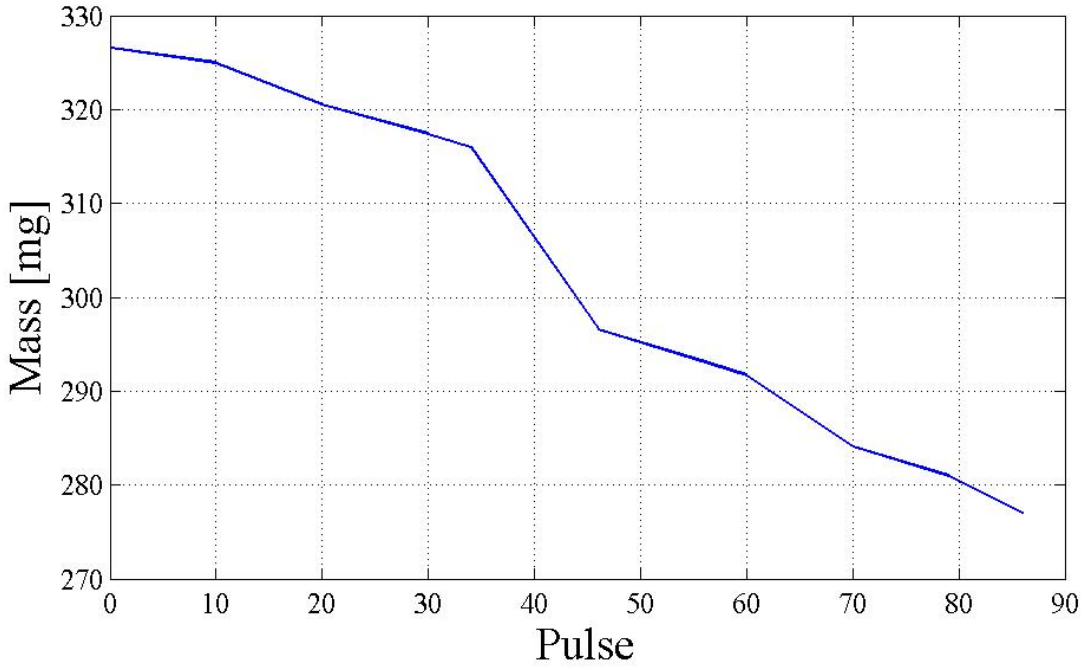

Figure 4.13: D77AY Mass Chart

Table 4.3 shows the average moss loss per firing interval for micro-thruster D77AY.

Table 4.3: D77AY Mass Loss

Firing Interval (pulses)	Average Mass Loss (mg)
1-10	0.16
11-20	0.45
21-30	0.31
31-34	0.35
35-45	1.764
46-55	0.31
56-60	0.36
61-70	0.76
71-79	0.344
80-87	0.56

Using the mass loss data from Figure 4.13 and Table 4.3 the specific impulse could be computed for the micro-thruster using the process in Figure 4.10. Figure 4.14 has the specific impulse per pulse information. The average specific impulse for the data was around 166 s.

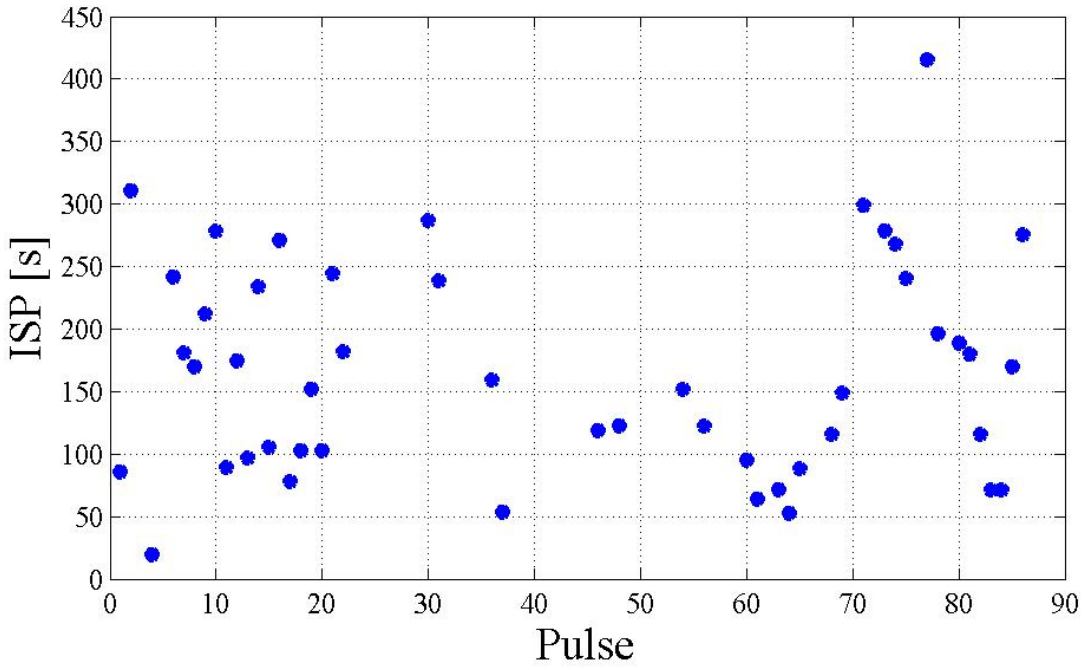

Figure 4.14: Specific Impulse of Micro-Thruster D77AY

Figure 4.15 shows the calculated impulse bit for micro-thruster D77AK from batch H638. For this micro-thruster, the impulse bit data showed an upward trend with the number of firings while showing variability with the increasing number of pulses. While the peak impulse bit was lower than the previous thruster data (D77AY), the peak impulse bit was around 1.8 mN-s. The minimum impulse bit was around 0.1 mN-s. This represented a smaller range of variability than micro-thruster D77AY. Both thrusters were from the same batch and were tested using the same hardware and same analysis techniques.

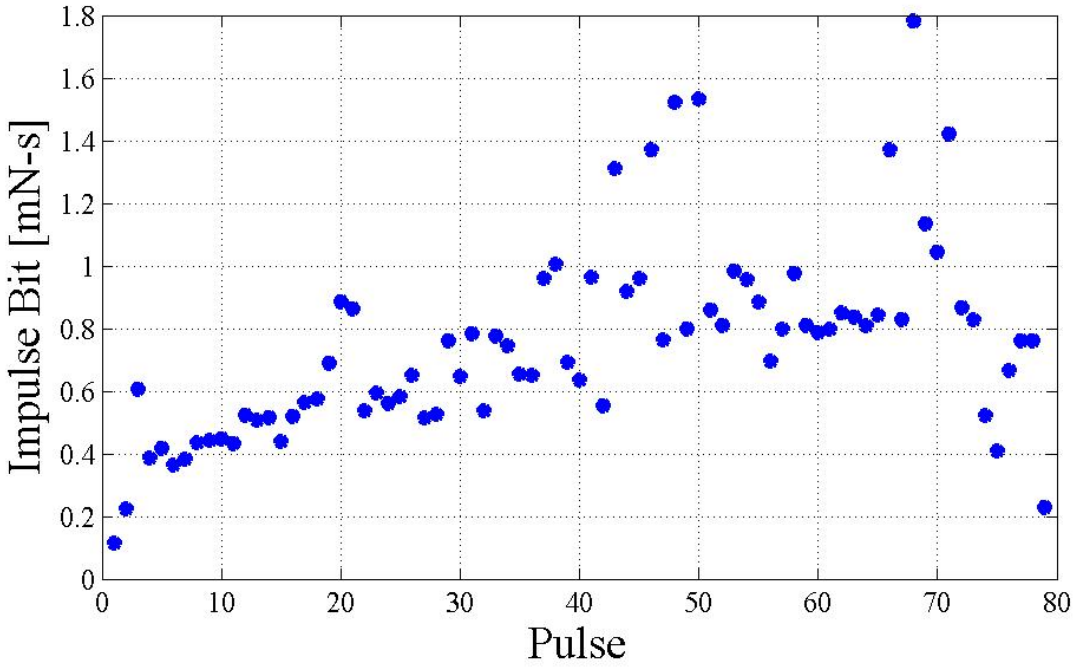

Figure 4.15: Micro-Thruster D77AK Impulse Bit

Table 4.4 shows the mass loss per firing interval of micro-thruster D77AK.

Table 4.4: D77AK Mass Loss

Firing Interval (pulses)	Average Mass Loss (mg)
1-10	1.29
11-20	0.19
21-30	0.23
31-40	0.27
41-50	0.28
51-59	0.233
60-70	0.418
71-79	0.389

Figure 4.16 shows a thruster mass comparison for Micro-thruster D77AK and D77AY. As noted both of these micro-thrusters are from the same propellant batch. The slope of the lines shown in the plot represents the rate of mass loss (mass loss per firing). D77AY had an initially large mass loss between firings 1 and 10, but then showed a fairly constant mass loss per firing. As was noted earlier, D77AY had a large mass loss between firings 39 and 45, but otherwise showed a fairly constant mass loss per firings. The slopes of these lines appears fairly consistent (neglecting the initial slope for D77AK and the large drop for D77AY), indicating a fairly repeatable mass loss per firing, however the differences in mean thrust lead to further questions about the differences between the two thrusters.

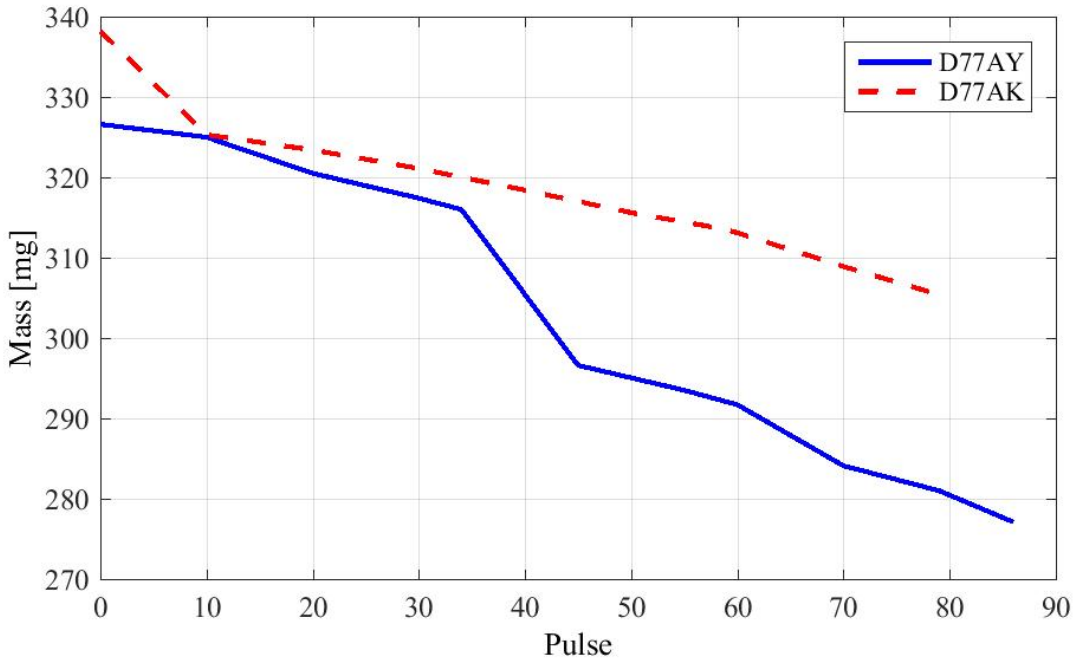

Figure 4.16: Micro-Thruster Mass Loss Comparison H638

Figure 4.17 represents the specific impulse for micro-thruster D77AK. The specific impulse was around 30 s for the initial ten firings. Significant variability was observed in the representative data after pulse number ten. The specific impulse peaked at 550 s around pulse number 50. The average specific impulse was observed to be around 263 s.

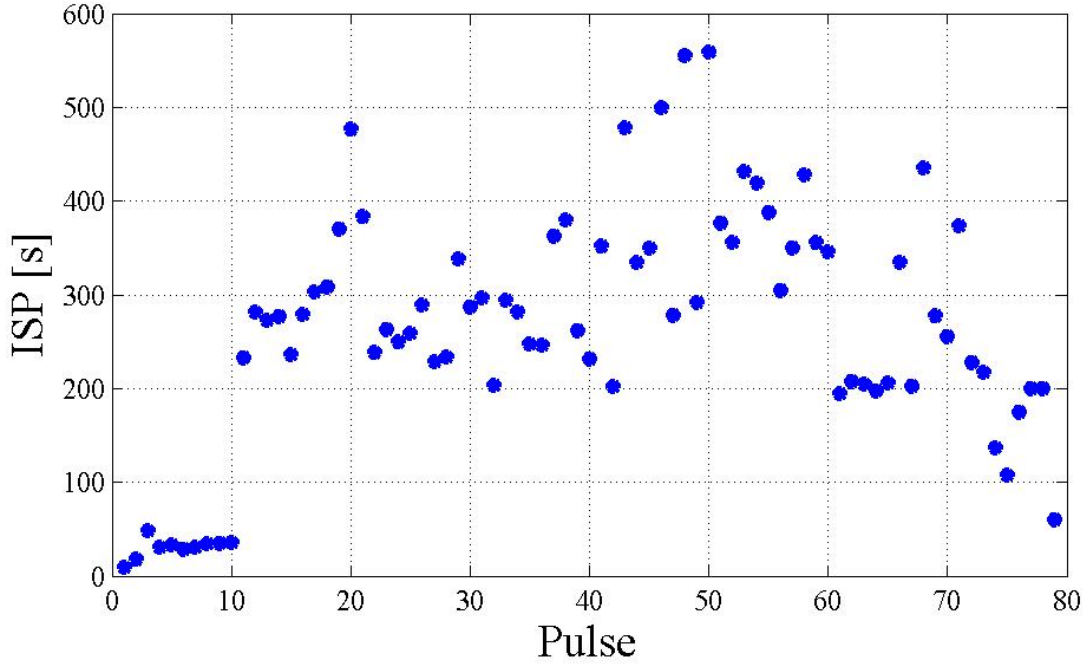

Figure 4.17: D77AK Specific Impulse Data

Figures 4.18 and 4.19 represent a revised method for displaying the impulse bit data for micro-thrusters D77AY and D77AK, respectively. This revised method was used for micro-thruster comparison and provided valuable information for tracking trends in the data. This method involved taking the summation of the impulse bit over a firing interval and calculating the average impulse bit on that interval. The first observation made between the two impulse bit charts is the low initial impulse bit. The hypothesis for this is the possibility of pink liquid left on the nozzle end creating a series of low impulses. Once the micro-thruster had past the first firing interval (up to 10 firings), their was an increase in impulse bit. The next point to make is the increasing trend in impulse bit measurements through all the firings.

This was common between both micro-thrusters. A physical explanation for this is the increasing length for the plasma to accelerate as the propellant ablates. It is hypothesized that the electro-magnetic effects of the plasma are greater than the electro-thermal. Thus, this observation would hold true. However, modeling and simulations of this effect were not completed for this thesis. Another observation between the two charts is the erratic behavior of the micro-thruster from 30 firings to 70 firings. It is believed that a void was reached in the propellant that caused uneven surface ablation. Through personal communications with DSSP [56], it was confirmed that erratic behavior of the micro-thruster could be caused by this anomaly. Through these personal communications, the impulse bit for these thrusters were determined to be within a range of 0.5mN-s and 0.8mN-s [56]. Around 0.75mN-s was expected for this particular batch.

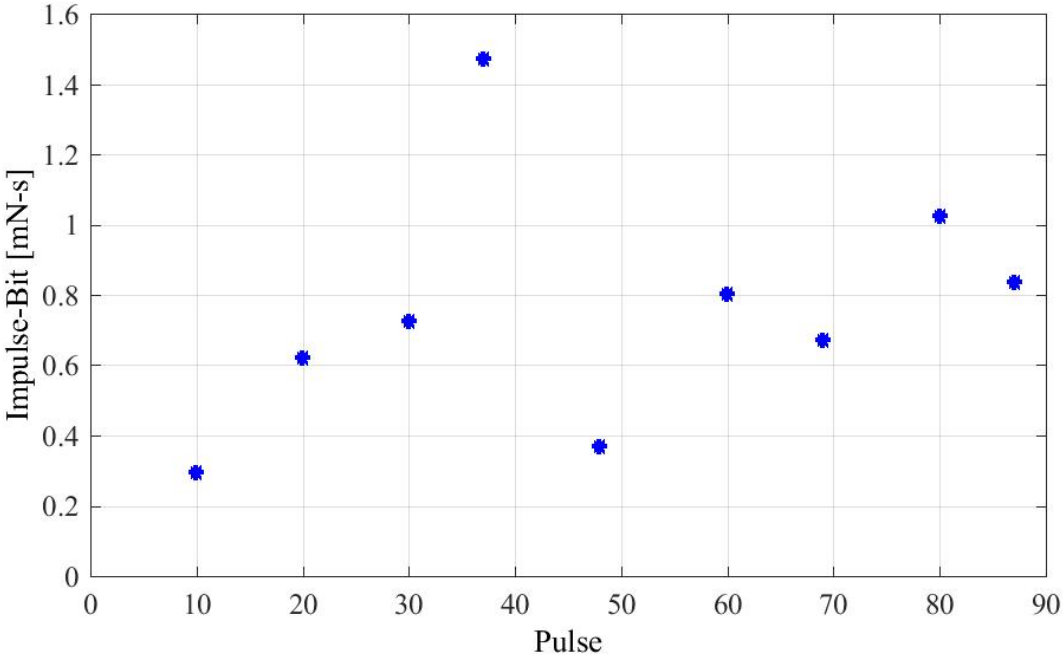

Figure 4.18: D77AY Impulse Bit Data Refined

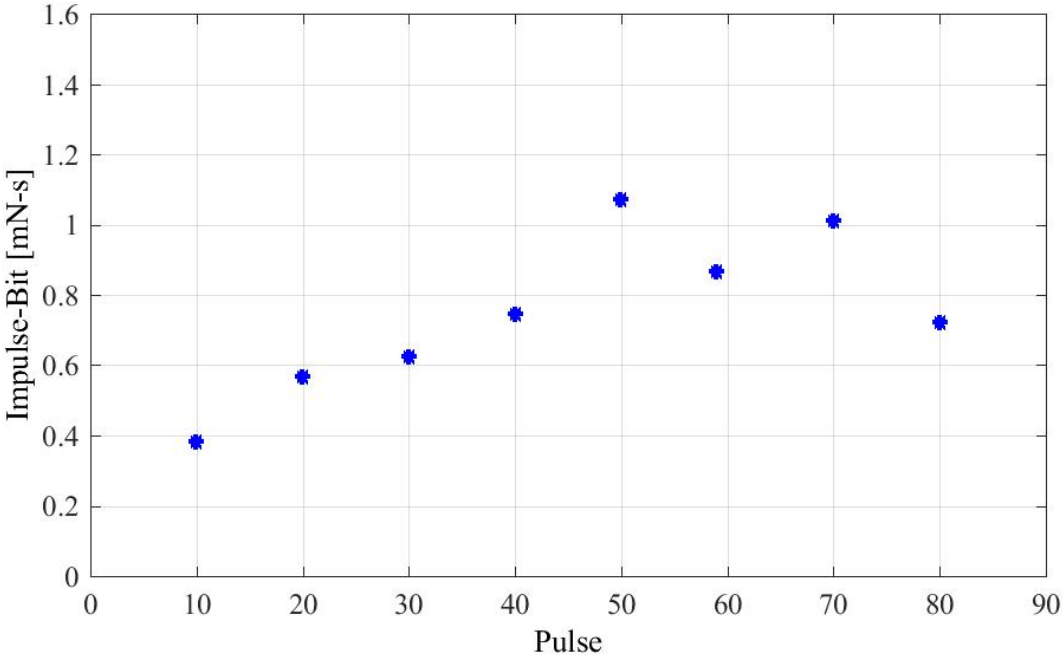

Figure 4.19: D77AK Impulse Bit Data Refined

Figures 4.20 and 4.21 represent a revised method for displaying the representative specific impulse data for micro-thrusters D77AY and D77AK, respectively. This revised method involved taking the summation of the impulse bit over a firing interval and the using the aggregate mass loss to create an average specific impulse for that range. This was believed to provide a more accurate representation of the specific impulse data based on laboratory measurement techniques in finding average mass loss. Consultation with DSSP representatives confirmed this information [57].

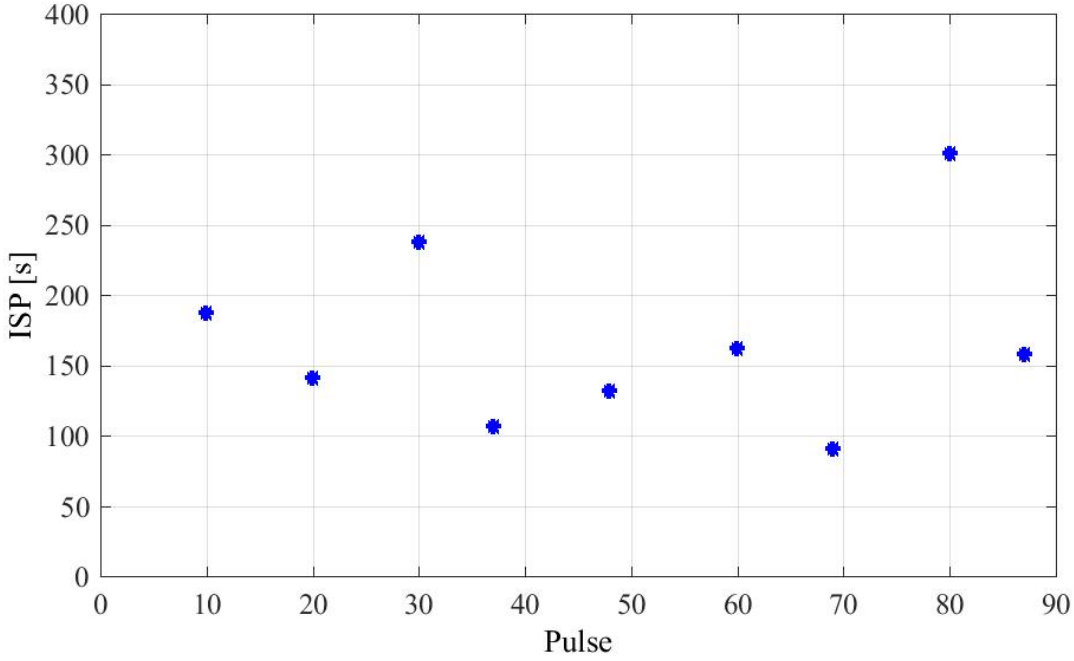

Figure 4.20: D77AY Specific Impulse Data Refined

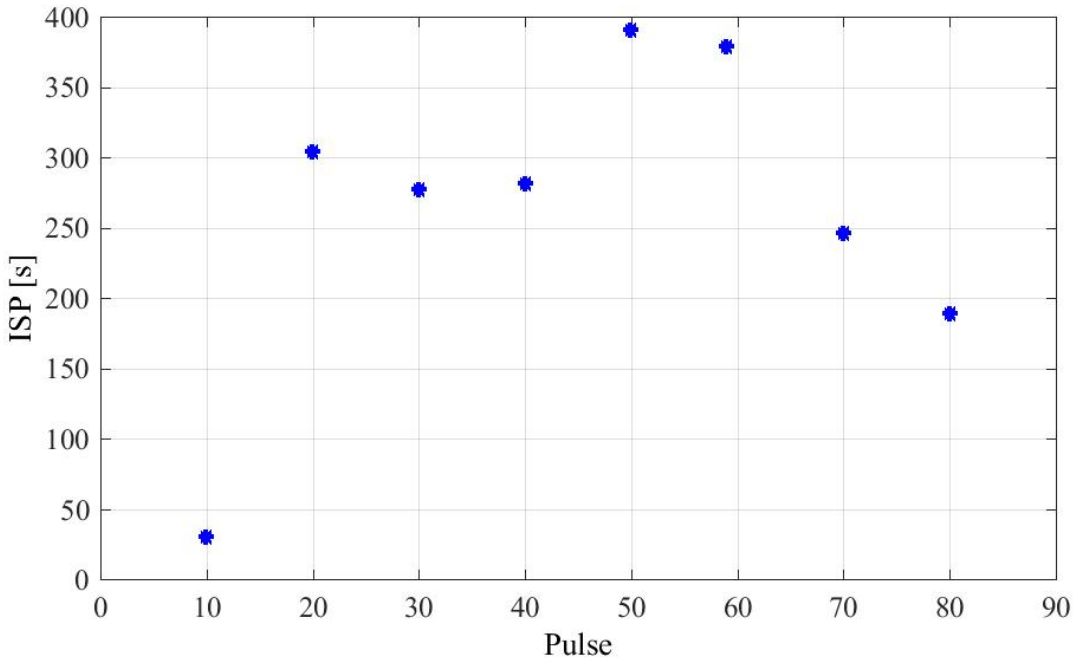

Figure 4.21: D77AK Specific Impulse Data Refined

One observation in the data represented in Figures 4.20 and 4.21 is the varying specific impulse for the initial firing interval (up to 10 firings). The specific impulse is higher for D77AY in this interval at around 190 s compared to D77AK which was around 30 s. This may be due to the fact that the mass loss was much greater for D77AK in this range than D77AY as seen in Figure 4.16. Also as seen in Figure 4.20 and 4.21, the impulse bit is lower for D77AY in this range than D77AK. The erratic micro-thruster behavior from 30 firings to 70 firings influenced the specific impulse results for both figures 4.20 and 4.21. As presented in Sawka and McPherson [22], the theoretical Isp for the HIPEP propellant used in these micro-thrusters is around 245 s.

4.4.3 Batch H806

Six micro-thrusters from batch H806 were fired during the test article atmospheric configuration phase. Three of the six micro-thrusters were used for bench top testing of the electronics to ensure proper firing sequence and circuit operation. Once this was completed three additional micro-thrusters from this batch were used for test article calibration. Figure 4.22 shows the pre-fire top and side views of micro-thruster UAH 47. Figure 4.23 shows a frame of the 2nd and final firing of UAH 22.

Figure 4.22: Micro-Thruster UAH47

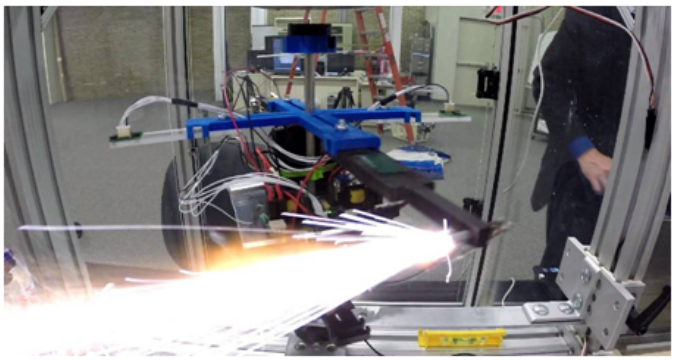

Figure 4.23: Micro-Thruster UAH 22 Firing

Most of the micro-thrusters in this particular batch failed to fire more than 10 firings. However, micro-thruster UAH 46 did produce fifty pulses before becoming inactive. Severe inner and outer electrode degradation was observed with UAH 46 as well as case burn through. Micro-thruster mass data was documented and can be seen in Figure 4.24.

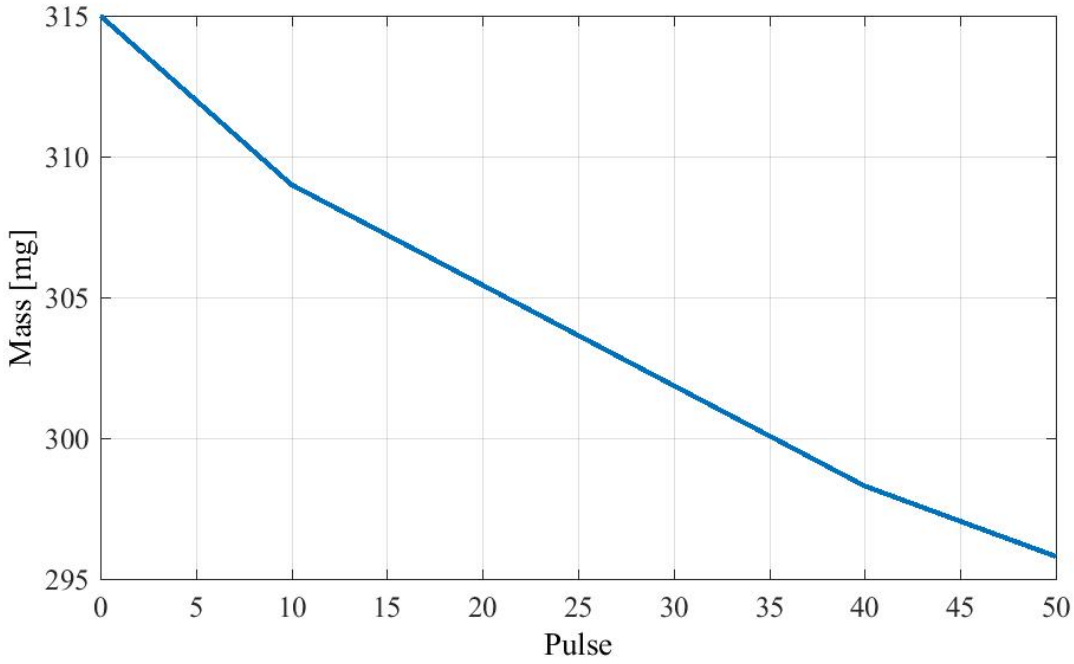

Figure 4.24: UAH 46 Micro-Thruster Mass Chart

4.4.4 Batch H898

Figure 4.25 shows an example of a micro-thruster from Batch H898. The pictures show a before and after frame. A difference in manufacturing was noticed with an extra amount of epoxy at the base joint and slightly different geometry with shearing at the firing end of the micro-thruster.

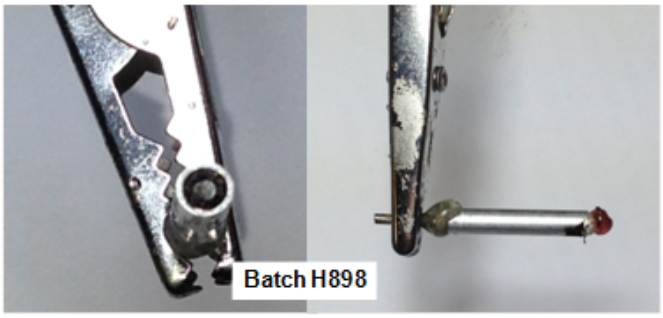

Figure 4.25: Micro-Thruster Batch H898

Three micro-thrusters from batch H898 were fired. The data collected was not analyzed due to low number of firings. One micro-thruster failed after 9 firings. Two other thrusters failed after 4 firings. Figure 4.26, shows a mass loss versus number of firing comparison for the three micro-thruster batch H898. The higher initial thruster mass compared to the earlier batches is the result of the excessive epoxy on the joint as mentioned above. As noted for thruster RR28A08, the sample size for these thrusters is too small to draw substantial conclusions, however even with the small number of firings; a significant difference can be seen between the three thrusters. The two thrusters that failed within 4 firings had a large initial mass loss as compared with the thruster which failed after 9 firings.

DSSP representatives were consulted about the failures for this batch of thrusters. DSSP indicated that new materials for the inner electrode for this batch of thrusters limited the microthruster to operational back pressure ranges below 10^{-3} torr. DSSP indicated that the thrusters would not work under atmospheric conditions. This consultation led to the requirements for pressure ignition testing (Appendix E) to de-

termine the maximum back pressure under which consistent firings could be achieved [56].

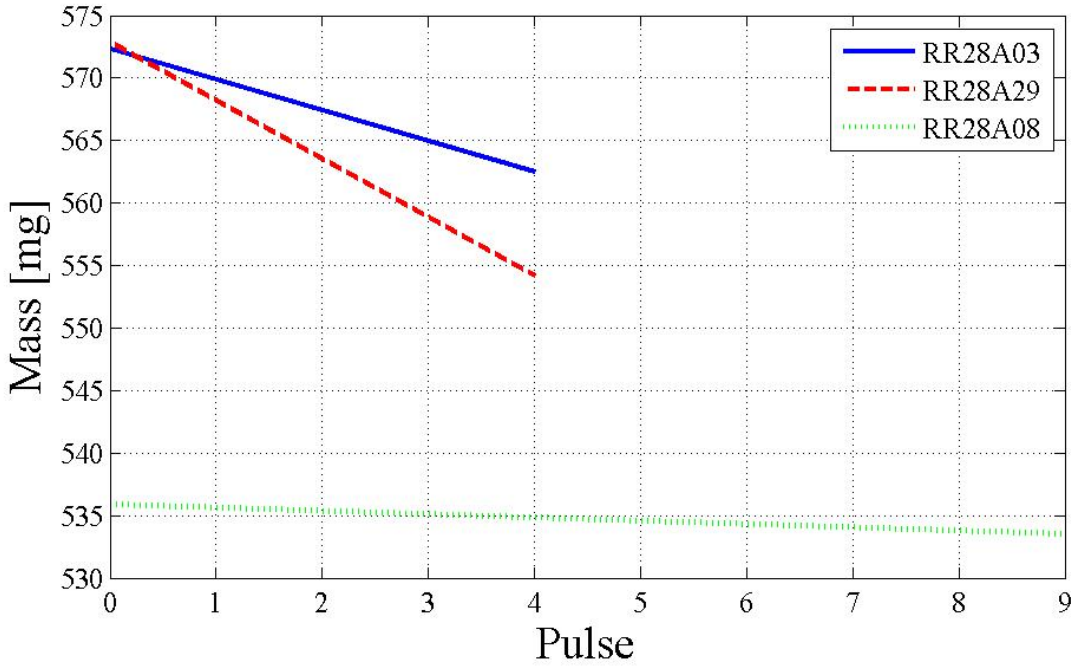

Figure 4.26: Thruster Mass Batch H898

4.5 Test Stand Gyroscope Calibration

A series of experiments were first conducted to assess the technique for calibrating the gyroscope. The gyroscope data was post-processed using an existing MATLAB script and plots were created. Figure 4.27 shows images from the high speed video before, during, and after frames of the pendulum impact from a preliminary assessment test. Figure 4.28, shows the raw gyroscope data and the angular velocity determined from the high speed images for one of the preliminary assessment tests. The two traces show reasonable agreement for this first order analysis providing

some confidence to the two techniques. The region of interest in the gyroscope data was from 0.06 seconds to 0.25 seconds as that was the point when impact occurred. These frames were selected from the high speed camera images for comparison.

Figure 4.27: Impact Images

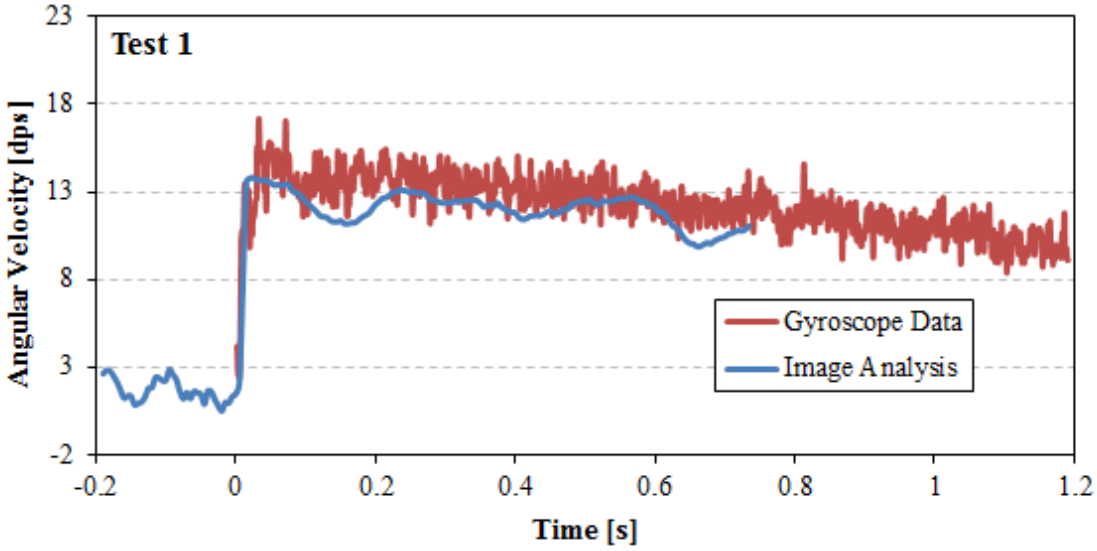

Figure 4.28: Impact Data

4.5.1 Gyroscope Sensor Uncertainty

Using the uncertainty methodology described in section 3.11, the equation for finding the total error for the gyroscope was developed. The datasheet from the manufacturer of the sensor reported a accuracy error of 4%. This value would stay constant throughout the uncertainty calculations. The random error varied based on the sample data. The equation for computing the total error of the gyroscope can be seen in the following expression,

$$U^2_{\omega_{gyro}} = S^2_{b_{i,gyro}} + S^2_{i,gyro} \tag{4.3}$$

where $S_{b_{i,gyro}}$ is the systematic error and $S_{i,gyro}$ is the random error. Table 4.5 shows the mean angular velocity, and total error for the gyroscope during each individual impact test. For test 2 and test 3 two values were recorded. The lower value is before impact and the higher value is after impact.

Table 4.5: Gyroscope Impact Test Summary

Test #	Mean Angular Velocity (dps)	Total Error (dps)
1	13.65	0.557
2	12.36	0.504
2	1.09	0.114
3	17.81	0.72
3	1.65	0.113
7	6.44	0.277
8	9.02	0.376
9	8.11	0.339
10	10.81	0.443
11	2.93	0.154
12	14.60	0.0.592
13	10.14	0.414
14	16.02	0.647
15	9.89	0.404
16	6.80	0.297

continued ...

Test #	Mean Angular Velocity (dps)	Total Error (dps)
17	22.64	0.912
18	23.00	0.926
20	11.40	0.467
21	8.57	0.365
22	16.34	0.661
23	12.38	0.506
25	9.107	0.378

The final equation for finding the uncertainty of the image data was more complicated. The data reduction equation for finding the angular velocity in the MATLAB algorithm for the image data is seen in the following expression,

$$\omega_{image} = \frac{\#pixels}{\#frames} \cdot \frac{length}{pixel} \cdot \frac{frame}{dt} \cdot \frac{1}{r} \tag{4.4}$$

where $\#pixels$ represents the number of pixels the center point moved over the timespace, dt, $\#frames$ is the amount of frames taken over the timespan, $\frac{length}{pixel}$ is the length scale for the images, $\frac{frame}{dt}$ is the frame rate. For most of the experiments the high speed camera captured images at 200 fps. This was varied between 100 to 200 frames per second throughout the experiment. Finally, r is the radius from reflector to the axis of rotation. Table 4.6 shows the variable convention used for the final uncertainty calculation.

Table 4.6: Variable Convention

Variable	Description	Uncertainty Value
A	# Pixels	± 5 Pixels
B	# Frames	0
C	Length Scale Factor	.01 in
D	$\frac{frame}{dt}$	.003 s (200 FPS) .007 s (100 FPS)
r	radius	.01 in

The number of pixel uncertainty was assumed to be around 5 based on observation of the MATLAB center detection routine. The uncertainty in the $\#frames$ is fixed so the value for this variable is 0. The length scale factor varied during the day the tests were performed. The frame rate uncertainty varied from 0.003 s to 0.007 s. The radius uncertainty was 0.01 inches based on the measurement tool used. The final uncertainty equation is as follows,

$$\frac{U_\omega}{\omega} = \sqrt{\frac{U_A}{A}^2 + \frac{U_B}{B}^2 + \frac{U_C}{C}^2 + \frac{U_D}{D}^2 + \frac{U_r}{r}^2} \tag{4.5}$$

Table 4.7: Image Impact Test Summary

Test #	Mean Angular Velocity (dps)	Total Error (dps)
1	12.23	0.926
2	11.30	0.923
2	0.941	0.941
3	16.38	0.934
3	1.50	0.623
7	5.82	0.812
8	7.96	0.854
9	7.25	0.811
10	9.45	0.840
11	2.56	0.753
12	12.85	0.844
13	8.96	0.641
14	14.38	0.851
15	8.91	0.866
16	6.22	1.041

continued ...

Test #	Mean Angular Velocity (dps)	Total Error (dps)
17	20.66	1.103
18	20.57	1.081
20	10.05	1.056
21	7.55	1.054
22	14.89	1.084
23	11.17	1.065
25	8.14	1.077

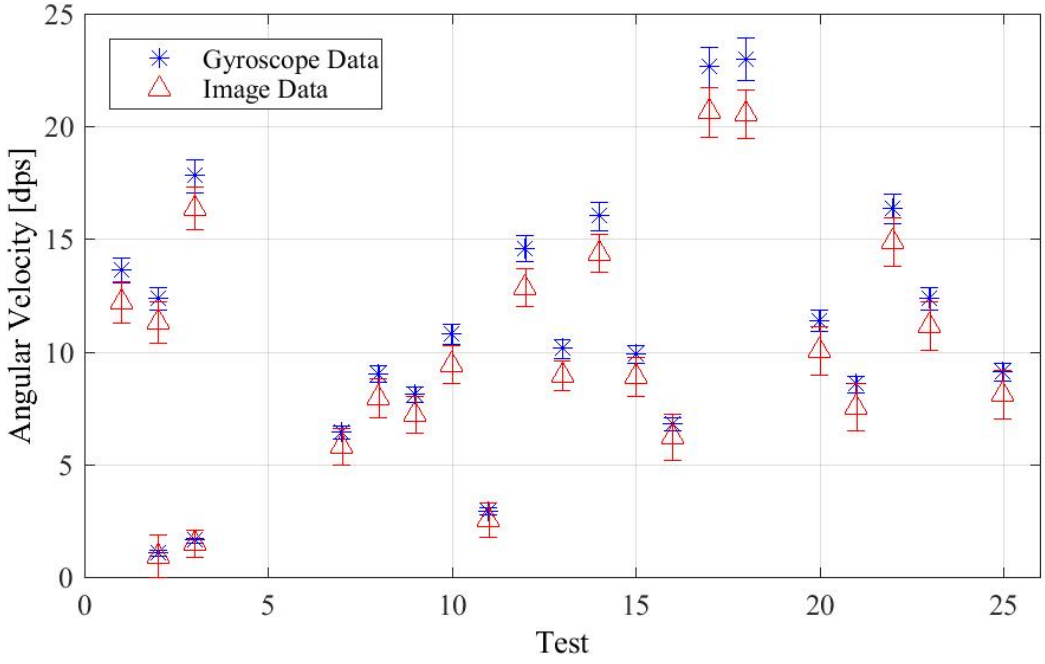

Figure 4.29: Gyroscope and Image Data Summary Comparison

The information from Table 4.5 and Table 4.7 were graphed in Figure 4.29. The red triangles indicate the mean angular velocity of the image data while the blue asterisks indicate the mean angular velocity for the gyroscope data. It should be noted that an initial movement was tracked before impact on test 2 and test 3. Two means are therefore represented in Figure 4.29 for tests 2 and 3. Due to technical issues during data recording tests 4, 5, 6, 19 and 24 did not save proper data. These points were excluded during the analysis. The region of interest for this thesis study are the verification measurements taken up to 15 degrees per second. Figure 4.30 shows a revised plot showing these values.

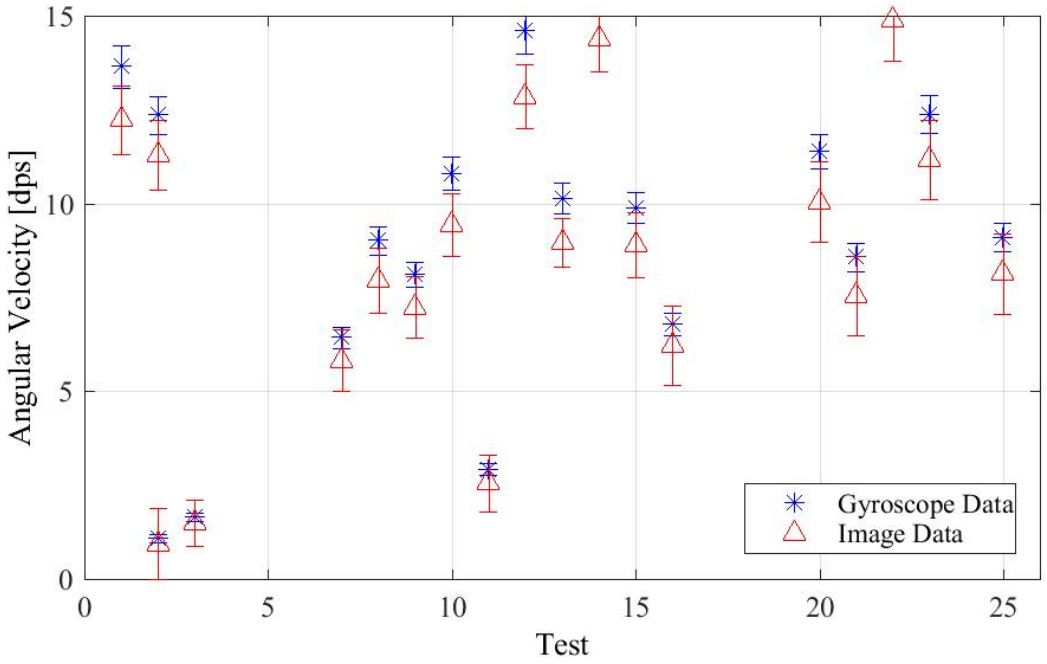

Figure 4.30: Gyroscope and Image Data Summary Comparison

Figure 4.30 shows the data only in the range for the thruster firings (less than 10 degrees per second). From this figure good agreement can be tracked through these points. The majority of the gyroscope angular velocity mean values are captured within the uncertainty bounds of the image data. This translates into a higher probability that the true value is within these bounds.

Figure 4.31 shows the absolute difference between the angular velocity mean values for the both the gyroscope and the image data. As the angular velocity increases the disparity between the image data and the gyroscope data increases. However, a good linear trend is observed which indicates a relatively constant percent difference.

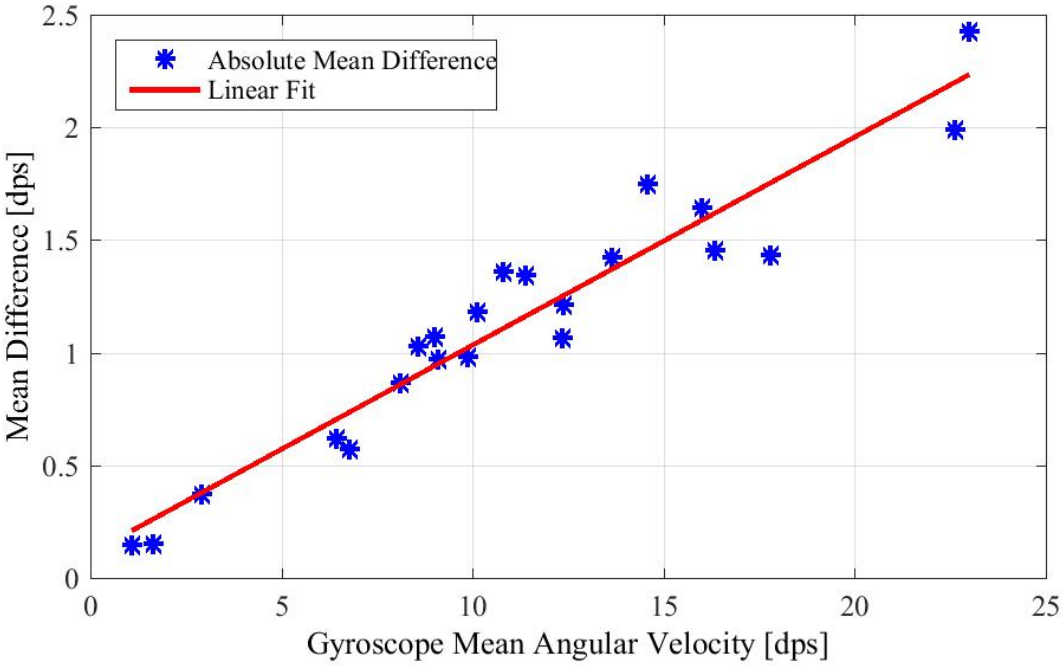

Figure 4.31: Absolute Mean Difference

Overall, the percent difference, as shown in Figure 4.32, between the angular velocity mean of the gyroscope and the image data shows no discrete trend. These percent differences range from 7.5% to 13.5%. While the range is large for this percent difference it does however show that the difference is very close to 10%. This percent difference is most likely caused by some bias in either the sensor or image data.

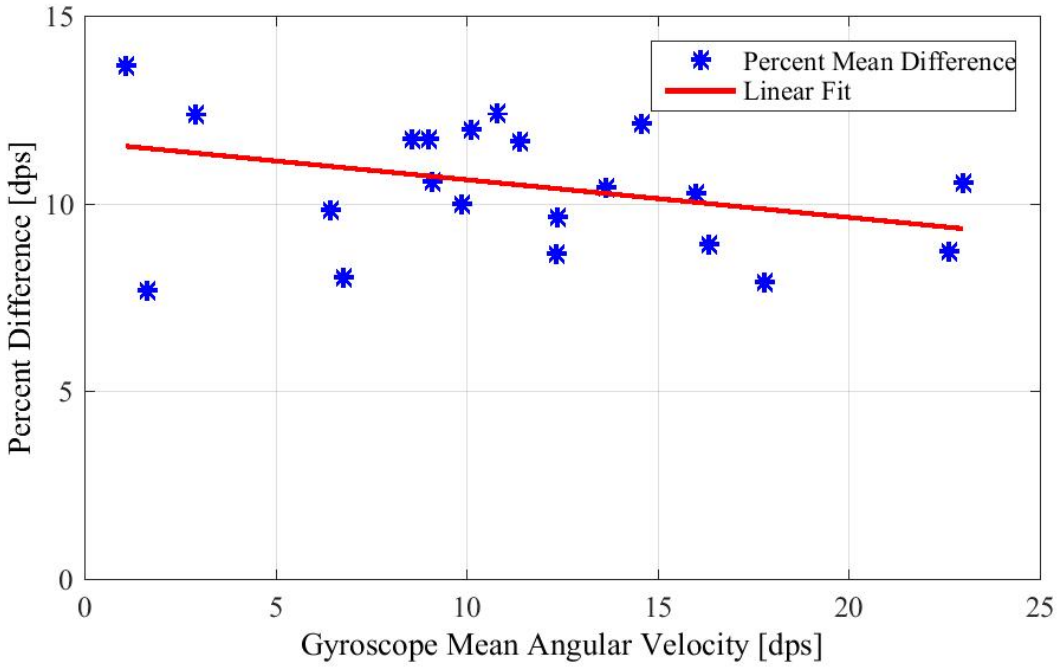

Figure 4.32: Percent Mean Difference

These verification tests showed good agreement between the gyroscope data and image data in the range of thruster firings. Since, the gyroscope data mean was within the uncertainty of the image mean it was determined that the manufactures accuracy value would be used for final uncertainty calculations. Through these ex-

periments it was also noted that some unidentified bias may also exist, but a method to quantify was not determined.

4.5.2 Uncertainty Calculations

With the verification tests completed the final impulse-bit uncertainty of the analyzed data seen in Figures 4.18 and 4.19 can be completed. Equation 3.21 shows the impulse bit equation used for the analysis in this chapter. The uncertainty equation for finding the impulse bit is expressed as follows,

$$\frac{U_{J_{ep}}}{J_{ep}} = \sqrt{\frac{U_I}{I}^2 + \frac{U_{\omega_1}}{\omega_2 - \omega_1}^2 + \frac{U_{\omega_2}}{\omega_2 - \omega_1}^2 + \frac{U_r}{r}^2} \tag{4.6}$$

where U_I is the uncertainty in the moment of inertia, U_{ω_1} is the uncertainty in the angular velocity before firing, U_{ω_2} is the uncertainty in the angular velocity after firing, and U_r is the uncertainty in the radius measurement. The values and uncertainty for the mass moment of inertia and radius are stated in Table 4.8. U_{ω_1} was determined by taking the uncertainty information from a series of non rotational experiments. In these tests the payload would remain unmoving while data was collected. This data was analyzed across all data points in a sample frame.

Table 4.8: Impulse Bit Uncertainty

Variable	Value	Uncertainty
I	9.863 x $10^{-4} kg{\cdot}m^2$	3.89 %
r	0.123825 m	0.0016 m
ω_1	0 dps	0.076 dps

The uncertainty in ω_2 varied with each individual firing. This was due to the varying angular velocities in the thruster firings. The angular velocity was multiplied by the manufactures accuracy error to find systematic error and then the data's random error was determined for each individual firing. The total error of these individual firings was calculated and applied to the final uncertainty for the impulse bit value. Table 4.9 and Figure 4.33 summarizes the uncertainty of the average impulse bit measurements made for micro-thruster D77AY. The average total error value was found for the appropriate firing intervals and then applied to the average impulse bit value (Figure 4.18). The same uncertainty analysis was completed for micro-thruster D77AK using the uncertainty equation above. Table 4.10 and Figure 4.34 summarize the uncertainty of the average impulse bit measurements made for micro-thruster D77AK.

Table 4.9: D77AY Impulse Bit Uncertainty

Firing Interval	Average Impulse-Bit [mN-s]	Uncertainty [mN-s]
1-10	0.294	0.029
11-20	0.621	0.048
21-30	0.723	0.054
31-37	1.470	0.095
38-48	0.368	0.055
49-60	0.802	0.043
61-69	0.672	0.062
70-80	1.023	0.074
81-87	0.837	0.066

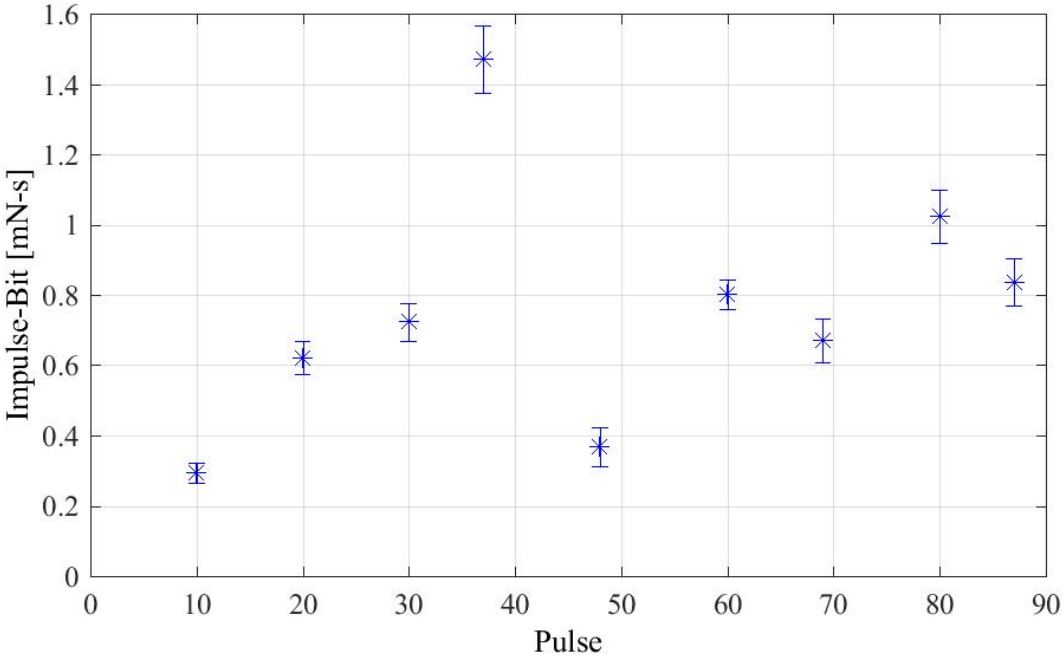

Figure 4.33: D77AY Impulse-Bit Uncertainty

Figure 4.33 shows the impulse-bit values for micro-thruster D77AY with uncertainty bars overlayed on the data. The percent uncertainty was highest for the first firing interval from 1-10 pulses. The percent uncertainty in this interval was approximately 16%. The uncertainty on the other data points ranged from 6.8%-8.1%. Overall, the greatest contributor to the uncertainty was ω_2.

Table 4.10: D77AK Impulse Bit Uncertainty

Firing Interval	Average Impulse-Bit [mN-s]	Uncertainty [mN-s]
1-10	0.383	0.034
11-20	0.566	0.044
21-30	0.625	0.048
31-40	0.745	0.055
41-50	1.071	0.073
51-59	0.866	0.061
60-70	1.010	0.069
71-80	0.720	0.055

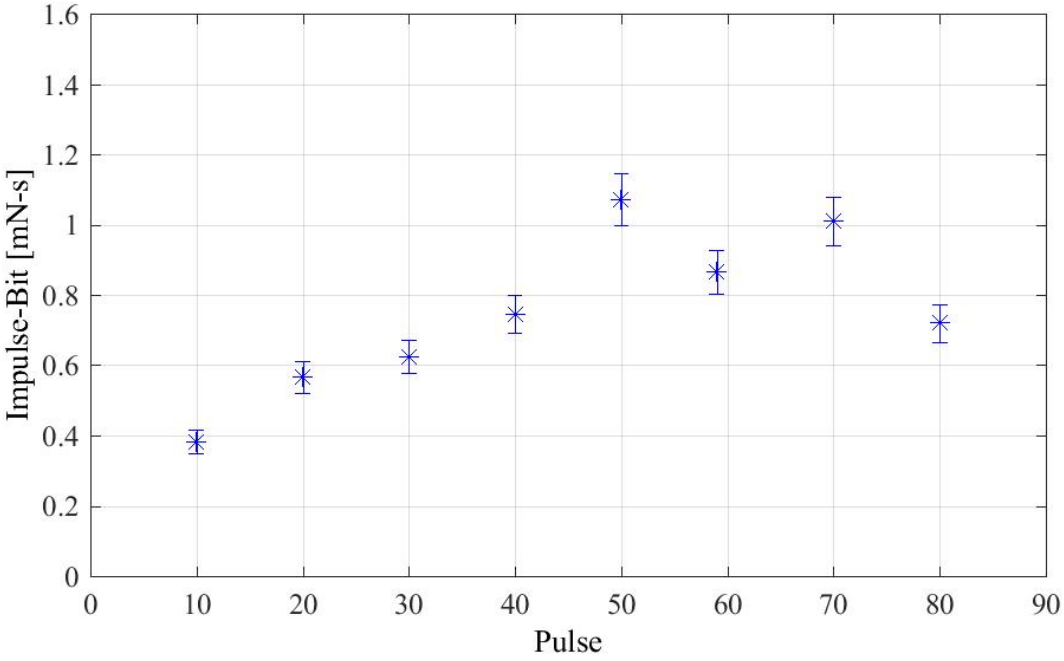

Figure 4.34: D77AK Impulse-Bit Uncertainty

Figure 4.34 shows the impulse-bit values for micro-thruster D77AK with uncertainty bars overlayed on the data. The percent uncertainty was highest for the first firing interval from 1-10 pulses. Unlike micro-thruster D77AY the percent uncertainty in this interval was at a lower 10%. The uncertainty on the other data points ranged from 6.8%-7.9%. The greatest contributor, again, to the overall uncertainty was the uncertainty in ω_2.

The same uncertainty analysis was completed for the specific impulse data seen in Figures 4.20 and 4.21. Equation 3.23 shows the impulse bit equation used for the analysis in this chapter. The uncertainty equation for finding the error in specific impulse is expressed as follows,

$$\frac{U_{Isp}}{Isp} = \sqrt{\frac{U_I}{I}^2 + \frac{U_{\omega_1}}{\omega_2 - \omega_1}^2 + \frac{U_{\omega_2}}{\omega_2 - \omega_1}^2 + \frac{U_r}{r}^2 + \frac{U_{m_{bit}}}{m_{bit}}^2} \tag{4.7}$$

The additional variables to calculate Isp are the mass bit per firing (m_{bit}) and the gravity constant. The uncertainty in gravity is negligible. The uncertainty for mass bit was 0.00005 grams. The mass bit uncertainty varied based on the firing interval. Mass loss information for both thruster can be seen in Figure 4.18. Table 4.11 and Figure 4.35 summarizes the uncertainty of the average specific impulse measurements made for micro-thruster D77AY. The average total error value was found for the appropriate firing intervals and then applied to the average specific impulse value (Figure 4.20). The same uncertainty analysis was completed for micro-thruster D77AK using the uncertainty equation above. Table 4.12 and Figure 4.36 summarize the uncertainty of the average impulse bit measurements made for micro-thruster D77AK.

Table 4.11: D77AY Specific Impulse Uncertainty

Firing Interval	Average Specific Impulse [s]	Uncertainty [s]
1-10	187.34	61.96
11-20	140.69	23.83
21-30	237.67	42.20
31-37	106.47	26.37
38-48	131.14	22.56
49-60	161.68	22.26
61-69	90.14	9.06
70-80	300.32	45.51
81-87	157.66	17.67

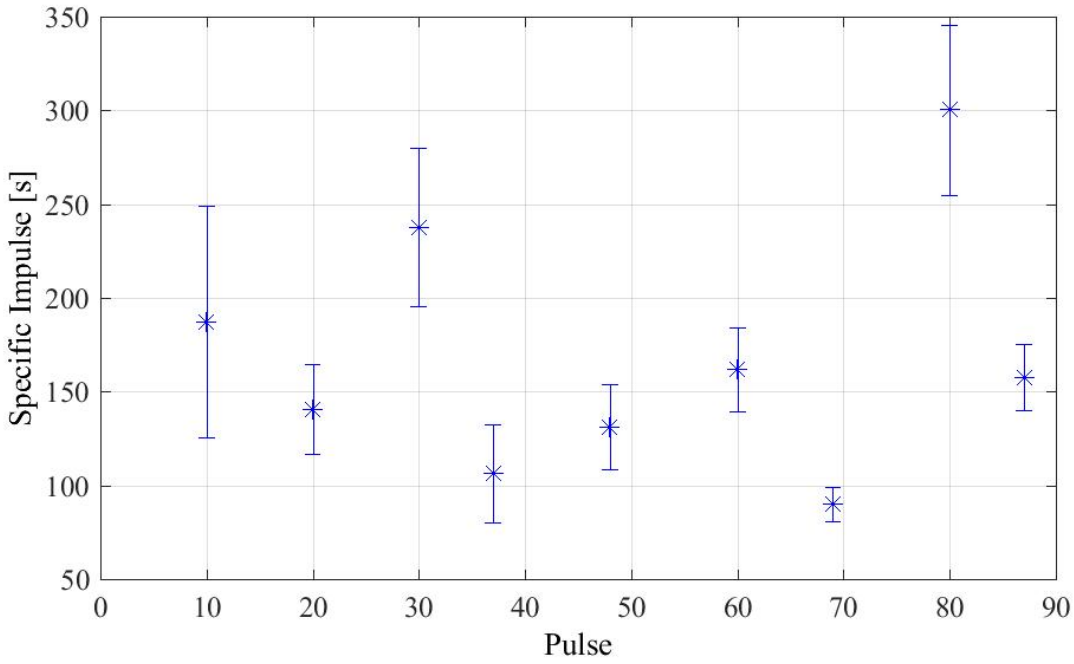

Figure 4.35: D77AY Specific Impulse Uncertainty

Figure 4.35 shows the specific impulse values for micro-thruster D77AY with uncertainty bars overlayed on the data. The percent uncertainty was highest for the first firing interval from 1-10 pulses. The percent uncertainty in this interval was approximately 37%. The uncertainty on the other data points ranged from 10%-18.7%. The greatest contributor to the overall uncertainty for the specific impulse was the mass measurement uncertainty.

Table 4.12: D77AK Specific Impulse Uncertainty

Firing Interval	Average Specific Impulse [s]	Uncertainty [s]
1-10	30.25	2.97
11-20	303.87	83.45
21-30	276.94	63.83
31-40	281.40	55.87
41-50	390.08	74.59
51-59	378.24	85.57
60-70	246.10	58.58
71-80	188.68	27.98

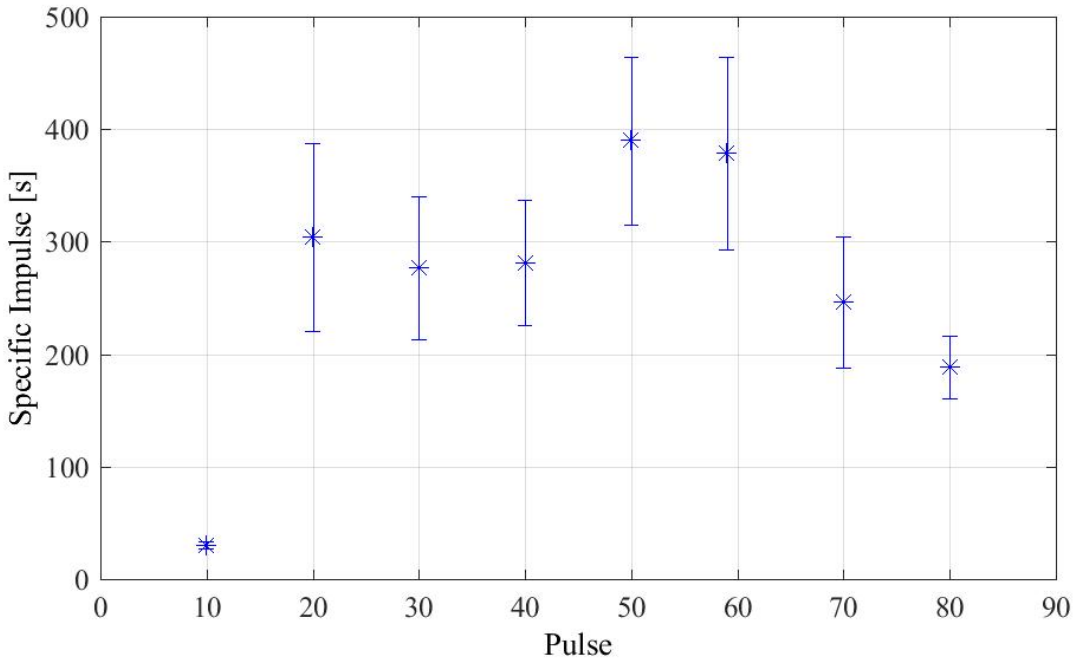

Figure 4.36: D77AK Specific Impulse Uncertainty

Figure 4.36 shows the specific impulse values for micro-thruster D77AK with uncertainty bars overlayed on the data. The percent uncertainty was highest for the second firing interval from 11-20 pulses. The percent uncertainty in this interval was approximately 27%. The uncertainty on the other data points ranged from 10.8%-23%. The greatest contributor to the overall uncertainty for the specific impulse was the mass measurement uncertainty.

CHAPTER 5

CONCLUSIONS

5.1 Summary

Electromagnetic pulsed micro-thrusters were tested with a new magnetically levitated thrust stand sensitive enough to measure milli-Newton second level impulses. The objectives of this research was to design, fabricate and test such technology through the application of scientific and engineering methods. The difficulties with the development process included: creating a low-friction environment, reducing environmental effects on control system instabilities and producing appropriate electronics for proper data collection and micro-thruster firing. Other challenges encountered during the research were programmatic challenges in understanding the firing procedure of the commercial pulsed micro-thrusters containing new technology.

The micro-thruster used in these experiments were commercial pulsed micro-thrusters manufactured by DSSP, LLC. These micro-thrusters were unique as they incorporated electrically-controlled solid propellant technology. This technology allowed for ignition and burn of the solid propellant when the appropriate amount of energy was applied to the thruster connections. The surface of the propellant would

ablate and the plasma generated would accelerate through the nozzle. Once the current was removed the ignition would be extinguished.

Several time reducing methods and techniques were utilized in order to make the technology more time efficient. The first time reducing method was the use of RP technology on campus to 3D print parts in the MAE machine shop. This allowed for overnight fabrication of critical testing components. Also, a non-linear dynamic process called, Poincaré - Lindstedt method, was utilized with the university's Vicon camera lab to make mass moment of inertia measurements of complex payload less time consuming. The impulse bit and specific impulse were determined through derivation of the total angular momentum equation.

The final mass moment of inertia calculation yielded a result of $3.37 lb{\cdot}in^2$ as the inertia for the test payload. The uncertainty analysis for the inertia calibration experiments conducted on baseline materials resulted in less than 1% error in theoretical and experimental mass moment of inertia calculations. This was expected based on assumptions made in determining the theoretical model equations. The final uncertainty on the test payload used in the experimentation was 3.89%. During the atmospheric test phase a single batch of thrusters received by the test team showed promise of proper functionality. The atmospheric tests verified proper function of the firing circuit and several new methods, such as circuit operations and measurement processes, were developed in order to expand on knowledge of the entire system.

A series of verification tests were performed with high speed imaging to calibrate the gyroscopic sensor used for taking angular velocity measurements and compare those values with image data. These tests showed good agreement in the micro-

thruster test regime with very good overlap in uncertainty. The overall impulse-bit uncertainty between the two thrusters analyzed in this study typically ranged from 6.8% - 8.1% with uncertainty spiking at 16% during one interval of testing. These values were expected due to the challenges associated with developing a high sensitivity test stand for the purpose of analyzing micro-thrusters of this size. Uncertainty for specific impulse was calculated to be higher typically ranging from 10% - 23%.

Multiple firings from the micro-thrusters were produced with varying performance results. The sensors were able to record data at low milli-Newton second resolution for impulse bit calculations. For one micro-thruster test the impulse-bit ranged from $0.5-2.75$ mN-s with the average specific impulse around 166 s. For another micro-thruster test the impulse-bit ranged from $0.1-1.8$ mN-s with the average specific impulse around 263 s. Many hypotheses have been created for the variability seen in the data. The leading cause is believed to be the erratic behavior from the new propellant technology due to aging. The voids in the propellant, as discussed in Chapter 4, may have produced uneven surface ablation. Another reason maybe uncertainties in the data collection system. Recommendations for lowering the system uncertainty can be seen in section 5.2 of this thesis. Overall, the results showed that the system performed as expected. The primary goals of thesis study were accomplished.

5.2 Future Recommendations

The development of this test stand was done such that it could be easily integrated into a vacuum chamber in order to perform reduced pressure testing on

the micro-thrusters. UAH has a facility with a large vacuum chamber capable of reducing environmental pressures down to 1×10^{-6} Torr. This could help evaluate thrusters at low-earth orbits. During the past two years, the team has shown the ability to do this by creating a method to integrating the test stand to the test cart for the vacuum chamber and then the cart underwent a series of vibration tests to ensure that the levitating payload would not observe increased instabilities due to vacuum chamber pump vibrations. When reducing pressure it becomes increasingly difficult for electrical components to effectively dissipate heat. As was the case with the electromagnet component of the magnetic levitation control. During vacuum chamber pump down it was observed that the electromagnet would exceed normal operating temperatures as seen during atmospheric testing. To mitigate this effect a heat exchanger design was proposed and tested to reduce electromagnet temperatures during operation. This vacuum chamber modification work is detailed in Appendix D.

In order to ensure that the micro-thrusters would repeatedly ignite as intended in a reduced pressure environment a series of test were conducted in a small vacuum chamber at the propulsion research center to identify pressure ignition limits. During the series of experiments two batches of micro-thrusters were tested with each one producing anomalies. During this phase the same batch of thrusters that worked at atmospheric pressure also repeated similar performance at reduced pressure. The data and issues with this experimental design are detailed in Appendix E of this thesis.

Initially, two closed loop controllability experiments were proposed in order to evaluate readiness of thrust stand and micro-thruster technology firing two thrusters simultaneously. The first was to generate constant maneuvers such as maintaining a constant spin rate on a single degree-of-freedom payload. The second closed loop controllability experiment will maintain an absolute orientation. However, the testing was limited to a series of controlled firings in a single direction using only one thruster setups. Tests were conducted for these thrusters and documented in this thesis.

Suggested improvements for future works would include final refinements to the test stand and payload. It is recommended that many inertia calibration experiments and test stand calibration experiments are conducted in order to increase sample size. Due to the high electrical flux caused by the 45 J of energy being dumped into the micro-thruster the sensors may see interference during the initial ignition phase of the firing. One refinement would be to protect the sensor via a faraday cage to mitigate this interference from the circuit. Another improvement would be to increase the size of the electromagnet. A bigger electromagnet would allow for more controlled levitation without additional effort. If the test were to be scaled up a bigger electromagnet would be necessary to levitate more weight effectively.

Finally, better balancing and measurement techniques for the payload should be evaluated in order to reduce uncertainty. It is critical that the center of mass of the payload is as close to the rotating axis as possible. An off axis center of mass can induce unwanted rotational effects that may skew measurements by introducing a gravity force. Another improvement would be to install an isolator on the gyroscope to reduce the noise in the signal. This may provide some reduction in error. Perform-

ing multiple inertia calibration experiments to increase sample size may be necessary in reducing the total error for the inertia calculation. The overall goals of the improvements would be to reduce the uncertainties such that allow the measurement of lower impulse bits. Since the impulse bit values are so low designing a test stand with high sensitivity and low uncertainty are tough to produce. The addition of another gyroscopic sensor may be evaluated to increase sample size and increase confidence in the angular velocity measurements. A more precise measurement scale may be required to take low mass measurements to decrease the uncertainty in specific impulse calculations.

APPENDICES

APPENDIX A

DESIGN EVOLUTION

This appendix outlines some of the design evolution during the development phase of the final product. Figure A.1 shows a concept found in the literature for the basic design of a levitating platform [55]. In this concept both the permanent magnet and position sensor are located at the top of the test stand. During the design evolution, it was determined that the test stand response was better with the position sensor on the bottom of the test stand for the intended purpose of the experiments outlined in this thesis.

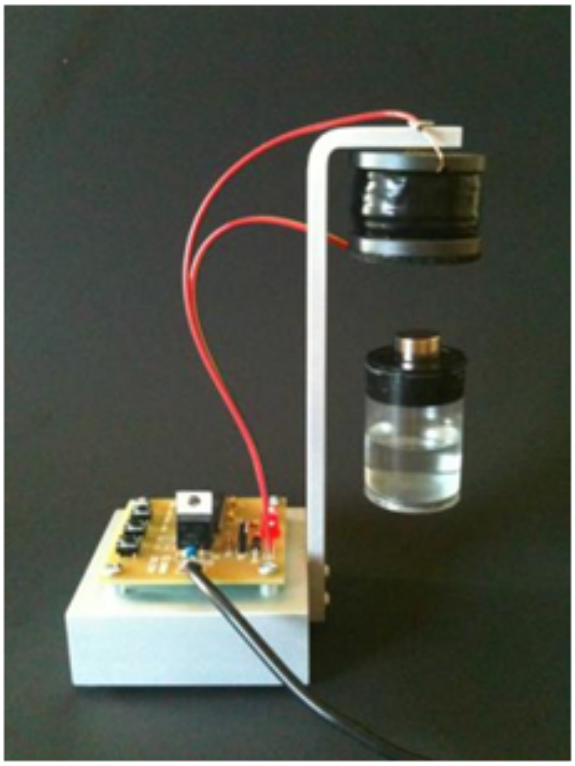

Figure A.1: Small Scale Magnetic Levitation Stand [55]

A.1 Development of Maglev Test Stand

During the test stand development phase a prototype was constructed using steel material to produce a magnetic levitation test stand for the purpose of proof of concept, seen in Figure A.2. The magnetic levitation controller (MLC) circuit was tested using a sample payload and the gains were adjusted as appropriate. With a new electromagnet, it was discovered that as the payload mass increased, the increased power required by the electromagnet to levitate the payload caused interference with the hall sensor feedback signal. This interference resulted in unstable oscillations of the payload. The maglev test stand was reconfigured so that the hall sensor was

removed from the top and placed at the bottom of the payload to increase the distance from the electromagnet. This change also required an additional feedback permanent magnet to be placed on the bottom of the payload.

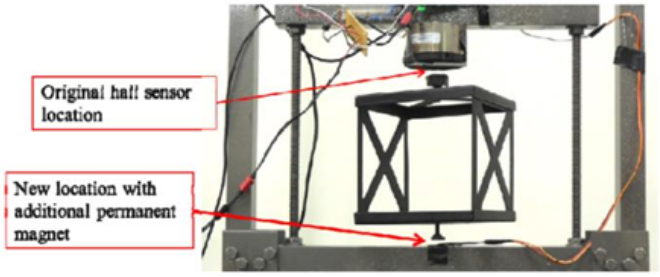

Figure A.2: Modified Configuration of Maglev Test Stand

The modifications can be seen in Figure A.2. In addition, it was observed that the new configuration was insensitive to moderate changes in payload mass and can be adjusted to accommodate larger masses. The placement of a permanent magnet at the bottom of the test stand also prevented the payload from falling off of the test stand when power is lost to the electromagnet or when the payload drops below the levitation range.

Once the proof of concept experiment was completed on the MLC, the magnetically levitating thrust stand hardware was revised using adjustable aluminum materials. The revised stand is shown in the vacuum chamber in Figure A.3. System rigidity and dimensional tolerances were improved as a result of the new design. The new design allowed for easy integration from atmospheric test environment to the vacuum chamber test cart.

Figure A.3: Revised Test Stand

After the new test stand was constructed, additional framework was added to apply panels to the outer edge in order to prevent environmental disturbances during atmospheric pressure testing. Clear abrasive resistant acrylic was selected as the material to complete the enclosure for the test stand. This can be seen in the Figure A.4.

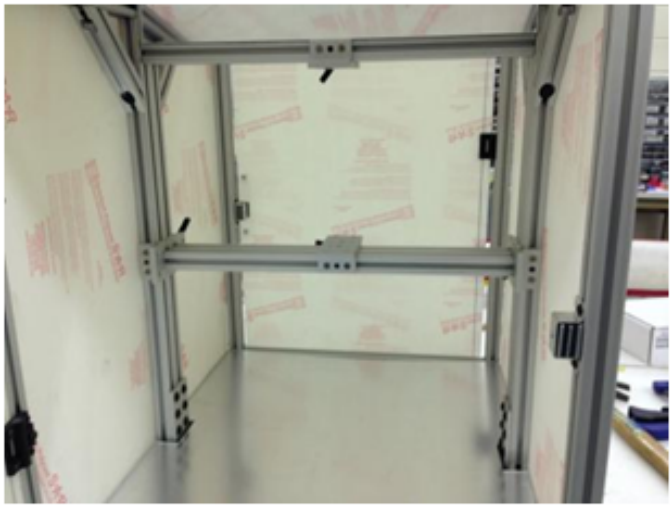

Figure A.4: Atmospheric Test Stand Enclosure

The final atmospheric test stand, seen in Figure A.5, was approximately 24″ x 24″ x 18″ in total volume. This relatively small size aided the mobility of the test stand without the sacrifice of security.

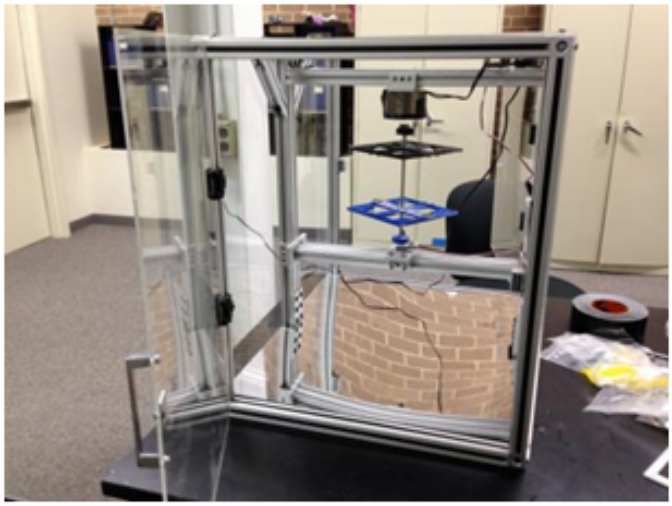

Figure A.5: Payload Inside Enclosed Test Stand

A.2 Circuit Box

Figure A.6 shows the circuit diagram for the MLC microcontroller. This control schematic was refined from a basic magnetic levitation circuit design in "Maglev Plus System Magnetic Levitation Experiment"[55]. The maglev circuit was also designed to use larger electromagnets without significant modifications to the components. The three components of the MLC that were modified were the power supply, electromagnet, and MOSFET. The switching electronics uses an N-Channel MOSFET with a fly back diode to accommodate potential reverse voltage caused by the inductive load. The MOSFET is a three-terminal device that has a control electrode, or gate, that draws no DC current since it is insulated from the substrate to which it is attached. The gate lies between the other two pins, the drain and source. When the gate of the MOSFET is grounded, no drain-to-source current flows for a positive drain voltage. MOSFETs are very useful for this type of circuit since they are excellent high-current voltage-controlled switches [49].

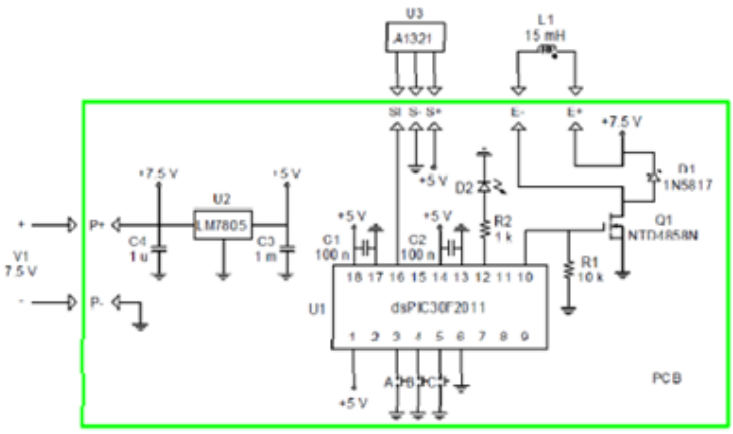

Figure A.6: MLC Circuit Design

The original MOSFET was replaced with a larger version to handle increased current draw. The preliminary experiments revealed that the increased current draw caused the MLC to function for only a short period of time before failure. While the current was well below the maximum level, the increased power caused significant heating of the MOSFET case during operation; potentially causing failure due to a decrease in maximum drain current vs. case temperature. To remedy this failure point a heat sink was added to reduce case temperature during operation.

While this improved levitation performance, with the sensor on the bottom, any swaying of the payload results in the permanent magnet moving away from the hall sensor. This motion, in some circumstances, contributed to a small undamped oscillation in the payload. In order to improve hall sensor feedback on the maglev system, rather than using a single hall sensor, a triad configuration of spaced hall sensors with passive averaging circuit was designed. The triad configuration results

in feedback being less sensitive to lateral swaying and improves the robustness of the payload levitation system.

A.3 Payload Design

A payload was designed in order to provide a platform for micro-thruster firing electronics. The platform used the available on-site rapid prototyping technology (RP). This technology greatly reduced manufacturing time and effort while increasing quality. The RP platform can be seen in Figure A.7. An improved component mounting system was included in the design. The side panels to the above design were removed in order to reduce total system weight. This further reduced instabilities in the MLC function. The dimensions of these RP plates were 6" x 6" x .25".

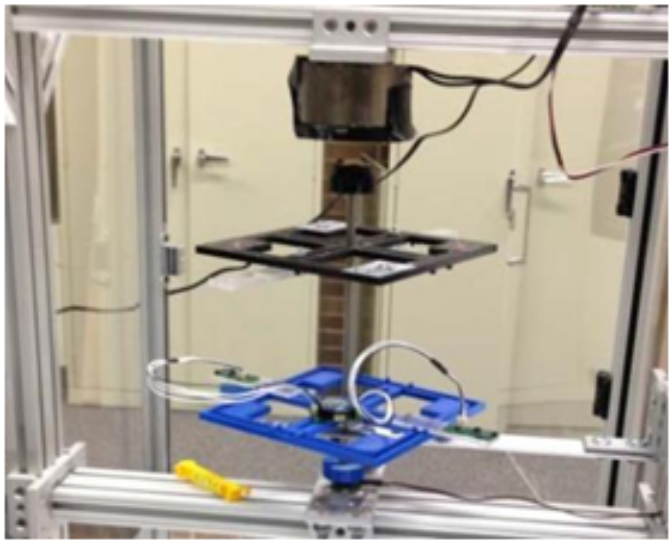

Figure A.7: 2nd Generation Payload

This replaced the original payload seen levitating in Figure A.2. The original payload was constructed from heavy metal which was bulky and was press fitted together at the top and bottom. This press fitting introduced uncertainty in the design by creating an off balanced payload. The vertical and rotational instabilities described in Chapter 3 were magnified.

Figure A.8 shows a CAD model of the first rapid prototyped test payload. The payload seen in the figure below increased rigidity and accuracy of placement of the required magnets. This was accomplished by designing specific locations for interfacing and screw hole placement in the CAD model. When the printed parts were complete screws could be placed in the appropriate locations for securing the payload. This increased accuracy helped reduced some of the instabilities associated with non-symmetrical structure.

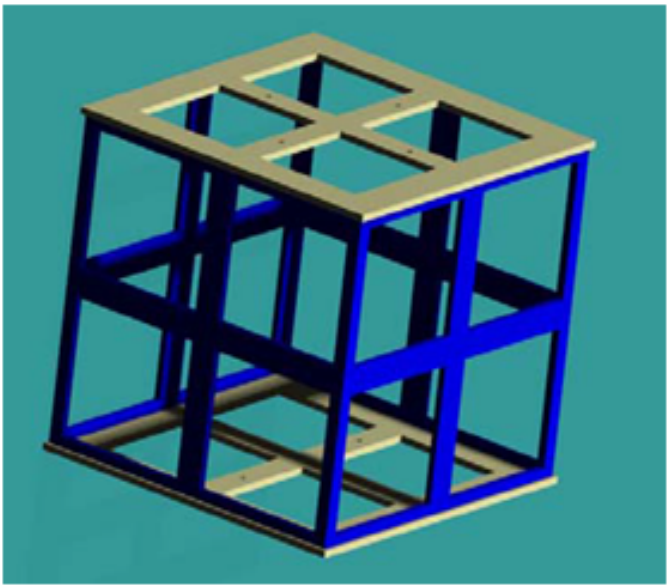

Figure A.8: Payload CAD Model

A.3.1 Firing Circuit

A notional design of a 300 V firing circuit using an inverting transformer was created. The circuit design for the firing system is shown in Figure A.9. The voltage and capacitors were chosen to match DSSP specifications (1000μF = 45J). The primary components used in generating 45 J of energy were the transformer and capacitor. The capacitor used was a PHOTO flash PF360-1000μ. The maximum voltage and capacitance was rated at 360 V and 1000 μF, respectively [42]. The inverter transformer used in the circuit was the Xenon Flash Tubes XFT-5683-3v. This transformer would step up 3 V input to a 300 V output [43].

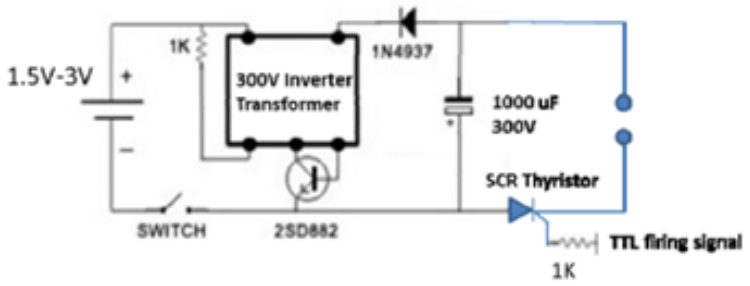

Figure A.9: Notional 300 V Firing Circuit

A new firing circuit shown below in Figure A.10 was developed to allow the SCR to function properly. The first change was to use a microprocessor to generate a pulse width modulated (PWM) signal at 10 kHz. The PWM signal controls flow through the primary coil of the transformer using a MOSFET. Since a microcontroller is now used, a separation between the high current and low current supplies has been created using two voltage regulators. Advantage of using a microprocessor to

generate the transformer input is that the frequency can be controlled and the firing decision and charge monitoring can all be monitored actively. The firing signal was transmitted using transistor-transistor logic (TTL) devices. For this type of trigger signal the digital output of a TTL device is typically between 0 and 0.5 V for low voltages and between 2.7 V and 5 V for high input signals [49].

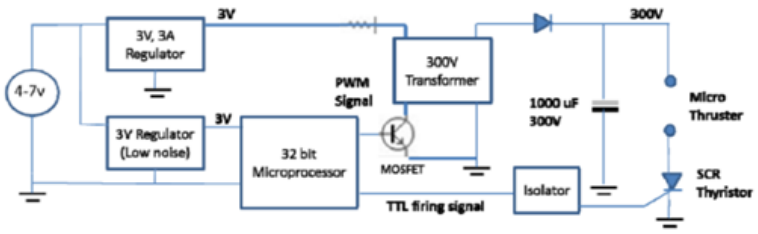

Figure A.10: 300 V Firing Circuit

The capacitor voltage was actively monitored using an adjustable comparator circuit connected to the microprocessor. This feature allowed the charging to be stopped once a defined voltage had been reached. An MOC3020 optically isolated SCR driver was used to interface electronic controls and power the SCR at high voltages. The opto-isolator creates a state of electrical isolation between the input and output circuits by transmitting the signal optically instead of hard wired electrical connection. The advantage of this component is to protect output circuits from excessive voltages that could damage critical components [49]. The microprocessor used in this development firing circuit was the PIC32 MX150F128B Microchip Technology microcontroller. The microprocessor consists of twenty-eight pins, has 128 KB of program memory, 32 KB of data memory and can operate at up to 50 MHz [46].

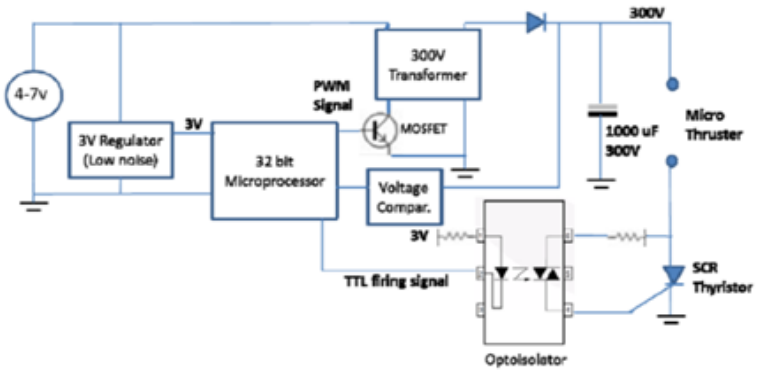

Figure A.11: Revised 300 V Firing Circuit with Comparator and Optoisolator

A.3.2 Electronics and Thruster Mounting

For the initial test setup the mounts were fabricated from 1/4″ thick clear scratch resistant acrylic material. The gyroscope was mounted to the RP plates while the accelerometers were mounted to the clear acrylic arms. The thrusters are inserted into through holes in the acrylic.

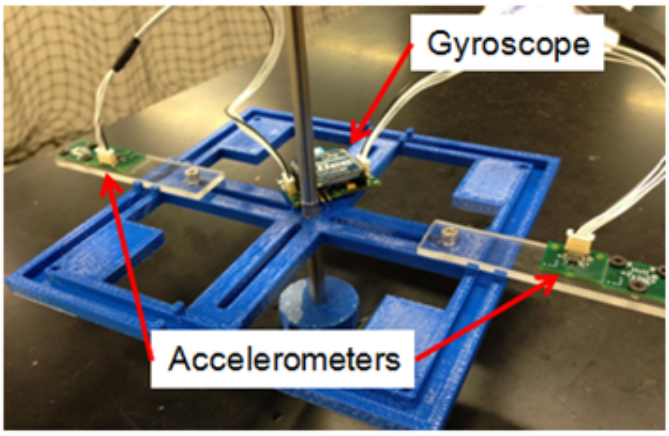

Figure A.12: Sensor Package

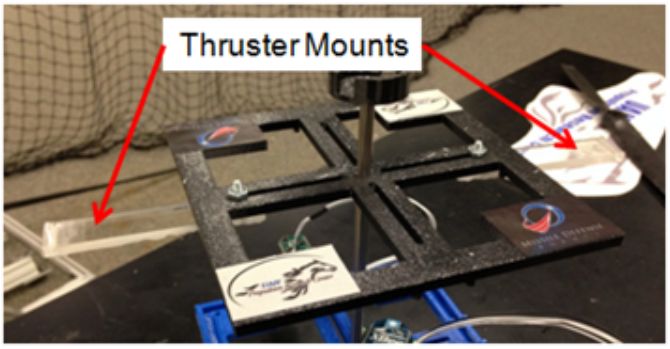

Figure A.13: Thruster Mounts

Once the sensors and thruster mounts were attached to the payload a preliminary test was performed, with manual excitation, in order to capture data from the wireless DAQ and save to the file. Figure A.14 shows the assembled system levitating in the atmospheric test enclosure.

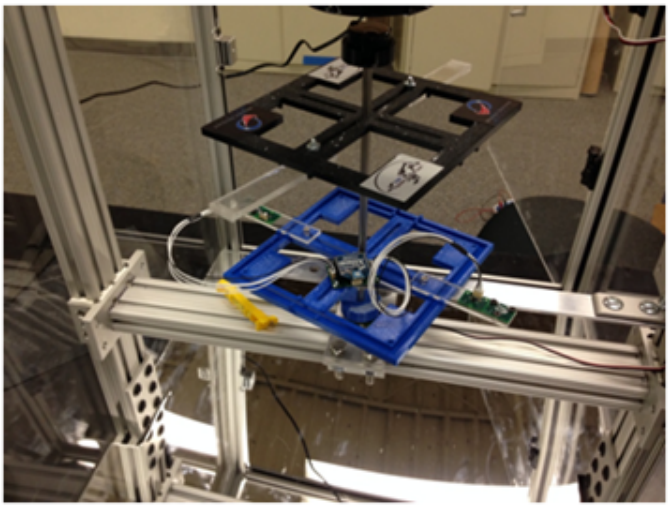

Figure A.14: Sensor Testing in Atmospheric Enclosure

The manual excitation experiment provided important information in the function of critical components. After the process for collecting data was completed the next step involved determining an initial method for analyzing data. A MATLAB script was created in order to analyze the sensor data. The sample data from the baseline sensor tests can be seen in the figures below. The figures show examples of post processed data collected from a manual excitation. The dual accelerometers have been converted to an angular acceleration. The data shows the resulting angular acceleration from two impacts, one at t = 0.0s, and another at t = 0.2s. The impact force is proportional to the measured angular acceleration and is found by multiplying by the system inertia. The data rate for this experiment was approximately 1000 Hz. This raw data was post-processed through a MATLAB script to output accelerometer data as angular acceleration (Figure A.17).

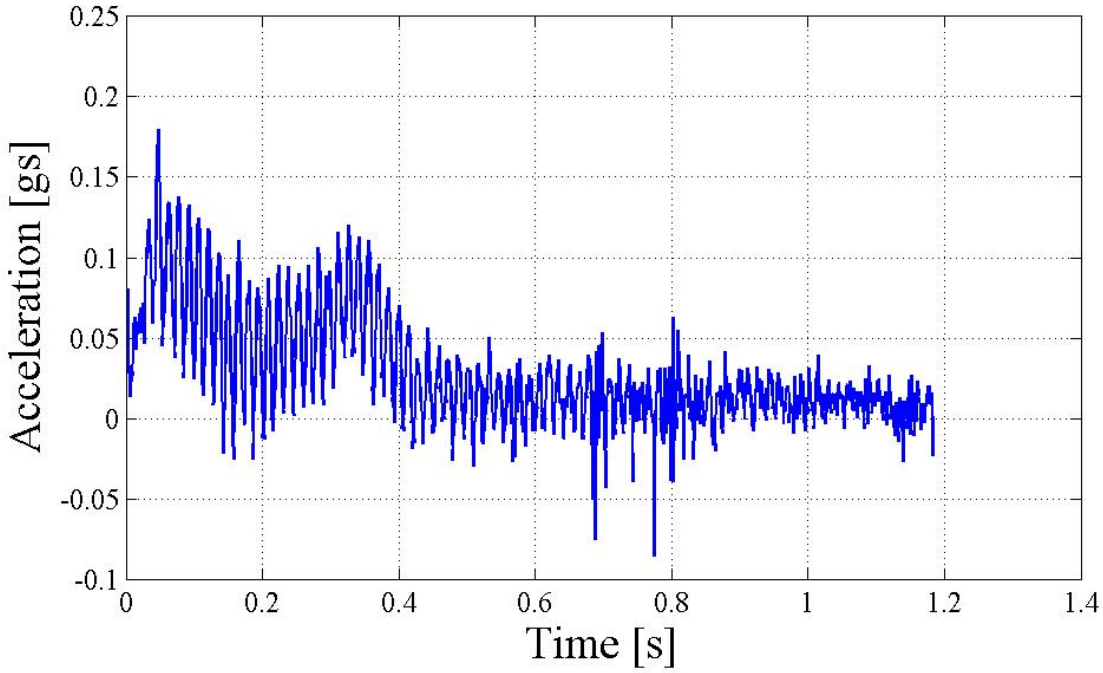

Figure A.15: Raw Accelerometer Data

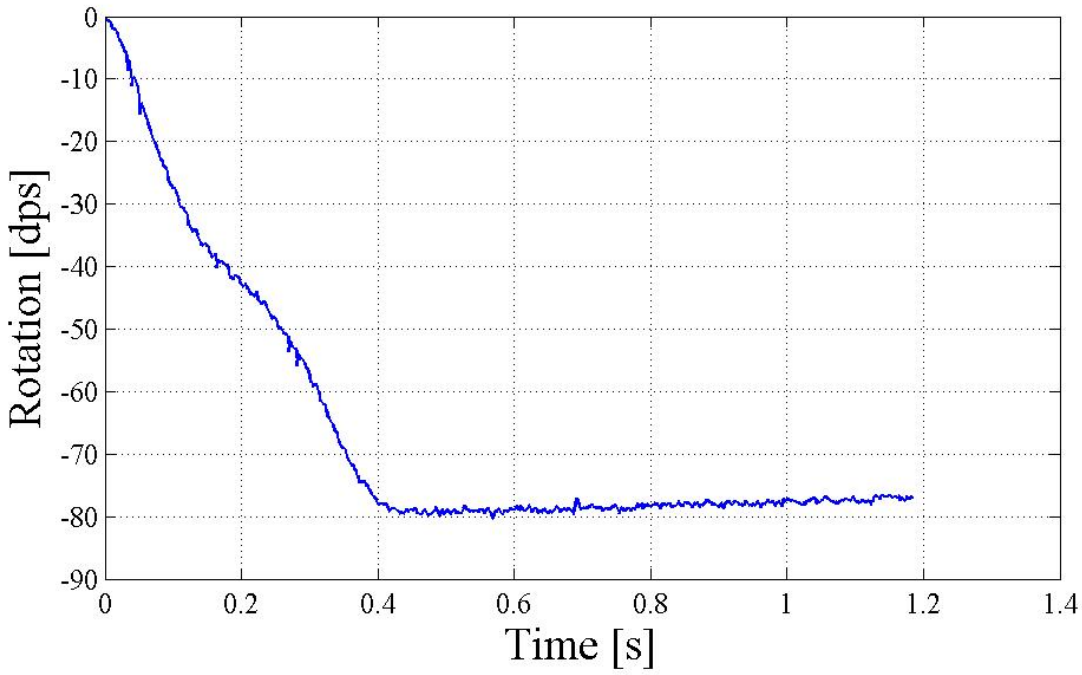

Figure A.16: Raw Gyroscope Data

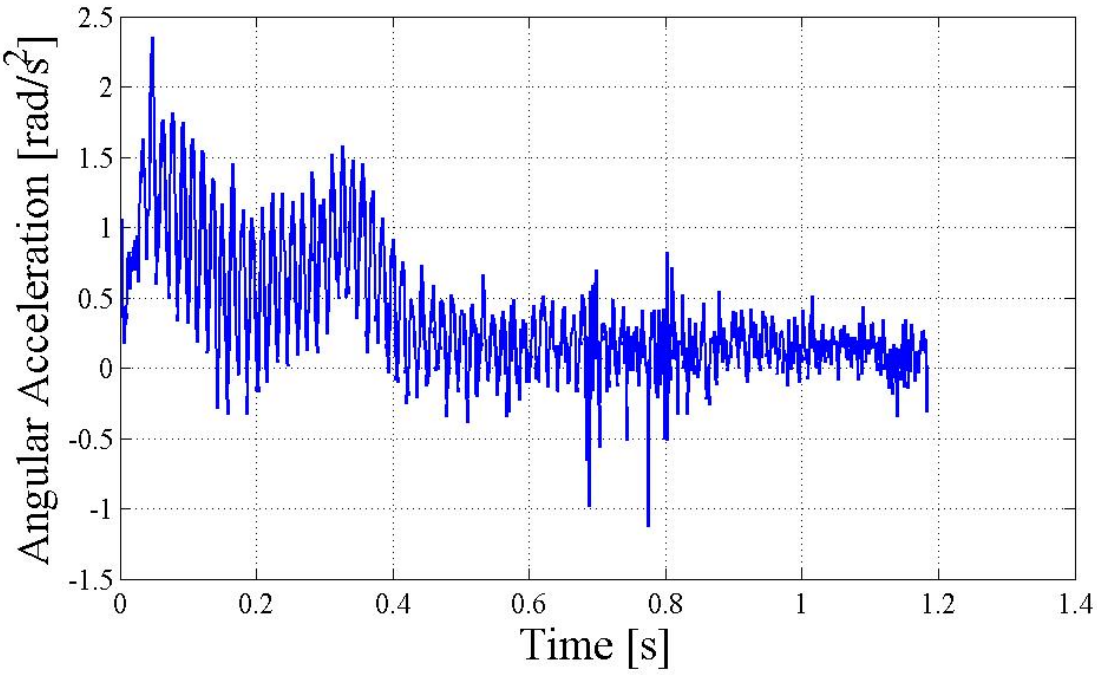

Figure A.17: System Angular Acceleration

Another series of subsystem tests were performed on the dual fire printed circuit board (DF PCB) unit. The pretest procedure consisted of setting up the controller and payload sensors before connecting the micro-thruster and electronics to the system. Once the payload was in stable levitation the thruster was installed in the thruster mount and the electrical leads were attached at the appropriate location on the micro-thruster. During the experiments, the thrusters were fired with a 1000μF capacitor charged to 300V (45 J of energy). The test was filmed using a video camera at 30fps. The Figure A.18 shows frames before, during, and after the micro-thruster firing.

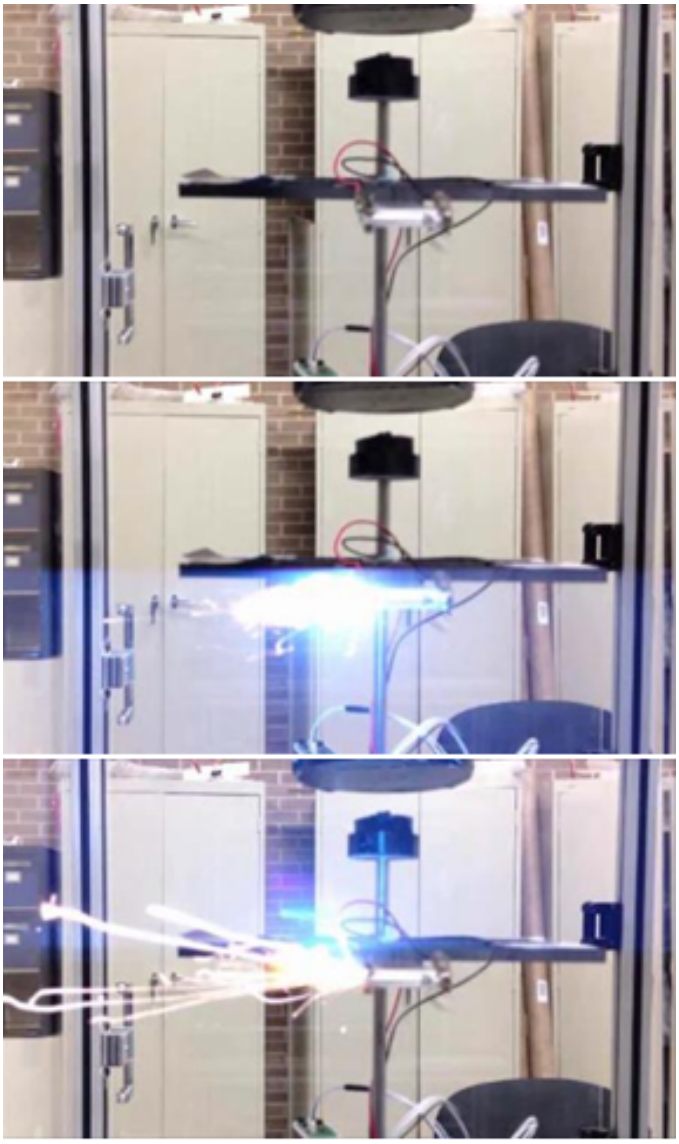

Figure A.18: Three Frame Sequence of Micro-Thruster Firing (30 FPS)

After this subsystem testing was complete the final firing components were added to the payload. A supporting plate made from super abrasive resistant clear acrylic for the DF PCB and sensor package. With the addition of mass to the payload

improvements had to be made to the MLC configuration. Figure A.19 shows the modified payload and Figure A.20 shows the propulsion payload in levitation.

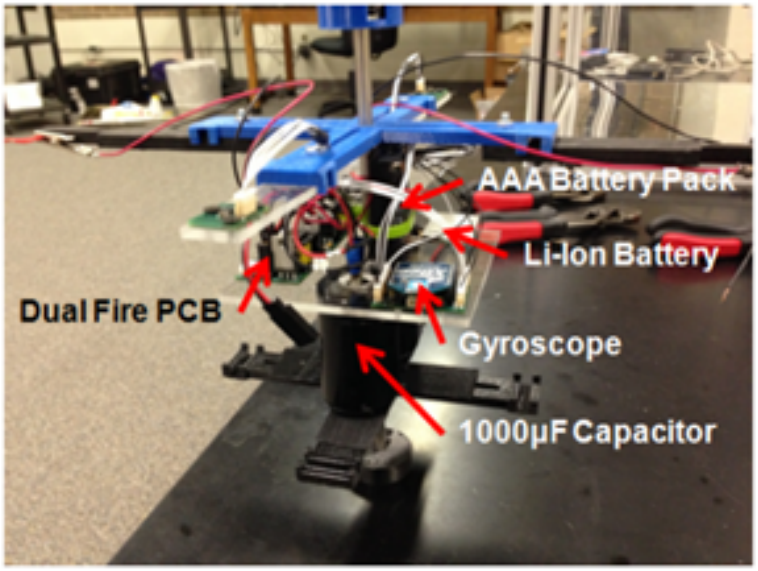

Figure A.19: Modified Controllability Payload

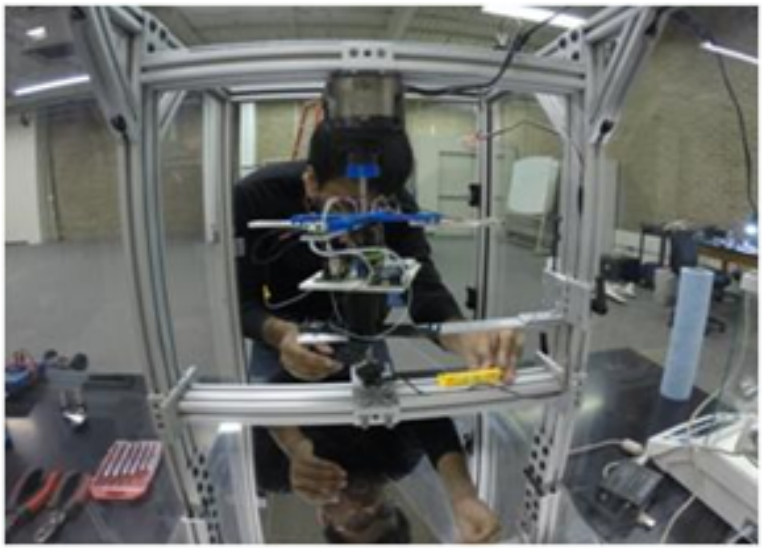

Figure A.20: Setting Up Payload

APPENDIX B

POINCARÉ-LINDSTEDT METHOD

The Poincaré-Lindstedt method is used for determining the periodic solutions of weakly nonlinear differential equations. Usually in the form of $\ddot{x}+x+\varepsilon h(x,\dot{x})=0$, where $0\leq\varepsilon << 1$ and $h(x,\dot{x})$ is an smooth function. The method is an improved version of perturbation theory that breaks down secular terms. It is good for approximating periodic solutions, but limited in use with transients or non-periodic solutions. To simplify the process it uses geometry to determine equations of motion. The method makes use of the Duffing Equation [35], a non-linear second-order differential equation used to model damped and driven oscillators. It is also used to model dynamical systems that exhibit chaotic behavior. The Duffing Equation is given by [36]:

$$\ddot{x} + \delta\dot{x} + \alpha_{stiff}x + \beta x^3 = \gamma cos(\omega_F t) \tag{B.1}$$

where the parameters δ, α_{stiff}, β, γ, and ω_F are assumed to be constants. The δ term controls the size of the damping, the α term controls the size of the stiffness, the β term controls the amount of non-linearity in the restoring force, γ controls the

amplitude of the periodic driving force and ω_F controls the frequency of the periodic driving force. Two critical assumptions are made to simplify the duffing equation for the inertia calibration experiment. The first assumption is that the connection strings introduce very little dampening to the results. The second assumption is that there is no periodic driving force. This means that δ and γ both go to zero.

$$\ddot{x} + \cancelto{0}{\delta\dot{x}} + \alpha_{stiff}x + \beta x^3 = \cancelto{0}{\gamma cos(\omega_F t)}$$

The simplified equation then becomes:

$$\ddot{x} + \alpha x + \beta x^3 = 0 \tag{B.2}$$

B.1 Inertia Calibration Test Equations

The basic setup of the inertia calibration experiment calls for vertical suspension of the payload using to very long strings that would be attached at connection points on the payload. The payload would then be offset by some initial angle and then allowed to oscillate freely until equilibrium is obtained. The Figure B.1 gives a top view of the setup and a front view. PT1 and PT2 represent the two connection points of the string on the payload. These points are primed after rotation, unprimed before.

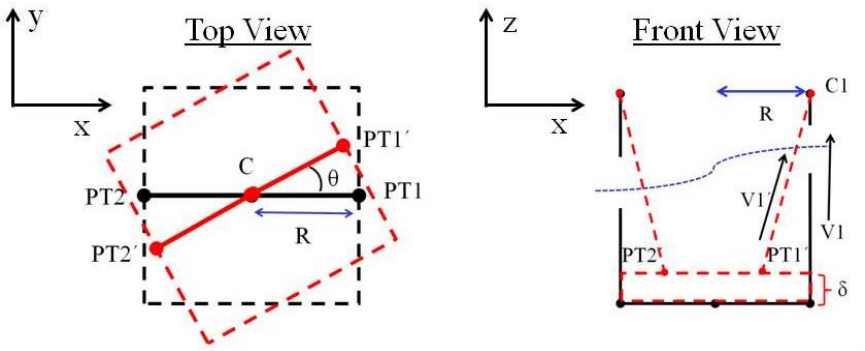

Figure B.1: Inertia Test Geometry

By symmetry both $PT1'$ and $PT2'$ raise the same δ_{twist}. After creating the initial geometric model the vectors associated with the different points on the payload must be defined. The vector for $PT1$ can be represented in the following expression:

$$PT1 = \begin{bmatrix} R & 0 & 0 \end{bmatrix}^T$$

The vector for $PT2$ is similar by symmetry, however the R becomes negative to represent the change in direction from the centerline. The vector for $PT1'$ can be represented in the following expression:

$$PT1' = \begin{bmatrix} RC\theta & RS\theta & \delta_{twist} \end{bmatrix}^T$$

The vector for $PT2'$ is similar by symmetry Both the x and y components become negative to represent the change in direction from the centerline. The δ_{twist} term

remains positive for PT2' since the rise for both points is in the same direction. At the very top of the front view is the point C1. The vector for C1 can be represented in the following expression:

$$C1 = \begin{bmatrix} R & 0 & L_{sus} \end{bmatrix}^T$$

The next step is to now define the vector $\vec{V_1}$ from PT1 to C1:

$$\vec{V_1} = C1 - PT1 = \begin{bmatrix} 0 & 0 & L_{sus} \end{bmatrix}^T$$

The vector $\vec{V_2}$ is the same due the length of the string being in the same direction. The vector $\vec{V_1}'$ can be defined in the following expression:

$$\vec{V_1}' = C1 - PT1' = \begin{bmatrix} R(1-C\theta) & -RS\theta & L_{sus} - \delta_{twist} \end{bmatrix}^T$$

The vectors for $PT1$ and $\vec{V_1}'$ have an unknown term δ. Since both $\vec{V_1}$ and $\vec{V_1}'$ have length L_{sus}, the magnitude of vector can be used to find the δ_{twist} term. Solving for the magnitude of the $\vec{V_1}'$ and using the quadratic formula yields the following equation:

$$\delta_{twist} = \frac{2L_{sus} \pm \sqrt{(2L_{sus})^2 - 4 \cdot 2 \cdot R^2(1-C\theta)}}{2} \tag{B.3}$$

Since the size of δ_{twist} cannot be greater than the length of L_{sus} the negative solution must be used. After further simplification the δ_{twist} term can be expressed in the following manner:

$$\delta = L_{sus}\left(1 - \sqrt{1 - 4\left(\frac{R}{L_{sus}}\right)^2 S^2\left(\frac{\theta}{2}\right)}\right) \tag{B.4}$$

The above δ_{twist} term is substituted in the equation for $\vec{V_1}$ which is the direction of the first string. The unit vector $\widehat{V_1}'$ can be defined in the tension direction by dividing through by $\mid \vec{V_1}' \mid = L_{sus}$. The unit vector $\widehat{V_1}'$ can be represented by:

$$\widehat{V_1}' = \left[\frac{R}{L_{sus}}\Big(1 - C\theta\Big) \quad -\frac{R}{L_{sus}}S\theta \quad \left(1 - \sqrt{1 - 4\Big(\frac{R}{L_{sus}}\Big)^2 S^2\Big(\frac{\theta}{2}\Big)}\right)\right]^T$$

Likewise for $PT2'$ by symmetry:

$$\widehat{V_2}' = \left[-\frac{R}{L_{sus}}\Big(1 - C\theta\Big) \quad \frac{R}{L_{sus}}S\theta \quad \left(1 - \sqrt{1 - 4\Big(\frac{R}{L_{sus}}\Big)^2 S^2\Big(\frac{\theta}{2}\Big)}\right)\right]^T$$

From symmetry we know that the tension in each string must be equal and that the vertical component must equal the weight of the payload. Therefore each of the two strings has a component W/2 in the z-direction. Since $\vec{F_1}' = T\widehat{V_1}', \vec{F_2}' = T\widehat{V_2}'$, the expression for T is as follows:

$$T = \frac{\frac{W}{2}}{\sqrt{1 - 4\left(\frac{R}{L_{sus}}\right)^2 S^2\left(\frac{\theta}{2}\right)}} \tag{B.5}$$

The force vector, $\vec{F_1}'$, can be seen in the following expression:

$$\vec{F_1}' = \begin{bmatrix} \left(\frac{W}{2}\right)\frac{\frac{R}{L_{sus}}(1-C\theta)}{\sqrt{1-4\left(\frac{R}{L_{sus}}\right)^2 S^2\left(\frac{\theta}{2}\right)}} & -\left(\frac{W}{2}\right)\frac{\frac{R}{L_{sus}}(1-S\theta)}{\sqrt{1-4\left(\frac{R}{L_{sus}}\right)^2 S^2\left(\frac{\theta}{2}\right)}} & \left(\frac{W}{2}\right) \end{bmatrix}^T$$

Likewise the force vector, $\vec{F_2}'$, by symmetry can be expressed by:

$$\vec{F_2}' = \begin{bmatrix} -F_{1_x}' & -F_{1_y}' & F_{1_z}' \end{bmatrix}^T$$

To sum the moments about the centerline, C:

$$\sum M_C = PT1' \times \vec{F_1}' + PT2' \times \vec{F_2}' \tag{B.6}$$

The moment of force is calculated around the z-axis by taking the cross product of the equation above. The following equation simplifies the cross product:

$$\sum M_z = -2RS\theta F_{1_x} + 2RC\theta F_{1_y} \tag{B.7}$$

Simplifying the sum of moment equation and substituting terms yields the following equation for mass moment of inertia:

$$I\ddot{\theta} = -\frac{WR^2}{L_{sus}} \frac{S\theta}{\sqrt{1 - 4\left(\frac{R}{L_{sus}}\right)^2 S^2\left(\frac{\theta}{2}\right)}} \tag{B.8}$$

If it is assumed that $\frac{\theta}{2}$ and $\frac{R}{L_{sus}}$ are much less than 1, then $\sqrt{1 - 4\left(\frac{R}{L_{sus}}\right)^2 S^2\left(\frac{\theta}{2}\right)} \approx 1$ and:

$$I\ddot{\theta} = -\frac{WR^2}{L_{sus}} S\theta \tag{B.9}$$

From a Taylor series expansion of $S\theta$ about $\theta_0 = 0$: $S(\theta) \approx \theta - \frac{1}{6}\theta^3 + O(\theta^5)$. Substituting this into the inertia equation and dividing through by I gives the following equation:

$$\ddot{\theta} + \frac{WR^2}{IL_{sus}}\theta - \frac{1}{6}\frac{WR^2}{IL_{sus}}\theta^3 = 0 \tag{B.10}$$

By defining $\varepsilon = \frac{1}{6}\frac{WR^2}{IL_{sus}}$ and $a = \frac{WR^2}{IL_{sus}}$ results in the following equation:

$$\ddot{\theta} + a\theta - \varepsilon\theta^3 = 0 \tag{B.11}$$

Making a change of variables $\tau = \omega t$ to the above equation gives:

$$\omega^2\theta'' + a\theta - \varepsilon\theta^3 = 0 \tag{B.12}$$

Using the expansions for θ and ω gives the following expressions:

$$\theta = \theta_0 + \varepsilon\theta_1 + O(\varepsilon^2)$$
$$\omega = \omega_0 + \varepsilon\omega_1 + O(\varepsilon^2) \tag{B.13}$$

Substituting this into the original equation and truncating the $O(\varepsilon^2)$ terms:

$$\omega_0{}^2\theta_0{}' + 2\varepsilon\omega_0\omega_1\theta_0{}'' + \varepsilon\omega_0{}^2\theta_1{}'' + a\theta_0 + \varepsilon a\theta_1 - \varepsilon\theta_0{}^3 + O(\varepsilon^2) \tag{B.14}$$

The $O(\varepsilon^2)$ can be truncated by using a technique called regular perturbation theory. This theory states that all the important information is captured by the first few terms - ideally, the first two - and that the higher-order terms represent only tiny corrections [35]. By collecting the powers of ε from the above equation, solving the system of differential equations using the initial conditions yield the following total solutions:

$$\theta(t) = bcos(\omega t) + \varepsilon\tfrac{b^3}{32a}(cos(\omega t) - cos(3\omega t))$$
$$\omega = \sqrt{a} - \tfrac{3b^2}{8\sqrt{a}}\varepsilon \tag{B.15}$$

During the process for solving for the system of differential equations some secular (terms growing without bound as $t\to\infty$), $C(\tau)$ terms must disappear or the solution will have infinite solutions. For this method to work with the experiment it must only contain a periodic solution. The above total solution equations are finally inserted into a MATLAB script with the Duffing Equation to solve for the mass moment of inertia. The following sections will give more detail as to how this is measured.

B.2 Inertia Calibration Experiment Setup

The ATOM lab is a powerful digital tracking solution that provides unrivaled data accuracy for 3D applications. It offers accurate, high speed, interference-free, and low latency real-time tracking for engineering-related studies. The ATOM lab has a 50 ft x 30 ft x 12 ft unobstructed volume and achieves accurate motion capture using 33 Vicon T40 series IR cameras [37]. The Vicon motion capture system is a state-of-the-art infrared marker-tracking system that offers millimeter resolution of 3D spatial displacements.

The system implemented consists of ten cameras outfitted with IR optical filters and an array of IR LEDs, and a set of reflective dots. The dots reflect the IR radiation emitted by the LEDs. All other light is filtered so that the system only recognizes the dots [38].

Reflectors were placed at specific locations on the payload. The payload was then suspended from the ATOM Lab ceiling via long, thin parachute chords. The IR LEDs of the cameras were set to the proper strobe and intensity setting for the reflectors and also to eliminate noise. The strobe setting controls the flashing of the infrared leds and the intensity setting controls the power emitted. A model of the payload was created on the Vicon camera software before testing. In order to make the Poincare-Lindstedt method work it was necessary to ensure that the length of the strings were much larger than the radius of the string attach points. The objective of suspending the payload was to then rotate the payload at an angle below 45° from the horizontal axis and then let it freely oscillate until it was back to the equilibrium

position. This back and forth oscillation was captured by the Vicon system with the x, y and z position of the reflectors recorded with respect to time. This data established a natural frequency of oscillation that allowed the user to measure the period of the oscillations. The period of these oscillations was the empirical data needed to insert into a MATLAB script, with equation 3.42, in order to calculate the necessary parameters to determine the mass moment of inertia of the payload. The Figure B.2 displays the ATOM lab setup with an example payload.

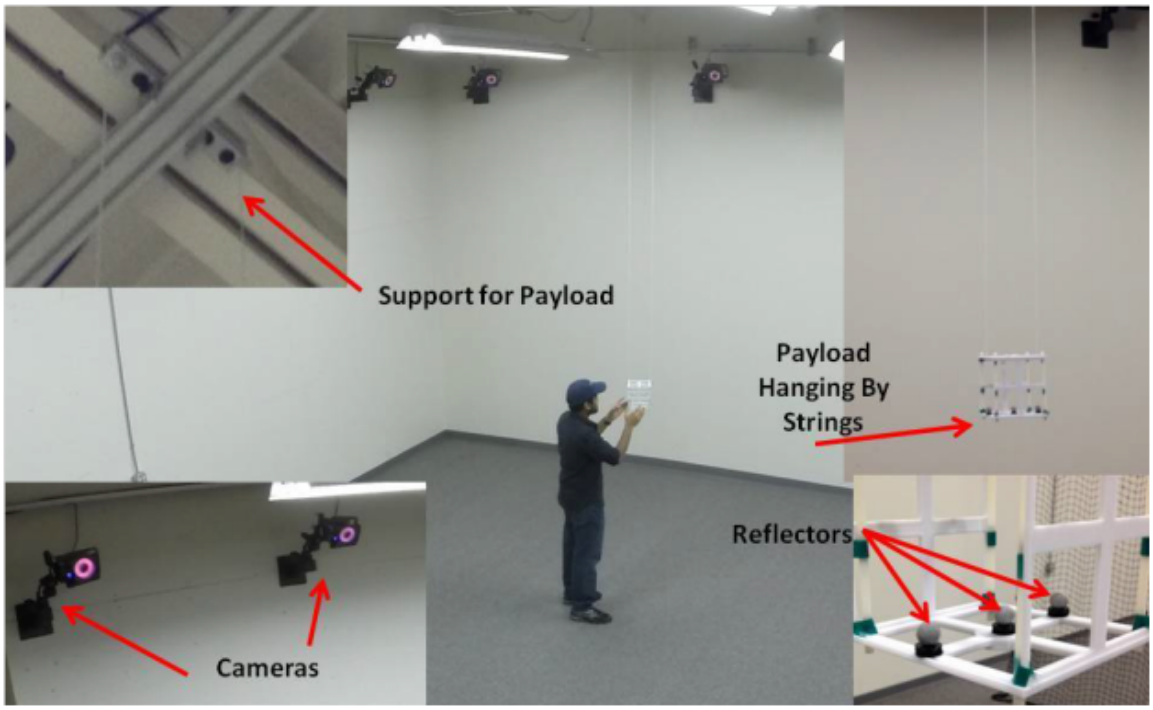

Figure B.2: ATOM Lab Setup

B.3 Baseline Inertia Calibration Experiments

In order to validate this method for the purpose of determining the mass moment of inertia of objects a series of baseline experiments were conducted with

simple payloads. The motivation for performing these experiments was to quantify possible systematic and bias errors with the Vicon camera system. The theoretical mass moment of inertia was calculated with a level of uncertainty and then compared to the experimental value.

B.3.1 Teflon Rod Data

A baseline test was performed with a Teflon rod. Ten tests were conducted with all parameters in an ideal setup. Five tests were then conducted and given a horizontal force by manual input before the periodic oscillations. Finally five tests were conducted with the length of the strings offset for the two connection points. It is assumed that the distribution of mass is uniform. These test conditions are discussed below.

Figure B.3, shows the ideal test setup for the inertia calibration experiment. The payload would hang from the top of the ATOM lab with long strings and an initial offset angle would be given to begin the test. The length of the strings would need to be a close as possible and no additional disturbances should be given.

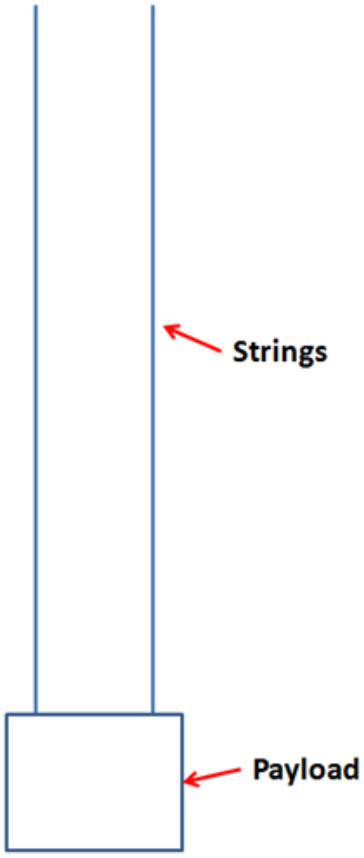

Figure B.3: Ideal Test Setup

Figure B.4, shows the diagram for the swing tests. In these tests along with making sure the length of the strings are the same and the offset angle were set a slight swinging motion was imputed manually to observe the effects on mass moment of inertia calculations.

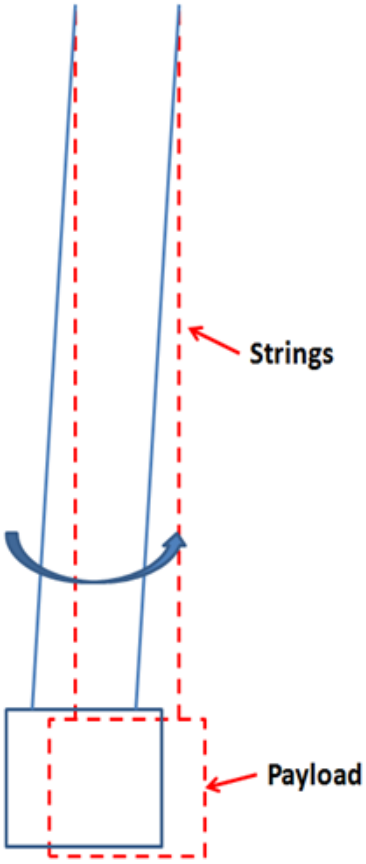

Figure B.4: ″Swing″ Tests

Figure B.5, represents a scenario where the length of the strings suspending the payload are not the same. The length was varied to give an horizontal offset angle of approximately 10°. All other uncertainties were limited as much as possible.

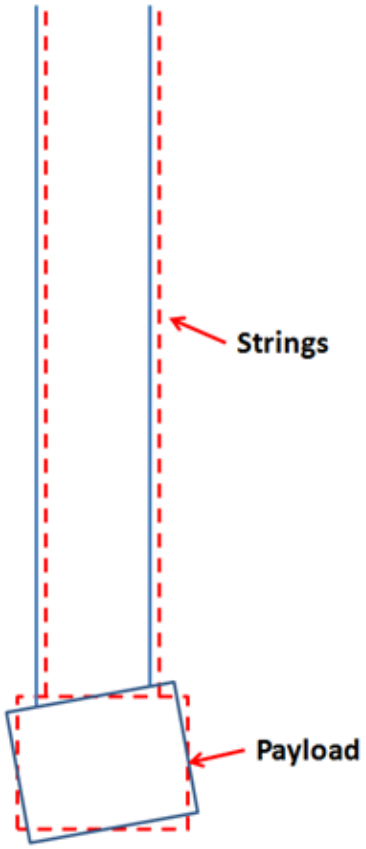

Figure B.5: Offset Tests

Figure B.6, shows the diagram of the Teflon rod. The equation for calculating the moment of inertia of the for a flat plate rotating about a perpendicular axis [32] is given by,

$$I = \frac{1}{12} M L^2, \tag{B.16}$$

where M is the total mass of the wood block, and L is the length. Two hooks were attached approximately 5.5 $''$ from the centerline axis. The mass moment of inertia for a particle is expressed by [32],

$$I = MR^2 \tag{B.17}$$

where R is the radius from the centerline axis. The necessary measurements for the mass moment of inertia calculation can be seen in Table B.1. With these measurements the theoretical mass moment of inertia was calculated to be 21.72 $lb{\cdot}in^2$.

Table B.1: Inertia Calibration Parameter Measurements

Teflon Mass	1.955 lbf ± 0.002 lbf
L	11.5 ″ ± 0.031 ″
Hook Mass	0.002 lbf ± 0.002 lbf
Hook Radius	5.5 ″ ± 0.0625 ″

The uncertainty in the theoretical calculation for the Teflon rod can be found with

$$U_{I,Teflon} = \sqrt{(\frac{1}{6}M{\cdot}L)^2U_L^2 + (\frac{1}{6}M{\cdot}L)^2U_M^2}$$

$$U_{I,hooks} = \sqrt{(MR)^2(U_R^2) + (R^2)^2U_M^2}$$

The total uncertainty of the theoretical Teflon rod was calculated to be 0.121 $lb{\cdot}in^2$.

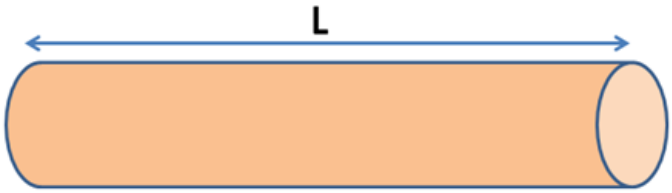

Figure B.6: Teflon Rod Diagram

Figure B.7 shows the experimental setup of the Teflon Rod baseline inertia calibration experiment in the ATOM laboratory. A series of tests were conducted and the results were documented in Table B.2.

Figure B.7: Experimental Setup with Teflon

Table B.2: Teflon Rod Experimental Results

	Average ($lb{\cdot}in^2$)	Standard Deviation ($lb{\cdot}in^2$)
10 Ideal Tests	21.894	0.214525
5 Swing Tests	22.033	0.254833
5 Offset Tests	21.6795	0.340063

Figure B.8 shows the periodic signals of the experimental and theoretical models. The first four periods of the data is analyzed and post processed in order to calculate the mass moment of inertia.

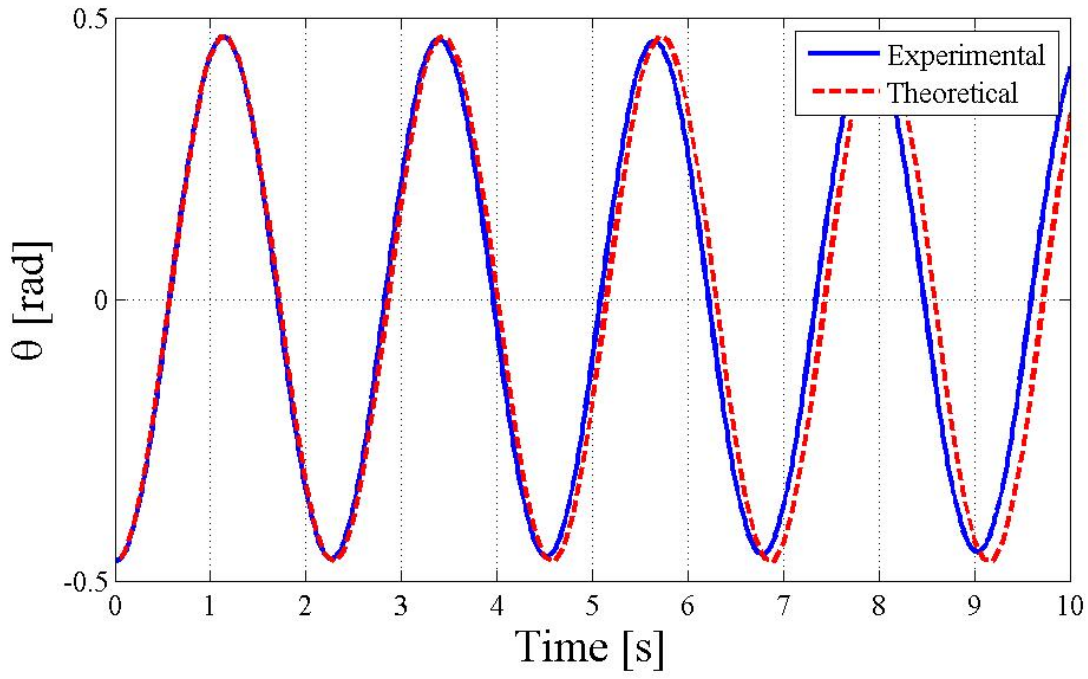

Figure B.8: Experimental and Theoretical Models

Figure B.9 shows the results of the theoretical and experimental values with uncertainty. As seen in the data below the experimental values overlap with the uncertainty within the theoretical measurement values. The error between the theoretical and average ideal experimental tests was approximately 0.8%. This is the level of expected error based on the assumptions made in the Poincaré-Lindstedt method.

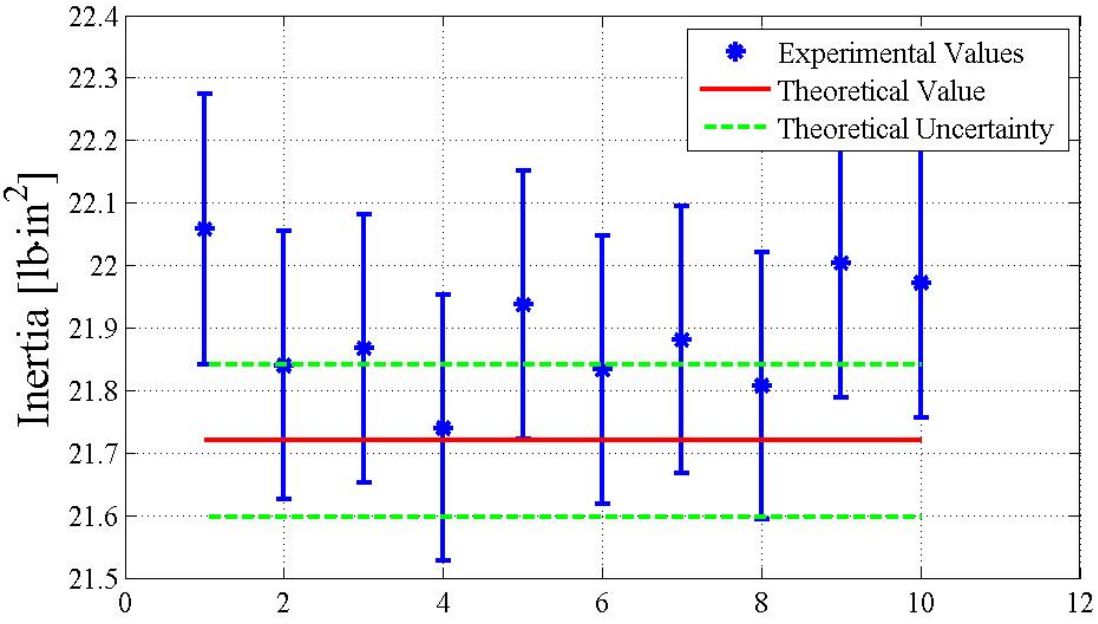

Figure B.9: Teflon Rod Baseline Experimental Data

APPENDIX C

CALIBRATION METHODS

C.1 Test Stand Calibration Techniques

The team has researched several methods in order to conduct test stand calibration and identify system uncertainties. These methods were compiled in the table below and organized based on physical contact and non-contact processes. Both types of methods involve calculating the kinetic energy transferred into the system and comparing to sensor data.

Table C.1: Test Stand Calibration Methods

Test Stand Calibration		
Type	Method	Description
Contact	Impact Pendulum (Elastic Collision)	Apply force by striking the payload with a spherical mass suspended by a string
	Impact Hammer (Elastic Collision)	Apply force by striking the payload with a rectangular mass suspended by several strings
	BB Pellet Impact (Inelastic Collision)	Apply force by striking thruster holder with pellets
Non Contact	Microbalance	Apply impulse via magnetic pulse to permanent magnet on thruster holder
	Angular Encoder/Vicon System	Place markers on payload and use cameras to extract angular velocity from position data

C.1.1 Contact Methods

Figure C.1 shows the two elastic collision methods for contact test stand calibration. These two methods are the impact pendulum and impact hammer. The impact pendulum scheme consists of hanging a sphere with some mass from a integrated support on the test stand via a thin, rigid string. In order to initiate the contact the sphere would be pulled back and released to strike the thruster holder on the levitating payload. The impact hammer works in a similar fashion, however, it uses four strings to suspend a rectangular object at an appropriate height to strike the thruster holder. While the impact pendulum is simple to setup and use the impact hammer has several advantages. Most important is the stability and consistency of the impact. The four strings would mitigate the off axial movements during operation. A high speed camera will be utilized for all calibration testing.

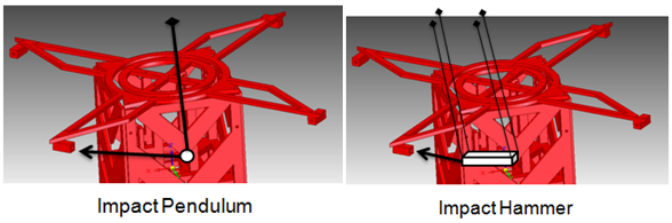

Figure C.1: Elastic Collision Methods: Impact Pendulum (left) and Impact Hammer (right)

The final contact method is the BB pellet impact method. This method would be an inelastic collision process involving a sticky tack substance and a BB barrel. The tack would be applied on top of the thruster holder and a BB pellet would be

accelerated from a barrel striking the tack. Upon impact the pellet would stick to the tack and the kinetic energy and mass of the pellet would be transferred to the levitating payload. Figure C.2 shows a diagram of this method.

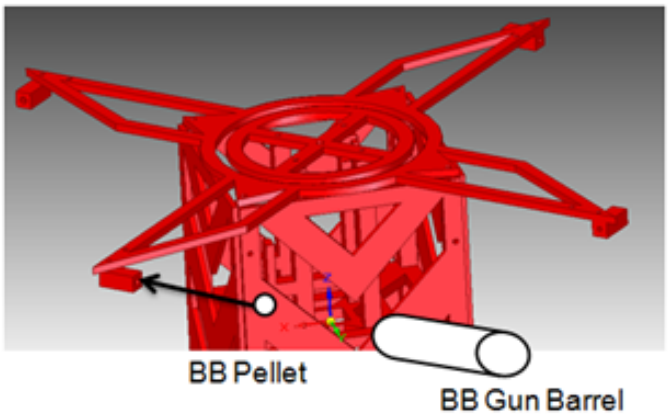

Figure C.2: Inelastic Collision Method

The physical concept for these methods would be calculating the kinetic energy of the striking mass and using the kinetic energy of rolling equation solve for the representative angular acceleration. The expression for the kinetic energy of rolling,

$$\omega = \left(\frac{2\Delta KE}{I}\right)^{1/2}, \tag{C.1}$$

where ω is the angular velocity, ΔKE is the change in kinetic energy, and I is the mass moment of inertia of the levitating system. Using this equation, the theoretical value for ω can be calculated and then compared to the gyroscopic data from the sensor package to determine the system uncertainty.

C.1.2 Non-Contact Methods

The first non-contact method described is the microbalance method. This calibration technique consists of applying a magnetic pulse to a permanent magnet on the levitating payload to force a rotational movement. The force can be calculated by conducting a separate test to use a mass measurement scale to find the force for varying electromagnetic voltages. Figure C.3 shows a diagram of this method.

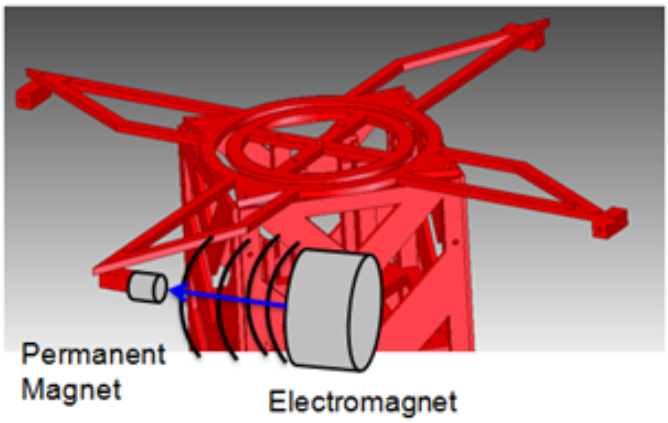

Figure C.3: Non Contact Method

Another method for computing the electro-static force is using the theoretical equations seen in the expression below,

$$F_q = \frac{1}{2}\varepsilon_0 \varepsilon_r E_e^2, \tag{C.2}$$

where ε_0 is the permittivity in a vacuum, ε_r is the relative permittivity which is approximately 1 for air or vacuum and E_e is the electric field on the surface of the electrode. While this method may be simple to reproduce calculating the electrostatic

force may be complicated and due to the non-contact nature of the method it may produce more variability in the results. The final method under consideration is the Vicon camera/angular encoder verification process. In this scheme, Vicon cameras or angular encoder would be used to collect position data of markers on the payload. The derivative of this data would be used to calculate the angular velocity of the levitating platform. This information can be compared to the information gathered by the sensor package to determine the level of uncertainty in the system. Figure C.4 shows a diagram of the process.

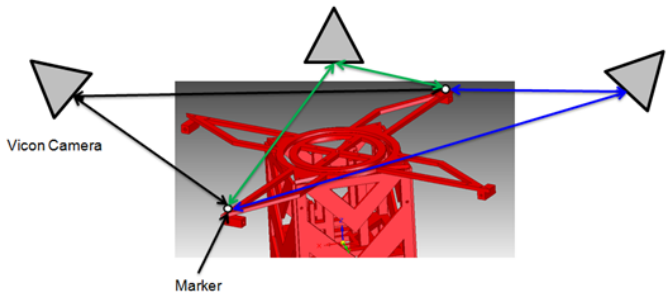

Figure C.4: Vicon Camera Method

APPENDIX D

VACUUM CHAMBER SETUP

The ultimate goal of the project is to evaluate performance characteristics of micro-thrusters in a reduced pressure environment. The UAH Propulsion Research Center (PRC) enabled such experimentation through the operation of the Large Vacuum Chamber Test Facility (LVCTF). In order to perform these tests the atmospheric test stand needed to be translated to the vacuum chamber test platform and a heat exchanger was designed to dissipate heat from the electromagnet in order to maintain nominal operation. The following sections will provide details into this phase of the vacuum chamber work.

D.1 Test Stand

The vacuum chamber test stand was designed to be fitted on the existing chamber test platform. One of the design considerations for the test stand was the vibrations induced from the vacuum chamber pumps. In operation the pumps transfer energy to the test stand through the structure . In order to reduce the vibrations to the MLC system on the test stand, vibration dampening sandwich mounts were

fabricated such as those seen in Figure D.1. After these necessary modifications were made the MLC components and heat exchanger components were added.

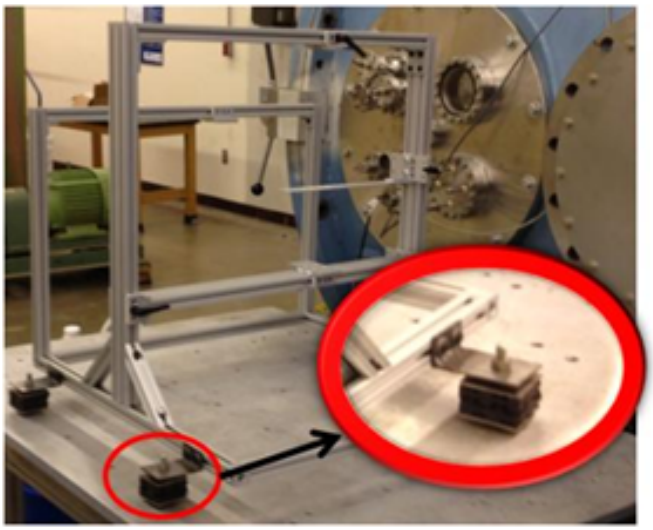

Figure D.1: Test Stand on Vacuum Chamber Cart

Due to the vibrations on the test stand the team performed part 1 of ″Shaker Trials″ to adjust the gains to MLC. During this test the payload, seen in Figure D.2, was held in a steady hover as the gains for the MLC were configured. The payload was in steady hover through the first 20 minutes of pump operation.

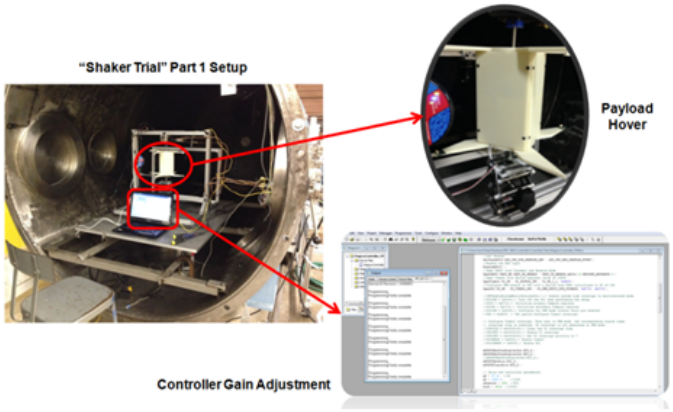

Figure D.2: Shaker Trial Setup

The shaker trials continued to find the point of minimum test stand vibrations within the vacuum chamber. For part I of the shaker trials the test stand was simply positioned at an optimal location and the gains were adjusted on the MLC. Once these baseline adjustments were made the test stand was enclosed in the Vacuum Chamber to simulate the operational environment with vibrations from the roughing pump. It was observed that the vibrations were magnified when the door was closed as opposed to remaining open. In part II of the shaker trials the vibrations were treated as acoustic pressure waves with the challenge to find the frequency nodes that would provide us a location of minimal vibrations (Figure D.3). In order to reduce the transfer of energy from the roughing pump a physical break was made in the guide rails that the supports of the pump and chamber rest on (Figure D.4). The test stand was pushed further back and the gains on the MLC were adjusted (Figure D.5). Little modifications were made to the configurations thus representing optimal settings for the controller.

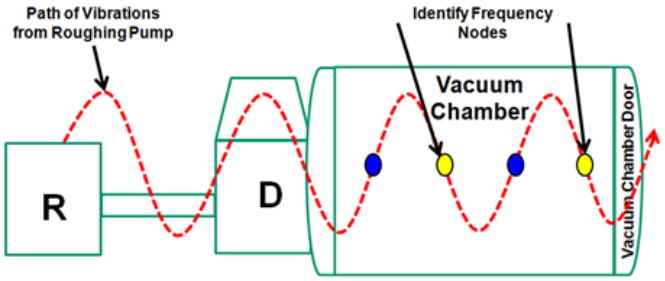

Figure D.3: Vacuum Chamber Vibrations

Figure D.4: Cutting Guide Rails

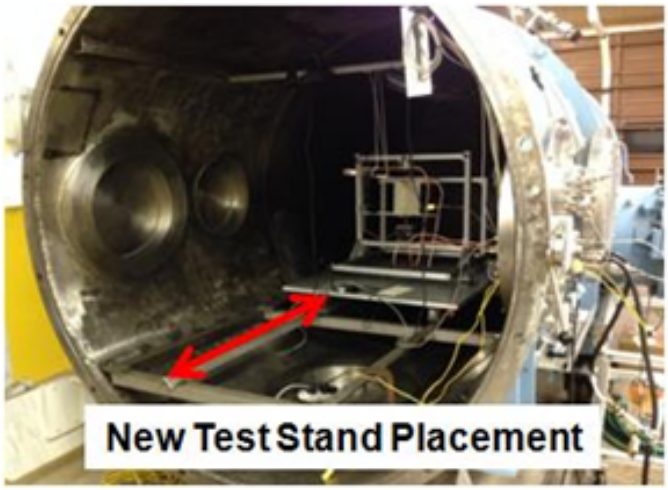

Figure D.5: Test Stand Placed at Vibration Node

D.2 Facility Information

The PRC Large Vacuum Chamber Test Facility (LVCTF) consists of a 4 meter long and 1.8 meter diameter cylindrical stainless clad chamber that can maintain base pressure down to 10^{-6} Torr. The testing capabilities for this facility include simulating high altitude atmospheric conditions for UAV vehicles and low orbit space conditions for small scale air-breathing and classical chemical and electric propulsion applications [44]. Figure D.6 shows the vacuum chamber located at the Johnson Research Center on the campus of UAH.

Figure D.6: LVCTF

Figure D.7 shows the interior of the vacuum chamber and the test platform used for experimentation.

Figure D.7: LVCTF Test Platform

D.3 Vacuum Chamber Payload

In an effort to improve high voltage safety, decrease uncertainty by increasing the precision of component mounting and decrease manufacturing time the research team elected to use available 3D printing capabilities located on campus to rapid prototype the next payload. SPITfire would be built in order to demonstrate UAHs capability of 3D printing components using thermoplastic materials. An Onboard Payload Stabilization Device (OPSD) would be installed as a ballasting measure for stabilizing the payload and reducing lateral rotations. Figure D.8 shows a rendering of the SPITfire concept. It will contain an internal skeleton that is protected by outer panels and 3D printed thruster mounts for improved placement accuracy. The team reviewed several options for material choices and ABS plastic was chosen for fabrication due to its relatively low cost and personnel experience.

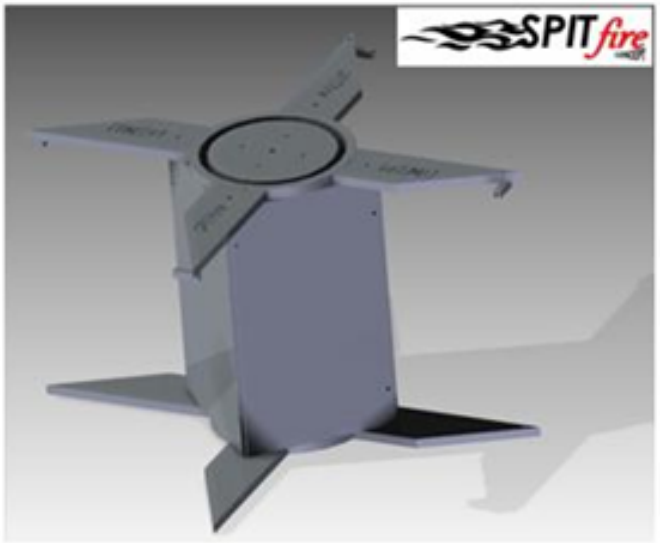

Figure D.8: SPITfire Concept

D.3.1 SPITfire Lite

The SPITfire Concept was measured to have a total structural mass of 1.23 lbm and a total material volume of 33.3 in^3. The rapid prototype process for all the pieces of the model took approximately 90 hours. The new refined 3D model, called SPITfire Lite, had a total structural mass of 0.78 lbm and a total material volume of 21.07 in^3. The redesigned payload and new knowledge of the printing process helped reduce the print time to 24 hours. This represents a total reduction of 37% for the total mass, 37% for the total material volume and 73% for the print time. Figure D.9 shows the new payload that will be used in the vacuum chamber testing.

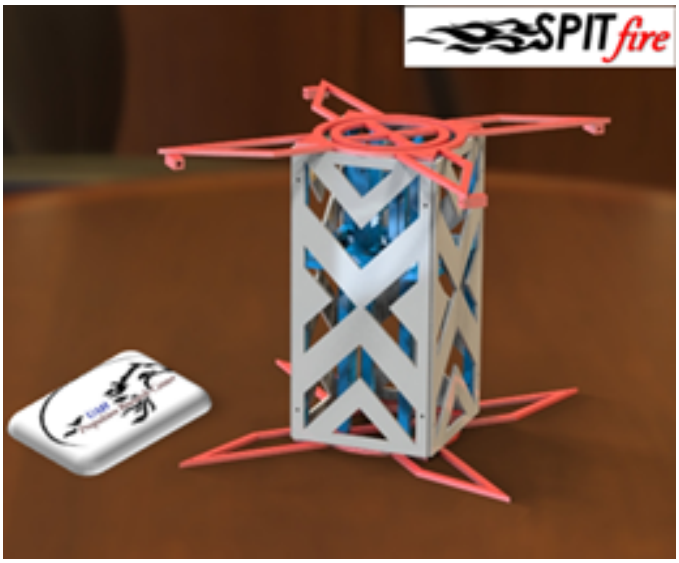

Figure D.9: SPITfire Lite

Final modifications were made to SPITfire Lite, the levitating payload. The electrical components were added to the payload and a dump circuit for the capacitors was included. This was a safety measure that would ensure that the testing personnel

would not have to make contact with the fully charged capacitors during the discharge sequence. This part of the circuit was added to the payload switchboard. Figure D.10 below shows the modified SPITfire payload.

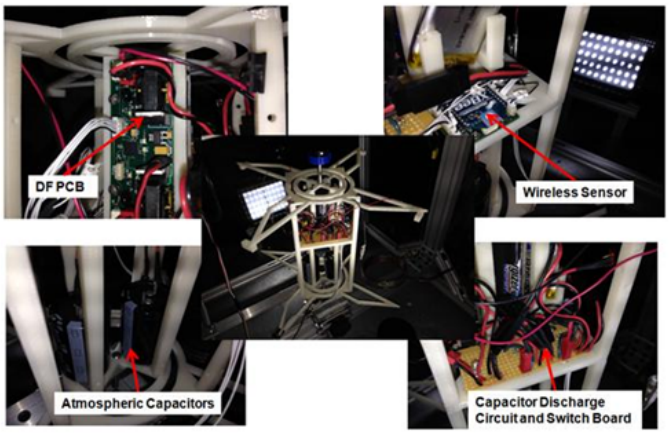

Figure D.10: SPITfire Lite Modifications

D.3.2 Vacuum Chamber Payload Circuit

One of the action items for starting vacuum chamber testing was to create a vacuum chamber payload with DSSP recommended capacitors for experimentation. A particular wet tantalum capacitor was chosen as a component to the new vacuum chamber payload due to its hermetic seal and operating temperature. The capacitor has an operating voltage of 100 V and 400 μF. This meant the creation of a capacitor bank with capacitors in series and parallel to reach the desired 1000 μF. With 7 capacitor sets of 3, the final capacitance was 933.33 μF. This will result in slight difference in firing capacitance . Figure D.11 shows the final circuit diagram.

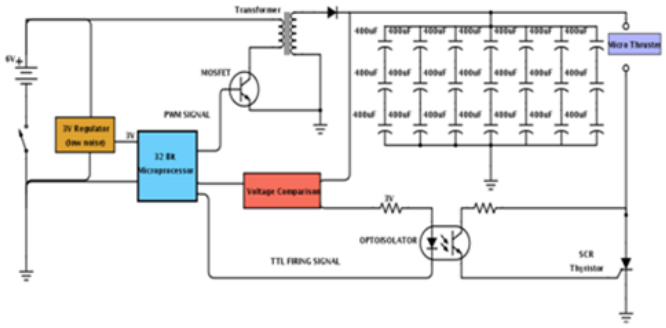

Figure D.11: Vacuum Chamber Circuit

Hermetically sealed capacitors were purchased to work in a vacuum chamber environment. These capacitors were placed on a breadboard and soldered based on a schematic presented earlier. These capacitors will handle up to 300 V and contain 933 μF of capacitance. These capacitors were recommended for use by DSSP. The capacitors can be seen in Figure D.12. In addition to mounting these components it was suggested that potting material be purchased and applied to the components to prevent arcing from the micro-thruster firing. A NASA approved low outgassing compound was suggested for evaluation and purchase. The potting epoxy would be a one component epoxy and would require less than 30 minutes for full cure on the capacitor bank.

Figure D.12: Hermetically Sealed Capacitors

D.3.3 Heat Exchanger

During the atmospheric testing phase elevated temperatures were observed from the electromagnet. Although the temperature of the electromagnet never exceeded the ideal operating temperature range, a decrease in magnet performance was observed at elevated electromagnet temperatures. Under high altitude conditions induced in a vacuum chamber there is a decrease in convective heat transfer. The decrease in heat transfer would cause an increase in electromagnet temperature, and a further decrease in electromagnet performance was expected. For these reasons, a heat exchanger system was designed, and implemented, which relied on conduction to lower the temperature of the electromagnet.

The design consisted of a copper coil that is wound around the electromagnet with cooled water passing through it. The water was cooled by pumping it through a series of condensers as shown in Figure D.13, which are surrounded by ice water

when a test is being performed. The condensers were placed outside of the vacuum chamber, and the water lines were routed through the chamber wall as shown in Figure D.14. A bypass valve was placed between the inlet and outlet water lines. The valve was adjusted in order to keep the current draw of the pump to a minimum.

Figure D.13: Heat Exchanger Condensers

Figure D.14: Heat Exchanger Connection

A series of K-type thermocouples were placed in the water lines in order to get temperatures at critical points in the system. The temperatures were recorded throughout a test and used to get thermodynamic properties. The heat transfer obtained through the use of the heat exchanger was determined using the obtained properties and equation D.1 [29]. The theoretical heat transfer was determined using equation D.2 [30]. By comparing these results the efficiency of the heat exchanger can be determined.

$$\dot{Q} = \dot{m} \cdot (h_2 - h_1) \tag{D.1}$$

$$\dot{Q} = q_{magnet} - q_{radiation} \tag{D.2}$$

In Equation 1 $\dot{Q}$ is the heat transfer of the heat exchanger, $\dot{m}$ is the mass flow rate, and h is the enthalpy corresponding to the water before and after it passes through the copper coil. The mass flow rate was determined by weighing the amount of water that passed through the coil over a pre-determined amount of time. In equation D.2, q_{magnet} is the heat production from the electromagnet and is determined using equation D.3, [30] while $q_{radiation}$ is the heat transfer due to radiation and is found through equation D.4 [30].

$$q_{magnet} = I^2 \cdot R \tag{D.3}$$

$$q_{radiation} = \varepsilon\sigma \cdot (T_m - T_{sur}) \tag{D.4}$$

In equation D.3, I is the current draw from the electromagnet, and R is the resistance across the electromagnet. From equation D.4, ε is the emissivity of the electromagnets surface, σ is the Stefan-Boltzmann constant, T_m is the temperature of the magnet, and T_{sur} is the temperature of the surroundings.

D.3.4 LabView and DAQ

Final wiring for the DAQ system and LabView program was completed in order to collect data from vacuum chamber experimentation. During the experimen-

tation, four thermocouple measurements would be processed as well as five pressure measurements. The four thermocouples would be distributed in the following manner: one on electromagnet surface, one in ambient, one in line with the heat exchanger inlet and one in line with the heat exchanger outlet. The four pressure readings would come from the vacuum chamber pumps as well as the chamber itself. Two vacuum chamber pressure measurements would be taken. The chamber pressure measurements will be redundant as both will be taken with different pressure sensors. The LabView program will be configured to convert the chamber pressure into altitude. The figures D.15 and D.16 show the DAQ wiring and front panel view of the LabView program, respectively.

Figure D.15: DAQ Wiring

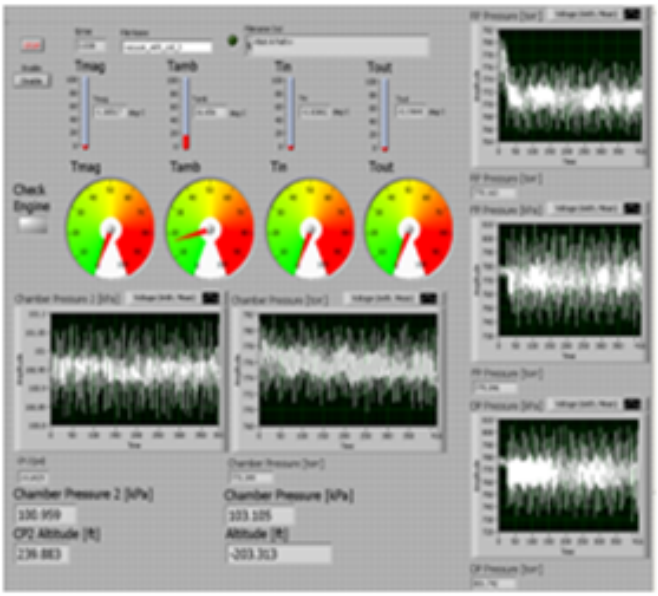

Figure D.16: LabView Front Panel

APPENDIX E

PRESSURE IGNITION EXPERIMENTATION

To perform additional testing on the micro-thrusters the UAH team conducted micro-thruster pressure ignition limit testing in order to determine the pressure range of proper function. The testing took place in the Propulsion Research Center (PRC) Plasma and Electrodynamics Research Laboratory from January to March 2015. The PRC has a small vacuum chamber, seen in Figure E.1, which has the ability to sustain vacuum pressures as low as 1×10^{-6} Torr. This will allow the test team to investigate the range of pressures that provides ideal conditions for proper functioning of the new DSSP micro-thruster. The micro-thruster will be placed inside the vacuum chamber on a static fire test stand with electrical connections to ignite the propellant. A camera will be placed outside the chamber viewing port to record the firings. An experiment schematic can be seen in Figure E.2.

E.1 Testing Process/Facility Information

The small vacuum chamber is located at the Johnson Research Center Plasma and Electrodynamics Laboratory. It can reach 1×10^{-3} Torr with the mechanical pump and uses a turbo-molecular pump to drive the vacuum down to pressures as

low as 1×10^{-6} Torr. During the preparation phase for pressure ignition testing, an additional vent valve was placed on the chamber to better control pressure throttling through the various ranges to be tested. Maintenance was performed on the mechanical pump to prepare for a series of experiments. Once maintenance was completed the vacuum chamber was pumped down to inspect the chamber for leaks. Once leak checking was completed a standard operating procedure was reviewed for this testing and was approved after necessary modifications were made.

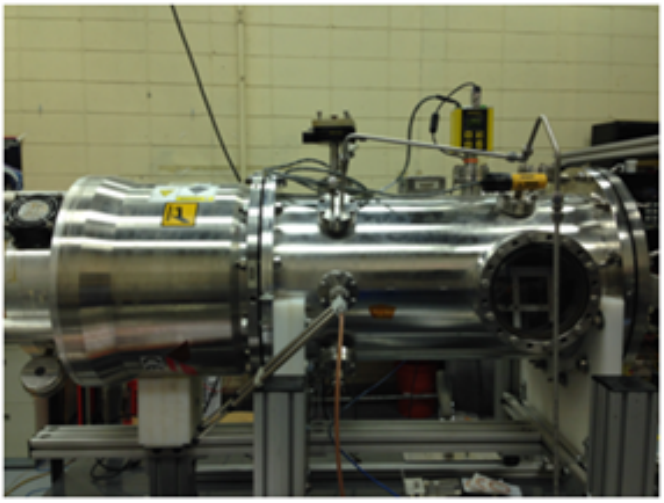

Figure E.1: Small Vacuum Chamber

As seen in Figure E.2, the static fire test stand was placed on the inside of the chamber while the electronics to fire the thruster and high speed camera were placed on the outside. For the static fire test stand a nonconductive plastic material was utilized and a circuit box consisting of the necessary firing electronics was constructed.

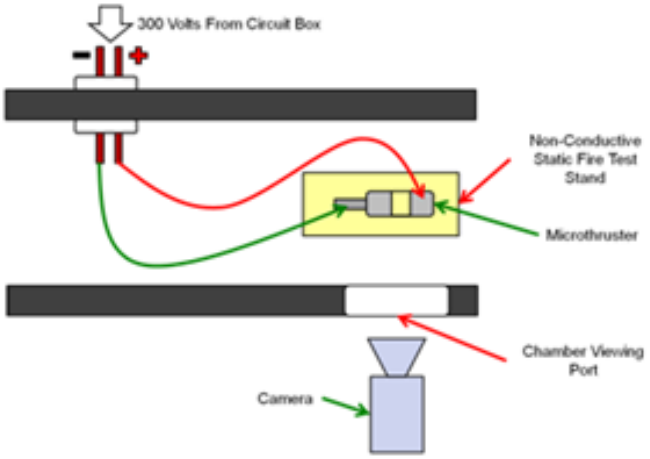

Figure E.2: Pressure Ignition Experiment Schematic

Originally the static fire test stand used an alligator clip to secure the thruster. After a series of test showed micro-thruster anomalies; refinements were made to the pressure ignition test setup and process. The first change was to the thruster static fire test stand. To eliminate the concern of structural damage to the outer electrode of the micro-thruster the clamp setup was replaced with a thruster holder, seen in Figure E.3. The micro-thruster would be inserted through a hole in the top of the arm and secure with electrical attachments on either end. This thruster holder would reduce pressure on the outer electrode while encasing the majority of the micro-thruster to prevent arcing across the surface.

Figure E.3: Thruster Holder

In order to improve visual data a halogen light was connected to the interior of the vacuum chamber (Figure E.5) and a high speed camera replaced the current GoPRO camera as shown in Figure E.4. The GoPRO was limited to 120 frames per second. The goal is to take images at a rate of 3000 frames per second in order to increase distinction between light and flame the flame profile.

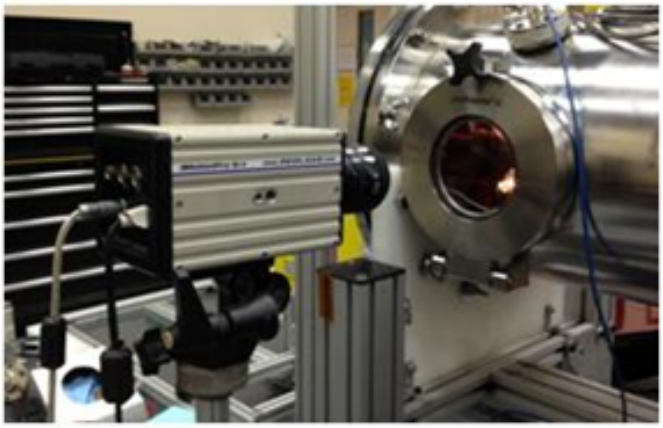

Figure E.4: Redlake High Speed Camera

Figure E.5: Halogen Lamp

E.2 Circuit Box

A circuit box located external to the vacuum chamber will supply the voltage needed to fire the micro-thruster. The circuit box will be connected to a high voltage connection on the chamber pass through port. The circuit box can be seen in Figure E.6 below.

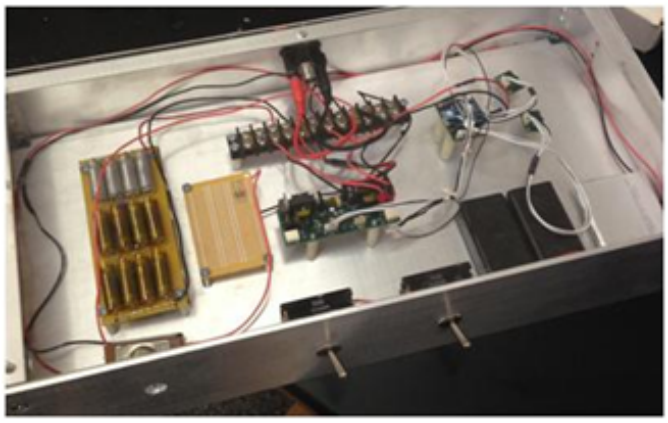

Figure E.6: Pressure Ignition Circuit Box

The components from the SPITfire payload were transferred to a project box and wired to include a dump circuit for the capacitor discharge sequence to improve high voltage safety. This will aid in performing diagnostics on the electrical components. The finals diagnostics included inspecting high voltage components via multimeter for proper response to conductor inputs. The sensor package was tested to ensure proper functionality of communication system from control station. Wireless communication and switches were tested to guarantee that the control circuit would arm and fire as expected. Final subsystem checks were accomplished on January 25th. After subsystem checks were complete the final vacuum chamber SOP was approved and preparations began for testing.

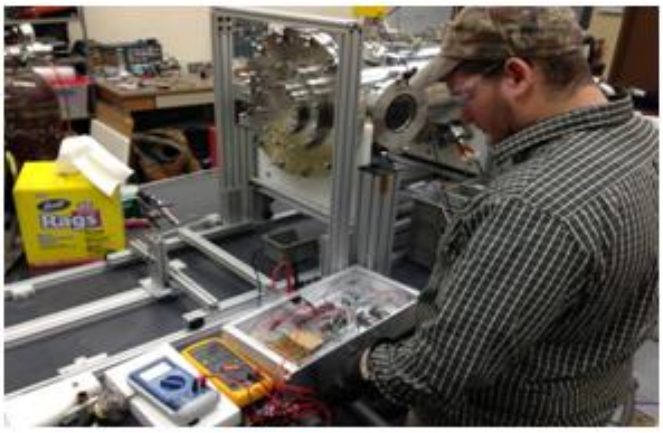

Figure E.7: Circuit Box Diagnostics

E.3 Pressure Ignition Data

Table E.1 summarizes the results for the pressure ignition experimentation that was conducted in preparation for vacuum chamber setup. It can be seen from the table that certain anomalies were observed during testing for two batches of thrusters. One batch ignited as intended and pressure ignition cutoff was not observed.

Table E.1: Pressure Ignition Test Summary

Batch	Date	Thruster	# Firings	Pressure	Notes/Results
H898	1/30/15	RR28A19	12	10^{-6} Torr – 740 Torr	Propellant Extrusion, Case Burn Through
	2/2/15	RR28A23	2	10^{-6} Torr – 740 Torr	Propellant Extrusion, Uncommanded Firing
H638	3/2/15	D77AC	15	740 Torr	Center Electrode Erosion
	3/4/15	D77AG	42	1 Torr – 740 Torr	Center Electrode Erosion, Double Firing (Reduced Pressure)
	3/18/15	D77AG	67	$5x10^{-1}$ Torr – 740 Torr	Double Firing (Reduced Pressure), Case Burn Through
	3/3/15	D77AC	0 (Extrusion Test)	$3x10^{-6}$ Torr – 740 Torr	No Propellant Extrusion Observed

During the pressure ignition experimentation test phase a high speed camera was utilized in order to capture the micro-thruster ignition and burn time from frame rate. As seen in Figure E.8, the tests were conducted at four different frame rates. At 6000 frames per second the images collected revealed a nominal burn time in the range of 0.00075 seconds to 0.00175 seconds. This information was needed to validate the thrust and impulse bit data collected using the accelerometers and gyroscope.

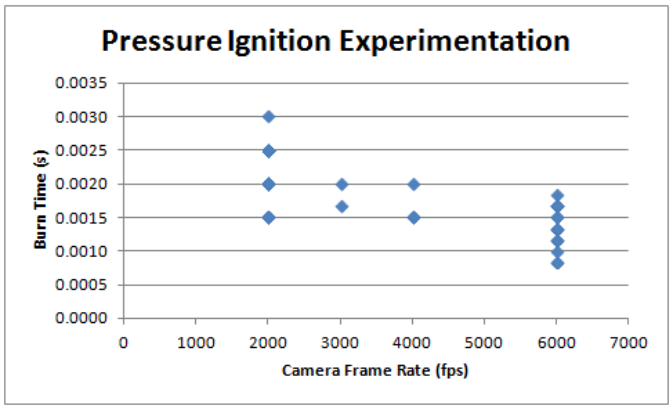

Figure E.8: Burn Time Vs. Camera Frame Rate

E.3.1 January 30, 2015 Pressure Ignition Test

The UAH team successfully completed two vacuum micro-thruster pressure ignition tests. Four frames were extracted from the high definition video taken during the test on January 30, 2015 as shown in Figure E.9. The micro-thruster being tested was one from the latest batch received by UAH. The minimum starting pressure of the vacuum chamber was 1.17×10^{-3} Torr. After two firings the micro-thruster failed to ignite despite the fact that 300 V was being supplied from the circuit box. Later

diagnostics of the circuit confirmed that the electronics were operating nominally. The micro-thruster was exposed to a low humidity environment prior to experimentation.

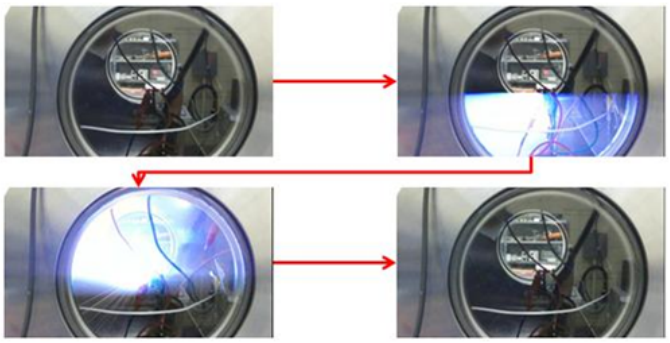

Figure E.9: RR28A19 Firing

Certain anomalies were observed through the duration of the January 30th test. Immediately following the 2nd firing of the micro-thruster at minimum pressure the propellant slug was ejected from the electrode and ceased firing. The propellant was discolored when ejected from the electrode as shown in Figure E.10.

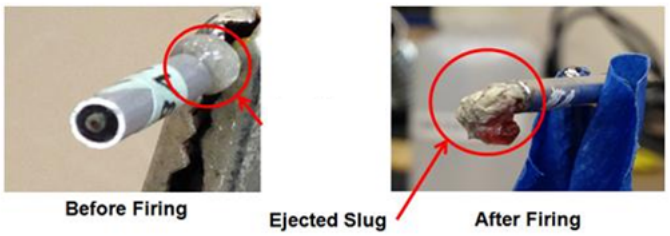

Figure E.10: RR28A19 Thruster

E.3.2 February 2, 2015 Pressure Ignition Test

The second test was conducted on February 2nd. The microthruster being tested was one from the latest batch received by UAH. The minimum starting pressure of the vacuum chamber was 1.1×10^{-3} Torr. After seven firings the microthruster failed to ignite despite the fact that 300 V was being supplied from the circuit box. Later diagnostics of the circuit confirmed that the electronics were operating nominally. Two anomalies were observed during the test. Between firings 1 and 2 the microthruster fired when uncommanded, seen in the image in the lower left as shown in Figure E.11. The other anolomy observed on firings seven through twelve is a case burn through. Several theories are being researched as to why such events occurred. It is to be noted that after successful completion of the tests an error was discovered with the pressure gauge and an incorrect reading was given. The actual pressure is expected to be lower than the pressure recorded.

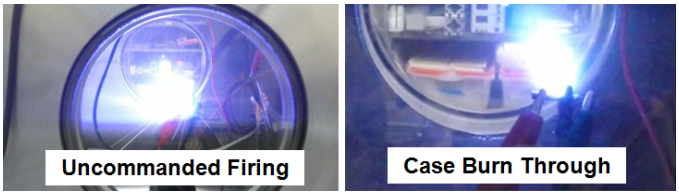

Figure E.11: RR28A23 Firing Anomalies

Some anomalies were noticed with micro-thruster RR28A23 from the February 2nd experiment. The micro-thruster tested was from batch H898. During the test, the propellant slug was ejected from the electrode before the first firing and then was ejected from the electrode to the base of the chamber when fired. This can be

seen in Figure E.12. Through the duration of the test the electrode was eroded in two different locations. The nozzle was badly damaged and the middle part of the outer electrode was eroded. This can be seen in Figure E.13 below. The nozzle damage is hypothesized to have the result of uneven propellant surface firing. This may have occurred during the propellant extrusion. The later erosion was due to electrical discharge from a void. This void was created by the ejected propellant and propellant surfaces within the thruster may have ignited causing an explosion.

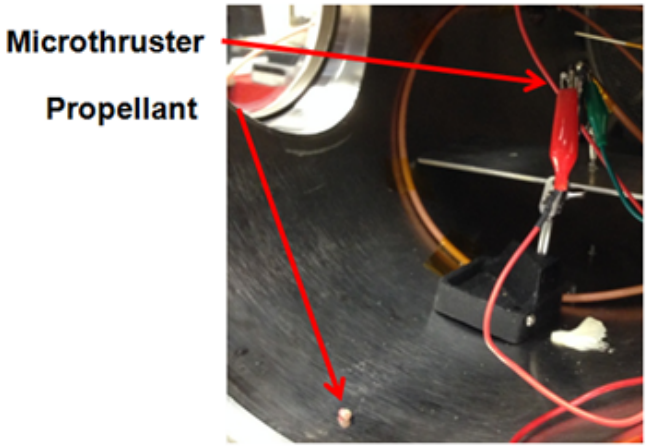

Figure E.12: RR28A23 Propellant Ejection

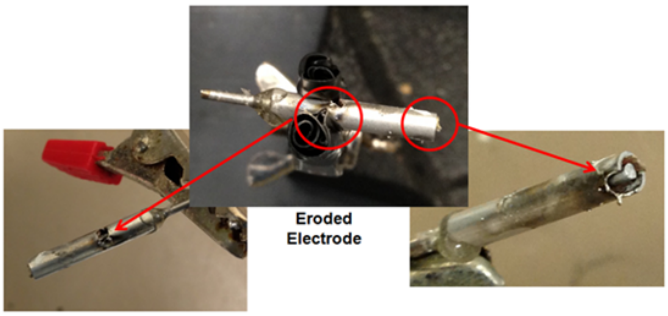

Figure E.13: RR28A23 Electrode Erosion

E.3.3 March 4, 2015 Pressure Ignition Test

The UAH team has performed an additional pressure ignition test on a micro-thruster from batch H638. This batch of micro-thrusters has proven to be the most reliable. The UAH team conducted this experiment on March 4, 2015. The test matrix was to start at atmospheric pressure and slowly reduce pressure until ignition cutoff. An example of the test matrix can be seen in the Table E.2.

Table E.2: Pressure Ignition Test Matrix

Setpoint	Firing	Pressure Range (Torr)
1	1 -22	$1x10^{2}$ - $7.5x10^{2}$
2	23 - 34	$1x10^{1}$ - $1x10^{2}$
3	35 - 46	$5x10^{0}$ - $1x10^{1}$
4	47 - 58	$1x10^{0}$ - $5x10^{0}$
5	69 - 70	$5x10^{-1}$ - $1x10^{0}$
6	70 - 81	$1x10^{-1}$ - $5x10^{-1}$
7	82 - 93	$5x10^{-2}$ - $1x10^{-1}$
8	93 - 104	$1x10^{-2}$ - $5x10^{-2}$
9	105 - 116	$5x10^{-3}$ - $1x10^{-2}$
10	117 - 128	$1x10^{-3}$ - $5x10^{-3}$
11	129 - 140	$5x10^{-4}$ - $1x10^{-3}$
12	141 - 152	$5x10^{-5}$ - $1x10^{-4}$

The test was suspended after 42 successful firings due to a malfunctioning component on the DF PCB. The damage was isolated to a blown transformer on the non-firing section of the circuit. A solution has been developed and employed

to correct the issue. Below are some comparison high speed photographs between atmospheric and reduced pressure firings.

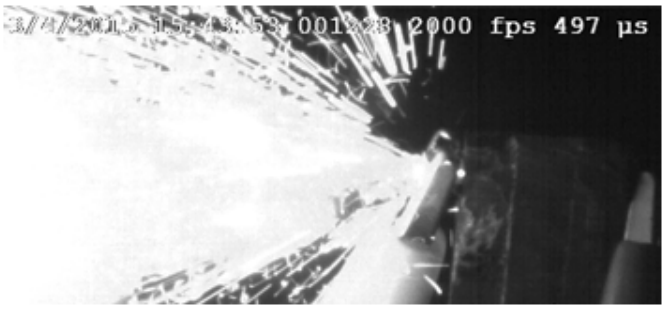

Figure E.14: Atmospheric Firing

Figure E.15: Reduced Pressure Firing

Figure E.16 below shows a picture of the modified circuit board following the repair to the circuit to fix a malfunctioning component.

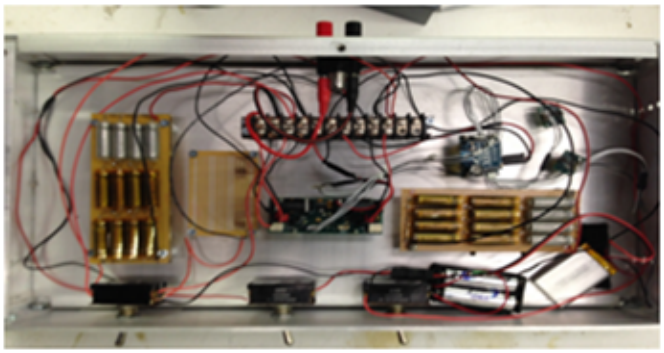

Figure E.16: Modified Circuit Board

Figure E.17 shows a post test image of the microthruster nozzle and definitive bowl shape propellant erosion is observed. The depth of the bowl is equal to the center electrode erosion.

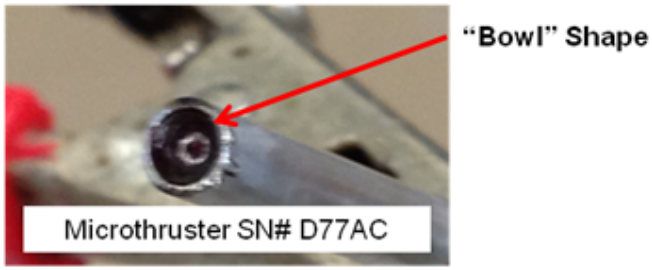

Figure E.17: Micro-Thruster D77AC (15 Pulses)

E.3.4 March 18, 2015 Pressure Ignition Test

On March 18, 2015 the UAH team returned to testing microthrusters from Batch H638. The pressure range of the test matrix included .5 Torr 750 Torr. The microthruster fired an additional 25 times before testing was completed. Figure E.18 below shows the post test from March 4th and March 18th. Visible outer and

inner electrode erosion is observed. The outer electrode was believed to have been caused by a case burn through and possible exterior arcing under a reduced pressure environment.

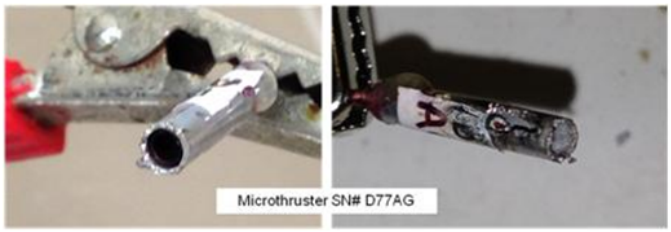

Figure E.18: Micro-Thruster D77AG (67 Pulses)

APPENDIX F

MATLAB SCRIPT

```
%Amit Patel

%Sensor Script

%5.30.15


clc

clear all


r = 0.111125; %meters

t = 0.123825; %meters


%% Import Data

A=load('C:\Users\Amit Patel\Desktop\PRC GRA\Microthruster Tests\...

7.25.14 Testing\Previous Batch\7.25.14 D77AK Test\Test79\79.txt');

%b=[1/3 1/3 1/3];

%a=[1];
```

```
%data=filtfilt(b,a,A);


%% Initialize Loop
B=A(:,4); %Separate Time Data
shift = 0;


%% Initial Loop
for i = 1:length(B)-1;
    shift2 = B(i);
    B(i) = B(i)+shift;
     if B(i+1)+shift - B(i)<0
         shift = shift+shift2;
     end
end
B(length(B))=B(length(B))+shift;
B;


%%


x(:,1)=A(:,1);
x(:,2)=A(:,2);
x(:,3)=A(:,3);
x(:,4)=B(:,1);
```

```
x(:,5)=A(:,5);

x(:,6)=A(:,6);


fig1 = figure('Position',[ 100 100 650 600]);

plot((x(:,4)*1.6/1000000),(x(:,1)/1000),'LineWidth',1)

xlabel('Time [s]')

ylabel('Acceleration [gs]')

title('Accelerometer 1','FontWeight','bold')

grid on

saveas(fig1,'Accelerometer 1','bmp')


fig2 = figure('Position',[ 100 100 650 600]);

plot((x(:,4)*1.6/1000000),(x(:,2)/1000),'LineWidth',1)

xlabel('Time [s]')

ylabel('Acceleration [gs]')

title('Accelerometer 2','FontWeight','bold')

grid on

saveas(fig2,'Accelerometer 2','bmp')


fig3 = figure('Position',[ 100 100 650 600]);

plot((x(:,4)*1.6/1000000),((x(:,1)+x(:,2)/2)/1000),'LineWidth',1)

xlabel('Time [s]')

ylabel('Acceleration [gs]')
```

```
title('Accelerometer Combined','FontWeight','bold')
grid on
saveas(fig3,'Accelerometer Combined','bmp')

fig4 = figure('Position',[ 100 100 650 600]);
plot((x(:,4)*1.6/1000000),((x(:,1)+x(:,2)/2)/(1000*r)),'LineWidth',1)
xlabel('Time [s]')
ylabel('Angular Acceleration [rad/s^2]')
title('System Angular Acceleration','FontWeight','bold')
grid on
saveas(fig4,'Angular Acceleration','bmp')

fig5 = figure('Position',[ 100 100 650 600]);
plot((x(:,4)*1.6/1000000),(x(:,3)*8.75/1000),'LineWidth',1)
xlabel('Time [s]')
ylabel('Rotation [dps]')
title('Gyroscope','FontWeight','bold')
grid on
saveas(fig5,'Gyroscope','bmp')


fig6 = figure('Position',[ 100 100 650 600]);
plot((x([400:600],4)*1.6/1000000),(x([400:600],3)*8.75/1000),'LineWidth',1)
```

```
xlabel('Time [s]')

ylabel('Rotation [dps]')

title('Gyroscope','FontWeight','bold')

grid on

saveas(fig6,'Gyroscope_trim','bmp')


initial=mean(x(1,3)*8.75/1000)

initialstdev=std((x(1,3)*8.75/1000))

average=mean((x([400:600],3)*8.75/1000))

stdev=std((x([400:600],3)*8.75/1000))

difference = average-initial



fig7 = figure('Position',[ 100 100 650 600]);

[hAx,hLine1,hLine2] = plotyy((x(:,4)*1.6/1000000),((x(:,1)+x(:,2)/2)/(1000*r)),...

    (x(:,4)*1.6/1000000),(x(:,3)*8.75/1000));

title('Sensor Data','FontWeight','bold')

xlabel('Time [s]')

ylabel(hAx(1),'Angular Acceleration [rad/s^2]') % left y-axis

set(hAx(1),'xlim',[0 1.2],'ylim',[-5 5])

ylabel(hAx(2),'Gyroscope [dps]') % right y-axis

set(hAx(2),'xlim',[0 1.2],'ylim',[-15 15])

grid on
```

```
saveas(fig7,'fo-sho','bmp')


z = (x(:,4)*1.6/1000000);

y = ((0.0009863*((x(:,1)+x(:,2)/2)/(1000*r)))/(t));

[ymx,loc] = max(y);

xmx = z(loc);


fig8 = figure('Position',[ 100 100 650 600]);

plot(z,y,xmx,ymx,'rv','MarkerFaceColor','r');

text(xmx,ymx,['\leftarrowMaxForce =  ',num2str(ymx)],...

'HorizontalAlignment','left')

xlabel('Time [s]')

ylabel('Thrust [N]')

title('Force vs Time','FontWeight','bold')

grid on

saveas(fig8,'Force vs Time','bmp')


%Impulse

fig9 = figure('Position',[100 100 650 650]);

i = ((0.0009863)*(x(:,3)*8.75/1000)*(pi/180))/(2*t);

[ymax,loc] = max(i);

xmax = z(loc);
```

```
plot(z,i,xmax,ymax,'rv','MarkerFaceColor','r');

text(xmax,ymax,['\leftarrowMaxImpulseBit =  ',num2str(ymax)],...

'HorizontalAlignment','left')

xlabel('Time [s]')

ylabel('Impulse Bit [kg*m/s]')

title ('Impulse Bit vs Time','FontWeight','bold')

grid on

saveas(fig9,'Impulse Bit vs Time','bmp')


mbit = .000389/1000; %kilograms


%Specific Impulse

fig10 = figure('Position',[100 100 650 650]);

i = ((0.0009863)*(x(:,3)*8.75/1000)*(pi/180))/(t*mbit*9.81);

[ymax,loc] = max(i);

xmax = z(loc);


plot(z,i,xmax,ymax,'rv','MarkerFaceColor','r');

text(xmax,ymax,['\leftarrowSpecificImpulse =  ',num2str(ymax)],...

'HorizontalAlignment','left')

xlabel('Time [s]')

ylabel('Isp [s]')

title ('Specific Impulse vs Time','FontWeight','bold')
```

```
grid on

saveas(fig10,'Specific Impulse','bmp')
```

APPENDIX G

UNCERTAINTY ANALYSIS EXAMPLE

Example of the Taylor Series Method Propagation for Thrust Uncertainty based on the measurement equation (4) for total force:

$$T = (T_1 + T_2) = \frac{I_{zz} a}{d\Delta x} \tag{G.1}$$

The general uncertainty expression (10) for the total force T becomes:

$$U_T^2 = \left(\frac{\partial r}{\partial I_{zz}}\right)^2 U_{I_{zz}}^2 + \left(\frac{\partial r}{\partial a}\right)^2 U_a^2 \tag{G.2}$$

Taking the derivatives of T with respect to the variables and dividing by T^2, we find

$$\left(\frac{U_T}{T}\right)^2 = \left(\frac{U_{I_{zz}}}{I_{zz}}\right)^2 + \left(\frac{U_a}{a}\right)^2 \tag{G.3}$$

As an example for the baseline shown in Figure 25 with the experimental values listed in Table 1, the resulting measurement acceleration is 0.14 G. Based on the digital accelerometer LIS3DH, the resulting 95% acceleration uncertainty is 5% (0.05). Acceleration uncertainty can be reduced by increasing both d and Δx.

Table G.1: Baseline Sensitivity Parameters

Parameter	Value
$T_{1,2}$	5 (mN)
d	8.5 (cm)
Δx	8.5 (cm)
I_{zz}	$5.2\times10^{-5}(kg-m^2)$

Based on the (13), inertia uncertainty of 3% and 8% result in total force uncertainty of 5% (0.25 mN) and 9% (0.45 mN), respectively. This shows that the inertia value of the payload should be known with 95% confidence to about the same level as the accelerometer measurement.

REFERENCES

[1] Coletti, M., F. Guarducci, and S.b. Gabriel. "A Micro PPT for Cubesat Application: Design and Preliminary Experimental Results."Acta Astronautica 69.3-4 (2011): 200-08.

[2] Krejci, David, Bernhard Seifert, and Carsten Scharlemann. "Endurance Testing of a Pulsed Plasma Thruster for Nanosatellites." Acta Astronautica 91 (2013): 187-93.

[3] Messier, Doug. "SpaceWorks Review Shows Sharp Growth Expected in Nano- and Microsat Market." Parabolicarc. N.p., 20 Feb. 2013. Web. 23 Feb. 2015.

[4] Wang, Anliang, Hongwei Wu, Haibin Tang, Yu Liu, and Xing Liang. "Development and Testing of a New Thrust Stand for Micro-thrust Measurement In vacuum Conditions." Vacuum 91 (2013): 35-40.

[5] Lun, J., and C. Law. "Direct Thrust Measurement Stand with Improved Operation and Force Calibration Technique for Performance Testing of Pulsed Microthrusters." Measurement Science and Technology 25.9 (2014): N.p.

[6] Yang, Yuan-Xia, Liang-Cheng Tu, Shan-Qing Yang, and Jun Luo. "A Torsion Balance for Impulse and Thrust Measurements of Micro-Newton Thrusters." Review of Scientific Instruments 83.1 (2012): 015105.

[7] Gong, Jingsong, Lingyun Hou, and Wenhua Zhao. "Experimental Study of a Low-thrust Measurement System for Thruster Ground Tests." Review of Scientific Instruments 85.3 (2014): 035102.

[8] Orieux, S., C. Rossi, and D. Esteve. "Thrust Stand for Ground Tests of Solid Propellant Microthrusters." Review of Scientific Instruments 73.7 (2002): 2694.

[9] Burton, R. L., and P. J. Turchi. "Pulsed Plasma Thruster." Journal of Propulsion and Power 14.5 (1998): 716-35.

[10] Polzin, Kurt A., Thomas E. Markusic, Boris J. Stanojev, Amado Dehoyos, and Benjamin Spaun. "Thrust Stand for Electric Propulsion Performance Evaluation." Review of Scientific Instruments 77.10 (2006): 105108.

[11] Antropov, N. N., Krivonosov, I. G., Popov, G. A., and Rudikov, A. I., "PPT Model Experimental Refinement," AIAA Paper 96-2728, July 1996.

[12] Antropov, N., Gomilka, L., Diakonov, G., Krivonosov, I., Popov, G., and Orlov, M., "Parameters of Plasmoids Injected by PPT," AIAA Paper 97-2921, July 1997.

[13] Kimura, I., Ogiwara, K., Takegahara, H., and Suzuki, Y., "Effect of Applied Magnetic Fields on a Solid-Propellant Pulsed Plasma Thruster," AIAA Paper 79-2098, Oct. 1979

[14] Palumbo, D. J., and Guman, W. J., "Continuing Development of the Short-Pulsed Ablative Space Propulsion System," AIAA Paper 72-1154, Nov. 1972.

[15] Polk, James, Anthony Pancotti, Thomas Haag, Scott King, Mitchell Walker, Joseph Blakely, and John Ziemer. "Recommended Practices in Thrust Measurement." IEPC-2013-440, 33rd International Electric Propulsion Conference, Washington, DC (October 2013): N.p.

[16] Lugini, Claudio, and Marcello Romano. "A Ballistic-pendulum Test Stand to Characterize Small Cold-gas Thruster Nozzles." Acta Astronautica 64.5-6 (2009): 615-25.

[17] Ziemer, J., "Performance Measurement Using a Sub-Micronewton Resolution Thrust Stand," Rev, Sci. Inst., Vol. 73, No. 10, 2002, pp. 3629-3637.

[18] Xu, Kunning G., and Mitchell L. R. Walker. "High-power, Null-type, Inverted Pendulum Thrust Stand." Review of Scientific Instruments 80.5 (2009): 055103.

[19] Haag, T. W. "Thrust Stand for Pulsed Plasma Thrusters." Review of Scientific Instruments 68.5 (1997): 2060

[20] Sawka, Wayne N., Arthur Katzakian, Jr., and Charles Grix. "Solid State Digital Propulsion Cluster Thrusters For Small Satellites Using High Performance Electrically Controlled Extinguishable Solid Propellants." 19th Annual AIAA/USU Conference on Small Satellites (2004): N.p.

[21] Nicholas, Andrew, Ted Finne, Ivan Galysh, Anthony Mai, Jim Yen, Wayne Sawka, Jeff Ransdell, and Shae Williams. "Spinsat Mission Overview." SpinSat Mission Overview (2012): N.p. 27th Annual AIAA/USU Conference on Small Satellites.

[22] Sawka, Wayne N., and Michael Mcpherson. "Electrical Solid Propellants: A Safe, Micro to Macro Propulsion Technology." 49th AIAA/ASME/SAE/ASEE Joint Propulsion Conference (2013): N.p.

[23] Kang, Suk-Jin, Hyea-Ran Cho, and Young-Keun Chang. "Development and Testing of a Micro-thruster Impulse Characterization System Utilizing Pendulum Swing Time Measurements." Sensors and Actuators A: Physical 148.2 (2008): 381-87.

[24] Zhou, Wei-Jing, Yan-Ji Hong, and Hao Chang. "A MicroNewton Thrust Stand for Average Thrust Measurement of Pulsed Microthruster." Rev. Sci. Instrum. Review of Scientific Instruments 84.12 (2013): 125115.

[25] Sutton, George Paul., and Oscar Biblarz. Rocket Propulsion Elements. Hoboken, NJ: Wiley, 2010. Print.

[26] Palm, William J. Introduction to MATLAB 7 for Engineers. Dubuque, IA: McGraw-Hill, 2005. Print.

[27] Barr, Michael. "Pulse Width Modulation." Embedded Systems Programming (2001): 103-04. Print.

[28] Tan, Kok Kiong., Qing-Guo Wang, and Chang Chieh. Hang. Advances in PID Control. London: Springer, 1999. Print.

[29] Incropera, F. P., and Dewitt, D. P. (2011). Fundamentals of Heat and Mass Transfer. John Wiley and Sons, Inc.

[30] Moran, M. J., Shapiro, H. N., Boettner, D. D., and Bailey, M. B. (2011). Fundamentals of Engineering Thermodynamics. John Wiley and Sons, Inc.

[31] Serway, R. A. and Jewett, Jr. J. W. Physics for Scientists and Engineers. 6th Ed. Brooks Cole. 2003. Print.

[32] Walker, Jearl, David Halliday, and Robert Resnick. Fundamentals of Physics. Hoboken, NJ: Wiley, 2008. Print.

[33] Palm, William J. System Dynamics. Boston, MA: McGraw-Hill, 2010. Print.

[34] Hibbeler, R. C. Engineering Mechanics: Statics. Upper Saddle River, NJ: Prentice Hall, 2010. Print.

[35] Strogatz, Steven H. Nonlinear Dynamics and Chaos: With Applications to Physics, Biology, Chemistry, and Engineering.Cambridge, MA: Westview, 2000. Print.

[36] Bender, Carl M., and Steven A. Orszag. Advanced Mathematical Methods for Scientists and Engineers. New York: Springer, 1999. Print.

[37] "Autonomous Tracking Optical Measurement Laboratory (ATOM)", University of Alabama in Huntsville, 2015. Web. 20 Feb. 2015.

[38] T-Series. Vicon Camera Systems, n.d. Web. 21 Feb. 2015

[39] Jahn, Robert G. Physics of Electric Propulsion. Mineola, NY: Dover Publications, 2006. Print.

[40] "Item EM400-6-212, 4.0" Diameter Round Electromagnet." On APW Company. APW Company, n.d. Web. 25 Apr. 2015.

[41] Hicks, Fernando Mier. Characterization on a Magnetically Levitated Testbed for Electrospray Propulsion Systems. Thesis. Massachusetts Institute of Technology, 2014. n.d. Print.

[42] "Xenon Flash Tubes Store." Photoflash Capacitors Photo 360v 330v. N.p., n.d. Web. 09 June 2015.

[43] "Xenon Flash Tubes Store." Components. N.p., n.d. Web. 09 June 2015.

[44] "Vacuum Chamber." The University of Alabama in Huntsville. N.p., 04 Jan. 2013. Web. 10 June 2015.

[45] "CubeSat Design Specification Rev. 13." California State Polytechnic University. Retrieved 2014-07-07.

[46] Microchip Technology Inc., "32-bit Microcontrollers (up to 256 KB Flash and 64 KB SRAM) with Audio and Graphics Interfaces, USB, and Advanced Analog," PIC32MX1XX/2XX datasheet, 2014

[47] ST Electronics, "MEMS motion sensor: ultra-stable three-axis digital output gyroscope," L3G4200D datasheet, 12/2010

[48] ST Electronics, "MEMS digital output motion sensor ultra low-power high performance 3-axes nano accelerometer," LIS3DH datasheet, May 2010

[49] Alciatore, David G., and Michael B. Histand. Introduction to Mechatronics and Measurement Systems. Boston: McGraw-Hill, 2003. Print.

[50] Bolton, W. Mechatronics: A Multidisciplinary Approach. Harlow, England: Pearson Prentice Hall, 2011. Print.

[51] Coleman, Hugh W., and W. Glenn. Steele. Experimentation and Uncertainty Analysis for Engineers. New York: Wiley, 1999. Print.

[52] International Organization for Standardization, Guide to the Expression of Uncertainty in Measurement, ISO, Geneva, 1993.

[53] MaxStream Inc., "XBee/XBee-PRO OEM RF Modules," XBee datasheet, 2007

[54] Shaw, Peter Vallis. Pulsed Plasma Thrusters for Small Satellites. Thesis. University of Surrey, 2011. N.p.: n.p., n.d. Print.

[55] "Maglev Plus System Magnetic Levitation Experiment." Magnetic Levitation Kits. N.p., n.d. Web. 31 July 2014.

[56] Dr. Shae Williams and DSSP/UAH Team, personal communication, July 6, 2015

[57] Dr. Shae Williams and DSSP/UAH Team, personal communication, July 28, 2014